Numerical simulation of microstructural residual stresses of hot bulk forming parts with targeted cooling

Von der Fakultät für Ingenieurwissenschaften,
Abteilung Bauwissenschaften
der Universität Duisburg-Essen
zur Erlangung des akademischen Grades

Doktor-Ingenieur

genehmigte Dissertation

von

Sonja Hellebrand, M.Sc.

Hauptberichter:	Prof. Dr.-Ing. habil. J. Schröder
Korreferenten:	Prof. Dr.-Ing. B.-A. Behrens

Tag der Einreichung:	11. Januar 2023
Tag der mündlichen Prüfung:	30. August 2023

Fakultät für Ingenieurwissenschaften,
Abteilung Bauwissenschaften
der Universität Duisburg-Essen
Institut für Mechanik
Prof. Dr.-Ing. habil. J. Schröder

Berichte des Instituts für Mechanik, Universität Duisburg-Essen
Nr. 29

Herausgeber:
Prof. Dr.-Ing. habil. J. Schröder

Organisation und Verwaltung:
Prof. Dr.-Ing. habil. J. Schröder
Institut für Mechanik
Fakultät für Ingenieurwissenschaften
Abteilung Bauwissenschaften
Universität Duisburg-Essen
Universitätsstraße 15
45141 Essen
Tel.: 0201 / 183 - 2682
Fax.: 0201 / 183 - 2680

ISBN 978-3-9821811-5-8

DOI: 10.17185/duepublico/79175
URN: urn:nbn:de:hbz:465-20231024-075456-3

Preface

Die vorliegende Arbeit entstand während meiner Tätigkeit als wissenschaftliche Mitarbeiterin am Institut für Mechanik (Abt. Bauwissenschaften, Fak. Ingenieurwissenschaften) an der Universität Duisburg-Essen im Rahmen des durch die Deutsche Forschungsgemeinschaft (DFG) finanzierten Projekts 374871564 (BE 1691/223-1/2, BR 5278/3-1/2, SCHR 570/33-1/2, Schwerpunktsprogramm SPP2013 „Eigenspannungen“). An dieser Stelle möchte ich der DFG für die finanzielle Unterstützung danken und darüber hinaus meine persönliche Wertschätzung einigen Menschen entgegenbringen, die das Gelingen dieser Arbeit maßgeblich beeinflusst haben.

Mein aufrichtiger Dank gilt dabei zunächst meinem Doktorvater, Herrn Prof. Dr.-Ing. habil. Jörg Schröder, welcher es mir ermöglichte unter seiner Leitung am Institut zu forschen und zu promovieren. In all den Jahren konnte ich mir seines Vertrauens, seiner Förderung und seines Rates stets sicher sein. Auch in komplizierten Lebenslagen lehrte er mich durch seine Ruhe, einen kühlen Kopf zu bewahren, und strahlte immer einen hohen Grad an Motivation aus. Des Weiteren danke ich Herrn Prof. Dr.-Ing. Bernd-Arno Behrens für die Übernahme des Korreferates sowie für die gute Zusammenarbeit während meiner gesamten Promotionszeit. Das gemeinsame Forschungsprojekt und die damit verbundene Verzahnung von Experiment und Simulation ermöglichte die erstandene Arbeit überhaupt.
Ich möchte außerdem Frau Jun.-Prof. Dr.-Ing. Lisa Scheunemann und Herrn Dr.-Ing. Dominik Brands meinen herzlichen Dank aussprechen, die mir bis heute Vorbilder sind. Nicht nur für fachliche sondern auch für persönliche Angelegenheiten nahmen sie sich stets Zeit. Vor allem zu Beginn meiner Tätigkeit leiteten sie mich an, sodass ich vieles lernen und mich weiterentwickeln konnte. Die zahlreichen interessanten Diskussionen bereicherten meinen Institutsalltag sehr. Auch danke ich Christoph Kock und Hendrik Wester, welcher mir immer mit Rat und Tat zur Seite standen und alle umformtechnischen Fragestellungen kleinschrittig und geduldig aufbereiteten.
Mein weiterer Dank geht an alle meine jetzigen und ehemaligen mechanischen Wegbegleiter am Institut für Mechanik, Solveigh Averweg, Marcos Margalho de Barros, Joachim Bluhm, Simon Fausten, Philipp Hartwig, Yasemin und Markus von Hoegen, Sascha Maassen, Simon Maike, Marvin Koßler, Simon Kugai, Matthias Labusch, Veronika Lemke, Rainer Niekamp, Mangesh Pise, Markus Prangs, Maximilian Reichel, Sabine Ressel, Mohammad Sarhil, Maximilian Scheunemann, Carina und Alexander Schwarz, Serdar Serdas, Julia Sunten und Nils Viebahn. Ich konnte mir immer sicher sein, Unterstützung und Hilfe zu erfahren, aber auch Motivation, Ablenkung und eine freundschaftliche Atmosphäre zu finden. Auch vielen Dank für die vielen von euch, die sich in ihrer Freizeit mit der Korrektur meiner Dissertation befasst haben.

Abschließend gilt mein herzlicher Dank meinen Eltern Dr. Monika Volmer-Uebing und Dr. Christian Uebing, welche mich immer ermutigt haben, meine Träume zu verfolgen, meiner Schwester Judith Uebing, die für notwendige Zerstreuung sorgte, sowie meiner Schwiegerfamilie, welche immer Interesse und Verständnis zeigte. Zu guter Letzt danke ich meinem Mann Matthias, der mich auf dem gesamten Weg begleitete und zu jeder Zeit bedingungslos hinter mir stand.

Essen, im Oktober 2023 Sonja Hellebrand

Abstract

The present work aims at the investigation of residual stresses in a component on several scales. For this purpose, a numerical simulation tool is developed using the Finite Element Method. An essential aspect of this approach, besides the discretization of the geometry to be investigated and the definition of the algebraic system of equations to be solved, is the definition of a suitable material model. The microheterogeneous structure of materials such as steel must be taken into account during the analysis. Since this work focuses on the numerical investigation of the evolution of residual stresses in hot bulk forming processes of steel components, a model for the representation of occurring phase transformation on the microscale is additionally required. To this end, a single-scale finite element model in combination with its constitutive equations is introduced, which is used to calculate effective material properties and resulting stresses especially during cooling of a hot bulk forming component. Different cooling routes influence the stress development in the component on all scales. Thus, multi-scale methods are a valuable tool for the analysis of macroscopic and microscopic residual stresses. Subsequently, different representative volume elements are discussed, which are used to describe a phase transformation in a microscopic boundary value problem within a multi-scale finite element method. This approach enables to calculate stresses during the cooling process as well as the final residual stress states at the different scales.

Zusammenfassung

Die vorliegende Arbeit verfolgt als Ziel die Untersuchung von Eigenspannungen in einem Bauteil auf mehreren Skalen. Zu diesem Zweck wird ein numerisches Simulationsmodell unter Verwendung der Finiten Elemente Methode entwickelt. Ein wesentlicher Aspekt dieses Ansatzes ist, neben der Diskretisierung der zu untersuchenden Geometrie und der Definition des zu lösenden algebraischen Gleichungssystems, die Festlegung eines geeigneten Materialmodells. Die mikroheterogene Struktur von Werkstoffen wie Stahl ist bei der Analyse zu berücksichtigen. Da in dieser Arbeit die numerische Betrachtung der Eigenspannungsentwicklung bei der Warmummassivformung von Stahlbauteilen im Vordergrund steht, ist zusätzlich ein Modell zur Darstellung auftretender Phasenumwandlungen auf der Mikroskala unerlässlich. Aus diesem Grund wird ein einskaliges Finite Elemente Modell in Kombination mit seinen konstitutiven Gleichungen eingeführt, mit dem die effektiven Materialeigenschaften und die resultierenden Spannungen insbesondere während der Abkühlung eines warmmassivumgeformten Bauteils berechnet werden. Unterschiedliche Abkühlrouten beeinflussen dabei die Spannungsentwicklung im Bauteil auf allen Skalen. Somit sind Multiskalenmethoden ein wertvolles Werkzeug für die Analyse makro- sowie mikroskopischer Eigenspannungen. Anschließend werden verschiedene repräsentative Volumenelemente eingeführt, die zur Beschreibung einer Phasenumwandlung in einem mikroskopischen Randwertproblem innerhalb einer multiskalen Finite Elemente Methode verwendet werden. Mit diesem Ansatz lassen sich sowohl die Spannungen während des Abkühlvorgangs als auch die endgültigen Eigenspannungszustände auf den verschiedenen Skalen bestimmen.

Contents

Glosssary

$\boldsymbol{B}^e$	element B-matrix
$\boldsymbol{b}$	body forces
$\boldsymbol{C}$	right Cauchy-Green deformation tensor
$\mathbb{C}$	material tangent
$\boldsymbol{d}_I$	discrete nodal displacement vector
$\delta\boldsymbol{d}_I$	virtual nodal displacement vector
$\Delta\boldsymbol{d}_I$	incremental nodal displacement vector
$\boldsymbol{D}$	global nodal displacement vector
$\boldsymbol{E}$	Green-Lagrange strain tensor
$\boldsymbol{F}$	deformation gradient
$\boldsymbol{I}$	second order identity tensor
$\boldsymbol{k}^e$, $\boldsymbol{K}$	element stiffness matrix and global stiffness matrix
$\boldsymbol{L}$	spatial velocity gradient
$\boldsymbol{N}$, $\boldsymbol{n}$	outer normal vector
$\mathbb{P}$	fourth order projection tensor
$\boldsymbol{P}$	first Piola-Kirchhoff stress tensor
$\boldsymbol{q}$	heat flux vector
$\boldsymbol{r}^e$, $\boldsymbol{R}$	element residual vector and global residual vector
$\boldsymbol{S}$	second Piola-Kirchhoff stress tensor
$\boldsymbol{u}$	discrete displacement vector
$\delta\boldsymbol{u}$	virtual displacement
$\Delta\boldsymbol{u}$	incremental displacement
$\boldsymbol{t}_0$, $\boldsymbol{t}$	traction vector
$\boldsymbol{X}$, $\boldsymbol{x}$	position vector in reference and actual configuration
$\dot{\boldsymbol{x}}$, $\boldsymbol{v}$	velocity
$\ddot{\boldsymbol{x}}$, $\boldsymbol{a}$	acceleration
$\boldsymbol{\varepsilon}$, $\dot{\boldsymbol{\varepsilon}}$	strain tensor and its rate in linearized strain theory
$\boldsymbol{\varepsilon}^{\theta}$	thermal strains
$\boldsymbol{\varepsilon}^{\mathrm{e}}$	elastic strains
$\boldsymbol{\varepsilon}^{\mathrm{p}}$	plastic strains
$\boldsymbol{\varepsilon}^{\mathrm{trip}}$	transformation induced plasticity strains
$\boldsymbol{\varepsilon}^{\mathrm{tv}}$	transformation volumetric strains
$\boldsymbol{\sigma}$	true stress or Cauchy stress
$\boldsymbol{\sigma}^{\mathrm{RS}}$	residual stress
$\boldsymbol{\sigma}^{\mathrm{RS}}_{\mathrm{I}}$	residual stress of first type
$\boldsymbol{\sigma}^{\mathrm{RS}}_{\mathrm{II}}$	residual stress of second type
$\boldsymbol{\sigma}^{\mathrm{RS}}_{\mathrm{III}}$	residual stress of third type
$\boldsymbol{\tau}$	nominal stress
$\boldsymbol{\varphi}$	mapping between configurations
$\boldsymbol{\xi}$	isoparametric coordinates

A	area
c^i	volume fraction of phase $i \in \{\mathrm{A}, \mathrm{M}, \mathrm{P}\}$ for austenite, martensite and pearlite
c_ρ	product of specific heat capacity and density
$\mathrm{d}X$, $\mathrm{d}x$	line elements
$\mathrm{d}A$, $\mathrm{d}a$	area elements
$\mathrm{d}V$, $\mathrm{d}v$	volume elements
$f(c^\mathrm{M})$	saturation function, $f(c^\mathrm{M} = 0) = 0$, $f(c^\mathrm{M} = 1) = 1$, e.g. $f(c^\mathrm{M}) = (2 - c^\mathrm{M})c^\mathrm{M}$
h	linear hardening parameter
h_TC	heat transfer coefficient
J	Jacobian
$k > 0$	heat conduction coefficient
K_JMAK	constant
K_trip	scalar parameter for TRIP strain rate
K_tv	volumetric expansion of atomic lattice
N_I	shape functions at node I
n	Avrami-exponent
Q_0	material parameter
r	heat source
t	time
y	yield stress
$\mathcal{B}$, $\mathcal{B}_0$	body or continuum in reference and actual configuration
$\partial\mathcal{B}$, $\partial\mathcal{B}_0$	boundary of the body in reference and actual configuration
α	strain like internal variable
α_T	heat conduction coefficient
β	stress-like conjugated variable
δ	exponential hardening parameter
η, $\dot{\eta}$	specific entropy and its rate
κ	bulk modulus
λ	plastic Lagrange multiplier
μ	shear modulus
Φ	yield surface
ρ	density
ψ, $\dot{\psi}$	free energy function and its time derivative
θ_0	initial temperature
θ, $\dot{\theta}$	actual temperature and its rate
θ_∞	ambient temperature
θ_Ms	martensitic start temperature
θ_M0	temperature independent material parameter
θ_RT	room temperature
ω	wighting factor for Gauss point

1 Introduction

Residual stresses are of major importance in the production of components and their application in the field of engineering. These internal stresses are superimposed with external stresses, which are a consequence of external forces and moments. The origin of residual stresses are manifold, e.g. they can be evoked by temperature gradients or phase transformations or other influencing factors. For a long time, residual stresses were considered to have a negative effect on various properties, such as service life, durability and usability by a reduction of failure limits or higher brittleness. As a consequence, the aim was to eliminate or at least minimize residual stresses in components, for instance by subsequent heat treatment after the manufacturing process or shot peening or laser peening as mechanical treatments, cf. Hall and Mudawar [66], Michaleris et al. [117], Camilleri et al. [24] and Cloots et al. [29]. However, this disregards the possibility that a change in properties can also have positive effects. Recent publications show, that residual stresses can be inserted in a component during its forming with improving its properties, see Kästner and Volk [88] and Volk [194; 195] among others. For instance, residual stresses can increase the service life of a component if they counteract the direction of the operational stress, i.e., compressive residual stresses can reduce crack formation or crack propagation under tensile loading. Nevertheless, it is important to note that residual stresses are always in equilibrium, i.e., if compressive residual stresses are induced in one part of the component, tensile residual stresses will result in another part. If possible, this last area should be selected in such a way that the tensile residual stresses occur in a lightly loaded part of the component, since they have a crack-opening effect. This targeted induction of residual stresses in the manufacturing process with a view to improving properties is therefore part of current research. Exemplary components in this context are crankshafts or connecting rodes, as shown in Figure 1.1.

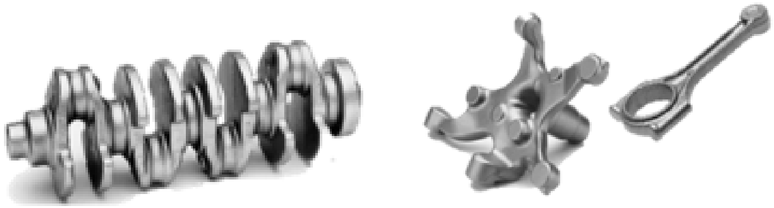

Figure 1.1: Exemplary components, for which current research focuses on the induction of targeted residual stress states: a crankshaft, a part of a wheel suspension and a connecting rod.

Following the definition of Macherauch et al. [108], residual stresses are classified by the scale, they act on. Residual stresses of first type are also called macroscopic stresses. They are in equilibrium over the complete component or at least several grains. Residual stresses of second and third type are referred to as microscopic stresses. They are distinguished in such a way that residual stresses of second type classify the fluctuations of the residual stresses of first type with respect to the average of one grains, while residual stresses of third type denote the difference between the true local stresses and the sum of the residual stresses of first and second type. This definition of residual stresses on multiple scales motivate the aim of this thesis: the multi-scale investigation of residual stresses in hot bulk forming parts.

These hot bulk forming processes offer the possibility to exploit different interactions, such as interactions of thermal, metallurgical or mechanical kind. They are based on the chemical composition of a material, are closely interlocked and influence each other mutually, see Figure 1.2. In general, the different process steps of hot bulk forming are heating, forming and cooling, each of them taking influence on the final residual stress profile of the component made from steel. Aspects as the choice of the chemical constitution, the heating temperature, the forming speed or the cooling route, among others, effect the outcoming component's properties. The initial heating leads to an austenization of the material and thereby a kind of elimination of previously present residual stresses due to manufacturing of the material and/or due to the forming of the initial geometry. After the forming step especially the last process step, the cooling, has major influence on the microstructural evolution. Depending on the cooling rate, the starting and target temperature, different phases can evolve from the austenitic parent phase. The resulting microstructures show varying properties, e.g. martensitic microstructures are known for very high strength while bainitic microstructures possess good ductility. These phase transformations are characterized by a change of the atomic lattice structure, often taken into account as a volumetric expansion of the atomic unit cell, which can also be accompanied by a shearing. As a consequence, macro- and microscopic residual stresses arise in the material.

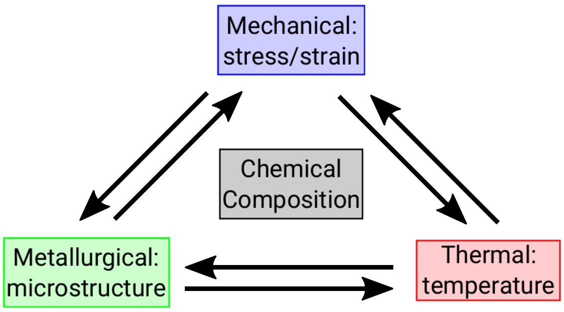

Figure 1.2: In hot bulk forming processes, it is possible to exploit the interactions of thermal, mechanical and metallurgical kind based on the chemical composition of the material under consideration.

Experimental investigations are an important tool to understand the relation between the manufacturing process and the final component's properties, since small changes can effect the properties immensely. In order to gain a profound knowledge of the connection of the different aspects, such as microscopic phase transformation or thermal distortion, it is inevitable to use numerical analysis tools. In general, the last decades proofed that the utilization of numerical methods to analyze or design structures in several engineering application are very useful. Such numerical investigation can provide information regarding stress and strain distributions inside the material. These cannot or can only be accessed with high efforts in experiments. Especially, the measurement of residual stresses are very complex and not always exact, particularly with respect to in depth measurements, see for instance ROHRBACH [146], KANDIL ET AL. [86] and ROSSINI ET AL. [148]. Many methods to determine residual stresses in the depth of a component are destructive and thereby, measurements cannot be taken twice. These include, among others, the deep hole drilling or the contour method. Measurements using non-destructive methods such as X-Ray diffraction, neutron diffraction or ultrasonic can be repeated, but they are only used to determine residual stresses in regions near the surface, i.e., up to a depth of a few micrometers for steel. Moreover, in order to determine residual stresses, a phenomenological theory is required. This means that the strains or displacements of a component are measured and then converted into stresses by means of suitable correlations, e.g. Hooke's law. This gives room for inaccuracies and hence, numerical simulations seem advantageous.

Such numerical methods to investigate residual stresses and/or to depict microscopic phase transformations are numerous. One possibility is the application of a phase field approach or a multi-phase field approach. First fundamental work regarding multi-phase models was presented by Steinbach et al. [173], Tiaden et al. [184] and Steinbach and Pezzolla [172]. These approaches map the microscale with possible grains in a fine resolution and give information about the growth of product phases in a parent phase. For example, the evolution of different martensitic variants in an initially austenitic microstructure can be represented, see e.g. Wang and Khachaturyan [196; 197], Artemev et al. [2], Levitas and Preston [104], Yeddu et al. [208], Mamivand et al. [114] or Yeddu [207]. Another possibility is to use single-scale phenomenological material models, which calculate the volume fractions of the individual phases and determine effective material parameters or effective stresses and material tangents thereon. In case of austenite-to-martensite phase transformation, early works to describe the transformation strain of the atomic lattice have been proposed by Bain and Dunkirk [7] and Bain and Griffiths [8]. Additionally, important developments for application of martensite formation as solid phase transformation are presented in Wechsler [198], Roitburd [147], Leblond et al. [100; 101], Fischer [46; 49; 50], Fischer et al. [47; 48], Petit-Grostabussiat et al. [142], Hallberg et al. [67; 68], Wolff et al. [203; 204; 205] and Mahnken et al. [110].

For the computation of such a classical phenomenological description of the material behavior the Finite Element Method (FEM) provides a suitable tool, which has first been established in the 1960's. The idea of the FEM is to approximate or simplify the solution of a problem, which would otherwise not be solvable or only with difficulty. Therefore, the computational domain is discretized in smaller areas (2D problem) or volumes (3D problem) of simple geometry, which are called finite elements. On each finite element, the material behavior is described in terms of continuum mechanical equations. As a consequence, an assembled algebraic system of equations on the whole domain is solved using numerical techniques to obtain the unknown function, see e.g. Wriggers [206], Bathe [13] and Zienkiewicz and Taylor [210]. The FEM is used in many different fields of engineering application such as civil engineering or biomechanics, to name just two. Moreover, multiscale finite element simulations offer the possibility to get an insight on the different scales. Therein, the macroscale refers to the component itself, while a subscale, the microscale, resolves the heterogeneous microstructure. Fundamental works, but not limited to, can be found in Smit [171], Suquet [175], Moulinec and Suquet [127], Smit et al. [170], Miehe et al. [121; 122], Feyel [44], Michel et al. [118], Terada et al. [182], Feyel and Chaboche [45], Geers et al. [57] and Schröder [161; 162] and from then on the method has been well established in many research fields. The main idea of the direct macro-micro transition approach or also called FE^2 method is to combine a macroscopic boundary value problem of the FEM with microscopic boundary value problems. Therefore, the macroscopic geometry is discretized with finite elements and in every macroscopic integration point a microscopic boundary value problem is attached. The latter describes microheterogeneous structures on a representative volume element (RVE). The term RVE has been established by HILL [78] as a microstructure with a sufficient number of inclusions, such that it describes the material response independent from surface tractions or displacements. From there on, different definitions of the RVE has been given, for instance by HASHIN [70], DRUGAN AND WILLIS [33], OSTOJA-STARZEWSKI [137] or STROEVEN ET AL. [174]. For a summary on RVEs, please refer to ZEMAN [209] and the references noted therein. For upscaling, i.e., for passing information from the microscopic boundary value problem to the macroscopic scale, homogenization techniques are required to determine averaged macroscopic quantities.

In general, stresses at component (macroscopic) level are determined by homogenization, i.e., by averaging the microscopic stress fluctuations. This means that possible tensile or compressive stress peaks of these fluctuations, which exceed the macroscopically averaged value in magnitude, cannot be measured. However, these are essential if the performance or service life of a component is to be predicted, since microcracks can occur as a result, which adversely affect the properties.

- In order to investigate residual stresses of different types in hot bulk forming processes, this work is organized as follows. *Section 2* summarizes the main aspects of the theory of continuum mechanics, which is a phenomenological field theory to describe field quantities for fluids or solids. The kinematics of a body, the concept of stress, which occurs as a consequence of outer or inner forces and moments, balance principles as well as the key aspects of material modeling are described.

- Afterwards in *Section 3*, the Finite Element Method is introduced starting with the definition of a boundary value problem, for which a variational form has to be set up. Furthermore, the linearization of the boundary value problem, which is solved applying Newton's method as well as the discretization with finite elements is discussed. In case of a thermo-mechanical coupling the balance of energy has to be taken into account and coupling terms to the mechanical part are required. In a last step, surface elements are defined which are helpful in order to depict a flux, e.g. a heat flux, over the boundary of the body.

- *Section 4* introduces the theory of phase transformation in solids. During the manufacturing process of components made of steels, phase transformations play an important role, since they influence the component's final properties. Several approaches are outlined, that are available for representing these in numerics. It is explained, what phases are, which one can occur and how their evolution can be modeled numerically. Different equations to compute the actual volume fractions of the phases are given, which are the well established Johnson-Mehl-Avrami-Kolmogorov equation and the Koistinen-Marburger differential equation. Moreover, phase transformations are one cause of residual stresses in the material, which also affect the out coming properties decisively. Thus, in this Section, the three different type of residual stresses are defined, based on the scale, they act on.

- A model to take into account phase transformations in a single-scale phenomenological material description is proposed in *Section 5*. As the name suggests, the temperature plays an important role in hot bulk forming processes. Thus, the model bases on an additive split of the strain tensor into five parts, namely elastic, plastic, thermal, transformation volumetric and transformation induced plasticity (TRIP) strains. Required material parameters for the individual phases present as well as the constitutive equations are derived.

- In *Section 6*, different two-dimensional numerical examples are analyzed. The first example serves for comparing different possibilities to compute the effective material behavior, of which one is chosen for following up computations. In course of numerically investigating the hot bulk forming process of a cylindrical specimen with eccentric hole, first the experimental set-up is presented. Thereby, different input parameters for the numerical analysis, such as the final volume fractions, are obtained. A convergence study regarding the discretization in space and time is carried out in a second step. Finally, the cooling step of the hot bulk forming process is investigated. Therefore, various cooling routes are considered, since different cooling paths result in different phase transformations which evoke different stress profiles. Additionally, residual stresses are obtained in the material which are discussed. Furthermore, phase-specific stress contributions as well as the influence of the TRIP strains are in focus of an investigation.

- Complementary to the two-dimensional analysis, three-dimensional computations are presented in *Section 7*. It is shown that it is inevitable to take into account the third direction during the cooling of hot bulk forming parts, since in 2D the heat can radiate over the outer boundary of the specimen but the heat dissipation over the height of the component is neglected.

- Since the previous computations have only been single-scale, it is not possible to distinguish the residual stresses into the three different types. Thus, in *Section 8* a two-scale Finite Element Method is derived, which is also known as FE^2 approach. This direct-micro-macro transition approach solves one boundary value problem on the macroscale and in each macroscopic integration point a microscopic boundary value problem is attached. In order to bridge the scales, a homogenization scheme is used. On the minor scale, the material model of Section 5 is adapted and the phase transformation is incorporated in order to analyze the influence of a microscopic phase transformation and the evolving stresses on the macroscopic behavior of the component. Therewith, the FE^2 method provides a suitable tool to analyze microscopic residual stresses as well as macroscopic residual stresses and to relate in between.

- This FE^2 approach shall be utilized in Section 10 to investigate the cooling of a specimen with taking into account a microscopic phase transformation. Therefore, at first, in *Section 9* different possible representative volume elements are defined and their advantages as well as disadvantages are discussed. In order to do so, macroscopic and microscopic quantities such as stress components, strain components or the equivalent plastic strains are compared. Furthermore, the influence of the grain orientation during a phase transformation is analyzed.

- Based thereon, suitable RVEs are chosen to carry out the two-scale analyses in *Section 10*. Therein, a mesh density and time step size study is carried out and the microscopic residual stress distribution is investigated. Quadratic measures of the microscopic fluctuations are evaluated in order to assess the influence of the microscopic residual stresses on the macroscopic residual stresses.

- *Section 11* gives a conclusion of the thesis and proposes different possibilities for future work.

In this work, all computations are carried out with the Finite Element Analysis Program (FEAP) in version 8.2, see Taylor [177], in combination with the Pardiso Solver, see Schenk and Gärtner [151], provided by the Intel Math Kernel Library in version 10.1.3.027.

2 Fundamentals of continuum mechanics

Real, physical materials show highly complex discrete structures with microstructural inhomogeneities on atomistic scale. Their behavior under external influences is determined by the interactions of atoms and molecules. However, such a detailed resolution of atomistic characteristics is often not necessary and far too costly for engineering application. As a method, which is more efficient but at the same time accurate enough, the theory of continuum mechanics as phenomenological field theory can be applied. It describes the motion and deformation of a body, which is assumed to be a continuum, as well as internal stresses resulting from that deformation. In order to do so, balance principles are fundamental to describe the physical laws, for which the real material structure is replaced by field quantities such as velocity or temperature for instance. The theory of continuum mechanics can be applied for fluids or solids to describe e.g. thermal or electromagnetic field quantities, such as temperature of magnetic flux. Details on the method of continuum mechanics are given in Truesdell and Noll [186], Eringen [36], Ogden [132] and Altenbach [1], among others. In the following, a summary on the kinematics, stresses and balance principles is given.

2.1 Kinematics

The first part of continuum mechanics is kinematics, which is concerned with geometrical aspects of a body's movement. It enables statements regarding local properties of deformation in the undeformed or deformed state. Therefore, a body in the euclidean space $\mathcal{B} \in \mathbb{R}^3$ is defined as a collection of material points $\mathcal{P}$, which are each given by a position vector, see Figure 2.1. In the undeformed or reference configuration $\mathcal{B}_0$ at initial time $t = t_0$ the position vector is given as $\boldsymbol{X}$ with respect to the origin of the space $\mathbf{0}$. The boundary of the body is denoted by $\partial\mathcal{B}_0$.

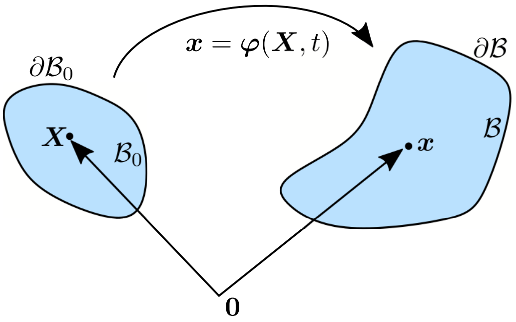

Figure 2.1: Relation of reference and actual configuration.

In order to describe the motion and deformation of the body, an actual configuration has to be defined at time $t = t_0 + \Delta t$, $\Delta t \neq 0$, with corresponding position vector $\boldsymbol{x}$ with respect to the origin $\mathbf{0}$. The actual and reference configuration are related by the motion function $\boldsymbol{\varphi}$, which describes the unique mapping of a material point from its position in the reference configuration to its position in the actual placement. It holds that

$$\boldsymbol{\varphi} : \mathcal{B}_0 \to \mathcal{B} \,, \qquad \boldsymbol{x} = \boldsymbol{\varphi}(\boldsymbol{X}, t) \text{ and } \boldsymbol{X} = \boldsymbol{\varphi}^{-1}(\boldsymbol{x}, t) \,. \tag{2.1}$$

The partial derivative of the mapping with respect to the reference position vector results in the so-called deformation gradient

$$\boldsymbol{F}(\boldsymbol{X},t) = \frac{\partial \boldsymbol{\varphi}(\boldsymbol{X},t)}{\partial \boldsymbol{X}}\,, \tag{2.2}$$

which represents the local, kinematic properties as a consequence of the body's deformation. The deformation gradient describes the transformation of a line element from reference to actual configuration, and hence can be interpreted as the length change of a line element inside the body $\mathcal{B}$, expressed as

$$\mathrm{d}\boldsymbol{x} = \boldsymbol{F}(\boldsymbol{X},t) \cdot \mathrm{d}\boldsymbol{X}\,. \tag{2.3}$$

In order to ensure the deformation of a body is invertible, it is required that the deformation gradient $\boldsymbol{F}$ is non-singular, i.e., $\det \boldsymbol{F} > 0$. Then, the inverse of Equation (2.3) results in

$$\mathrm{d}\boldsymbol{X} = \boldsymbol{F}^{-1}(\boldsymbol{X},t) \cdot \mathrm{d}\boldsymbol{x}\,, \tag{2.4}$$

with $\boldsymbol{F}^{-1}$ as inverse tensor of the deformation gradient. Similar to line elements, the following relations for area elements, $\mathrm{d}\boldsymbol{a}$ and $\mathrm{d}\boldsymbol{A}$, and volume elements, $\mathrm{d}v$ and $\mathrm{d}V$, in actual and reference configuration, respectively, can be formulated as well. The Jacobian is defined as $J := |\det \boldsymbol{F}|$, such that it holds that

$$\mathrm{d}v \;=\; J\mathrm{d}V \quad \text{and} \quad \mathrm{d}\boldsymbol{a} \;=\; J\boldsymbol{F}^{-T} \cdot \mathrm{d}\boldsymbol{A}\,. \tag{2.5}$$

The presented relations in Equations (2.3) and (2.5) are known as transport theorems, which are also depicted in Figure 2.2.

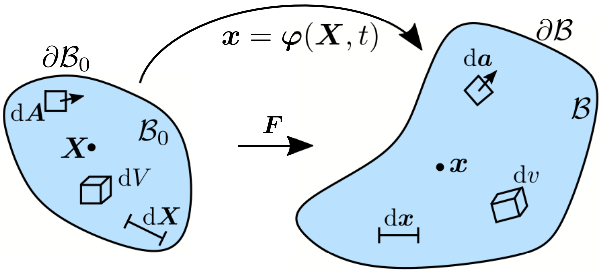

Figure 2.2: Visualization of transport theorems for line element, area element and volume element.

The Jacobian J represents a measure of the volume change during deformation. Thus, $J < 0$ stands for a penetration of the body by itself which is highly non-physical and permitted. For an alternative representation of the deformation gradient, the displacement vector $\boldsymbol{u}$ can be used. It is defined as the difference of the position vector in actual and reference configuration, i.e.,

$$\boldsymbol{u}(\boldsymbol{X},t) := \boldsymbol{x}(\boldsymbol{X},t) - \boldsymbol{X}\,. \tag{2.6}$$

For the purpose of computing the part of a body's deformation which evokes internal forces inside the body, the deformation gradient is multiplicatively decomposed into a stretch and a rotational part. The polar decomposition reads

$$\boldsymbol{F} \;=\; \boldsymbol{R} \cdot \boldsymbol{U} \;=\; \boldsymbol{V} \cdot \boldsymbol{R}\,, \tag{2.7}$$

with $\boldsymbol{R}$ as orthogonal rotation tensor, i.e., $\boldsymbol{R}\cdot\boldsymbol{R}^{\mathrm{T}}=\boldsymbol{I}$ and $\det\boldsymbol{R}=1$, that causes a rigid body rotation. The symmetric and positive definite tensors $\boldsymbol{U}:=(\boldsymbol{F}^{\mathrm{T}}\cdot\boldsymbol{F})^{\frac{1}{2}}$ and $\boldsymbol{V}:=(\boldsymbol{F}\cdot\boldsymbol{F}^{\mathrm{T}})^{\frac{1}{2}}$, i.e., it holds $\boldsymbol{U}=\boldsymbol{U}^{\mathrm{T}}$ and $\boldsymbol{V}=\boldsymbol{V}^{\mathrm{T}}$, are called right (material) and left (spatial) stretch tensors, respectively. They describe a dilatation, meaning stretching or compression, along their principal axis.

Taking into account line elements in actual and reference configuration, $\mathrm{d}\boldsymbol{x}$ and $\mathrm{d}\boldsymbol{X}$, the following relations can be derived with help of Equation (2.3)

$$\mathrm{d}\boldsymbol{x}\cdot\mathrm{d}\boldsymbol{x}=\mathrm{d}\boldsymbol{X}\cdot\underbrace{(\boldsymbol{F}^{\mathrm{T}}\cdot\boldsymbol{F})}_{:=\boldsymbol{C}}\cdot\mathrm{d}\boldsymbol{X}\quad\text{and}\qquad\mathrm{d}\boldsymbol{X}\cdot\mathrm{d}\boldsymbol{X}=\mathrm{d}\boldsymbol{x}\cdot\underbrace{((\boldsymbol{F}^{-1})^{\mathrm{T}}\cdot\boldsymbol{F}^{-1})}_{:=\boldsymbol{B}^{-1}}\cdot\mathrm{d}\boldsymbol{x}\,.\tag{2.8}$$

Thereby, the right Cauchy-Green deformation tensor $\boldsymbol{C}$ and the left Cauchy-Green (Finger) deformation tensor $\boldsymbol{B}$ are defined in reference and actual configuration as

$$\boldsymbol{C}:=\boldsymbol{U}^2=\boldsymbol{F}^T\cdot\boldsymbol{F}\quad\text{and}\qquad\boldsymbol{B}:=\boldsymbol{V}^2=\boldsymbol{F}\cdot\boldsymbol{F}^{\mathrm{T}}\,.\tag{2.9}$$

Since these deformation measures are based on the square of line elements in reference configuration $\mathrm{d}\boldsymbol{X}^2$ and in actual configuration $\mathrm{d}\boldsymbol{x}^2$, they do not preserve information about the rotation of the body $\mathcal{B}$. The difference of such line elements gives strain tensors, which are the Green-Lagrange strain tensor $\boldsymbol{E}$ in reference configuration and the Almansi strain tensor $\boldsymbol{A}$ in actual placement, i.e.,

$$\mathrm{d}\boldsymbol{x}^2-\mathrm{d}\boldsymbol{X}^2=\mathrm{d}\boldsymbol{x}\cdot(\boldsymbol{I}-\boldsymbol{B}^{-1})\cdot\mathrm{d}\boldsymbol{x}\qquad\Rightarrow\ \boldsymbol{A}=\frac{1}{2}(\boldsymbol{I}-\boldsymbol{B}^{-1})\,,\tag{2.10}$$

$$\mathrm{d}\boldsymbol{x}^2-\mathrm{d}\boldsymbol{X}^2=\mathrm{d}\boldsymbol{X}\cdot(\boldsymbol{C}-\boldsymbol{I})\cdot\mathrm{d}\boldsymbol{X}\qquad\Rightarrow\ \boldsymbol{E}=\frac{1}{2}(\boldsymbol{C}-\boldsymbol{I})\,,\tag{2.11}$$

with $\boldsymbol{I}$ as second order unity tensor. They are symmetric, i.e., $\boldsymbol{A}=\boldsymbol{A}^{\mathrm{T}}$, $\boldsymbol{E}=\boldsymbol{E}^{\mathrm{T}}$, and related by the deformation gradient by $\boldsymbol{E}=\boldsymbol{F}^{\mathrm{T}}\cdot\boldsymbol{A}\cdot\boldsymbol{F}$ and $\boldsymbol{A}=(\boldsymbol{F}^{\mathrm{T}})^{-1}\cdot\boldsymbol{E}\cdot\boldsymbol{F}^{-1}$, respectively. Their respective counterparts are the Lagrange-Karni-Rainer tensor $\boldsymbol{K}^{\mathrm{R}}$ and the Eulerian-Karni-Rainer tensor $\boldsymbol{K}$ as

$$\boldsymbol{K}^{\mathrm{R}}=\frac{1}{2}(\boldsymbol{I}-\boldsymbol{C}^{-1})\quad\text{and}\quad\boldsymbol{K}=\frac{1}{2}(\boldsymbol{B}-\boldsymbol{I})\,.\tag{2.12}$$

In addition to the displacement given in Equation (2.6), the velocity and acceleration of a material point can be defined in reference and actual configuration. In general, a velocity or acceleration field is defined as partial derivative of the considered tensor field with respect to time. Thus, it holds for the reference placement that

$$\dot{\boldsymbol{x}}(\boldsymbol{X},t)=\frac{\partial\boldsymbol{\varphi}(\boldsymbol{X},t)}{\partial t}=\dot{\boldsymbol{\varphi}}(\boldsymbol{X},t)\,,\tag{2.13}$$

$$\ddot{\boldsymbol{x}}(\boldsymbol{X},t)=\frac{\partial^2\boldsymbol{\varphi}(\boldsymbol{X},t)}{\partial t^2}=\ddot{\boldsymbol{\varphi}}(\boldsymbol{X},t)\,,\tag{2.14}$$

and for the actual placement that

$$\boldsymbol{v}(\boldsymbol{x},t)=\dot{\boldsymbol{x}}(\boldsymbol{X},t)=\dot{\boldsymbol{x}}(\boldsymbol{\varphi}^{-1}(\boldsymbol{x},t),t)\,,\tag{2.15}$$

$$\boldsymbol{a}(\boldsymbol{x},t)=\ddot{\boldsymbol{x}}(\boldsymbol{X},t)=\ddot{\boldsymbol{x}}(\boldsymbol{\varphi}^{-1}(\boldsymbol{x},t),t)\,.\tag{2.16}$$

Analogously to the partial derivative of a tensor field with respect to time, a derivative with respect to space of the quantities can be defined. Hence, the spatial velocity gradient $\boldsymbol{L}$ as the partial derivative of the velocity $\boldsymbol{v}$ with respect to position vector $\boldsymbol{x}$ is given as

$$\boldsymbol{L} = \operatorname{grad} \boldsymbol{v}(\boldsymbol{x}, t) = \frac{\partial \boldsymbol{v}(\boldsymbol{x}, t)}{\partial \boldsymbol{x}} . \tag{2.17}$$

It can be additionally decomposed into a symmetric tensor $\boldsymbol{D}$ and a skew-symmetric spin tensor $\boldsymbol{W}$ as

$$\boldsymbol{D} = \frac{1}{2}(\boldsymbol{L} + \boldsymbol{L}^{\mathrm{T}}) \quad \text{and} \quad \boldsymbol{W} = \frac{1}{2}(\boldsymbol{L} - \boldsymbol{L}^{\mathrm{T}}) . \tag{2.18}$$

Therewith, the rate of the Green-Lagrange strain tensor $\dot{\boldsymbol{E}}$ results in

$$\dot{\boldsymbol{E}} = \boldsymbol{F}^{\mathrm{T}} \cdot \boldsymbol{D} \cdot \boldsymbol{F} . \tag{2.19}$$

The material velocity gradient $\dot{\boldsymbol{F}}$ is defined as partial derivative of the deformation gradient with respect to time

$$\begin{aligned} \dot{\boldsymbol{F}}(\boldsymbol{X}, t) &= \frac{\partial \boldsymbol{F}(\boldsymbol{X}, t)}{\partial t} = \frac{\partial}{\partial t}\Big(\frac{\partial \boldsymbol{\varphi}(\boldsymbol{X}, t)}{\partial \boldsymbol{X}}\Big) = \frac{\partial}{\partial \boldsymbol{X}}\Big(\frac{\partial \boldsymbol{\varphi}(\boldsymbol{X}, t)}{\partial t}\Big) \\ &= \frac{\partial}{\partial \boldsymbol{X}}\big(\dot{\boldsymbol{x}}(\boldsymbol{X}, t)\big) = \operatorname{Grad}(\dot{\boldsymbol{x}}(\boldsymbol{X}, t)) . \end{aligned} \tag{2.20}$$

Therewith, the spatial deformation gradient can be reformulated to

$$\boldsymbol{L} = \frac{\partial \boldsymbol{v}(\boldsymbol{x}, t)}{\partial \boldsymbol{x}} = \frac{\partial \dot{\boldsymbol{x}}(\boldsymbol{X}, t)}{\partial \boldsymbol{x}} = \frac{\partial \dot{\boldsymbol{x}}(\boldsymbol{X}, t)}{\partial \boldsymbol{X}} \cdot \frac{\partial \boldsymbol{X}}{\partial \boldsymbol{x}} = \dot{\boldsymbol{F}}(\boldsymbol{X}, t) \cdot \boldsymbol{F}^{-1}(\boldsymbol{X}, t) , \tag{2.21}$$

which is equivalent to $\dot{\boldsymbol{F}} = \boldsymbol{L} \cdot \boldsymbol{F}$. The volumetric strain ε_V and the associated logarithmic strain ε^H are given as

$$\varepsilon_V = \frac{\mathrm{d}v - \mathrm{d}V}{\mathrm{d}V} = \det \boldsymbol{F} - 1 \quad \text{and} \quad \varepsilon^H = \ln(1 + \varepsilon_V) . \tag{2.22}$$

In the linearized theory, in which small strains are assumed, it holds that the strain is the symmetric gradient of the displacement, i.e.,

$$\boldsymbol{\varepsilon} = \frac{1}{2}(\operatorname{Grad} \boldsymbol{u} + \operatorname{Grad}^{\mathrm{T}} \boldsymbol{u}) . \tag{2.23}$$

2.2 The concept of stress

As a consequence of outer forces and moments, acting on the body and causing deformation of the body, inner forces and stress fields occur inside the body. Since the microstructural characteristics are neglected, stresses can be interpreted as averaged value of the measure of internal forces in one volume element. They can be computed by cutting principle, see Figure 2.3.

Assuming an imaginary section through the body $\mathcal{B}$ at time t, the traction vector $\boldsymbol{t}(\boldsymbol{x}, \boldsymbol{n}, t)$ on cutting surface $\mathrm{d}\boldsymbol{a}$ exists due to external forces. Such a cutting surface is defined by an outward normal vector $\boldsymbol{n}$ orthogonal to the cut. The traction vector and normal vector can be related by means of Cauchy's theorem

$$\boldsymbol{t}(\boldsymbol{x}, \boldsymbol{n}, t) = \boldsymbol{\sigma}(\boldsymbol{x}, t) \cdot \boldsymbol{n} , \tag{2.24}$$

with the symmetric Cauchy stress tensor $\boldsymbol{\sigma}$. Analogously, the following applies to the reference configuration with normal vector $\boldsymbol{N}$, traction vector $\boldsymbol{t}_0(\boldsymbol{X},\boldsymbol{N},t_0)$ at time t_0, position vector $\boldsymbol{X}$ and cutting surface $\mathrm{d}\boldsymbol{A}$. Therefore, it holds with unsymmetric first Piola-Kirchhoff stress tensor $\boldsymbol{P}$

$$\boldsymbol{t}_0(\boldsymbol{X},\boldsymbol{N},t_0) = \boldsymbol{P}(\boldsymbol{X},t_0)\cdot\boldsymbol{N}\,. \tag{2.25}$$

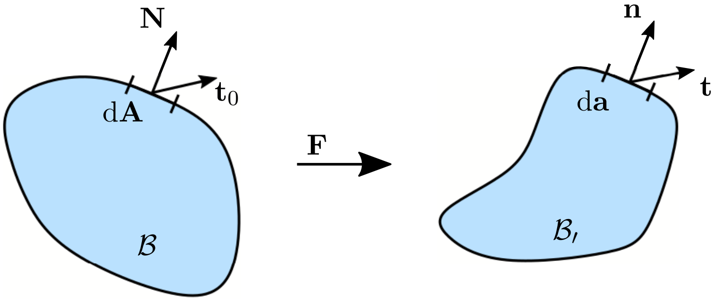

Figure 2.3: Visualization of transport theorems for line element, area element and volume element.

The Cauchy stress is also called true stress, since it refers to the actual configuration, while the first Piola-Kirchhoff stress tensor, which is in reference configuration, is called nominal stress tensor. Taking into account Equation $(2.5)_2$ both can be related by

$$\begin{aligned} &\boldsymbol{\sigma}(\boldsymbol{x},t)\cdot\boldsymbol{n}\,\mathrm{d}a = \boldsymbol{P}(\boldsymbol{X},t_0)\cdot\boldsymbol{N}\,\mathrm{d}A \\ \Leftrightarrow\quad &\boldsymbol{\sigma}(\boldsymbol{x},t)\cdot\, J\boldsymbol{F}^{-\mathrm{T}}\cdot\mathrm{d}\boldsymbol{A} = \boldsymbol{P}(\boldsymbol{X},t_0)\cdot\mathrm{d}\boldsymbol{A} \qquad \Rightarrow \boldsymbol{\sigma}\cdot J\boldsymbol{F}^{-\mathrm{T}} = \boldsymbol{P}\,. \end{aligned} \tag{2.26}$$

The symmetric second Piola-Kirchhoff stress tensor $\boldsymbol{S}$ relates forces in reference configuration to an area element in actual configuration

$$\boldsymbol{S} = \boldsymbol{F}^{-1}\cdot\boldsymbol{P} \;= J\boldsymbol{F}^{-1}\cdot\boldsymbol{\sigma}\cdot\boldsymbol{F}^{-\mathrm{T}} \tag{2.27}$$

and is thereby only of numerical interest. It does not give the opportunity for physical interpretation. Moreover, for the symmetric Kirchhoff stress tensor $\boldsymbol{\tau}$ it holds

$$\boldsymbol{\tau} = J\,\boldsymbol{\sigma} \quad\Rightarrow\quad \boldsymbol{S} = \boldsymbol{F}^{-1}\cdot\boldsymbol{\tau}\cdot\boldsymbol{F}^{-\mathrm{T}}\,. \tag{2.28}$$

2.3 Balance principles

The fundamental relations of continuum mechanics are described by the balance principles which are material independent and of axiomatic nature. The latter indicates that there are no counterexamples and that they cannot be derived based on other laws. Instead, they rely on observations and experiences. Balance principles are independent of the continuum or its material. In the following, these principles, namely the balance of mass, the balance of (linear) momentum, the balance of moment of momentum (balance of angular momentum), the balance of energy (first law of thermodynamics) and the entropy inequality (second law of thermodynamics) are introduced. First of all, integral forms are derived which, as global statements, refer to the entire continuum. Subsequently, if the quantities to be balanced are sufficiently smooth, local formulations can also be derived on parts of the body.

To formulate the balance equations, the divergence theorem is utilized, which reads for vector quantity $\boldsymbol{\phi}$ on body $\mathcal{B}$ with boundary $\partial\mathcal{B}$ and outer normal vector $\boldsymbol{n}$

$$\int_{\mathcal{B}} \operatorname{Div}\boldsymbol{\phi}\,\mathrm{d}V = \int_{\partial\mathcal{B}} \boldsymbol{\phi}\cdot\boldsymbol{n}\,\mathrm{d}A\,. \tag{2.29}$$

The **Balance of mass** ensures the conservation of mass in case that there is neither mass transfer across the surface nor an internal increase or loss of mass. The total mass m of body $\mathcal{B}$ with density ρ in actual configuration at time t is defined as

$$m = \int_{\mathcal{B}} \rho(\boldsymbol{x},t)\,\mathrm{d}v\,, \tag{2.30}$$

while M stands for the mass of the body $\mathcal{B}_0$ with density ρ_0 in reference configuration

$$M = \int_{\mathcal{B}_0} \rho_0(\boldsymbol{X})\,\mathrm{d}V\,. \tag{2.31}$$

The balance principle states that

$$M = m = \mathit{const.}\,, \tag{2.32}$$

which implies

$$\dot{m} = 0\,. \tag{2.33}$$

Starting with the transport theorem in Equation $(2.5)_1$ it follows that $\rho = \rho_0 J$. Thus, the time derivative can be computed to obtain the global statement of the balance of mass as

$$\begin{aligned} \dot{m} &= \frac{\mathrm{d}}{\mathrm{d}t}\int_{\mathcal{B}} \rho\,\mathrm{d}v = \frac{\mathrm{d}}{\mathrm{d}t}\int_{\mathcal{B}_0} \rho J\,\mathrm{d}V = \int_{\mathcal{B}_0} \dot{\rho}J + \rho\dot{J}\,\mathrm{d}V \\ &= \int_{\mathcal{B}_0} (J\rho\operatorname{div}\dot{\boldsymbol{x}} + \dot{\rho}J)\,\mathrm{d}V = \int_{\mathcal{B}} (\rho\operatorname{div}\dot{\boldsymbol{x}} + \dot{\rho})\,\mathrm{d}v = 0\,, \end{aligned} \tag{2.34}$$

with

$$\dot{J} = \frac{\partial\det\boldsymbol{F}}{\partial t} = \frac{\partial\det\boldsymbol{F}}{\partial\boldsymbol{F}} : \frac{\partial\boldsymbol{F}}{\partial t} = \det\boldsymbol{F}\,\boldsymbol{F}^{-\mathrm{T}} : \dot{\boldsymbol{F}} = J\operatorname{div}\dot{\boldsymbol{x}}\,. \tag{2.35}$$

Thus, the local form of the balance of mass results in

$$\dot{\rho} + \rho\operatorname{div}\dot{\boldsymbol{x}} = 0\,. \tag{2.36}$$

The **Balance of (linear) momentum**, also called Cauchy's first equation of motion, describes the behavior of the body $\mathcal{B}$ under any mechanical force. It states that the time rate of change of the total momentum $\boldsymbol{l}$, namely $\dot{\boldsymbol{l}}$, during the deformation of a body is equal to the sum of all external surface and volume forces $\boldsymbol{f}$ acting on the body. The definitions read

$$\boldsymbol{l} = \int_{\mathcal{B}} \rho\,\dot{\boldsymbol{x}}\,\mathrm{d}v \quad\text{and}\quad \boldsymbol{f} = \int_{\mathcal{B}} \rho\,\boldsymbol{b}\,\mathrm{d}v + \int_{\partial\mathcal{B}} \boldsymbol{t}\,\mathrm{d}a\,, \tag{2.37}$$

with $\rho\,\boldsymbol{b}$ as body forces and $\boldsymbol{t}$ as traction vector on surface $\partial\mathcal{B}$. Applying Cauchy's theorem and the divergence theorem given in Equations (2.24) and (2.29) one obtains

$$\begin{aligned}\dot{\boldsymbol{l}} = \boldsymbol{f} \quad \Leftrightarrow \quad & \int_{\mathcal{B}} \rho\,\ddot{\boldsymbol{x}}\,\mathrm{d}v = \int_{\mathcal{B}} \rho\,\boldsymbol{b}\,\mathrm{d}v + \int_{\partial\mathcal{B}} \boldsymbol{t}\,\mathrm{d}a \\ \Leftrightarrow & \int_{\mathcal{B}} \big(\operatorname{div}\boldsymbol{\sigma} + \rho\,(\boldsymbol{b} - \ddot{\boldsymbol{x}})\big)\,\mathrm{d}v = \boldsymbol{0}\,. \end{aligned} \tag{2.38}$$

The local form of the balance of linear momentum in actual configuration results in

$$\operatorname{div}\boldsymbol{\sigma} + \rho\,(\boldsymbol{b} - \ddot{\boldsymbol{x}}) = \boldsymbol{0}\,, \tag{2.39}$$

which can be transformed to the reference configuration with

$$\int_{\mathcal{B}} \operatorname{div}\boldsymbol{\sigma}\,\mathrm{d}v = \int_{\partial\mathcal{B}} \boldsymbol{\sigma}\cdot\boldsymbol{n}\,\mathrm{d}a = \int_{\partial\mathcal{B}_0} \boldsymbol{\sigma}\cdot J\boldsymbol{F}^{-\mathrm{T}}\,\mathrm{d}\boldsymbol{A} = \int_{\partial\mathcal{B}_0} \boldsymbol{P}\,\mathrm{d}\boldsymbol{A} = \int_{\mathcal{B}_0} \operatorname{Div}\boldsymbol{P}\,\mathrm{d}V \tag{2.40}$$

as

$$\operatorname{Div}\boldsymbol{P} + \rho_0\,(\boldsymbol{b} - \ddot{\boldsymbol{x}}) = \boldsymbol{0}\,. \tag{2.41}$$

The **Balance of angular momentum** or Cauchy's second equation of motion states that the time rate of change of the angular momentum $\boldsymbol{h}_{\tilde{0}}$ with respect to a certain reference point, here named $\tilde{\boldsymbol{0}}$, is equal to the angular momentum resulting from the external forces $\boldsymbol{m}_{\tilde{0}}$ during a deformation of body $\mathcal{B}$, i.e.,

$$\dot{\boldsymbol{h}}_{\tilde{0}} \;=\; \boldsymbol{m}_{\tilde{0}}\,. \tag{2.42}$$

Those two terms are defined as

$$\boldsymbol{h}_{\tilde{0}} = \int_{\mathcal{B}} \rho\,\boldsymbol{x}\times\dot{\boldsymbol{x}}\,\mathrm{d}v \text{ and } \boldsymbol{m}_{\tilde{0}} = \int_{\mathcal{B}} \boldsymbol{x}\times\rho\,\boldsymbol{b}\,\mathrm{d}v \;+\; \int_{\partial\mathcal{B}} \boldsymbol{x}\times\boldsymbol{t}\,\mathrm{d}a\,. \tag{2.43}$$

Therein, the lever arm is denoted by $\boldsymbol{x}$. For the time derivative of the angular momentum it holds with transport theorem, time derivative of Jacobian and local form of balance of mass in Equations (2.5).1, (2.35) and (2.36)

$$\dot{\boldsymbol{h}}_{\tilde{0}} = \frac{\mathrm{d}}{\mathrm{d}t}\int_{\mathcal{B}} \rho\boldsymbol{x}\times\dot{\boldsymbol{x}}\,\mathrm{d}v = \int_{\mathcal{B}} \rho\,\boldsymbol{x}\times\ddot{\boldsymbol{x}}\,\mathrm{d}v\,. \tag{2.44}$$

Regarding the angular momentum, it holds that

$$\boldsymbol{m}_{\tilde{0}} = \int_{\mathcal{B}} \boldsymbol{x}\times\rho\,\boldsymbol{b}\,\mathrm{d}v \;+\; \int_{\partial\mathcal{B}} \boldsymbol{x}\times\boldsymbol{\sigma}\cdot\boldsymbol{n}\,\mathrm{d}a = \int_{\mathcal{B}} \big(\boldsymbol{x}\times\rho\,\boldsymbol{b} + \boldsymbol{x}\times\operatorname{div}\boldsymbol{\sigma} + \boldsymbol{I}\times\boldsymbol{\sigma}\big)\,\mathrm{d}v\,, \tag{2.45}$$

such that one obtains the global statement as

$$\dot{\boldsymbol{h}}_{\tilde{0}} \;=\; \boldsymbol{m}_0 \quad \Leftrightarrow \quad \int_{\mathcal{B}} \boldsymbol{I}\times\boldsymbol{\sigma}\,\mathrm{d}v = \boldsymbol{0}\,. \tag{2.46}$$

The local form of the balance of angular momentum describes the symmetry of the Cauchy stress tensor as

$$\boldsymbol{I}\times\boldsymbol{\sigma} = \boldsymbol{0} \quad \Leftrightarrow \quad \boldsymbol{\sigma} \;=\; \boldsymbol{\sigma}^{\mathrm{T}}\,. \tag{2.47}$$

The **Balance of energy** or first law of thermodynamics postulates that the time rate of change of the total energy in a continuum equals the external energy supply. Therefore, the total energy is composed of internal energy E and kinetic energy K, while the external energy supply is described by the heat supply Q and the power of the mechanical work P by external surface and volume forces. In the general case, other non-thermo-mechanical energies would have to be added as external energy supply. These include, e.g., chemical or electrical terms. In the following, ϵ denotes the specific internal energy, $\boldsymbol{q}$ is the heat flux vector and r stands for the external heat source, such that it holds

$$\begin{aligned} E &= \int_{\mathcal{B}} \rho\,\epsilon\,\mathrm{d}v\,, & P &= \int_{\mathcal{B}} \dot{\boldsymbol{x}}\cdot\rho\,\boldsymbol{b}\,\mathrm{d}v + \int_{\partial\mathcal{B}} \dot{\boldsymbol{x}}\cdot\boldsymbol{t}\,\mathrm{d}a\,, \\ K &= \int_{\mathcal{B}} \frac{1}{2}\rho\,\dot{\boldsymbol{x}}\cdot\dot{\boldsymbol{x}}\,\mathrm{d}v\,, & Q &= \int_{\mathcal{B}} \rho\,r\,\mathrm{d}v - \int_{\partial\mathcal{B}} \boldsymbol{q}\cdot\boldsymbol{n}\,\mathrm{d}a\,. \end{aligned} \tag{2.48}$$

Thus, the first law of thermodynamics can be expressed as

$$\frac{\mathrm{d}}{\mathrm{d}t}(E+K) = Q+P \quad \Leftrightarrow \quad \dot{E}+\dot{K} = Q+P\,, \tag{2.49}$$

with time derivatives

$$\dot{E} = \int_{\mathcal{B}} \rho\,\dot{\epsilon}\,\mathrm{d}v\,, \quad \dot{K} = \int_{\mathcal{B}} \rho\,\dot{\boldsymbol{x}}\cdot\ddot{\boldsymbol{x}}\,\mathrm{d}v\,. \tag{2.50}$$

The global statement of the balance of energy results in

$$\begin{aligned} &\int_{\mathcal{B}} \rho\,\dot{\epsilon}\,\mathrm{d}v + \int_{\mathcal{B}} \rho\,\dot{\boldsymbol{x}}\cdot\ddot{\boldsymbol{x}}\,\mathrm{d}v = \int_{\mathcal{B}} \rho\,r\,\mathrm{d}v - \int_{\partial\mathcal{B}} \boldsymbol{q}\cdot\boldsymbol{n}\,\mathrm{d}a + \int_{\mathcal{B}} \dot{\boldsymbol{x}}\cdot\rho\,\boldsymbol{b}\,\mathrm{d}v + \int_{\partial\mathcal{B}} \dot{\boldsymbol{x}}\cdot\boldsymbol{t}\,\mathrm{d}a \\ &\Leftrightarrow \quad \int_{\mathcal{B}} \rho\,\dot{\epsilon}\,\mathrm{d}v = \int_{\mathcal{B}} \big(\rho\,r - \operatorname{div}\boldsymbol{q} + \boldsymbol{D}:\boldsymbol{\sigma}\big)\,\mathrm{d}v\,, \end{aligned} \tag{2.51}$$

whereas the local form reads

$$\rho\,\dot{\epsilon} - \boldsymbol{\sigma}:\boldsymbol{D} - \rho\,r + \operatorname{div}\boldsymbol{q} = 0\,. \tag{2.52}$$

Introducing the free Helmholtz energy function ψ, the specific internal energy can be related via temperature θ and the specific entropy η as

$$\epsilon = \psi + \theta\eta \quad \text{with time derivative} \quad \dot{\epsilon} = \dot{\psi} + \dot{\theta}\eta + \theta\dot{\eta}\,. \tag{2.53}$$

In the linearized framework of small strains, the symmetric part of the spatial velocity gradient $\boldsymbol{D}$ in Equation (2.52) is replaced by

$$\dot{\boldsymbol{\varepsilon}} = \frac{1}{2}\big(\mathrm{Grad}^{\mathrm{T}}\,\dot{\boldsymbol{u}} + \mathrm{Grad}\,\dot{\boldsymbol{u}}\big)\,, \tag{2.54}$$

such that one obtains using Equation (2.53)

$$\rho\,(\dot{\psi} + \dot{\theta}\eta + \theta\dot{\eta}) - \boldsymbol{\sigma}:\dot{\boldsymbol{\varepsilon}} - \rho\,r + \operatorname{div}\boldsymbol{q} = 0\,. \tag{2.55}$$

The **Entropy inequality** or second law of thermodynamics states that the total energy in a system cannot be increased or decreased, but that one form of energy can be converted into another form of energy while maintaining a constant total energy. There is no indication of the direction of the energy transformation or information whether the process is reversible or irreversible. Here, reversible means that energy can be made usable again, i.e., it can be returned to mechanical work. For irreversible processes, where this is not the case, the entropy H serves as a measure of the non-available energy, which is defined as

$$H = \int_{\mathcal{B}} \rho\,\eta\,\mathrm{d}v \quad \text{with} \quad \dot{H} = \int_{\mathcal{B}} \rho\,\dot{\eta}\,\mathrm{d}v\,. \tag{2.56}$$

Therewith, the second law of thermodynamics can be formulated as

$$\dot{H} \;\geq\; \int_{\mathcal{B}} \frac{1}{\theta}\,\rho\,r\,\mathrm{d}v \;-\; \int_{\partial\mathcal{B}} \frac{1}{\theta}\,\boldsymbol{q}\cdot\boldsymbol{n}\,\mathrm{d}v\,, \tag{2.57}$$

which is also called Clausius-Duhem inequality. Since the entropy can only increase, it states that its time derivative has to be greater or equal to the sum of the entropy, which is supplied by heat production within the body and the heat flux over the surface. Application of the divergence theorem results in the local form

$$\rho\,\dot{\eta} \geq \frac{1}{\theta}\rho\,r - \operatorname{div}\Big(\frac{\boldsymbol{q}}{\theta}\Big) \quad \Leftrightarrow \quad -\rho\,(\dot{\epsilon} - \theta\dot{\eta}) + \boldsymbol{\sigma} : \boldsymbol{D} - \frac{1}{\theta}\,\boldsymbol{q}\cdot\operatorname{grad}\theta \geq 0\,. \tag{2.58}$$

In the linearized framework of small strains it holds

$$-\,\rho\,(\dot{\psi} + \dot{\theta}\eta) + \boldsymbol{\sigma} : \dot{\boldsymbol{\varepsilon}} - \frac{1}{\theta}\,\boldsymbol{q}\cdot\operatorname{grad}\theta \geq 0\,. \tag{2.59}$$

2.4 Fundamental aspects on material modeling

The previously defined balance principles are of axiomatic nature and therewith universal, independent of the chosen continuum and its material. In order to analyze such characteristics of the body, additional relations are necessary to find additional equations to solve for all unknown quantities. There are two possibilities to find such constitutive equations, namely inductively, i.e., based on experiments, or deductively, i.e., almost fully theoretically. For the latter, the balance principles serve as a valid and non-violable basis. Based on the balance laws, there are 14 equations: the scalar balance of mass (1), the vectorial balance of momentum (3), the tensorial balance of angular momentum (9) and in case of thermo-mechanical material behavior the scalar balance of energy (1). Assuming the body forces $\rho\boldsymbol{b}$ and external heat source r to be known, the 19 remaining quantities therein are the density ρ, the motion $\boldsymbol{\varphi}$, the stresses $\boldsymbol{\sigma}$, the internal energy ϵ, the temperature θ, the entropy η and the heat flux $\boldsymbol{q}$. Thus, five additional equations are to be defined to describes the continuum's behavior as response to outer forces. For this purpose, constitutive equations have to be given, which link all phenomenological variables with each other, that describe the macroscopic behavior. This is achieved by means of algebraic equations or differential or integral equations, which can include stresses, strains, temperature, heat flux, etc. In general, the choice of constitutive parameters and quantities is completely subjective.

The constitutive equations are defined in such a way that the material behavior of a material point is locally linked to the points in its immediate environment, i.e., it can be uniquely described by a set of constitutive variables which depend on process variables. The process is defined as the temporal change of the constitutive parameters in this material point. Thus, for an arbitrary constitutive quantity a at time t the functional relation results in

$$a = a[\boldsymbol{x}(\boldsymbol{X}, t), t]]\,. \tag{2.60}$$

In addition to the constitutive equations, material symmetries, such as forms of isotropy, and kinematic constraints, e.g. the assumption of plastic incompressibility, are included in the field of material theory. This theory bases on the following eight axioms: causality, determinism, equipresence, local action, fading memory, physical consistency, material objectivity and material symmetry.

- In case of a thermo-mechanical process, the principle of **causality** states that the displacement $\boldsymbol{u}$ and the temperature θ are assumed to be measurable and independent quantities. Further quantities, that depend on $\boldsymbol{u}$ and θ but cannot be directly computed based on the second law of thermodynamics, are called dependent constitutive variables, for instance stresses, heat flux, free energy or entropy.
- By the principle of **determinism** all those dependent constitutive quantities are uniquely determined by the time history of the independent variables.
- The set of independent variables is the same for all constitutive equations according to the principle of **equipresence**.
- **Local action** means that one material point $\mathcal{P}$ in an actual configuration is fully determined by its direct environment and its material behavior is not influenced by the motion of material points outside this environment.
- Furthermore, the principle of **fading memory** states that events or states further in the past have a negligible influence on the instantaneous behavior of constitutive function or quantity.
- Following the principle of **consistency**, constitutive equations must not violate the balance equations.
- The principle of **material objectivity** postulates that material laws do not change if the frame of the local observer differs by an arbitrary rigid body motion or if an arbitrary rigid body motion is superimposed on the motion of the material section. For material point $\mathcal{P}$ with position vector $\boldsymbol{X}$ in reference configuration at time t_0, there are two deformed states $\boldsymbol{x}(\boldsymbol{X},t)$ and $\hat{\boldsymbol{x}}(\boldsymbol{X},\hat{t})$ given, which are related by a rigid body motion and a time transformation. Then it holds

  $$\hat{\boldsymbol{x}}(\boldsymbol{X},\hat{t}) = \boldsymbol{Q}(t)\cdot\boldsymbol{x}(\boldsymbol{X},t) + c(t) \quad \text{with} \quad \hat{t} = t - t_0\,. \tag{2.61}$$

  Therein, $\boldsymbol{Q}$ is an arbitrary, time dependent and orthogonal second order tensor describing a rigid body motion, i.e., $\boldsymbol{Q} \in \mathcal{SO}(3) := \{\boldsymbol{S} \in \mathbb{R}^{3\times3} | \boldsymbol{S}\cdot\boldsymbol{S}^{\mathrm{T}} = \boldsymbol{I}\,, \det\boldsymbol{S} = 1\}$ also called special orthogonal group, and c is a vector describing a translation. Deformed configurations that can be related in such a way are then called objectively equivalent. For scalar a, vector $\boldsymbol{a}$ and second-order tensor $\boldsymbol{A}$ material objectivity can be expressed with an arbitrary $\boldsymbol{Q} \in \mathcal{SO}(3)$ as

  $$a^* = a\,, \quad \boldsymbol{a}^* = \boldsymbol{Q}\cdot\boldsymbol{a}\,, \quad \boldsymbol{A}^* = \boldsymbol{Q}\cdot\boldsymbol{A}\cdot\boldsymbol{Q}^{\mathrm{T}}\,. \tag{2.62}$$

- The principle of **material symmetry** states that constitutive equations are independent with respect to the transformations of the coordinate system by the symmetry group $\mathcal{G} \in \mathcal{SO}(3)$, which consists of all distance-preserving rotations that keep the material microstructure invariant in the Euclidean space. Considering a mapping between two reference configurations $\mathcal{B}_0 \to \mathcal{B}_0^\star$ with $\boldsymbol{X} \mapsto \boldsymbol{X}^\star$, then it holds for the position vector $\boldsymbol{X}$ in reference configuration

$$\boldsymbol{X}^\star = \boldsymbol{Q} \cdot \boldsymbol{X} \quad \forall \boldsymbol{Q} \in \mathcal{G}\,, \tag{2.63}$$

and for the deformation gradient and the right Cauchy-Green deformation tensor

$$\boldsymbol{F}^\star = \frac{\partial \boldsymbol{x}}{\partial \boldsymbol{X}^\star} = \frac{\partial \boldsymbol{x}}{\partial \boldsymbol{X}} \cdot \frac{\partial \boldsymbol{X}}{\partial \boldsymbol{X}^\star} = \boldsymbol{F} \cdot \boldsymbol{Q}^{\mathrm{T}}\,, \quad \boldsymbol{C}^\star = \boldsymbol{Q} \cdot \boldsymbol{C} \cdot \boldsymbol{Q}^{\mathrm{T}}\,. \tag{2.64}$$

In case the symmetry group is the whole group

$$\mathcal{O}(3) := \{\boldsymbol{S} \in \mathbb{R}^{3\times3} | \boldsymbol{S} \cdot \boldsymbol{S}^{\mathrm{T}} = \boldsymbol{I}\,, \det \boldsymbol{S} = \pm 1\}\,, \tag{2.65}$$

the material is isotropic material, otherwise it is called anisotropic.

3 Fundamentals on the Finite Element Method

Finite elements (FE) have been named first back in the beginnings of the sixties of the 20th century by researches in aerospace industry, to which terms such as the isoparametric concept, shape functions or the patch test among others were introduced in this context. Well known important scientists who have contributed to the fundamentals in Finite Element Method (FEM) are e.g. Argyris, Clough, Zienkiewicz and Irons but one should not forget about the contributions of Hrennikoff, Courant, Ritz and Galerkin, where it is to mention that the list is definitely not exclusive. An interesting view on the history of the FEM is given in Felippa [42]. Up to the 1980s, the FEM has been a well known concept and commercially established in numerous application in civil engineering, statics, aerodynamics, hemodynamics and so on. Next to that, the main advantages are the generality of the concept, the strong and provable mathematical formulation and the simplicity of the approach.

In the last decades, the FEM has been established as an efficient strategy for the numerical treatment of constructive problems in engineering. There is a wide range of applications such as structural mechanics in civil engineering, aircraft or shipbuilding, mechanical engineering, coupled problems of heat conduction or with electric or magnetic fields as well as fluid mechanics. Therein, nonlinearities of different origins can occur, for instance geometric nonlinearities or large deformations, physical nonlinearities, stability problems, nonlinear boundary conditions or coupled problems, which make an analytical computation hardly possible or not possible at all. In that case the FEM provides an efficient numerical tool to compute approximate solutions to such nonlinear problems by solving a complex system of differential equation. This section gives an overview of the main steps of a Finite Element Analysis. First, the boundary value problem is defined and a variational formulation of the balance laws is discussed. Afterwards, the linearization and the discretization with elements of simple geometry is described. For more details the reader is kindly referred to e.g. Wriggers [206], Bathe [13] and Zienkiewicz and Taylor [210].

3.1 Boundary value problem

A (nonlinear) boundary value problem is defined as combination of three things: a continuum body $\mathcal{B}_0$, a set of differential equations and suitable boundary conditions on the boundary of the body $\partial\mathcal{B}_0$. For the set of differential equations for an isothermal and quasi-static process, the local forms of the balance of linear and angular momentum, the kinematics and the underlying material law are given by

$$\begin{array}{l|l} \text{linear momentum} & \operatorname{Div}\boldsymbol{P} + \rho_0(\boldsymbol{b} - \ddot{\boldsymbol{x}}) = \boldsymbol{0}\,, \\ \text{angular momentum} & \boldsymbol{P}\cdot\boldsymbol{F}^{\mathrm{T}} = \boldsymbol{F}\cdot\boldsymbol{P}^{\mathrm{T}}\,, \\ \text{kinematics} & \boldsymbol{F}(\boldsymbol{X},t) = \operatorname{Grad}\boldsymbol{x}\,, \\ \text{material law} & \boldsymbol{P} = \partial_{\boldsymbol{F}}\psi \end{array} \tag{3.1}$$

with free energy function ψ. In this context of a boundary value problem, the local form of the balance of momentum is also called strong form of the equilibrium. The boundary conditions are split into two types, Neumann and Dirichlet boundary conditions, respectively. The first defines the derivative of the restricted value while the second one sets the value of the quantity itself, i.e.,

$$\boldsymbol{u} = \boldsymbol{u}_0 \text{ on } \partial\mathcal{B}_{0\boldsymbol{u}} \quad \text{and} \quad \boldsymbol{P}\cdot\boldsymbol{N} = \boldsymbol{t}_0 \text{ on } \partial\mathcal{B}_{0\boldsymbol{t}}\,, \tag{3.2}$$

which have to satisfy

$$\partial\mathcal{B}_{0\boldsymbol{u}} \cup \partial\mathcal{B}_{0\boldsymbol{t}} = \partial\mathcal{B}_0 \quad \text{and} \quad \partial\mathcal{B}_{0\boldsymbol{u}} \cap \partial\mathcal{B}_{0\boldsymbol{t}} = \emptyset\,. \tag{3.3}$$

This means that the surface of the body is divided into disjunct parts, $\partial\mathcal{B}_{0\boldsymbol{u}}$ and $\partial\mathcal{B}_{0\boldsymbol{t}}$, which cannot overlap. At the same time, however, it is required that for every point of the entire surface of the body either a Dirichlet or a Neumann boundary condition must be described.

3.2 Variational formulation

In most cases, partial differential equations (PDEs) cannot be solved analytically at all, or only with difficulties. Therefore, the idea is to determine an approximated solution of a boundary value problem via the FEM. In order to do so, variational principles are applied to the strong form of the equilibrium to obtain the weak form G_u. With the help of this calculus of variations, stationary points of the equations under consideration can be determined by taking into account small variations of these same functions or functionals. Thereby, the boundary value problem can be formulated in terms of an algebraic system of equation. The FEM then approximates the solution by minimizing an associated error function. Thus, for the isothermal case, the presented local form or strong from of the balance of momentum in Equation (3.1) is considered. For reasons of simplification, the acceleration term $\ddot{\boldsymbol{x}}$ is neglected. The unknown fields are the displacements in every direction, i.e., it is solved for the vector $\boldsymbol{u}$. In order to find the solution of such a PDE, the Galerkin method is utilized, which transforms a continuous problem to a discrete one. Therefore, the strong form of the equilibrium is multiplied with a test function and integrated over the body, which is also referred to as domain. With the test function $\delta\boldsymbol{u} \in \{\delta\boldsymbol{u}|\delta\boldsymbol{u} = \boldsymbol{0} \text{ on } \partial\mathcal{B}_0\}$ it yields

$$G_u(\boldsymbol{u},\delta\boldsymbol{u}) := -\int_{\mathcal{B}_0} \big(\operatorname{Div}\boldsymbol{P} + \rho_0\boldsymbol{b}\big)\cdot\delta\boldsymbol{u}\,\mathrm{d}V = 0\,, \tag{3.4}$$

which can be reformulated with $\operatorname{Div}\boldsymbol{P}\cdot\delta\boldsymbol{u} = \operatorname{Div}(\boldsymbol{P}\cdot\delta\boldsymbol{u}) - \boldsymbol{P} : \operatorname{Grad}\delta\boldsymbol{u}$ and the divergence theorem to

$$G_u(\boldsymbol{u},\delta\boldsymbol{u}) := \underbrace{\int_{\mathcal{B}_0} \boldsymbol{P} : \operatorname{Grad}\delta\boldsymbol{u}\,\mathrm{d}V}_{G_u^{\text{int}}} \underbrace{- \int_{\mathcal{B}_0} \rho_0\boldsymbol{b}\cdot\delta\boldsymbol{u}\,\mathrm{d}V - \int_{\partial\mathcal{B}_0} \boldsymbol{t}_0\cdot\delta\boldsymbol{u}\,\mathrm{d}A}_{G_u^{\text{ext}}} = 0\,. \tag{3.5}$$

Therein, G_u^{int} and G_u^{ext} denote the work of the internal and external forces, respectively. The first term can also be rewritten in terms of the symmetric second Piola-Kirchhoff stress tensor $\boldsymbol{S}$ and the Green-Lagrange strain tensor $\boldsymbol{E}$, since it holds

$$\begin{aligned} \boldsymbol{P} : \operatorname{Grad}\delta\boldsymbol{u} &= (\boldsymbol{F}\cdot\boldsymbol{S}) : \operatorname{Grad}\delta\boldsymbol{u} = \boldsymbol{S} : (\boldsymbol{F}^{\mathrm{T}}\cdot\operatorname{Grad}\delta\boldsymbol{u}) \\ &= \boldsymbol{S} : \frac{1}{2}\big(\boldsymbol{F}^{\mathrm{T}}\cdot\operatorname{Grad}\delta\boldsymbol{u} + \operatorname{Grad}^{\mathrm{T}}\delta\boldsymbol{u}\cdot\boldsymbol{F}\big) \\ &= \boldsymbol{S} : \delta\boldsymbol{E} = \frac{1}{2}\boldsymbol{S} : \delta\boldsymbol{C} \end{aligned} \tag{3.6}$$

with $\operatorname{Grad}\delta\boldsymbol{u} = \boldsymbol{S} : \frac{1}{2}\big(\boldsymbol{F}^{\mathrm{T}}\cdot\delta\boldsymbol{F} + \delta\boldsymbol{F}^{\mathrm{T}}\cdot\boldsymbol{F}\big)$, which leads to

$$G_u(\boldsymbol{u},\delta\boldsymbol{u}) = \int_{\mathcal{B}_0} \boldsymbol{S} : \delta\boldsymbol{E}\,\mathrm{d}V - \int_{\mathcal{B}_0} \rho_0\boldsymbol{b}\cdot\delta\boldsymbol{u}\,\mathrm{d}V - \int_{\partial\mathcal{B}_0} \boldsymbol{t}_0\cdot\delta\boldsymbol{u}\,\mathrm{d}A = 0\,. \tag{3.7}$$

With a push forward transformation, the weak form of equilibrium can also be formulated in the actual configuration. Applying the symmetric Cauchy stress tensor $\boldsymbol{\sigma} = \frac{1}{J}\boldsymbol{P}\cdot\boldsymbol{F}^{\mathrm{T}}$ and the transport theorem given in Equation (2.5) one obtains

$$G_u(\boldsymbol{u},\delta\boldsymbol{u}) := \int_{\mathcal{B}} \boldsymbol{\sigma} : \operatorname{grad}^{\mathrm{sym}}\delta\boldsymbol{u}\,\mathrm{d}v - \int_{\mathcal{B}} \rho\boldsymbol{b}\cdot\delta\boldsymbol{u}\,\mathrm{d}v - \int_{\partial\mathcal{B}} \boldsymbol{t}\cdot\delta\boldsymbol{u}\,\mathrm{d}a = 0\,, \tag{3.8}$$

in which the symmetric gradient is defined as $\operatorname{grad}^{\mathrm{sym}}\delta\boldsymbol{u} := \frac{1}{2}(\operatorname{grad}\delta\boldsymbol{u} + \operatorname{grad}^{\mathrm{T}}\delta\boldsymbol{u})$. In the linearized theory it then holds that $\delta\boldsymbol{\varepsilon} = \operatorname{grad}^{\mathrm{sym}}\delta\boldsymbol{u}$.

In case there is a total potential energy function Π^{tot} to describe the body, the principle of virtual work, which leads to Equation (3.5), is equivalent to find a stationary point of Π^{tot}, i.e.,

$$\delta\Pi^{\mathrm{tot}} = \mathrm{D}\Pi(\boldsymbol{u})\cdot\delta\boldsymbol{u} = \frac{\mathrm{d}}{\mathrm{d}\alpha}\Pi(\boldsymbol{u}+\alpha\delta\boldsymbol{u})|_{\alpha=0}\,, \quad \Pi^{\mathrm{tot}} = \Pi^{\mathrm{int}} + \Pi^{\mathrm{ext}} \quad \longrightarrow \text{stat.} \tag{3.9}$$

with D as total derivative and

$$\Pi^{\mathrm{int}} = \int_{\mathcal{B}_0} \psi(\boldsymbol{F}(\boldsymbol{u}))\,\mathrm{d}\mathcal{B}_0 = \int_{\mathcal{B}_0} \frac{\partial\psi}{\partial\boldsymbol{F}} : \delta\boldsymbol{F}\,\mathrm{d}\mathcal{B}_0 = \int_{\mathcal{B}_0} \boldsymbol{P} : \operatorname{Grad}\delta\boldsymbol{u}\,\mathrm{d}V\,, \tag{3.10}$$

$$\Pi^{\mathrm{ext}} = -\int_{\mathcal{B}_0} \rho_0\boldsymbol{b}\cdot\boldsymbol{u}\,\mathrm{d}V - \int_{\partial\mathcal{B}_0} \boldsymbol{t}_0\cdot\boldsymbol{u}\,\mathrm{d}A\,. \tag{3.11}$$

3.3 Linearization

The weak form of equilibrium G_u has to be linearized in order to apply a numerical scheme to solve complex, nonlinear system of equations. In FEM an often used approach is the Newton-Raphson iteration scheme to solve $G_u = 0$. A Taylor series expansion around point $\boldsymbol{u} = \boldsymbol{u}_k$ gives the general linearization of the weak form of equilibrium as

$$\operatorname{Lin} G_u(\boldsymbol{u}_k,\delta\boldsymbol{u},\Delta\boldsymbol{u}) = G(\boldsymbol{u}_k,\delta\boldsymbol{u}) + \Delta G(\boldsymbol{u}_k,\delta\boldsymbol{u},\Delta\boldsymbol{u})\,. \tag{3.12}$$

That means to compute the directional derivative in point $\boldsymbol{u}_k$ in direction $\Delta\boldsymbol{u}$ with increment $\Delta\boldsymbol{u}(\boldsymbol{u}_k,\delta\boldsymbol{u},\Delta\boldsymbol{u}) = \frac{\mathrm{d}}{\mathrm{d}\epsilon}\Big[G(\boldsymbol{u}_k + \epsilon\Delta\boldsymbol{u},\delta\boldsymbol{u})\Big]|_{\epsilon=0} = \mathrm{D}G(\boldsymbol{u}_k,\delta\boldsymbol{u})\cdot\Delta\boldsymbol{u}$. Considering only conservative forces, i.e., the external part vanishes, one obtains from Equation (3.7) together with Equation (3.6)

$$\begin{aligned}\operatorname{Lin} G_u(\boldsymbol{u}_k,\delta\boldsymbol{u},\Delta\boldsymbol{u}) = &\int_{\mathcal{B}_0} \frac{1}{2}\boldsymbol{S} : \delta\boldsymbol{C}\,\mathrm{d}V - \int_{\mathcal{B}_0} \rho_0\boldsymbol{b}\cdot\delta\boldsymbol{u}\,\mathrm{d}V - \int_{\partial\mathcal{B}_0} \boldsymbol{t}_0\cdot\delta\boldsymbol{u}\,\mathrm{d}A \\ &+ \int_{\mathcal{B}_0} \frac{1}{2}\delta\boldsymbol{C} : \mathbb{C} : \frac{1}{2}\Delta\boldsymbol{C}\,\mathrm{d}V + \int_{\mathcal{B}_0} \boldsymbol{S} : \frac{1}{2}\Delta\delta\boldsymbol{C}\,\mathrm{d}V\,.\end{aligned} \tag{3.13}$$

This linearized form is solved with respect to $\Delta\boldsymbol{u}_{n+1}$ in each iteration step of the Newton-Raphson scheme under the assumption that it holds $\operatorname{Lin} G = 0$. The update by incremental displacement is then computed by $\boldsymbol{u}_{n+1} = \boldsymbol{u}_n + \Delta\boldsymbol{u}_{n+1}$ in iteration step $n+1$. The termination criterion is given as $|\Delta\boldsymbol{u}_{n+1}| < tol$.

3.4 Discretization

In the FE theory, there are two kinds of approximations: The first one concerns the approximation of the body by finite elements and the second one regards field quantities such as displacements or stresses. The main idea of the FEM is to decompose the physical body $\mathcal{B}_0$ into a certain number n_{ele} of finite elements $\mathcal{B}^e$ of simple geometry, see Figure 3.1,

$$\mathcal{B}_0 \approx \mathcal{B}^h = \bigcup_{e=1}^{n_{\text{ele}}} \mathcal{B}^e \,. \tag{3.14}$$

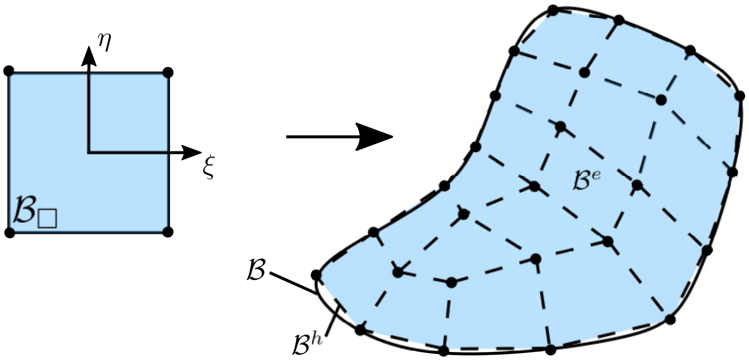

Figure 3.1: The discretization of a physical body $\mathcal{B}$ with finite elements $\mathcal{B}^e$ based on an isoparametric element $\mathcal{B}_\square$.

Therein and in the following, the index h indicates approximated quantities. The boundary $\partial\mathcal{B}_0$ is thus approximated by $\partial\mathcal{B}_0^h$. The isoparametric concept states that the same ansatz functions are used to interpolate unknown field quantities as well as the geometry. Advantages are that only one set of ansatz functions has to be defined and that the same integration points can be used in every element. Based on the position vectors in reference and actual configuration, $\boldsymbol{X}$ and $\boldsymbol{x}$, respectively, one defines the approximation of the geometry in both configurations for one element as

$$\boldsymbol{X}(\boldsymbol{\xi}) = \sum_{I=1}^{n_{\text{node}}} N_I(\boldsymbol{\xi})\boldsymbol{X}_I \quad \text{and} \quad \boldsymbol{x}(\boldsymbol{\xi}) = \sum_{I=1}^{n_{\text{node}}} N_I(\boldsymbol{\xi})\boldsymbol{x}_I \,, \tag{3.15}$$

with n_{node} as number of nodes per element and I as actual node with natural coordinates $\boldsymbol{\xi}$ in the isoparametric element $\mathcal{B}_\square$. The ansatz functions at node I are denoted by N_I, whereas $\boldsymbol{X}_I$ and $\boldsymbol{x}_I$ denote the nodal position vectors. Both can be related by $\boldsymbol{x}_I = \boldsymbol{X}_I + \boldsymbol{d}_I$ with the discrete nodal displacements $\boldsymbol{d}_I$. The transformation between coordinates in actual configuration, reference configuration and isoparametric element is illustrated in Figure 3.2. It is subject to the condition that the transformation has to be uniquely determined, and that nodes, edges or faces are preserved.

Based on the ansatz functions, the physical, virtual and incremental displacements are given as

$$\boldsymbol{u} \approx \boldsymbol{u}^h = \sum_{I=1}^{n_{\text{node}}} N_I(\boldsymbol{\xi})\boldsymbol{d}_I\,,$$

$$\delta\boldsymbol{u} \approx \delta\boldsymbol{u}^h = \sum_{I=1}^{n_{\text{node}}} N_I(\boldsymbol{\xi})\delta\boldsymbol{d}_I \quad \text{and} \quad \Delta\boldsymbol{u} \approx \Delta\boldsymbol{u}^h = \sum_{I=1}^{n_{\text{node}}} N_I(\boldsymbol{\xi})\Delta\boldsymbol{d}_I\,. \tag{3.16}$$

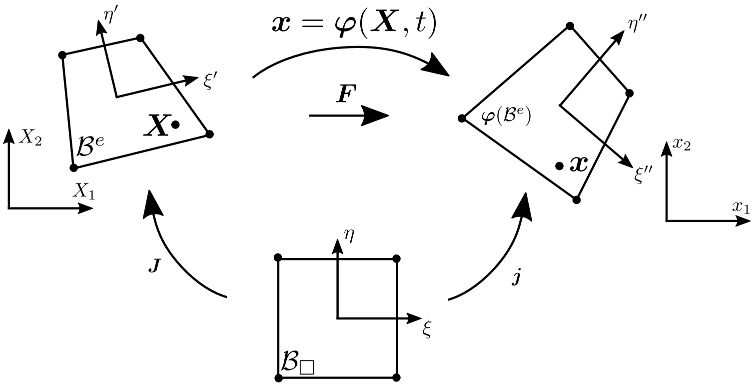

Figure 3.2: Based on the isoparametric concept, the parametric element can be mapped onto an element in reference configuration or actual configuration, respectively.

In order to solve the linearized form in Equation (3.13), derivatives of the field quantities are to be defined. Therefore, the Jacobian maps between the isoparametric element and the actual or reference configuration, which is given as

$$\boldsymbol{J} = \frac{\partial \boldsymbol{X}}{\partial \boldsymbol{\xi}} \quad \text{and} \quad \boldsymbol{j} = \frac{\partial \boldsymbol{x}}{\partial \boldsymbol{\xi}}\,. \tag{3.17}$$

It holds that the derivatives of the ansatz functions with respect to the reference placement can be computed as

$$\frac{\partial N_I}{\partial \boldsymbol{X}} = \frac{\partial N_I}{\partial \boldsymbol{\xi}}\frac{\partial \boldsymbol{\xi}}{\partial \boldsymbol{X}} = \boldsymbol{J}^{-\mathrm{T}}\frac{\partial N_I}{\partial \boldsymbol{\xi}}\,. \tag{3.18}$$

As abbreviation one writes $N_{I,a} := \frac{\partial N_I}{\partial X_a}$ with $a \in \{1,2\}$ for the two-dimensional case and $a \in \{1,2,3\}$ for the three-dimensional case.

In the following, the so-called Voigt notation is used to represent symmetric tensors in a reduced order, e.g. a fourth-order tensor is reduced to a second-order tensor and a second-order tensor is reduced to a vector, see Appendix A. Thus, the discretization of the virtual and incremental right Cauchy-Green tensor and the Green-Lagrange strain tensor, respectively, are introduced as

$$\frac{1}{2}\delta\boldsymbol{C}^h = \sum_{I=1}^{n_{\text{node}}} \boldsymbol{B}_I\delta\boldsymbol{d}_I\,, \qquad \frac{1}{2}\Delta\boldsymbol{C}^h = \sum_{I=1}^{n_{\text{node}}} \boldsymbol{B}_I\Delta\boldsymbol{d}_I\,, \tag{3.19}$$

$$\delta\boldsymbol{E}^h = \sum_{I=1}^{n_{\text{node}}} \boldsymbol{B}_I\delta\boldsymbol{d}_I\,, \qquad \Delta\boldsymbol{E}^h = \sum_{I=1}^{n_{\text{node}}} \boldsymbol{B}_I\Delta\boldsymbol{d}_I\,, \tag{3.20}$$

with the B_I-matrix

$$\boldsymbol{B}_I = \begin{bmatrix} F_{11}N_{I,1} & F_{21}N_{I,1} & F_{31}N_{I,1} \\ F_{12}N_{I,2} & F_{22}N_{I,2} & F_{32}N_{I,2} \\ F_{13}N_{I,3} & F_{23}N_{I,3} & F_{33}N_{I,3} \\ F_{11}N_{I,2}+F_{12}N_{I,1} & F_{21}N_{I,2}+F_{22}N_{I,1} & F_{31}N_{I,2}+F_{32}N_{I,1} \\ F_{12}N_{I,3}+F_{13}N_{I,2} & F_{22}N_{I,3}+F_{23}N_{I,2} & F_{32}N_{I,3}+F_{33}N_{I,2} \\ F_{11}N_{I,3}+F_{13}N_{I,1} & F_{21}N_{I,3}+F_{23}N_{I,1} & F_{31}N_{I,3}+F_{33}N_{I,1} \end{bmatrix} . \tag{3.21}$$

In the linearized theory, the the spatial derivative of the displacements and the approximation of the strain related quantities are given as

$$\frac{\partial \boldsymbol{u}}{\partial \boldsymbol{X}} = \sum_{I=1}^{n_{\text{node}}} \frac{\partial N_I}{\partial \boldsymbol{X}} \boldsymbol{d}_I \qquad \boldsymbol{\varepsilon} \approx \boldsymbol{\varepsilon}^h = \sum_{I=1}^{n_{\text{node}}} \boldsymbol{B}_I^u \boldsymbol{d}_I \, , \tag{3.22}$$

$$\delta\boldsymbol{\varepsilon} \approx \delta\boldsymbol{\varepsilon}^h = \sum_{I=1}^{n_{\text{node}}} \boldsymbol{B}_I^u \delta\boldsymbol{d}_I \, , \qquad \Delta\boldsymbol{\varepsilon} \approx \Delta\boldsymbol{\varepsilon}^h = \sum_{I=1}^{n_{\text{node}}} \boldsymbol{B}_I^u \Delta\boldsymbol{d}_I \, , \tag{3.23}$$

with the B_I^u-matrix for the displacement defined as

$$\boldsymbol{B}_I^u = \begin{bmatrix} N_{I,1} & & \\ & N_{I,2} & \\ & & N_{I,3} \\ N_{I,2} & N_{I,1} & \\ & N_{I,3} & N_{I,2} \\ N_{I,3} & & N_{I,1} \end{bmatrix} . \tag{3.24}$$

Based on these approximations, the weak form of the balance of linear momentum, which is given in Equation (3.7), can be discretized in each finite element, denoted by e, as

$$G^e(\boldsymbol{d}^e, \delta\boldsymbol{d}^e) = \sum_{I=1}^{n_{\text{node}}} \delta\boldsymbol{d}_I^{\mathrm{T}} \int_{\mathcal{B}^e} \boldsymbol{B}_I^{\mathrm{T}} \cdot \boldsymbol{S} \, \mathrm{d}V - \sum_{I=1}^{n_{\text{node}}} \delta\boldsymbol{d}_I^{\mathrm{T}} \int_{\mathcal{B}^e} N_I \rho_0 \boldsymbol{b} \, \mathrm{d}V - \sum_{I=1}^{n_{\text{node}}} \delta\boldsymbol{d}_I^{\mathrm{T}} \int_{\partial\mathcal{B}^e} N_I \boldsymbol{t}_0 \, \mathrm{d}A \, . \tag{3.25}$$

The integral terms can be simplified by introduction of the nodal residual vector $\boldsymbol{r}_I$ to

$$G^e(\boldsymbol{d}^e, \delta\boldsymbol{d}^e) = \sum_{I=1}^{n_{\text{node}}} \delta\boldsymbol{d}_I^{\mathrm{T}} \boldsymbol{r}_I = (\delta\boldsymbol{d}^e)^{\mathrm{T}} \boldsymbol{r}^e \tag{3.26}$$

$$\text{with} \quad \boldsymbol{r}_I = \int_{\mathcal{B}^e} \boldsymbol{B}_I^{\mathrm{T}} \cdot \boldsymbol{S} \, \mathrm{d}V - \delta\boldsymbol{d}_I^{\mathrm{T}} \int_{\mathcal{B}^e} N_I \rho_0 \boldsymbol{b} \, \mathrm{d}V - \delta\boldsymbol{d}_I^{\mathrm{T}} \int_{\partial\mathcal{B}^e} N_I \boldsymbol{t}_0 \, \mathrm{d}A \, ,$$

in which $\delta\boldsymbol{d}^e$ and $\boldsymbol{r}^e$ stand for the virtual displacement vector and the residual vector of one element with

$$\delta\boldsymbol{d}^e = \left[(\delta\boldsymbol{d}_1)^{\mathrm{T}}, \ldots, (\delta\boldsymbol{d}_{n_{\text{node}}})^{\mathrm{T}}\right]^{\mathrm{T}} \quad \text{and} \quad \boldsymbol{r}^e = \left[(\boldsymbol{r}_1)^{\mathrm{T}}, \ldots, (\boldsymbol{r}_{n_{\text{node}}})^{\mathrm{T}}\right]^{\mathrm{T}} . \tag{3.27}$$

The remaining terms in the linearization, see Equation (3.13), can be divided into a material ΔG^{mat} and a geometrical part ΔG^{geo} given as

$$\Delta G^{\text{mat}} = \int_{\mathcal{B}_0} \frac{1}{2}\delta\boldsymbol{C} : \mathbb{C} : \frac{1}{2}\Delta\boldsymbol{C} \, \mathrm{d}V \quad \text{and} \quad \Delta G^{\text{geo}} = \int_{\mathcal{B}_0} \boldsymbol{S} : \frac{1}{2}\Delta\delta\boldsymbol{C} \, \mathrm{d}V \, . \tag{3.28}$$

For one element it holds that

$$\Delta G^{e,\mathrm{mat}}(\boldsymbol{d}^e, \delta\boldsymbol{d}^e, \Delta\boldsymbol{d}^e) = \sum_{I=1}^{n_\mathrm{node}} \sum_{J=1}^{n_\mathrm{node}} \delta\boldsymbol{d}_I^\mathrm{T} \int_{\mathcal{B}^e} \boldsymbol{B}_I^\mathrm{T} : \mathbb{C} : \boldsymbol{B}_J \, \mathrm{d}V \Delta\boldsymbol{d}_J \,, \tag{3.29}$$

$$\Delta G^{e,\mathrm{geo}}(\boldsymbol{d}^e, \delta\boldsymbol{d}^e, \Delta\boldsymbol{d}^e) = \sum_{I=1}^{n_\mathrm{node}} \sum_{J=1}^{n_\mathrm{node}} \delta d_I^a \int_{\mathcal{B}^e} (N_{I,A}\delta_{ab}N_{J,B}) S^{AB} \, \mathrm{d}V \Delta d_J^b \,. \tag{3.30}$$

In the last equation, an index notation is used to derive the linearized virtual Cauchy-Green tensor with Kronecker delta δ_{AB}

$$\frac{1}{2}\Delta\delta C_{AB} = \frac{1}{2}(\delta F_A^a \, \delta_{ab} \, \Delta F_B^b + \Delta F_A^a \, \delta_{ab} \, \delta F_B^b) = \sum_{I=1}^{n_\mathrm{node}} \sum_{J=1}^{n_\mathrm{node}} N_{I,A} \, \delta d_I^a \, \delta_{ab} \, N_{J,B} \, \Delta d_J^b \tag{3.31}$$

with virtual and incremental deformation gradient

$$\delta F_A^a = \sum_{I=1}^{n_\mathrm{node}} N_{I,A} \, \delta d_I^a \quad \text{and} \quad \Delta F_A^a = \sum_{I=1}^{n_\mathrm{node}} N_{I,A} \, \Delta d_I^a \,. \tag{3.32}$$

An analogous abbreviation as before leads to

$$\Delta G^{e,\mathrm{mat}} = \sum_{I=1}^{n_\mathrm{node}} \sum_{J=1}^{n_\mathrm{node}} \delta\boldsymbol{d}_I^\mathrm{T} \boldsymbol{k}_{IJ}^{e,\mathrm{mat}} \Delta\boldsymbol{d}_J \quad \text{with} \quad \boldsymbol{k}_{IJ}^{e,\mathrm{mat}} = \int_{\mathcal{B}^e} \boldsymbol{B}_I^\mathrm{T} : \mathbb{C} : \boldsymbol{B}_J \, \mathrm{d}V \,, \tag{3.33}$$

$$\Delta G^{e,\mathrm{geo}} = \sum_{I=1}^{n_\mathrm{node}} \sum_{J=1}^{n_\mathrm{node}} \delta\boldsymbol{d}_I^\mathrm{T} \boldsymbol{k}_{IJ}^{e,\mathrm{geo}} \Delta\boldsymbol{d}_J \quad \text{with} \quad \boldsymbol{k}_{IJ}^{e,\mathrm{geo}} = \int_{\mathcal{B}^e} (N_{I,A}N_{J,B}) S^{AB} \, \mathrm{d}V \,, \tag{3.34}$$

and thus one obtains

$$\mathrm{Lin}\, G^e = \sum_{I=1}^{n_\mathrm{node}} \delta\boldsymbol{d}_I^\mathrm{T} \boldsymbol{r}_I^e + \sum_{I=1}^{n_\mathrm{node}} \sum_{J=1}^{n_\mathrm{node}} \delta\boldsymbol{d}_I^\mathrm{T} \boldsymbol{k}_{IJ}^e \Delta\boldsymbol{d}_J \quad \text{with} \quad \boldsymbol{k}_{IJ}^e = \boldsymbol{k}_{IJ}^{e,\mathrm{mat}} + \boldsymbol{k}_{IJ}^{e,\mathrm{geo}} \,. \tag{3.35}$$

The element stiffness matrices, which are defined as

$$\boldsymbol{k}^e = \begin{bmatrix} k_{11} & k_{12} & \dots & k_{1n_\mathrm{node}} \\ k_{21} & k_{22} & \dots & k_{1n_\mathrm{node}} \\ \vdots & \vdots & & \vdots \\ k_{n_\mathrm{node}1} & k_{n_\mathrm{node}2} & \dots & k_{n_\mathrm{node}n_\mathrm{node}} \end{bmatrix} , \tag{3.36}$$

and the element residual vectors $\boldsymbol{r}^e$ are assembled over all elements n_ele to the global stiffness matrix and global residual vector

$$\boldsymbol{K} = \mathop{\mathbf{A}}_{e\,=\,1}^{n_\mathrm{ele}} \boldsymbol{k}^e \qquad \text{and} \qquad \boldsymbol{R} = \mathop{\mathbf{A}}_{e\,=\,1}^{n_\mathrm{ele}} \boldsymbol{r}^e \,. \tag{3.37}$$

Together with the global form of the virtual and incremental displacement vectors $\delta\boldsymbol{D}$ and $\Delta\boldsymbol{D}$, respectively,

$$\delta\boldsymbol{D} = \left[(\delta\boldsymbol{d}^1)^\mathrm{T} \quad \dots \quad (\delta\boldsymbol{d}^{n_\mathrm{ele}})^\mathrm{T}\right]^\mathrm{T} , \quad \Delta\boldsymbol{D} = \left[(\Delta\boldsymbol{d}^1)^\mathrm{T} \quad \dots \quad (\Delta\boldsymbol{d}^{n_\mathrm{ele}})^\mathrm{T}\right]^\mathrm{T} , \tag{3.38}$$

the linear system of equation, that has to be solved with, for instance, the Newton-Raphson iteration scheme with respect to $\Delta\boldsymbol{D}$, can be described as

$$\delta\boldsymbol{D}^T\left(\boldsymbol{K}\Delta\boldsymbol{D}+\boldsymbol{R}\right)=\boldsymbol{0} \tag{3.39}$$

The result

$$\Delta\boldsymbol{D}=-\boldsymbol{K}^{-1}\boldsymbol{R}, \tag{3.40}$$

represents the update of the global nodal displacement vector $\boldsymbol{D} \Leftarrow \boldsymbol{D}+\Delta\boldsymbol{D}$ which is iterated until the global residual vector falls below a certain tolerance $|\boldsymbol{R}| < tol$.

Due to the occurring nonlinearities the integrals cannot be solved analytically in most cases. Thus, the Gauss integration procedure as a numerical integration scheme is utilized, which leads to small inaccuracies of the method. It replaces the integrals with a sum over the integrand, i.e., the function that has to be integrated, is evaluated at certain points, the so-called Gauss or integration points, and related weighting factors, i.e.,

$$\begin{aligned}\int_x\int_y\int_z f(x,y,z)\,\mathrm{d}z\,\mathrm{d}y\,\mathrm{d}x &= \int_0^1\int_0^{1-\xi}\int_0^{1-\xi-\eta} f(\xi,\eta,\zeta)\,\det(\boldsymbol{J})\,\mathrm{d}\zeta\,\mathrm{d}\eta\,\mathrm{d}\xi \\ &\approx \sum_i^{n_p} w_i f(\xi_i,\eta_i,\zeta_i)\det(\boldsymbol{J}(\xi_i,\eta_i,\zeta_i))\,. \end{aligned} \tag{3.41}$$

Therein, f denotes the integrand and n_p stands for the number of Gauss points with coordinates (ξ_i,η_i,ζ_i) in the isoparametric element. Moreover, one weighting factors w_i is associated to every Gauss point i. Details on the possible two- or three-dimensional isoparametric elements with integration points and weights are given in Section 3.6.

3.5 Thermo-mechanical coupled problem

In the previous Sections 3.1 - 3.4, the FEM has been introduced for the simple case of static, isothermal material behavior. In order to take into account the temperature evolution, the boundary value problem, given in Section 3.1, has to be extended by the balance of energy, see Equation (2.52). Thus, it is also solved with respect to temperature as an additional degree of freedom. The associated boundary conditions for the temperature θ and the heat flux $\boldsymbol{q}$ over the boundary of the continuum are defined by

$$\theta=\theta_0 \text{ on } \partial\mathcal{B}_{0\theta} \quad \text{and} \quad \boldsymbol{q}\cdot\boldsymbol{N}=q_0 \text{ on } \partial\mathcal{B}_{0\boldsymbol{q}}\,, \tag{3.42}$$

$$\text{with} \quad \partial\mathcal{B}_{0\theta}\cup\partial\mathcal{B}_{0\boldsymbol{q}}=\partial\mathcal{B}_0 \quad \text{and} \quad \partial\mathcal{B}_{0\theta}\cap\partial\mathcal{B}_{0\boldsymbol{q}}=\emptyset\,. \tag{3.43}$$

In case of a thermo-mechanical coupled problem, Equations (3.2), (3.3), (3.42) and (3.43) have to hold. Analogously to the isothermal case, the Galerkin method is applied in order to derive the weak form of the balance of energy, i.e., the strong form is multiplied with a scalar test function $\delta\theta \in \{\delta\theta|\delta\theta=0 \text{ on } \partial\mathcal{B}_0\}$, such that one obtains

$$G_\theta(\boldsymbol{u},\theta,\delta\theta)=\int_{\mathcal{B}_0}\left(\rho\,\dot{\epsilon}-\boldsymbol{\sigma}:\boldsymbol{D}-\rho\,r+\operatorname{div}\boldsymbol{q}\right)\delta\theta\,\mathrm{d}V=0\,. \tag{3.44}$$

Therein, r denotes a heat source or sink and ϵ is the specific internal energy. For the discretization of the weak form of the balance of energy and the subsequent linearization, one approximates the temperature and its related quantities by

$$\theta \approx \theta^h = \sum_{I=1}^{n_{\text{node}}} N_I d_I \,, \quad \delta\theta \approx \delta\theta^h = \sum_{I=1}^{n_{\text{node}}} N_I \delta d_I \,, \quad \Delta\theta \approx \Delta\theta^h = \sum_{I=1}^{n_{\text{node}}} N_I \Delta d_I \,, \tag{3.45}$$

$$\operatorname{grad} \delta\theta \approx \operatorname{grad} \delta\theta^h = \sum_{I=1}^{n_{\text{node}}} \boldsymbol{B}_I^\theta \delta d_I \,, \quad \operatorname{grad} \Delta\theta \approx \operatorname{grad} \Delta\theta^h = \sum_{I=1}^{n_{\text{node}}} \boldsymbol{B}_I^\theta \Delta d_I \tag{3.46}$$

with the so called B_I^θ-matrix for the temperature defined as $B_I^{\theta\mathrm{T}} = \begin{bmatrix} N^I_{,1} & N^I_{,2} & N^I_{,3} \end{bmatrix}$. Note that for a fully thermo-mechanically coupled problem, the weak form of balance of linear momentum has to be linearized with respect to the displacement and also with respect to the temperature. To this end, the weak form of the balance of linear momentum in Equation (3.8) is extended to

$$G_u(\boldsymbol{u}, \theta, \delta\boldsymbol{u}) := \int_{\mathcal{B}} \boldsymbol{\sigma} : \operatorname{grad}^{\text{sym}} \delta\boldsymbol{u} \, \mathrm{d}v - \int_{\mathcal{B}} \rho \boldsymbol{b} \cdot \delta\boldsymbol{u} \, \mathrm{d}v - \int_{\partial\mathcal{B}} \boldsymbol{t} \cdot \delta\boldsymbol{u} \, \mathrm{d}a = 0 \,. \tag{3.47}$$

Details on the linearization of the weak forms in Equations (3.44) and (3.47) can be found in Appendix B. The final element stiffness matrix $\boldsymbol{k}^e$ is of the form

$$\left[\begin{array}{c|c} \boldsymbol{k}^e_{\boldsymbol{uu}} & \boldsymbol{k}^e_{\boldsymbol{u}\theta} \\ \hline \boldsymbol{k}^e_{\theta\boldsymbol{u}} & k^e_{\theta\theta} \end{array}\right] . \tag{3.48}$$

Therein, the block matrix $\boldsymbol{k}^e_{\boldsymbol{uu}}$ and the column vector $\boldsymbol{k}^e_{\boldsymbol{u}\theta}$ result from the linearization of the weak form of balance of linear momentum G_u with respect to the displacement $\boldsymbol{u}$ and the temperature θ, respectively, while the row vector $\boldsymbol{k}^e_{\theta\boldsymbol{u}}$ and the scalar entry $\boldsymbol{k}^e_{\theta\theta}$ result from the the linearization of the weak form of balance of energy G_θ with respect to the displacement $\boldsymbol{u}$ and the temperature θ, respectively.

3.6 Elements in 2D and 3D

In this work, two- and three-dimensional boundary value problems are analyzed. Therefore, quadrilaterals and hexahedrons with linear or quadratic ansatz functions are chosen to discretize the physical body, see Figure 3.3. In the following, the ansatz functions of the four- and nine-noded two-dimensional quadrilaterals are presented as isoparametric elements, for the three-dimensional case see Appendix C.

For the linear element, the four ansatz functions are given as

$$\begin{aligned} N_1(\xi,\eta) &= \frac{1}{2}(1-\xi)(1-\eta)\,, & N_2(\xi,\eta) &= \frac{1}{2}(1+\xi)(1-\eta)\,, \\ N_3(\xi,\eta) &= \frac{1}{2}(1+\xi)(1+\eta)\,, & N_4(\xi,\eta) &= \frac{1}{2}(1-\xi)(1+\eta)\,. \end{aligned} \tag{3.49}$$

The ansatz functions for the corner nodes of a nine-noded quadratic element are given as

$$\begin{aligned} N_1(\xi,\eta) &= \frac{1}{4}(\xi^2-\xi)(\eta^2-\eta)\,, & N_2(\xi,\eta) &= \frac{1}{4}(\xi^2+\xi)(\eta^2-\eta)\,, \\ N_3(\xi,\eta) &= \frac{1}{4}(\xi^2+\xi)(\eta^2+\eta)\,, & N_4(\xi,\eta) &= \frac{1}{4}(\xi^2-\xi)(\eta^2+\eta)\,, \end{aligned} \tag{3.50}$$

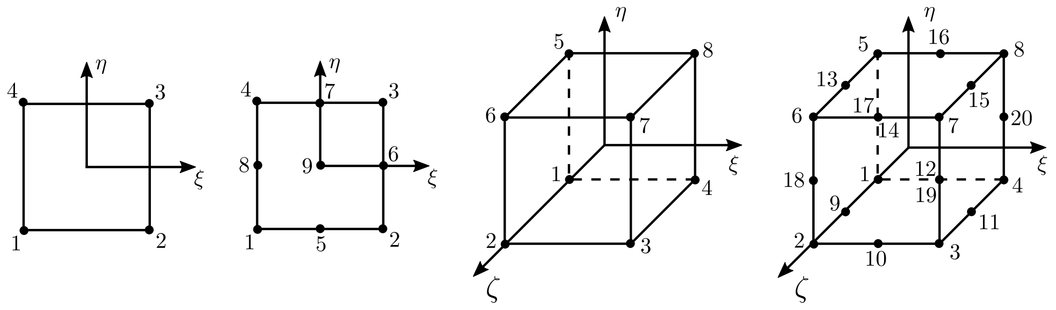

Figure 3.3: Two-dimensional quadrilateral with four or nine nodes and three-dimensional hexahedrons with eight or twenty nodes.

and the nodes on the edges of a quadratic element are

$$\begin{aligned} N_5(\xi,\eta) &= \frac{1}{2}(\eta^2-\eta)(1-\xi^2)\,, \qquad & N_6(\xi,\eta) &= \frac{1}{2}(\xi^2+\xi)(1-\eta^2)\,, \\ N_7(\xi,\eta) &= \frac{1}{2}(\eta^2+\eta)(1-\xi^2)\,, \qquad & N_8(\xi,\eta) &= \frac{1}{2}(\xi^2-\xi)(1-\eta^2)\,, \end{aligned} \tag{3.51}$$

and for the center node

$$N_9(\xi,\eta) = (1-\xi^2)(1-\eta^2)\,. \tag{3.52}$$

For the numerical integration, the number of Gauss points n_p and their respective coordinates depends on the chosen element, see Table 3.1 and Appendix C.

Table 3.1: Gauss points with weighting factors.

dimension	n_{node}	n_p	i	coordinates of GP		weighting
				ξ_i	η_i	w_i
2D	4	4	1	$-1/\sqrt{3}$	$-1/\sqrt{3}$	1
			2	$+1/\sqrt{3}$	$-1/\sqrt{3}$	1
			3	$-1/\sqrt{3}$	$+1/\sqrt{3}$	1
			4	$+1/\sqrt{3}$	$+1/\sqrt{3}$	1
2D	9	9	1	$-\sqrt{3/5}$	$-\sqrt{3/5}$	25/81
			2	0	$-\sqrt{3/5}$	40/81
			3	$+\sqrt{3/5}$	$-\sqrt{3/5}$	25/81
			4	$-\sqrt{3/5}$	0	40/81
			5	0	0	64/81
			6	$+\sqrt{3/5}$	0	40/81
			7	$-\sqrt{3/5}$	$\sqrt{3/5}$	25/81
			8	0	$\sqrt{3/5}$	40/81
			9	$+\sqrt{3/5}$	$\sqrt{3/5}$	25/81

3.7 Surface elements for the heat flux

Depending on the boundary value problem that has to be solved, the description of hydrostatic pressure or heat transfer over the boundary of the body is inevitable to consider. Therefore, the application of surface elements is a useful tool. As the name suggests, surface elements ($\mathcal{B}_S^e$) describe physical processes on the boundary of the body. Thus, their dimension is always reduced by one with respect to the continuum, i.e., area elements are defined for three-dimensional boundary value problems and line elements for two-dimensional boundary value problems. The nodes and the degree of the ansatz functions correspond to the underlying discretization of the body as shown in Figure 3.4a.

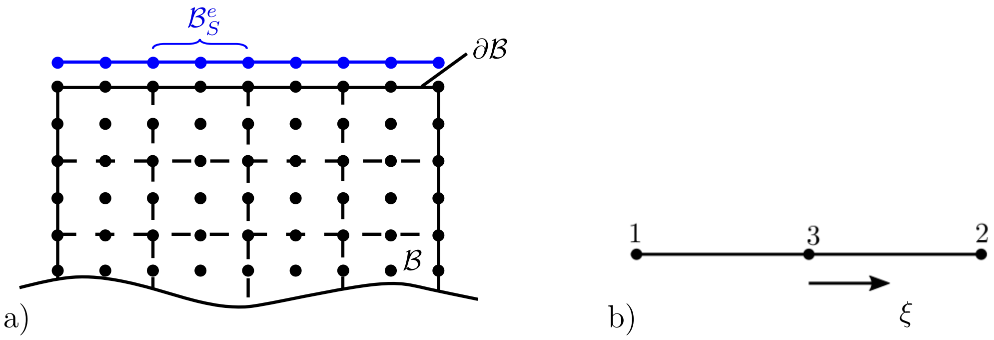

Figure 3.4: a) Two-dimensional body $\mathcal{B}$ discretized with quadratic elements and application of quadratic surface elements $\mathcal{B}_S^e$ on boundary $\partial\mathcal{B}$ and b) parametric element with node numbering and origin of the coordinate system.

The heat flux over the boundary of the continuum is described by the integral term

$$G_\theta^{\text{ext}} = -\int_{\partial\mathcal{B}_0} \boldsymbol{q}\cdot\boldsymbol{N}\,\delta\theta\,\mathrm{da}\,, \tag{3.53}$$

in the weak form of the balance of energy, see Appendix B. Recalling the assumption that $\boldsymbol{q} = -k\,\mathrm{grad}\,\theta$ with positive heat conduction coefficient $k > 0$, the heat transition at the boundary is given by

$$q_{\text{surf}} = h_{\text{TC}}(\theta - \theta_\infty)A\,, \tag{3.54}$$

with h_{TC} as heat transfer coefficient, which depends on θ as actual temperature, θ_∞ as ambient temperature of the medium and A as area of the element. For the numerical implementation, a Robin type boundary condition or boundary condition of third kind is utilized to describe the heat flux through the surface area of the component. Such a Robin type boundary condition is defined as a linear combination of the value and its derivative at the surface, which, in this work, is considered to apply the temperature loss to the surrounding medium, see e.g. Gustafson and Abe [65], Jung and Langer [85], Knothe and Wessels [92] and Barrogqueiro et al. [9] for the application to a thermal problem. In case of a two-dimensional boundary value problem for which nine-noded quadrilaterals are chosen for the discretization, the quadratic ansatz functions for the one-dimensional surface elements are defined as

$$N_1(\xi) = \frac{1}{2}\xi(\xi-1)\,, \quad N_2(\xi) = \frac{1}{2}\xi(\xi+1) \quad \text{and} \quad N_3(\xi) = (1-\xi^2)\,. \tag{3.55}$$

The node numbering and the location of the origin of the coordinate system of the parametric element can be found in Figure 3.4b. In Table 3.2, the location of the integration points and their respective weights are given, see Wriggers [206], Bathe [13] or Zienkiewicz and Taylor [210]. The discretized form on element level is obtained as

$$G_\theta^{e,\mathrm{ext}} = - \sum_{I=1}^{n_{\mathrm{node}}} \delta \boldsymbol{d}_I^{\mathrm{T}} \int_{\partial \mathcal{B}_0^e} N_I \, \boldsymbol{q} \cdot \boldsymbol{n} \, \mathrm{d}A \,. \tag{3.56}$$

Table 3.2: Gauss points with weighting factors for surface elements.

dimension	n_{node}	n_p	i	coordinates of GP ξ_i	weighting w_i
1D	3	3	1	$-\sqrt{3}/\sqrt{5}$	$5/9$
			2	$+\sqrt{3}/\sqrt{5}$	$5/9$
			3	0	$8/9$

4 Phase transformation and residual stresses

The manufacturing process of steel components consists of a large variety of processes. Casting, forging, rolling and others methods are used not only to form the desired geometry but also to introduce specific component properties such as extended usability. Phase transformations or residual stresses among others, which are explained in this section, are of particular importance in this context.

4.1 Theory of phase transformation

In general, the term "phaseßtands for a spatial area within the body under consideration which has the same material parameters. However, differences may occur caused by the texture or the designated grain orientations, for instance. This means that within a phase, for example, the density, the chemical composition or the mechanical material properties are homogeneous. It is crucial that a phase does not have to be spatially coherent - the assignment to a phase is made purely on the basis of the present material properties. Different phases are consequently characterized on the basis of their individual properties. In steel materials many different phases can be considered such as austenite, bainite, cementite, ferrite, graphite, ledeburite, martensite, pearlite and spheroidite. Several can be present simultaneously, but also only partially. The stability of a phase is usually based on temperature or pressure, among other factors. Based on these dependencies, phase diagrams can be created for a material. One very well known is the iron-carbon diagram, as given in Figure 4.1a. Furthermore, time-temperature-transformation diagrams provide indispensable information about the microstructural evolution of a material or alloy during heat treatment, see Figure 4.1b.

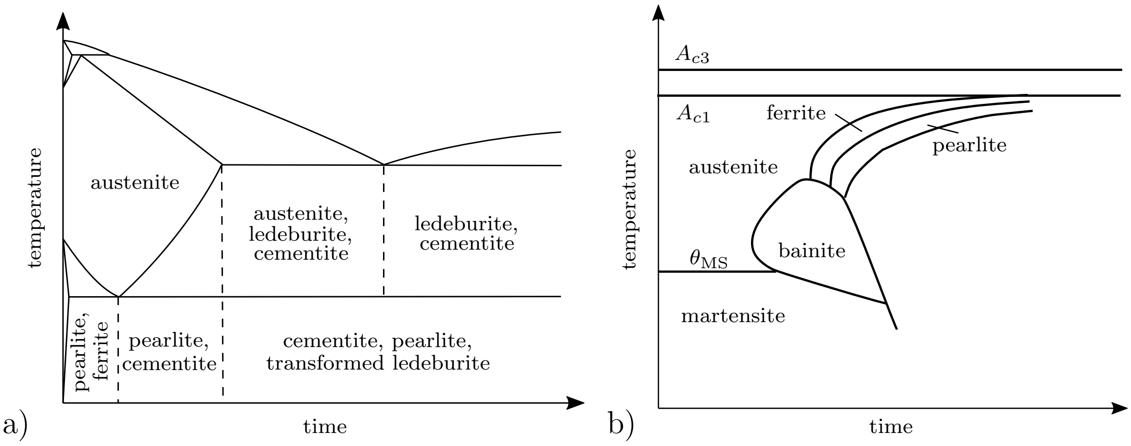

Figure 4.1: Sketch of the iron-carbon phase diagram and b) exemplary time-temperature-transformation (TTT) diagram, in which θ_{Ms} denotes the temperature when martensite starts to form in austenite during cooling. Furthermore, A_{c1} stands for the temperature, at which the formation of austenite begins during heating and A_{c3} stands for the temperature, at which the transformation from ferrite to austenite stops during heating.

Phase transformation processes can be roughly divided into two types: diffusion controlled and diffusionless phase transformations. The first group of diffusion controlled phase transformations is evoked by relatively slow cooling processes, regarding e.g. the diffusion of iron, carbon or other alloying elements. One example is the growth of ferrite or pearlite in an austenitic parent phase. The second group describes fast cooling with high cooling rates, so that no diffusion of e.g. iron or carbon takes place inside the material. That is a main characteristic of a martensitic phase transformation in an austenitic material. For the mathematical description of the evolution of phase fractions in diffusion controlled phase transformations the Johnson-Mehl-Avrami-Kolmogorov (JMAK) equation is classically utilized, see Section 4.1.1 and KOLMOGOROV [94], AVRAMI [3; 4; 5] and JOHNSON AND MEHL [84]. In case of fast phase transformations without diffusion, Koistinen and Marburger proposed the Koistinen-Marburger differential equation, see Section 4.1.2 and KOISTINEN AND MARBURGER [93].

Moreover, the microstructures that are formed can be grouped on the basis of the phase that is found most. If a component made from steel is cooled very slow, the microstructure is dominated by ferrite or spheroidized cementite. Otherwise, in case of not such slow cooling, one can roughly subdivide the evolving microstructures into martensitic (diffusionless), bainitic (partly diffusion controlled) or pearlitic (mainly diffusion controlled) structures, cf. HOUGARDY [80]. More precisely, it is possible to differentiate within one group of microstructures. For instance, martensite can be either plate-martensite or lath-martensite in dependence of the carbon concentration present, see NISHIYAMA [130]. Similar it holds for bainite, which forms as upper or lower bainite, which happens also based on the carbon concentration, see e.g. BHADESHIA AND CHRISTIAN [21] and TAKAHASHI AND BHADESHIA [176].

In the 20th century, many investigations, numerically as well as experimentally, deal with solid phase transformations. A good overview on the different methods is given in CHRISTIAN [28]. All approaches have in common that a phase transformation comes along with a rearrangement of the atomic lattice accompanied by a volumetric change of the unit cell. But, the approaches to numerically model the microstructural evolution or phase transformation differ fundamentally from each other. One common method are phenomenological material models on the macroscale, which effectively represent the microscopic phase transformation and its characteristics. Therein, the term “macroscalerrefers to the length-scale of the considered component, which is often measured in milimeter or on an even greater scale. A smaller scale, referred to as the “microscaleïs not explicitly resolved. It would depict the microstructure with its heterogeneities, different phases, grains or atoms. Thus, the length-scale would be micrometer, nanometer or even smaller.

Considering the austenite-to-**martensite** phase transformation, early examples are the works of BAIN AND DUNKIRK [7] and BAIN AND GRIFFITHS [8], in which the so-called Bain strains are proposed. They describe the transformation of an austenitic unit cell to a martensitic unit cell considering only pure lattice strains as volumetric expansion, for instance. Thereby, three different martensitic variants are obtained, which are schematically illustrated in Figure 4.2. Further quite famous works regarding martensite formation as a solid phase transformation have been presented by WECHSLER [198] and ROITBURD [147]. Other recent single-scale models have been proposed in LEBLOND ET AL. [100; 101], FISCHER [46; 49; 50], FISCHER ET AL. [47; 48], PETIT-GROSTABUSSIAT ET AL. [142], WOLFF ET AL. [203; 204; 205], HALLBERG ET AL. [67; 68] and MAHNKEN ET AL. [110], while LEVITAS [102], FISCHER ET AL. [51] and LEVITAS ET AL. [105] focus on microstructural resolution with application of suitable homogenization schemes. A recent review article concerning phase transformations and other characteristics of inelastic materials can be found in LEVITAS [103]. Moreover, FARAHANI ET AL. [41] analyze the austenite-to-martensite phase transformation in carbon steel pipes, while the authors in Tian et al. [185] contribute to the investigation of a quenching process resulting in bainitic and martensitic product phase.

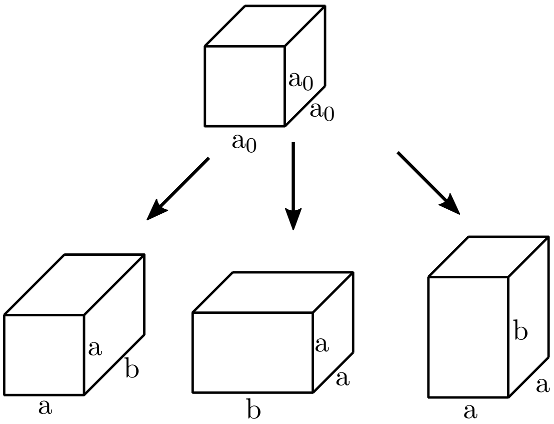

Figure 4.2: The three Bain groups to depict different variants of martensite, cf. Bhattacharya [22], with a_0 as edge length of a face-centered cubic austenitic unit cell and a, b as edge length of a body-centered tetragonal martensitic unit cell, adopted from Behrens et al. [15].

In case of a diffusion controlled phase transformation from austenite to **bainite**, **ferrit** or **pearlite**, the JMAK equation is utilized as stated above and further explained in Section 4.1.1. In the last years, many investigations regarding this diffusion controlled phase transformation in steels during heat treatment have been published. For instance in Babu and Kumar [6] the quenching process of a cylindrical specimen in water has been analyzed by comparison of different numerical approaches to model phase transition. Time-temperature-transformation (TTT) diagrams have been found to offer accurate results. Similar approaches utilizing TTT diagrams in combination with the JMAK equation, comparisons to other approaches such as cellular automata, atomistic simulations or phase field models can be found in Pietrzyk et al. [143] and Militzer et al. [123]. Mahnken et al. [111] and Hütter et al. [81] focus on bainite formation. Further works regarding phase transformations from austenite to bainite, pearlite, ferrite and also martensite during heat treatment of steels are Pernach et al. [141], Ilmola et al. [82], Esfahani et al. [37] and Chen et al. [27]. These works also partly consider related residual stress distributions.

In contrast to the previously mentioned models, polycrystalline models provide the ability to represent the crystalline structure and resolve the phases with grain accuracy, see for example Roters et al. [149] and Mahnken et al. [112; 113]. Gierden et al. [61] reviews on the FE-FFT-based method. The idea ot the latter is the combination of a Finite Element Analysis on macroscopic level with a Fast Fourier transformation on microscopic level to depict polycrystalline material behavior. It provides an alternative to the classical micro-macro transition approach, which is introduced in detail in Section 8.

Furthermore, multi-scale simulation approaches describe a third possibility and form a kind of middle level between the purely macroscopic view and the high resolution of individual grains. In Turteltaub and Suiker [187] a multi-scale formulation for an effective mesoscopic stiffness tensor taking into account the lattice and lower and upper microscale are given. Therein, the mesoscale refers to a level, on which different phases are resolved. Martensitic phase transformations in terms of multi-scale analysis are given in Sengupta et al. [164; 165]. Regarding shape memory alloys undergoing a martensitic phase transformation a multi-scale model is proposed in Bartel and Hackl [11], in which also a good overview summarizing recent works can be found. A single-phase alloyed cylindrical specimen after quenching is examined in Fernández et al. [43], while Han et al. [69] give a multi-scale approach to investigate thermal residual stresses in a three-phase cylinder. In Barroqueiro et al. [10] a reduced multi-scale model for heat treatment is proposed, which takes into account thermal effects, residual stresses and phase transformation. Prüger et al. [144] study the influence of the microstructure morphology during the austenite-to-martensite phase transformation for TRIP-steels. Therein, TRIP refers to transformation induced plasticity. In general, TRIP-steels are a class of high-strength steels, which possess an outstanding combination of high strength and good ductility. A fully coupled thermo-mechanical approach on two scales including phase transformations is given in Schicchi et al. [152].

Not to be forgotten is also the large set of phase field or multi-phase field models, which, following the name, are very well suited for the simulation of a phase transformation on the microscale, see e.g. Steinbach et al. [173], Tiaden et al. [184] and Steinbach and Pezzolla [172]. Multi-phase field models are used to calculate elastic stresses and thermodynamic quantities that may occur due to phase transitions. Such approaches are used to investigate phase transformations in the material during the production process of a component, for instance. This last group is of high interest and part of very current research but not in focus of this work. The interested reader is kindly referred to e.g. Mamivand et al. [114], Schmitt et al. [154], Schmitt [153], Schneider et al. [155; 156; 157], Schoof et al. [159; 160], Basak and Levitas [12], Herrmann et al. [77], Esfahani et al. [38], Paliwal et al. [140] and Schoof [158].

4.1.1 JMAK equation

In the late 1930's and early 1940's, respectively, an expression of the phase fractions in dependence of time has been proposed in Kolmogorov [94], Avrami [3; 4; 5] and Johnson and Mehl [84]. The Johnson-Mehl-Avrami-Kolmogorov (JMAK) equation describes the isothermal solid transformation from one phase to another phase, which are called parent and product phase. The initial state of the material fully consists of the parent phase, although the product phase is thermodynamically favorable. In its most simplified form, for a final state with 100 % product phase, it is given as

$$c(t) = 1 - \exp(-K_{\text{JMAK}}\, t^n) \tag{4.1}$$

with phase fraction c of the product phase, time t, Avrami-exponent n and constant K_{JMAK}. The Avrami-exponent n depends on time, temperature and the transformation progress and describes the geometry of the nucleus as well as the evolution over time. In contrast, constant K_{JMAK} is only in dependence of temperature to describe the migration speed and nucleation.

It is important to notice that there are crucial assumptions made for the derivation of Equation (4.1). Avrami assumed that nucleation always occurs randomly and homogeneous, that the growth rate is independent of the state of transformation and that the phase growths with same rate in all directions. In case that the final state shows a mixture of parent and product phase, Equation (4.1) can be adopted to

$$c(t) = c_{\text{eq}}(1 - \exp(-K_{\text{JMAK}}\, t^n)) \tag{4.2}$$

with c_{eq} denoting the final volume fraction of the product phase.

In general, both parameters, n and K_{JMAK}, can be computed based on isothermal TTT diagrams. Therefore, the curves specifying the beginning and the end of the transformation must be known, see Figure 4.3. They are indicated by indices 01 and 99, respectively. Since it holds that $c(t_{01}) = 0.01\, c_{\text{eq}}$ and $c(t_{99}) = 0.99\, c_{\text{eq}}$, one can determine both unknowns, n and K_{JMAK}, for actual time t and actual temperature θ as

$$n = \frac{\ln\big(\ln \frac{1}{0.01}\big) - \ln\big(\ln \frac{1}{0.99}\big)}{\ln t_{99} - \ln t_{01}} \quad \text{and} \quad \ln K_{\text{JMAK}} = \ln\big(\ln \frac{1}{0.99}\big) - n\, \ln t_{01}\,. \tag{4.3}$$

Details on the derivation of Equations (4.3) are presented in Appendix D.

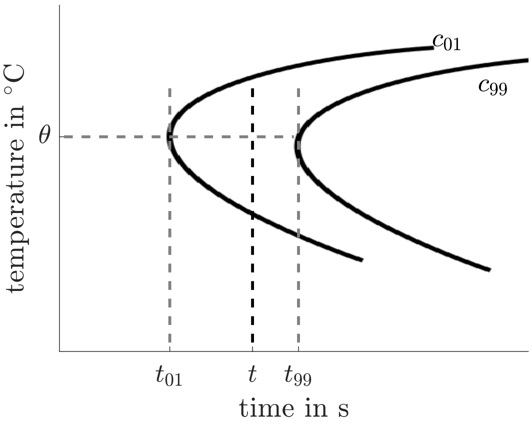

Figure 4.3: Schematic representation of a time-temperature deformation diagram to determine the coefficients n and K_{JMAK} in the JMAK equation. c_{01} and c_{99} specify the curves of the product phase fraction at the beginning and end of phase transformation.

4.1.2 Koistinen-Marburger equation

In order to describe diffusionless phase transformations, Kostinen and Marburger postulated a numerical approach in Koistinen and Marburger [93]. It describes the monotonous increase of the martensitic volume fraction in an initially austenitic phase when the temperature θ falls below the martensitic start temperature θ_{Ms}. Then the actual martensitic volume fraction c^{M} is defined as

$$c^{\text{M}}(\theta) = 1 - \exp\Big(-\frac{\theta_{\text{Ms}} - \theta}{\theta_{\text{M0}}}\Big) \quad \text{for} \quad \theta \leq \theta_{\text{Ms}}\,. \tag{4.4}$$

Therein, θ_{M0} denotes a temperature independent material parameter. As input for the calibration of θ_{M0} the final temperature, for instance room temperature, which is denoted as θ_{RT}, as well as the final volume fraction of martensite c^{M}_{RT} at that temperature are to be known initially. Then, the following relation is valid

$$c^{\text{M}}_{\text{RT}} = 1 - \exp\Big(-\frac{\theta_{\text{Ms}} - \theta_{\text{RT}}}{\theta_{\text{M0}}}\Big) \quad \Leftrightarrow \quad \theta_{\text{M0}} = -\frac{\theta_{\text{Ms}} - \theta_{\text{RT}}}{\ln(1 - c^{\text{M}}_{\text{RT}})}\,. \tag{4.5}$$

It is to be noticed that this quite simple form of the Koistinen-Marburger equation is only valid in case of monotonous cooling processes and thus it has to be a one-way phase transformation form austenite to martensite, see e.g. WOLFF ET AL. [203].

4.2 Residual stresses

In general, stresses are divided into inner and outer stresses, which are superimposed. Therein, outer stresses are applied to a body from the outside, such as gravitational forces or other loads and moments. Inner stresses occur within the material itself, they are independent from outer forces or moments. At this point it has to be noticed that total stress-free components do not exist. Both types are essential for evaluating the failure limit of a component. Such inner stresses can improve but also decrease the component's properties, e.g. the strength. In a closed system, residual stresses are defined as stresses in absence of outer forces or moments, which are in equilibrium. They are classified into three types of residual stresses by the scale, they act on, following MACHERAUCH ET AL. [108], KLOOS [91] and WITHERS AND BHADESHIA [201]. Thus, residual stresses of first type are homogeneous over or a part of the component containing multiple grains. The related inner forces are in equilibrium concerning arbitrary cuts through the component. Changes in this balance lead to macroscopic deformation of the component. Residual stresses of second type refer to a grain or a smaller domain. The inner forces and moments are in equilibrium with respect to a certain number of grains, which is sufficiently large. Changes in balance do not lead to a macroscopic deformation. This also holds for residual stresses of third type, which are defined in the range of the atomic lattice.

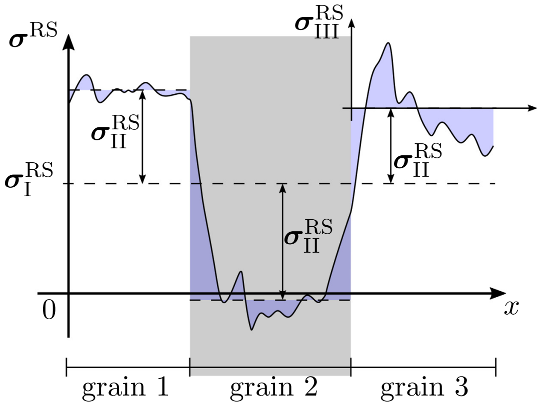

Figure 4.4: Classification of residual stresses into three types, $\boldsymbol{\sigma}_{\mathrm{I}}^{\mathrm{RS}}$, $\boldsymbol{\sigma}_{\mathrm{II}}^{\mathrm{RS}}$ and $\boldsymbol{\sigma}_{\mathrm{III}}^{\mathrm{RS}}$, based on the scale they act on.

In general, observed residual stresses are always a mix of different types of residual stresses which are superimposed. In this context, residual stresses of first type $\boldsymbol{\sigma}_{\mathrm{I}}^{\mathrm{RS}}$ describe an averaged value over several grains, while residual stresses of second type $\boldsymbol{\sigma}_{\mathrm{II}}^{\mathrm{RS}}$ classify the stress fluctuations of that average with respect to the average of the individual grain. Residual stresses of third type $\boldsymbol{\sigma}_{\mathrm{III}}^{\mathrm{RS}}$ are the deviations of the true local stresses of the sum of the residual stresses of first and second type, see Figure 4.4. This can be summarized by following relation

$$\boldsymbol{\sigma}^{\mathrm{RS}} = \boldsymbol{\sigma}_{\mathrm{I}}^{\mathrm{RS}} + \boldsymbol{\sigma}_{\mathrm{II}}^{\mathrm{RS}} + \boldsymbol{\sigma}_{\mathrm{III}}^{\mathrm{RS}} \,. \tag{4.6}$$

Origins of residual stresses are numerous, see KLOOS [91] and WITHERS AND BHADESHIA [202]. They can be differentiated into stress-induced, material-induced or production-induced. Stress-induced residual stresses are a consequence of mechanical, thermal or chemical impact, while material-induced residual stresses are due to heterogeneous materials such as different phases or atomic defects. The third group, production-induced residual stresses result from forming, joining, separating among others. In general, there are also thermal, mechanical and metallurgical interactions to be considered, recall Figure 1.2. Residual stresses of first type can be evoked by e.g. thermal processes such as quenching or by partially plastic deformation of the material as a consequence of inhomogeneous stress distributions. Residual stresses of second type result of heterogeneous microstructures and residual stresses of third type are related to that atomic defects, which can be vacancies, interstitials or antisites for the one-dimensional case. In higher dimension, it is distinguished between grain interfaces, twinning defects or pores for instance.

Residual stresses in metal forming

One method to insert residual stresses in a component during its manufacturing process is offered by hot bulk forming. Such processes roughly consist of three steps: heating, forming and cooling. The latter two, forming and cooling, take most influence on the final stress state inside the material. Especially the cooling step, which can occur fast or slow, and thus evoke a diffusionless or diffusion controlled phase transformation in the material, has to be analyzed in this context. Therein, one aspect of metal heat treatment is the quenching from austenitization temperature to room temperature to achieve predefined or adjust the component's properties. Therefore, three different groups of cooling media are distinguished, which are immersion cooling (e.g. water or oil), splash cooling (e.g. with a spray) or film cooling (e.g. a liquid film applied on the component). Macherauch and Vöhringer [107] discuss different aspects during quenching which have influence on the stress evolution. In order to distinguish between for instance thermal shrinking, material hardening and transformation stresses among many other factors acting on residual stresses, a cylindrical specimen is investigated under different conditions, such that pure thermal shrinking or pure transformational stresses can be observed individually. Further influence factors are investigated by Grum et al. [63]. The authors emphasize the impact if high mass or low mass specimen are considered. In Nallathambi et al. [128], an isothermal staggered FEM scheme is proposed and successfully applied to an L-profile made from Cr-alloyed steel 100Cr6. During quenching simulation, the accuracy of heat transfer coefficients (HTC) plays an important role. Medina-Juárez et al. [116] show that even accurate HTCs does not inherently lead to a quantitatively fitting prediction of residual stresses, since often tensile stresses are overestimated while compressive stresses are underestimated.

5 Thermo-mechanical material modeling of phase transformation

Various approaches can be used for thermo-mechanical modeling of material behavior. A purely macroscopic phenomenological material model allows time and cost efficient calculation of the stress response and deformation behavior. It is useful for the investigation of macroscopic residual stresses (first type), see Sections 6 and 7. If the material is microscopically heterogeneous, a homogenization model must be applied, which is utilized to determine macroscopic field quantities and properties in terms of microstructural parameters and local properties of the heterogeneous material. Several homogenization methods have been developed to replace the partial different equations (balance laws) by homogenized ones. Therefore, effective material properties are taken into account, which describe the overall behavior of the considered material and can be obtained by observation and experimental measurements. Another group of material models, which do not resolve the microstructure, base on semi-analytical homogenization methods, in which effective stresses and tangent moduli are computed by the rule of mixture. Well known semi-analytical homogenization models have been defined by Eshelby [39; 40], Hashin and Shtrikman [72; 73; 74], Hill [79], Budiansky [23], Mori and Tanaka [126], Norris [131] and Hashin [71], see Section 8. In contrast, a two-scale approach based on the direct mirco-macro transition allows to depict the microscale in detail. Thus, microscopic characteristics as well as the phase transformation are explicitly represented by means of a multi-scale finite element analysis, see Section 8, which is utilized in Sections 9 and 10. Microscopic fluctuations of the stresses and other field quantities are taken into account fully resolved, which is one benefit of multi-scale methods.

In this work, different thermo-mechanical material formulations are presented, which can be roughly distinguished into

- **“phenomenological“(PH)** material models: effective material parameters are determined in order to solve homogenized partial differential equations,
- **“semi-analytical multi-phase“(SAMP)** material models: stresses and tangent moduli are computed for each phase individually; afterwards, effective stresses and tangent moduli are determined by the rule of mixture,
- **“multi-scale“** material methods: in contrast to these groups of single-scale approaches, the third group utilizes multi-scale formulations such as the FE^2 method, see Section 8; homogenization techniques are applied to compute the effective behavior.

This chapter is organized as follows. First, the equations for an elasto-plastic material model taking into account an additive split of the strains into elastic and plastic parts are derived. Second, this basic concept is extended such that the additive decomposition of the strain tensor consists of five components for single-scale modeling, which are elastic, plastic, thermal and transformation volumetric strains as well as strains due to transformation induced plasticity (TRIP). Then, phase-specific material parameters are determined, taking into account austenite and martensite as phases occurring during diffusionless cooling or austenite and pearlite for diffusion controlled cooling for the Cr-alloyed steel 100Cr6. Afterwards, the constitutive equations are provided and possibilities to compute the effective material behavior are discussed.

5.1 Isothermal elasto-plastic material model

Ductile materials such as steel exhibit elastic material behavior up to a certain limit, the yield stress, which is represented by Hook's law. When this yield point is exceeded, plastic deformations occur in the material, i.e., irreversible strains occur which do not influence the stresses. Therefore, in the regime of small strains, an additive decomposition of the total strains into elastic and plastic components is used

$$\boldsymbol{\varepsilon} = \boldsymbol{\varepsilon}^{\mathrm{e}} + \boldsymbol{\varepsilon}^{p}\,, \tag{5.1}$$

cf. LUBLINER [106]. Thereby, the elastic strains are computed by $\boldsymbol{\varepsilon}^{\mathrm{e}} = \boldsymbol{\varepsilon} - \boldsymbol{\varepsilon}^{\mathrm{p}}$. They are proportional to the occurring stresses $\boldsymbol{\sigma}$, which are related by the fourth-order elasticity tensor $\mathbb{C}$ by $\boldsymbol{\sigma} = \mathbb{C} : \boldsymbol{\varepsilon}^{\mathrm{e}}$. In general, the stress can be split into a deviatoric and an isochoric part, i.e., $\boldsymbol{\sigma} = \boldsymbol{\sigma}^{\mathrm{dev}} + \boldsymbol{\sigma}^{\mathrm{vol}}$ with $\boldsymbol{\sigma}^{\mathrm{dev}} = 2\mu\,\mathbb{P} : \boldsymbol{\varepsilon}^{\mathrm{e}}$ and $\boldsymbol{\sigma}^{\mathrm{vol}} = \kappa\,\mathrm{tr}\,\boldsymbol{\varepsilon}^{\mathrm{e}}\boldsymbol{I}$. Therein, the fourth-order projection tensor $\mathbb{P}$ is defined as $\mathbb{P} = \mathbb{I} - \frac{1}{3}\boldsymbol{I} \otimes \boldsymbol{I}$ and κ and μ denote bulk and shear modulus, respectively.

In case of violating the threshold of elastic deformation, the occurring plastic strain is characterized as an irreversible deformation of the considered continuum as a consequence of outer forces. If the material behavior is elasto-plastic, the definition of the actual configuration does not only depend on the position of a point in the continuum but also on the loading path. In order to describe the material behavior a flow rule, a hardening law and a yield criterion are required. For the computation of the plastic strain increment, a so-called radial return algorithm can be utilized. In the following, details on the numerical formulation of an isothermal elasto-plastic material model without phase transformation based on the linearized theory are given, see e.g. ORTIZ AND POPOV [136] and ORTIZ AND MARTIN [135]. For further reading, especially with respect to finite deformation, it is referred to SIMO [168], SIMO AND MIEHE [167], MIEHE [119] and SIMO AND HUGHES [166].

Constitutive model of associative elasto-plasticity
Assuming the additive split in Equation (5.1), the stresses $\boldsymbol{\sigma}$ are induced by the elastic strain component. For the plastic strain increment, a constitutive equation is to be defined. Therefore, a scalar-valued free energy function ψ is defined in dependence of an internal variable α and the elastic strains $\boldsymbol{\varepsilon}^{\mathrm{e}}$, i.e.,

$$\psi = \psi(\boldsymbol{\varepsilon}^{\mathrm{e}}, \alpha) = \hat{\psi}^{\mathrm{e}}(\boldsymbol{\varepsilon}^{\mathrm{e}}) + \hat{\psi}^{\mathrm{p}}(\alpha)\,, \tag{5.2}$$

which is split into an elastic $\hat{\psi}^{\mathrm{e}}$ and a plastic part $\hat{\psi}^{\mathrm{p}}$. For the formulation of the constitutive equation of the stresses, the Clausius-Duhem-Inequality is evaluated with the time derivative $\dot{\psi} = \partial_{\boldsymbol{\varepsilon}^{\mathrm{e}}}\psi : \dot{\boldsymbol{\varepsilon}}^{\mathrm{e}} + \partial_{\alpha}\psi\,\dot{\alpha}$ as

$$\begin{aligned} \mathcal{D} = \boldsymbol{\sigma} : \dot{\boldsymbol{\varepsilon}} - \dot{\psi} &= \boldsymbol{\sigma} : (\dot{\boldsymbol{\varepsilon}}^{\mathrm{e}} + \dot{\boldsymbol{\varepsilon}}^{\mathrm{p}}) - (\partial_{\boldsymbol{\varepsilon}^{\mathrm{e}}}\psi : \dot{\boldsymbol{\varepsilon}}^{\mathrm{e}} + \partial_{\alpha}\psi\,\dot{\alpha}) \\ &= (\boldsymbol{\sigma} - \partial_{\boldsymbol{\varepsilon}^{\mathrm{e}}}\psi) : \dot{\boldsymbol{\varepsilon}}^{\mathrm{e}} + \boldsymbol{\sigma} : \dot{\boldsymbol{\varepsilon}}^{\mathrm{p}} - \partial_{\alpha}\psi\,\dot{\alpha} \geq 0\,. \end{aligned} \tag{5.3}$$

Thus, it holds for the stresses that $\boldsymbol{\sigma} = \partial_{\boldsymbol{\varepsilon}^{\mathrm{e}}}\psi$ and the reduced dissipation is given as $\mathcal{D}_{\mathrm{int}} = \boldsymbol{\sigma} : \dot{\boldsymbol{\varepsilon}}^{\mathrm{p}} + \beta\,\dot{\alpha} \geq 0$ with stress-like conjugated variable $\beta = -\partial_{\alpha}\psi$. A convex domain $\mathbb{E}$ limited by the yield surface is defined based on yield criterion Φ as

$$\mathbb{E} = \{\boldsymbol{\sigma} \in \mathbb{R}^{3\times 3} | \Phi(\boldsymbol{\sigma}, \beta) \leq 0\}\,. \tag{5.4}$$

On the boarder of that elastic domain, it holds that $\Phi = 0$, inside the domain $\Phi < 0$ is fulfilled. An associated flow rule is assumed, which means that the flow direction is normal to the yield surface. Hence, the plastic strain increment is defined in terms of the outer normal vector $\boldsymbol{n}$ on the yield surface, see Figure 5.1.

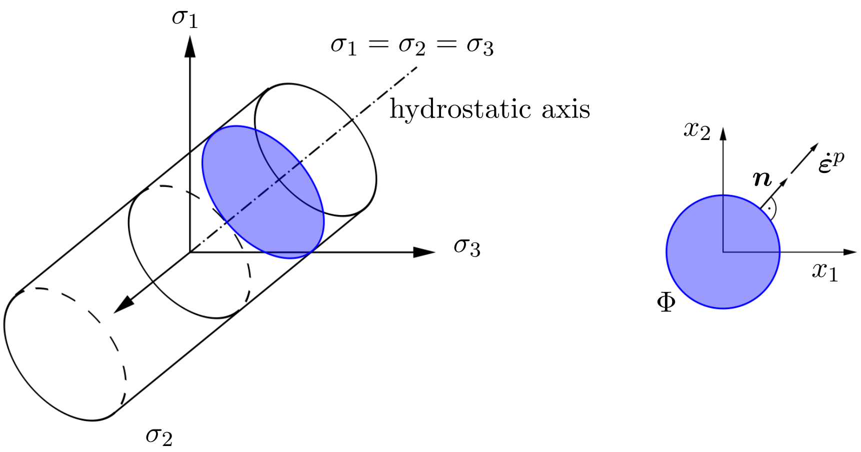

Figure 5.1: Schematic representation of the von Mises yield criterion with hydrostatic axis, i.e., $\sigma_1 = \sigma_2 = \sigma_3$, yield criterion Φ and flow direction of $\dot{\boldsymbol{\varepsilon}}^{\mathrm{p}}$ as outer normal vector $\boldsymbol{n}$.

The principle of maximum dissipation states that the dissipation reaches its maximum at the border of the elastic domain. Thus, the equation $\Phi = 0$ must be evaluated to find the maximal stress state in comparison to all admissible stress states, which are given by $\mathbb{E}$.

$$\mathcal{D}_{\mathrm{int}}(\boldsymbol{\sigma}, \beta) \; - \; \mathcal{D}_{\mathrm{int}}(\boldsymbol{\sigma}^*, \beta^*, \Theta^*) \; \geq \; 0\,. \tag{5.5}$$

The optimization problem using the method of Lagrange multipliers with $\lambda \geq 0$ can be formulated as

$$\mathcal{L}(\boldsymbol{\sigma}, \beta) = -\mathcal{D}_{\mathrm{int}}(\boldsymbol{\sigma}, \beta) + \lambda \Phi(\boldsymbol{\sigma}, \beta) \qquad \to \qquad \text{stat}\,. \tag{5.6}$$

The resulting equations are given as

$$\begin{aligned} \partial_{\boldsymbol{\sigma}} \mathcal{L} &= -\dot{\boldsymbol{\varepsilon}}^{\mathrm{p}} + \lambda \, \partial_{\boldsymbol{\sigma}} \Phi = \mathbf{0}\,, \\ \partial_{\beta} \mathcal{L} &= -\dot{\alpha} + \lambda \, \partial_{\beta} \Phi = 0\,, \\ \partial_{\lambda} \mathcal{L} &= \Phi \;=\; 0 \end{aligned} \tag{5.7}$$

with the Kuhn-Tucker conditions

$$\lambda \geq 0\,, \qquad \Phi \leq 0\,, \qquad \lambda\Phi \;=\; 0\,. \tag{5.8}$$

They describe the loading and unloading process as optimization conditions. The associative flow rule and the evolution of the internal variable read

$$\dot{\boldsymbol{\varepsilon}}^p = \lambda \, \partial_{\boldsymbol{\sigma}} \Phi = \lambda \boldsymbol{n}\,, \quad \text{and} \quad \dot{\alpha} = \lambda \, \partial_{\beta} \Phi\,. \tag{5.9}$$

All equations are summarized in Table 5.1. In case linear hardening occurs, i.e., $\hat{\psi}^p(\alpha) = y\alpha + \frac{1}{2}h\alpha^2$, the yield criterion depends on a linear hardening parameter h and yield stress y, see Simo and Hughes [166],

$$\Phi = \| \operatorname{dev} \boldsymbol{\sigma} \| - \sqrt{\frac{2}{3}}\beta \quad \text{with} \quad \beta = y + h\alpha\,. \tag{5.10}$$

Table 5.1: Set of equations for associative elasto-plasticity, cf. SIMO AND HUGHES [166].

stored energy	$\psi = \psi(\boldsymbol{\varepsilon}^{\mathrm{e}}, \alpha) = \hat{\psi}^{\mathrm{e}}(\boldsymbol{\varepsilon}^{\mathrm{e}}) + \hat{\psi}^{\mathrm{p}}(\alpha)$
additive strain decomposition	$\boldsymbol{\varepsilon} = \boldsymbol{\varepsilon}^{\mathrm{e}} + \boldsymbol{\varepsilon}^{\mathrm{p}}$
stresses	$\boldsymbol{\sigma} = \partial_{\boldsymbol{\varepsilon}^{\mathrm{e}}} \psi(\boldsymbol{\varepsilon}^{\mathrm{e}}, \alpha)$
conjugated internal variable	$\beta = -\partial_{\alpha} \psi(\boldsymbol{\varepsilon}^{\mathrm{e}}, \alpha)$
reduced internal dissipation	$\mathcal{D}_{\mathrm{int}} = \boldsymbol{\sigma} : \dot{\boldsymbol{\varepsilon}}^{\mathrm{p}} + \beta\, \dot{\alpha} \, \geq \, 0$
flow rule	$\dot{\boldsymbol{\varepsilon}}^{\mathrm{p}} = \lambda\, \partial_{\boldsymbol{\sigma}} \Phi(\boldsymbol{\sigma}, \beta)$
evolution of internal variable	$\dot{\alpha} = \lambda\, \partial_{\beta} \Phi(\boldsymbol{\sigma}, \beta)$
Kuhn-Tucker conditions	$\lambda \, \geq \, 0 \,, \, \Phi \, \leq \, 0 \,, \, \lambda \Phi \, = \, 0$

5.2 Additive decomposition of strain tensor for a non-isothermal model

Hot bulk forming processes show complex interactions of thermal, mechanical and metallurgical characteristics. In order to distinguish between occurring phenomena, the split of the total strains is extend to five different parts based on the formulation in MAHNKEN ET AL. [110]. In addition to the elastic and plastic strains, the proposed material model takes also into account thermal strains $\boldsymbol{\varepsilon}^{\theta}$, transformation induced plasticity strains $\boldsymbol{\varepsilon}^{\mathrm{trip}}$ and transformation volumetric strains $\boldsymbol{\varepsilon}^{\mathrm{tv}}$, i.e.,

$$\boldsymbol{\varepsilon} = \boldsymbol{\varepsilon}^{\mathrm{e}} + \boldsymbol{\varepsilon}^{\theta} + \boldsymbol{\varepsilon}^{\mathrm{p}} + \boldsymbol{\varepsilon}^{\mathrm{trip}} + \boldsymbol{\varepsilon}^{\mathrm{tv}} \,. \tag{5.11}$$

Furthermore, to incorporate occurring phase transformations, quantities are weighted by the phase fractions present. For these phase fractions, denoted as c^i with e.g. $i \in \{\mathrm{A}, \mathrm{P}, \mathrm{M}\}$ as austenite, pearlite or martensite, respectively, it has to hold that $\sum_i c^i = 1$. In case of more phases or different phases present, the relation can be adapted accordingly.

5.2.1 Elastic and plastic strains

Based on the assumption of the additive strain split in Equation (5.11), the elastic strains $\boldsymbol{\varepsilon}^{\mathrm{e}}$ are computed as $\boldsymbol{\varepsilon}^{\mathrm{e}} = \boldsymbol{\varepsilon} - \boldsymbol{\varepsilon}^{\theta} - \boldsymbol{\varepsilon}^{\mathrm{p}} - \boldsymbol{\varepsilon}^{\mathrm{trip}} - \boldsymbol{\varepsilon}^{\mathrm{tv}}$. The relation to the stresses $\boldsymbol{\sigma} = \mathbb{C} : \boldsymbol{\varepsilon}^{\mathrm{e}}$, which has been presented in Section 5.1, is valid. Furthermore, the derivations regarding the plastic flow rule utilizing a radial return algorithm, which have been presented in Section 5.1, can be applied.

5.2.2 Transformation volumetric strains

As described in Section 4.1, phase transformations can be related to a lattice shearing accompanied with a volumetric expansion of the unit cell, which has to be considered as strain component. Thus, the transformation volumetric strains are defined as

$$\boldsymbol{\varepsilon}^{\mathrm{tv}} = \frac{1}{3} K_{\mathrm{tv}} \boldsymbol{I} \,, \tag{5.12}$$

with material constant K_{tv}, which gives the volumetric expansion of the atomic lattice and depends on the chemical composition of the investigated material. It has to be noted that the transformation volumetric strains only apply for the product phases, here martensite or pearlite, since it describes the relation of the unit cell with respect to the parent phase, i.e., here the austenitic unit cell. Furthermore, it is assumed that the volumetric expansion occurs homogeneously in each direction as simplification. The influence of a non-homogeneous volumetric strain should not be forgotten and is hence subject of later analysis.

5.2.3 Thermal strains

Phase transformations can be induced by fast cooling of the material, for instance by a quenching process. In general, it is distinguished between diffusion controlled and diffusionless cooling. Both have in common that with a change of temperature a contraction or expansion of the materials is evoked, which can be described by a thermal strain, given as volumetric strain

$$\boldsymbol{\varepsilon}^{\theta} = \alpha_{\mathrm{T}}(\theta - \theta_0)\boldsymbol{I}\,. \tag{5.13}$$

Therein, α_{T} is the heat expansion coefficient, θ and θ_0 are actual and initial temperature, respectively. In the following, the notation $\boldsymbol{\varepsilon}^{\mathrm{te}} = \boldsymbol{\varepsilon}^{\theta} + \boldsymbol{\varepsilon}^{\mathrm{e}}$ will be used. At this point it is to be noticed that by using Equation (5.13) an isotropic change as a consequence of changes in temperature is taken into account.

5.2.4 Transformation induced plasticity strains

Plastic strains do not only evolve, when the stress exceeds the yield stress but also in case of a phase transformation. The TRIP effect is caused by microscopic changes of atomic regions, which refers to e.g. lattice shearing as observed during an austenite-to-martensite or austenite-to-pearlite phase transformation for instance. It occurs even in martensitic or pearlitic regions with stress values far below the yield stress. First experimental observations and explanations date back to the 1960's. Two mechanisms, namely the Greenwood-Johnson effect and the Magee effect, respectively, have been proposed in order to explain transformation plasticity. In Greenwood and Johnson [62] it is postulated that the weaker phase, e.g. austenite in comparison to martensite, shows plastic straining due to the volumetric expansion of the martensitic atomic lattice. The Magee effect, proposed in Magee and Paxton [109], correlates external loading and the formation of favorable martensitic variants, which differ by orientation. Based thereon, many investigations have been done and numerical approaches have been proposed. For instance, Olson and Azrin [134] describe the behavior of TRIP steels experimentally. Other applications can be found in Coret et al. [31] or Kim et al. [89], in which the authors investigate phase transformation plasticity also experimentally.

A famous numerical approach is the formulation of Leblond's transformation induced plasticity model for martensite given in Leblond [99]. Here, the deviatoric part of the phase transformation, i.e., shear components, are neglected which means that only the Greenwood-Johnson effect is taken into account. In the work of Mitter [124], a first analytical approach has been presented, which has been further developed in Fischer [46; 49; 50] and Fischer et al. [48], to give a complete micromechanical model which considers the Magee effect as well. The importance of that effect, meaning the effect of the orientation of the martensitic variants, has already been shown by Gautier et al. [56].

More recently, Kang and Im [87] and Mahnken et al. [110] analyze the cooling process, in particular quenching, resulting in martensite formation based on an additive decompositions of the strains in the regime of small strains. Hallberg et al. [68] present a thermo-mechanically coupled model for finite strain plasticity incorporating martensitic transformation. Further approaches are given by Kubler et al. [95] or Connolly et al. [30], who describe a mean field approach as self consistent method and the integration of a model including TRIP into a Marciniak-Kuczyński model, cf. Marciniak and Kuczyński [115].

Following the classical formulation for martensite of Leblond [99], the rate of the TRIP strains is defined as

$$\dot{\boldsymbol{\varepsilon}}^{\mathrm{trip}} = \frac{3}{2} K_{\mathrm{trip}} \operatorname{dev} \boldsymbol{\sigma} f'(c^{\mathrm{M}}) \dot{c}^{\mathrm{M}} \tag{5.14}$$

with K_{trip} as scalar TRIP coefficient, the deviatoric part of the stress tensor $\operatorname{dev} \boldsymbol{\sigma}$, the rate $\dot{c}^{\mathrm{M}}$ of the martensitic volume fraction c^{M} and the derivative f' of a saturation function f. This function, which depends on the martensitic volume fraction c^{M}, has to fulfill $f(0) = 0$ and $f(1) = 1$. In the following, f is chosen as $f(c^{\mathrm{M}}) = (2 - c^{\mathrm{M}})c^{\mathrm{M}}$ with $f'(c^{\mathrm{M}}) = 2(1 - c^{\mathrm{M}})$ as proposed by Denis et al. [32]. This can be formulated analogously for the pearlitic phase.

5.3 Interpolation of material parameters

The used material parameters, such as bulk and shear modulus κ, μ, heat conduction coefficient k, product of density and specific heat capacity, abbreviated as c_ρ, thermal expansion coefficient α_{T}, TRIP-coefficient K_{trip}, volumetric expansion of the atomic lattice K_{tv}, linear hardening parameter h or yield stress y depend either on the temperature or on the temperature and the accumulated plastic strains, as proposed in Uebing et al. [191]. Necessary data for the calibration of appropriate material parameters is provided by the Institute of Forming Technology and Machines (IFUM), Leibniz University Hannover, by thermodynamic simulations using the software JMatPro [83]. Based on the chemical composition of the considered material, the named material parameters, among others, are obtained for each phase individually, see e.g. Behrens et al. [15]. In case of Cr-alloyed steel 100Cr6 (1.3505) which is of interest in later numerical investigations, the chemical composition is given in Table 5.2.

Table 5.2: Chemical composition of the investigated steel alloy 100Cr6 used for material data generation with JMatPro.

	C	**Si**	**Mn**	**P**	**S**	**Cr**	**Mo**	**Fe**
100Cr6	0.99	0.25	0.35	0.025	0.015	1.475	0.1	balance

Two interpolation schemes are utilized in order to compute the actual phase-specific values in every time step. A first data set gives information regarding the thermal and elastic material behavior, i.e., κ in MPa, μ in MPa, k in J/(mm s K), c_ρ in N/(K mm^2) and α_{T} in 1/K. Therefore, data are generated at 25 °C and ranging from 50 °C to 950 °C in equidistant steps of 50 °C, cf. Behrens et al. [15]. In dependency of the temperature θ, the value of each of those material parameters can be identified by piecewise linear interpolation between the sampling points. For temperatures below 50 °C and above 950 °C, the value of the according limiting sampling points is utilized. An illustration is given in Figure 5.2.

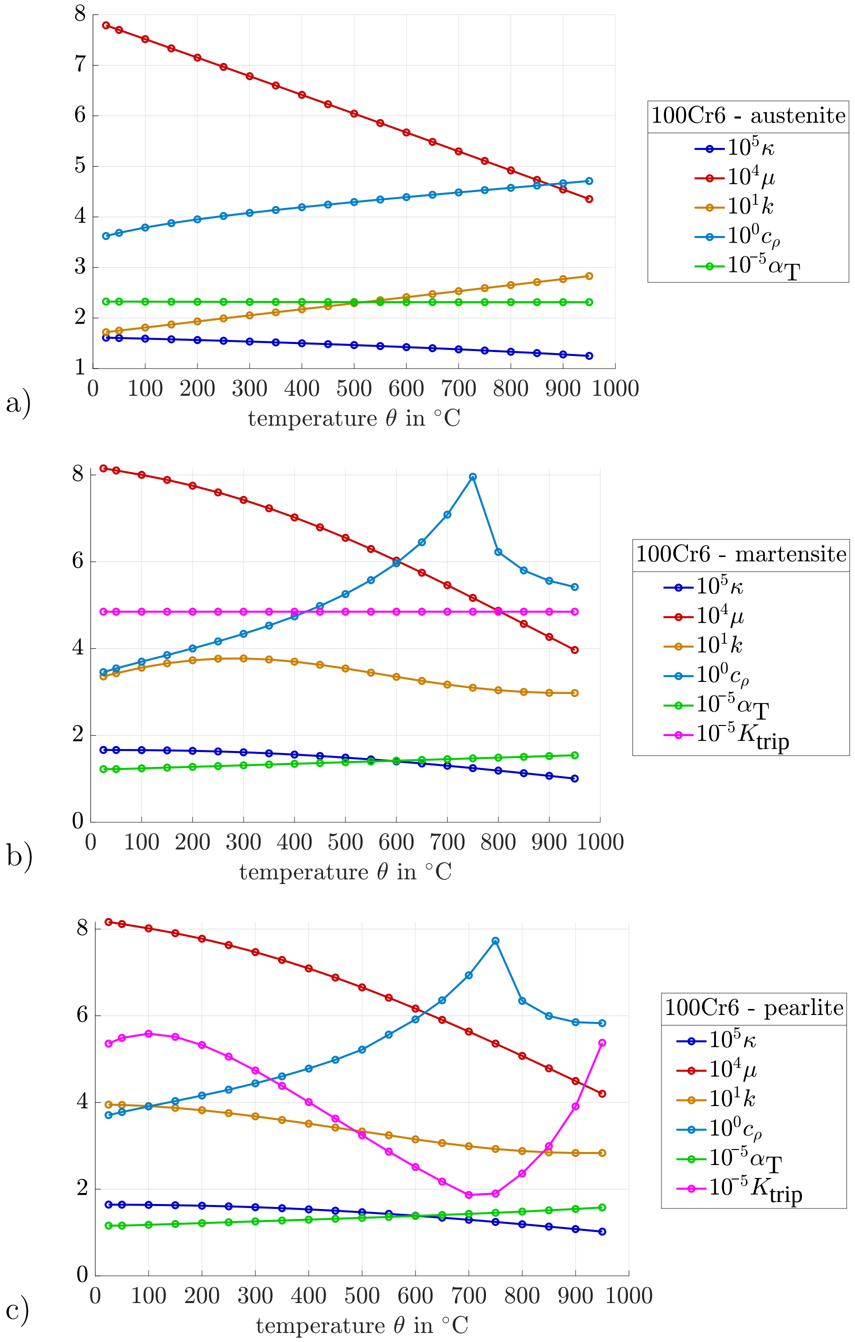

Figure 5.2: Piecewise linear interpolation of thermal and elastic material parameters exemplary for a) austenite, b) martensite and c) pearlite of material 100Cr6. The TRIP coefficients are only necessary for the product phases, which are martensite and pearlite. Data generated with JMatPro [83] by IFUM, LU Hannover.

Furthermore, a second data set is utilized to determine the yield stress y and the linear hardening parameter h in case of plastic material behavior. This second data set gives information of y and h in terms of the accumulated plastic strains (internal variable) in range of $\alpha \in [0, 4]$ and for certain temperatures $\theta \in [25\,°\mathrm{C}, 1050\,°\mathrm{C}]$. The provided data are in tabular format as sketched in Table 5.3. In the following, the subscript n refers to the last time step, while the actual time step would be denoted by subscript $n+1$. Assuming for the values of temperature θ_n and accumulated plastic strains α_n that it holds that $\theta_{i-1} \leq \theta_n < \theta_i$ and $\alpha_{j-1} \leq \alpha_n < \alpha_j$, the following two-step interpolation scheme described below is applied. At this point, it should be mentioned that values of e.g. $\alpha = 4$ do not relate to theory of small strains, i.e., it has to be ensured that these values do not occur.

Table 5.3: Tabular data provided for the interpolation of yield stress y and linear hardening parameter h based on temperature θ and equivalent plastic strain α.

	$\dots$	θ_{i-1}	θ_i	$\dots$
$\vdots$		$\vdots$	$\vdots$	
α_{j-1}	$\dots$	$y_{j-1,i-1}$	$y_{j-1,i}$	$\dots$
α_j	$\dots$	$y_{j,i-1}$	$y_{j,i}$	$\dots$
$\vdots$		$\vdots$	$\vdots$	

A first interpolation step of the scheme sketched in Figure 5.3 is done row-wise with respect to the temperature, which can be formulated as

$$\begin{aligned} y(\alpha_{j-1}, \theta) &= y_{j-1,i-1} + \frac{y_{j-1,i} - y_{j-1,i-1}}{\theta_i - \theta_{i-1}} (\theta - \theta_{i-1}) \,, \\ y(\alpha_j, \theta) &= y_{j,i-1} + \frac{y_{j,i} - y_{j,i-1}}{\theta_i - \theta_{i-1}} (\theta - \theta_{i-1}) \,. \end{aligned} \tag{5.15}$$

Based on these new data points, a second interpolation step, which is done column-wise with respect to the accumulated plastic strains, can be executed to obtain the sought-after value of the yield stress y as

$$y(\alpha_n, \theta_n) = y(\alpha_{j-1}, \theta_n) + \underbrace{\frac{y(\alpha_j, \theta_n) - y(\alpha_{j-1}, \theta_n)}{\alpha_j - \alpha_{j-1}}}_{=h} (\alpha_n - \alpha_{j-1}) \,. \tag{5.16}$$

Moreover, the slope of the second linear interpolation can be considered as linear hardening parameter h as highlighted in Figure 5.3.

Exemplary, the yield curves for different phases of material 100Cr6 are shown in Figure 5.4. As can be seen, the yield stresses of martensite and pearlite are higher than that of austenite. At 25 °C, for example, the yield stress of martensite is even more than twice as high. Pearlite is only slightly stiffer than the parent phase austenite. For high temperatures and high accumulated plastic strains, both austenite and pearlite show softening material behavior. This must be specifically dealt with in the numerical investigation. For this purpose, it is checked whether the current yield stress is lower than the stress of the previous time step and, if this is the case, the current yield stress is corrected. That means that the yield stress is set to the value of the previous time step.

5.4 Constitutive modeling

In addition to Table 5.1, a von Mises yield criterion with linear hardening is taken into account $\Phi = \|\operatorname{dev} \boldsymbol{\sigma}\| - \sqrt{\frac{2}{3}}\beta$ with stress-like conjugated variable β depending on yield

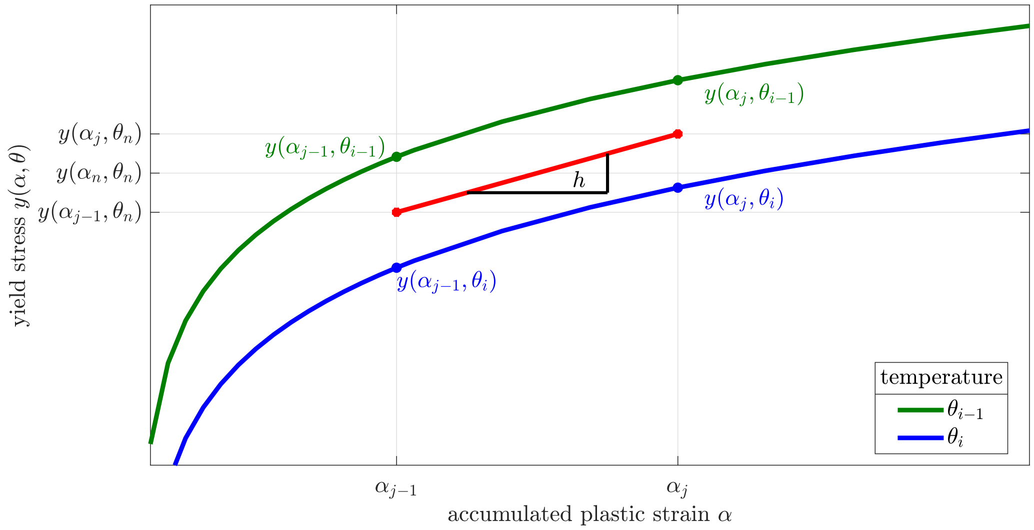

Figure 5.3: Two-step interpolation scheme for yield stress y and linear hardening parameter h based on the temperature θ and the accumulated plastic strains α.

stress y, linear hardening parameter h and strain-like internal variable α. Additionally, the free energy function in case of a temperature dependent process is given as

$$\begin{aligned} \psi(\boldsymbol{\varepsilon}^{\text{te}}, \theta, \alpha) = & \frac{1}{2} \kappa \, (\operatorname{tr} \boldsymbol{\varepsilon}^{\text{te}})^2 \; + \; \mu \| \operatorname{dev} \boldsymbol{\varepsilon}^{\text{te}} \|^2 \; - \; c_\rho (\theta \ln \frac{\theta}{\theta_0} - \theta + \theta_0) \\ & - \; 3 \alpha_{\text{T}} \kappa (\theta - \theta_0) \; \operatorname{tr} \boldsymbol{\varepsilon}^{\text{te}} \; + \; f(\alpha) \end{aligned} \tag{5.17}$$

Furthermore, the function $f(\alpha)$ is used to describe the hardening of the material. This replaces the potential $\hat{\psi}^P(\alpha) = y\alpha + \frac{1}{2} h \, \alpha^2$ for the classical description of linear hardening by taking into account the piecewise linear interpolation of the material data described in Section 5.3, and exemplary indicated in Figure 5.2. In order to ensure numerical stability, the material subroutine is evaluated based on the temperature of the last time step. Thereby, all material parameters are stepwise constant.

If the temperature falls below the martensitic start temperature and an austenite-to-martensite phase transformation occurs, the atomic lattice shears from face-centered cubic (fcc) to body-centered tetragonal (bct) unit cells. This can be interpreted as a consequence of inner stresses in the lattice. Thus, the bct unit cells represent a kind of relaxed state and hence, the strain-like variable α, also known as accumulated plastic strains, is reset to zero. This is realized individually and uniquely for each integration point during the formation of martensite. In case of an austenite-to-pearlite phase transformation this relaxation is analogously considered.

As the simulative analysis of the cooling step of hot bulk forming processes is in focus of this work, only a one-way coupling between temperature and mechanical displacement is taken into account. That means, that the temperature influences the displacement, but the influence of the displacement on the temperature is neglected, see e.g. UEBING ET AL. [192].

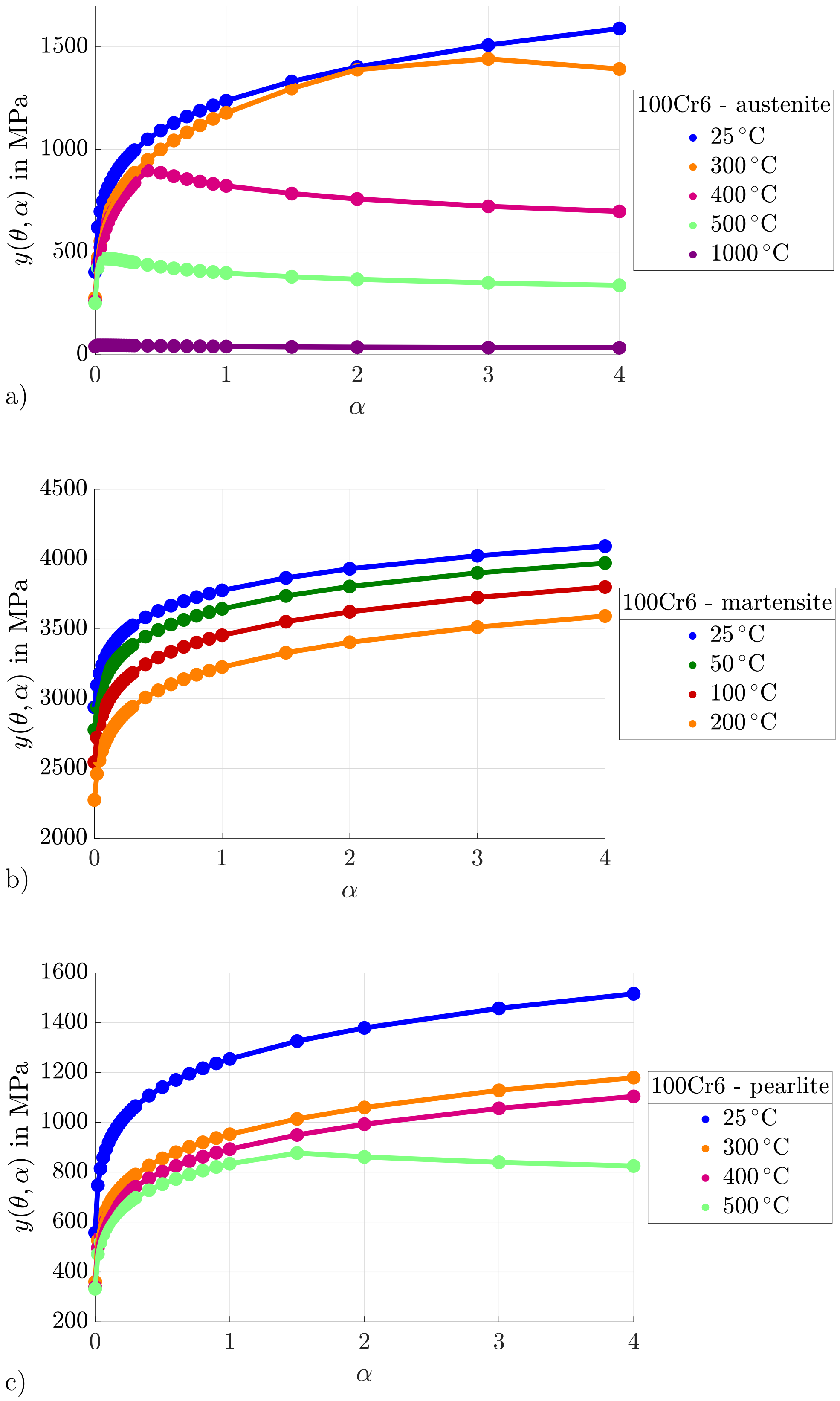

Figure 5.4: Phase-specific data for isothermal yield curves, which is interpolated in a two-step scheme for a) austenite, b) martensite and c) pearlite of material 100Cr6. Data generated with JMatPro [83] by IFUM, LU Hannover.

5.5 Different approaches to determine effective material behavior

Many materials show inhomogeneities and heterogeneities when resolving the microscale. In the considered Cr-alloyed steel 100Cr6, different phases can be present dependent on the manufacturing of a component or its treatment. Here, the focus is each time on two phases, austenite (A) and martensite (M) as described in Section 4.1 for hot bulk forming processes with diffusionless cooling and on austenite (A) and pearlite (P) in case of diffusion controlled cooling. In the following, two “phenomenologicalmmaterial models and one “semi-analytical multi-phasemmaterial model are derived.

5.5.1 Phenomenological material model with effective material parameters

In order to solve homogenized partial differential equations as part of a “phenomenological“description, effective material parameters are required. Voigt [193] and Reuss [145] proposed two possibilities, which are based on the volume fractions of the occurring phases. In this work, the focus is on the three phases austenite, martensite and pearlite, of which two phases are present during one computation, either austenite and martensite or austenite and pearlite. Thus, the respective volume fraction is denoted by c^i of phase $i \in \{A, M\}$ or $i \in \{A, P\}$. It always has to be fulfilled that

$$\sum_i c^i = 1\,. \tag{5.18}$$

Taking into account a Voigt average of the material parameters, i.e., an arithmetic mean, one obtains for the effective material parameters $(\bullet)^{\text{eff}}_{\text{ari}}$

$$(\bullet)^{\text{eff}}_{\text{ari}} = \sum_i c^i (\bullet)^i\,, \tag{5.19}$$

with $(\bullet)^i$ as one material parameter of phase i and $(\bullet) \in \{\kappa, \mu, k, c_\rho, \alpha_{\text{T}}\}$. Analogously, considering a Reuss average, which is an harmonic mean, leads to

$$(\bullet)^{\text{eff}}_{\text{har}} = \big(\sum_i c^i ((\bullet)^i)^{-1}\big)^{-1} = \big(\sum_i \frac{c^i}{(\bullet)^i}\big)^{-1} \tag{5.20}$$

for $(\bullet) \in \{\kappa, \mu, k, c_\rho, \alpha_{\text{T}}\}$. Figure 5.5 illustrates these averages exemplary for the product of the density and the specific heat capacity, abbreviated as c_ρ in case of an austenite-to-martensite phase transformation. For high temperatures the microstructure is homogeneous and only austenite contributes to the effective material behavior. For lower temperatures, the martensitic volume increases, so that both phases have an impact on the effective quantities ${c_\rho}^{\text{eff}}_{\text{ari}}$ and ${c_\rho}^{\text{eff}}_{\text{har}}$.

Since only two phases occur in each of the different hot bulk forming processes, it is defined for the remaining two material parameters K_{tv} and K_{trip}

$$
\begin{aligned}
{K_{\text{tv}}}^{\text{eff}} &= c^{\text{M}} {K_{\text{tv}}}^{\text{M}} \quad \text{or} \quad {K_{\text{tv}}}^{\text{eff}} = c^{\text{P}} {K_{\text{tv}}}^{\text{P}} && (5.21)\\
\text{and} \quad {K_{\text{trip}}}^{\text{eff}} &= c^{\text{M}} {K_{\text{trip}}}^{\text{M}} \quad \text{or} \quad {K_{\text{trip}}}^{\text{eff}} = c^{\text{P}} {K_{\text{trip}}}^{\text{P}}\,. && (5.22)
\end{aligned}
$$

This is a consequence of ${K_{\text{tv}}}^{\text{A}} = {K_{\text{trip}}}^{\text{A}} = 0$. With this sets of effective material parameters, the PDEs can be solved with respect to the overall stresses and tangent moduli of the heterogeneous material. An exemplary algorithmic box is provided in Table 5.4 for fast cooling with a diffusionless austenite-to-martensite phase transformation.

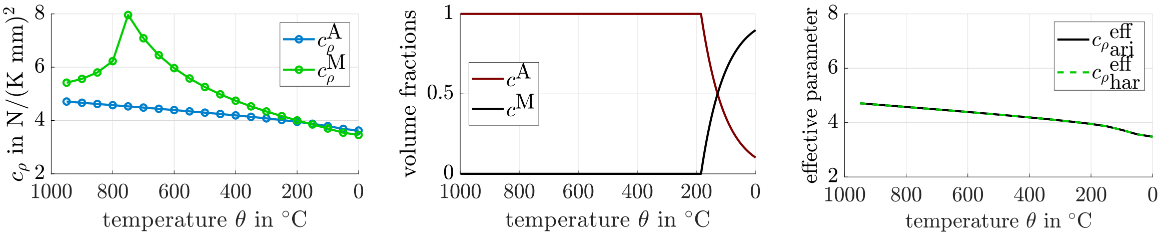

Figure 5.5: Exemplary computation of the effective material parameters $c_\rho{}^{\mathrm{eff}}_{\mathrm{ari}}$ and $c_\rho{}^{\mathrm{eff}}_{\mathrm{har}}$ according to the volume fractions present; for the product of the specific heat capacity and the density, abbreviated as c_ρ.

5.5.2 Semi-analytical multi-phase single-scale approach

The previously described formulation based on effective material parameters cannot account for phase-specific effects. Large differences in material parameters such as yield stress are no longer resolved in a phase-specific manner. It is also crucial that the accumulated plastic strains are only considered in a smeared fashion. An atomic lattice relaxes by shearing from face-centered cubic austenitic unit cells to body-centered tetragonal unit cells of martensite, i.e., the accumulated plastic strains previously stored in the austenitic phase are reset. This cannot be taken into account in effective material modeling. This motivates a formulation referred to here as SAMP material modeling. Therein, stresses and material tangent are computed for each phase individually and afterwards averaged arithmetically by

$$\mathbb{C}^{\mathrm{eff}} = c^{\mathrm{A}}\mathbb{C}^{\mathrm{A}} + c^{\mathrm{M}}\mathbb{C}^{\mathrm{M}} \quad \text{and} \quad \boldsymbol{\sigma}^{\mathrm{eff}} = c^{\mathrm{A}}\boldsymbol{\sigma}^{\mathrm{A}} + c^{\mathrm{M}}\boldsymbol{\sigma}^{\mathrm{M}} \,. \tag{5.23}$$

This can be formulated analogously in case of a diffusion controlled austenite-to-pearlite phase transformation during slower cooling.

Using the definitions above, the following algorithm can be implemented, see Table 5.5. At first, the accumulated plastic strains induced by the forming step are initialized for the austenitic phase. Secondly, the martensitic volume fraction is computed with the Koistinen-Marburger differential equation, cf. Equation (4.4), or the pearlitic volume fraction is determined with the JMAK equation, see Equation (4.2). Based on the temperature, material parameters for all present phases are computed. Therewith, the next step is a classical radial return algorithm for each individual phase. Thus, the stress tensors $\boldsymbol{\sigma}^i$ as well as the tangent moduli $\mathbb{C}^i$ are determined for each phase. To derive the effective quantities, a simple arithmetic mean value is computed based on the actual volume fraction of each phase, see Equation (5.23).

Table 5.4: Material modeling at time step t_{n+1} using "phenomenologicallycomputed effective material parameters. Exemplary algorithm for a diffusionless phase transformation from austenite to martensite.

```
$t = 0\,\mathrm{s}$ initialize history of accumulated plastic strains resulting from hot bulk
        forming if necessary, see Section 6.2.2
(I)    Get temperature $\theta_n$ and total strains $\boldsymbol{\varepsilon}_{n+1}$
(II)   Compute martensitic volume fraction
       $c^{\mathrm{M}}_{n+1}(\theta_n) = \begin{cases} 1 - \exp\left(-\frac{\theta_{\mathrm{Ms}}-\theta_n}{\theta_{\mathrm{M0}}}\right) & \text{for } \theta_n \le \theta_{\mathrm{Ms}} \\ 0 & \text{else} \end{cases}$
       and saturation function $f_{n+1}(c^{\mathrm{M}}_{n+1}) = (2 - c^{\mathrm{M}}_{n+1})c^{\mathrm{M}}_{n+1}$ with $f'_{n+1}(c^{\mathrm{M}}_{n+1}) = 2(1 - c^{\mathrm{M}}_{n+1})$
(III)  Get history values of accumulated plastic strains $\alpha_n$, plastic strains $\boldsymbol{\varepsilon}^{\mathrm{p}}_n$,
       TRIP strains $\boldsymbol{\varepsilon}^{\mathrm{trip}}_n$ and martensitic volume fraction $c^{\mathrm{M}}_n$
(IV)   Interpolate material parameters $\kappa, \mu, k, c_\rho, \alpha_{\mathrm{T}}, K_{\mathrm{trip}}, K_{\mathrm{tv}}$ for $\theta_n$, see Section 5.3
(V)    Compute thermal strains $\boldsymbol{\varepsilon}^{\mathrm{tv}}_{n+1} = \frac{1}{3}K_{\mathrm{tv}}\boldsymbol{I}$
       and transformation volumetric strains $\boldsymbol{\varepsilon}^{\theta}_{n+1} = \alpha_{\mathrm{T}}(\theta_n - \theta_0)\boldsymbol{I}$
(VI)   Compute elastic trial strains $\boldsymbol{\varepsilon}^{\mathrm{e,trial}}_{n+1} = \boldsymbol{\varepsilon}_{n+1} - \boldsymbol{\varepsilon}^{\mathrm{p}}_n - \boldsymbol{\varepsilon}^{\mathrm{trip}}_n - \boldsymbol{\varepsilon}^{\mathrm{tv}}_{n+1} - \boldsymbol{\varepsilon}^{\theta}_{n+1}$
       and deviatoric trial stresses $\operatorname{dev}\boldsymbol{\sigma}^{\mathrm{trial}}_{n+1} = 2\mu \operatorname{dev}\boldsymbol{\varepsilon}^{\mathrm{e,trial}}_{n+1}$
       and deviatoric trial tangent $\mathbb{C}^{\mathrm{trial}}_{n+1} = \frac{2\mu}{\gamma}\mathbb{P}$ with $\mathbb{P} = \mathbb{I} - \frac{1}{3}\boldsymbol{I} \otimes \boldsymbol{I}$
           with $\gamma = 1 + 3\mu K_{\mathrm{trip}} f'(c^{\mathrm{M}}_{n+1})\Delta c^{\mathrm{M}}_{n+1}$ and $\Delta c^{\mathrm{M}}_{n+1} = c^{\mathrm{M}}_{n+1} - c^{\mathrm{M}}_n$
(VII)  Compute yield stress $y_{n+1}(\theta_n, \alpha_n)$ by two-step interpolation scheme, see Section 5.3
(VIII) Compute yield criterion $\Phi^{\mathrm{trial}}_{n+1} = \|\operatorname{dev}\boldsymbol{\sigma}^{\mathrm{trial}}_{n+1}\| - \sqrt{\frac{2}{3}}y_{n+1}$
       if $\Phi^{\mathrm{trial}}_{n+1} \le 0$ then
           $\alpha_{n+1} = \alpha_n$, $\boldsymbol{\varepsilon}^{\mathrm{p}}_{n+1} = \boldsymbol{\varepsilon}^{\mathrm{p}}_n$, $\boldsymbol{\varepsilon}^{\mathrm{trip}}_{n+1} = \boldsymbol{\varepsilon}^{\mathrm{trip}}_n$
           $\operatorname{dev}\boldsymbol{\sigma}_{n+1} = \operatorname{dev}\boldsymbol{\sigma}^{\mathrm{trial}}_{n+1}$, $\mathbb{C}_{n+1} = \mathbb{C}^{\mathrm{trial}}_{n+1}$
       else radial return algorithm
           (i)   Solve residuum function
                 $r(\Delta\lambda) = \frac{\|\operatorname{dev}\boldsymbol{\sigma}^{\mathrm{trial}}_{n+1}\| - 2\mu\Delta\lambda}{\gamma} - \sqrt{\frac{2}{3}}y_{n+1} = 0$
           (ii)  Update $\alpha_{n+1} = \alpha_n + \sqrt{\frac{2}{3}}\Delta\lambda_{n+1}$  $\boldsymbol{\varepsilon}^{\mathrm{p}}_{n+1} = \boldsymbol{\varepsilon}^{\mathrm{p}}_n + \Delta\lambda_{n+1}\boldsymbol{n}_{n+1}$
           (iii) Update deviatoric stresses $\operatorname{dev}\boldsymbol{\sigma}_{n+1} = \frac{1}{\gamma}\left(\operatorname{dev}\boldsymbol{\sigma}^{\mathrm{trial}}_{n+1} - 2\mu\Delta\lambda_{n+1}\boldsymbol{n}_{n+1}\right)$
           (iv)  Compute tangent moduli with Jacobian $J(\Delta\lambda) = \partial r(\Delta\lambda)/\partial\Delta\lambda$
                 $\mathbb{C}_{n+1} = \frac{2\mu}{\gamma}\mathbb{P} - \Delta\lambda\frac{(2\mu)^2}{\gamma}\frac{1}{\|\operatorname{dev}\boldsymbol{\sigma}^{\mathrm{trial}}_{n+1}\|}(\mathbb{P} - \boldsymbol{n}_{n+1} \otimes \boldsymbol{n}_{n+1}) + \left(\frac{2\mu}{\gamma}\right)^2 \frac{1}{J}\boldsymbol{n}_{n+1} \otimes \boldsymbol{n}_{n+1}$
(IX)   Update TRIP strains $\boldsymbol{\varepsilon}^{\mathrm{trip}}_{n+1} = \boldsymbol{\varepsilon}^{\mathrm{trip}}_n + \frac{3}{2}K_{\mathrm{trip}} \operatorname{dev}\boldsymbol{\sigma}_{n+1} f'_{n+1}(c^{\mathrm{M}}_{n+1})\Delta c^{\mathrm{M}}_{n+1}$
       and elastic strains $\boldsymbol{\varepsilon}^{\mathrm{e}}_{n+1} = \boldsymbol{\varepsilon}_{n+1} - \boldsymbol{\varepsilon}^{\mathrm{p}}_{n+1} - \boldsymbol{\varepsilon}^{\mathrm{trip}}_{n+1} - \boldsymbol{\varepsilon}^{\mathrm{tv}}_{n+1} - \boldsymbol{\varepsilon}^{\theta}_{n+1}$
(X)    Add volumetric stresses $\boldsymbol{\sigma}^{\mathrm{eff}}_{n+1} = \operatorname{dev}\boldsymbol{\sigma}_{n+1} + \kappa \operatorname{tr}\boldsymbol{\varepsilon}^{\mathrm{e}}_{n+1}\boldsymbol{I}$
       and volumetric tangent $\mathbb{C}^{\mathrm{eff}}_{n+1} = \mathbb{C}_{n+1} + \kappa\boldsymbol{I} \otimes \boldsymbol{I}$
```

Table 5.5: Material modeling at time step t_{n+1} computing phase specific stresses and material tangent, which are averaged for effective stresses and tangent moduli utilizing the “semi-analytical multi-phaseäpproach. Exemplary algorithm for a diffusionless phase transformation from austenite to martensite.

```
$t = 0\,\mathrm{s}$ initialize history of accumulated plastic strains resulting from hot bulk
          forming if necessary, see Section 6.2.2
--------------------------------------------------------------------------------
(I)    Get temperature $\theta_n$ and total strains $\boldsymbol{\varepsilon}_{n+1}$
(II)   Compute martensitic volume fraction
       $c^{\mathrm{M}}_{n+1}(\theta_n) = \begin{cases} 1 - \exp\left(-\frac{\theta_{\mathrm{Ms}} - \theta_n}{\theta_{\mathrm{M0}}}\right) & \text{for } \theta_n \leq \theta_{\mathrm{Ms}} \\ 0 & \text{else} \end{cases}$
       and saturation function $f_{n+1}(c^{\mathrm{M}}_{n+1}) = (2 - c^{\mathrm{M}}_{n+1})c^{\mathrm{M}}_{n+1}$ with $f'_{n+1}(c^{\mathrm{M}}_{n+1}) = 2(1 - c^{\mathrm{M}}_{n+1})$
For all phases, here austenite (A) and martensite (M), do:
    (III)  Get history values of accumulated plastic strains $\alpha_n$, plastic strains $\boldsymbol{\varepsilon}^{\mathrm{p}}_n$,
           TRIP strains $\boldsymbol{\varepsilon}^{\mathrm{trip}}_n$ and martensitic volume fraction $c^{\mathrm{M}}_n$
    (IV)   Interpolate material parameters $\kappa, \mu, k, c_\rho, \alpha_{\mathrm{T}}, K_{\mathrm{trip}}, K_{\mathrm{tv}}$ for $\theta_n$, see Section 5.3
    (V)    Compute thermal strains $\boldsymbol{\varepsilon}^{\mathrm{tv}}_{n+1} = \frac{1}{3}K_{\mathrm{tv}}\boldsymbol{I}$
           and transformation volumetric strains $\boldsymbol{\varepsilon}^{\theta}_{n+1} = \alpha_{\mathrm{T}}(\theta_n - \theta_0)\boldsymbol{I}$
    (VI)   Compute elastic trial strains $\boldsymbol{\varepsilon}^{\mathrm{e,trial}}_{n+1} = \boldsymbol{\varepsilon}_{n+1} - \boldsymbol{\varepsilon}^{\mathrm{p}}_n - \boldsymbol{\varepsilon}^{\mathrm{trip}}_n - \boldsymbol{\varepsilon}^{\mathrm{tv}}_{n+1} - \boldsymbol{\varepsilon}^{\theta}_{n+1}$
           and deviatoric trial stresses $\operatorname{dev}\boldsymbol{\sigma}^{\mathrm{trial}}_{n+1} = 2\mu \operatorname{dev}\boldsymbol{\varepsilon}^{\mathrm{e,trial}}_{n+1}$
           and deviatoric trial tangent $\mathbb{C}^{\mathrm{trial}}_{n+1} = \frac{2\mu}{\gamma}\mathbb{P}$ with $\mathbb{P} = \mathbb{I} - \frac{1}{3}\boldsymbol{I} \otimes \boldsymbol{I}$
               with $\gamma = 1 + 3\mu\, K_{\mathrm{trip}} f'(c^{\mathrm{M}}_{n+1})\Delta c^{\mathrm{M}}_{n+1}$ and $\Delta c^{\mathrm{M}}_{n+1} = c^{\mathrm{M}}_{n+1} - c^{\mathrm{M}}_n$
    (VII)  Compute yield stress $y_{n+1}(\theta_n, \alpha_n)$ by two-step interpolation scheme, see Section 5.3
    (VIII) Compute yield criterion $\Phi^{\mathrm{trial}}_{n+1} = \|\operatorname{dev}\boldsymbol{\sigma}^{\mathrm{trial}}_{n+1}\| - \sqrt{\frac{2}{3}}y_{n+1}$
           if $\Phi^{\mathrm{trial}}_{n+1} \leq 0$ then
               $\alpha_{n+1} = \alpha_n$, $\boldsymbol{\varepsilon}^{\mathrm{p}}_{n+1} = \boldsymbol{\varepsilon}^{\mathrm{p}}_n$, $\boldsymbol{\varepsilon}^{\mathrm{trip}}_{n+1} = \boldsymbol{\varepsilon}^{\mathrm{trip}}_n$
               $\operatorname{dev}\boldsymbol{\sigma}_{n+1} = \operatorname{dev}\boldsymbol{\sigma}^{\mathrm{trial}}_{n+1}$, $\mathbb{C}_{n+1} = \mathbb{C}^{\mathrm{trial}}_{n+1}$
           else radial return algorithm
               (i)   Solve residuum function
                     $r(\Delta\lambda) = \frac{\|\operatorname{dev}\boldsymbol{\sigma}^{\mathrm{trial}}_{n+1}\| - 2\mu\Delta\lambda}{\gamma} - \sqrt{\frac{2}{3}}y_{n+1} = 0$
               (ii)  Update $\alpha_{n+1} = \alpha_n + \sqrt{\frac{2}{3}}\Delta\lambda_{n+1}$,  $\boldsymbol{\varepsilon}^{\mathrm{p}}_{n+1} = \boldsymbol{\varepsilon}^{\mathrm{p}}_n + \Delta\lambda_{n+1}\boldsymbol{n}_{n+1}$
               (iii) Update deviatoric stresses $\operatorname{dev}\boldsymbol{\sigma}_{n+1} = \frac{1}{\gamma}\left(\operatorname{dev}\boldsymbol{\sigma}^{\mathrm{trial}}_{n+1} - 2\mu\Delta\lambda_{n+1}\boldsymbol{n}_{n+1}\right)$
               (iv)  Compute tangent moduli with Jacobian $J(\Delta\lambda) = \partial r(\Delta\lambda)/\partial\Delta\lambda$
                     $\mathbb{C}_{n+1} = \frac{2\mu}{\gamma}\mathbb{P} - \Delta\lambda\frac{(2\mu)^2}{\gamma}\frac{1}{\|\operatorname{dev}\boldsymbol{\sigma}^{\mathrm{trial}}_{n+1}\|}(\mathbb{P} - \boldsymbol{n}_{n+1} \otimes \boldsymbol{n}_{n+1}) + \left(\frac{2\mu}{\gamma}\right)^2 \frac{1}{J}\boldsymbol{n}_{n+1} \otimes \boldsymbol{n}_{n+1}$
    (IX)   Update TRIP strains $\boldsymbol{\varepsilon}^{\mathrm{trip}}_{n+1} = \boldsymbol{\varepsilon}^{\mathrm{trip}}_n + \frac{3}{2}K_{\mathrm{trip}} \operatorname{dev}\boldsymbol{\sigma}_{n+1} f'_{n+1}(c^{\mathrm{M}}_{n+1})\Delta c^{\mathrm{M}}_{n+1}$
           and elastic strains $\boldsymbol{\varepsilon}^{\mathrm{e}}_{n+1} = \boldsymbol{\varepsilon}_{n+1} - \boldsymbol{\varepsilon}^{\mathrm{p}}_{n+1} - \boldsymbol{\varepsilon}^{\mathrm{trip}}_{n+1} - \boldsymbol{\varepsilon}^{\mathrm{tv}}_{n+1} - \boldsymbol{\varepsilon}^{\theta}_{n+1}$
    (X)    Add volumetric stresses $\boldsymbol{\sigma}_{n+1} = \operatorname{dev}\boldsymbol{\sigma}_{n+1} + \kappa \operatorname{tr}\boldsymbol{\varepsilon}^{\mathrm{e}}_{n+1}\boldsymbol{I}$
           and volumetric tangent $\mathbb{C}_{n+1} = \mathbb{C}_{n+1} + \kappa\boldsymbol{I} \otimes \boldsymbol{I}$
(XI)   Average stresses, tangent moduli and material parameters
       $(\bullet)_{n+1} = (1 - c^{\mathrm{M}}_{n+1})\,(\bullet)^{\mathrm{A}}_{n+1} + c^{\mathrm{M}}_{n+1}\,(\bullet)^{\mathrm{M}}_{n+1}$  for  $(\bullet) \in \{\boldsymbol{\sigma}, \mathbb{C}, \kappa, k, c_\rho, \alpha_{\mathrm{T}}\}$
```

6 Two-dimensional single-scale analysis of thermo-mechanically coupled problems

Numerical analysis of hot bulk forming processes offers a cost-, time-, and resources efficient possibility compared to experimental production which is closely associated with "trial and error". In general, hot bulk forming is characterized by complex interaction of thermal, mechanical and metallurgical fields. Their exploitation using numerical tools enables the adaption of the manufacturing process to achieve predefined component's properties, which are beneficial with respect to e.g. lifetime, wear resistance or strength. Auspicious manufacturing processes with desired component properties can be finally produced and evaluated after the numerical design. Thereby, the close connection of numerical investigations and experiments allows for an efficient process design and serves for validation of the utilized material models.

Thus, it is inevitable to set up material models, wich can be used to reflect the experimental behavior on macroscopic level as a first step. Therefore, the first study compares the different macroscopic material models, which have been proposed in Section 5 as "phenomenological (PH)änd "semi-analytical multi-phase (SAMP)mmodel. A generalized geometry with different boundary conditions is defined for that purpose. Afterwards, a more complex geometry is investigated which accounts as example for industrial application. For the latter, a mesh density and time step size study is carried out as first step to ensure the discretization's quality. Based thereon, different cooling routes are considered and compared with respect to the resulting (residual) stress distributions. Afterwards, phase-specific contributions and the influence of the transformation induced plasticity (TRIP) is emphasized.

6.1 How to compute effective material behavior

As proposed in Section 5.5, different approaches to determine the effective material behavior are considered. The first two belong to the group of PH material models, i.e., the material parameters are averaged by an arithmetic or a harmonic mean. The third one refers to a description of a SAMP material, for which phase-specific stresses and tangent moduli are determined and afterwards averaged based on the actual volume fractions of the occurring phases. For the comparison of these three approaches for single-scale material modeling, a two-dimensional rectangular geometry with dimensions $1\,\mathrm{mm} \times 10\,\mathrm{mm}$ made from the Cr-alloyed steel 100Cr6 (1.3505) is taken into account and discretized with 6×30 nine-noded quadrilateral elements. Different boundary conditions are combined, in order to compare the thermal, mechanical and, last but not least, thermo-mechanical material behavior, see Figure 6.1a-d. The initial temperature of the specimen is set to $\theta_0 = 500\,^\circ\mathrm{C}$, so that the material is fully austenitic. In the case of rapid cooling, which is applied, an diffusionless austenite-to-martensite phase transformation takes place. Martensite starts to evolve at temperatures below the martensitic start temperature, which is given as $\theta_{\mathrm{Ms}} = 185\,^\circ\mathrm{C}$ for the considered material. In the final state at room temperature $\theta_{\mathrm{RT}} \approx 20\,^\circ\mathrm{C}$, $87\,\%$ martensite and $13\,\%$ retained austenite are present. The actual temperature θ, the decrease of the austenitic volume fraction c^{A} and different stress components σ_{11}, σ_{22} and σ_{12} are compared for four different boundary value problems, cases a to d, in the marked point near the upper edge, see the cross x in Figure 6.1.

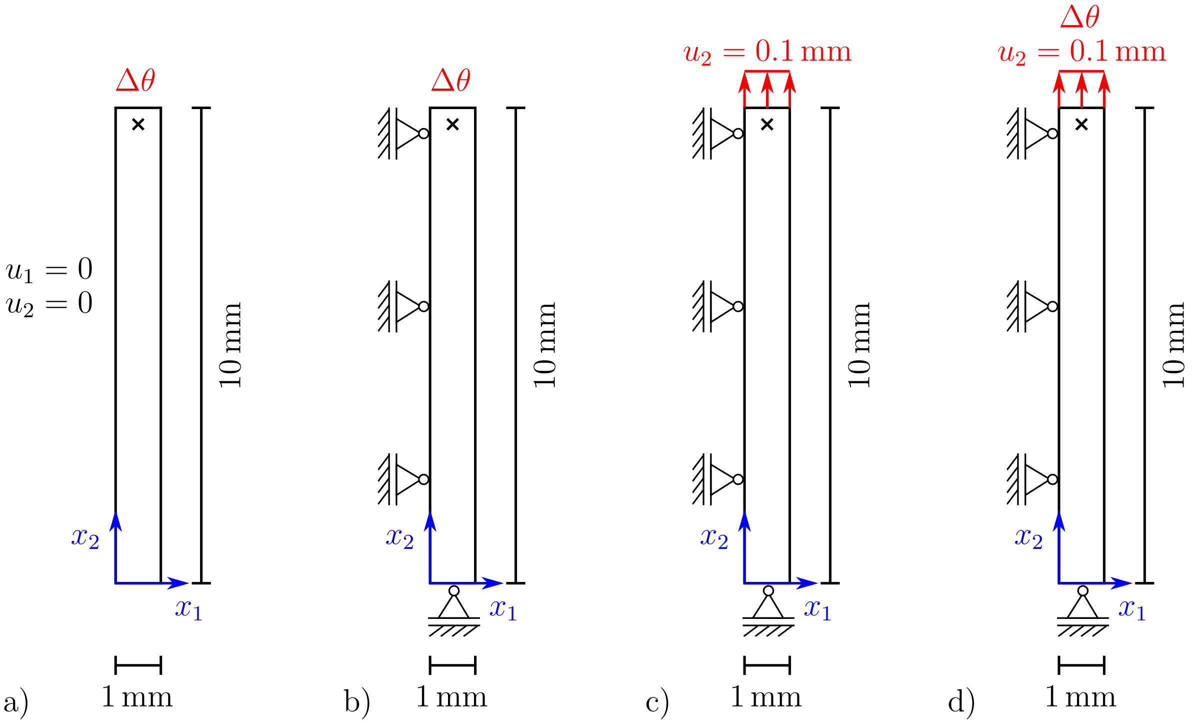

Figure 6.1: Two-dimensional rectangular geometry considered in cases a to d: a) solving only the balance of energy, b) applying a cooling on the top edge, c) uniaxial tension and d) combination of tension and cooling. The marker x indicates the point of investigation.

6.1.1 Case a - balance of energy

In case a, see Figure 6.1a, all nodal displacement degrees of freedom are fixed, so that only the balance of energy is solved, i.e., $u_1 = 0$ and $u_2 = 0$ holds for all nodes. On the top edge, a cooling Dirichlet boundary condition is applied, i.e., the nodes are cooled from $\theta_0 = 500\,°\mathrm{C}$ by $\Delta\theta = -480\,°\mathrm{C}$ to room temperature in ten seconds. Subsequently, the temperature is held constant at the top edge until the specimen is completely cooled, i.e., until the temperature gradient vanishes. For all other boundary nodes a zero Neumann bound is defined with respect to the temperature. As shown for the examined integration point x in Figure 6.2, the different single-scale homogenization approaches are in good accordance for the linear cooling, which leads to a nearly linear stress increase in components σ_{11} and σ_{22}, respectively. Due to the phase transformation and the volumetric expansion of the atomic lattice, these tensile stresses are reduced and as a final value $\sigma_{11} \approx \sigma_{22} \approx 1800\,\mathrm{MPa}$ is obtained. As expected, no shear stresses σ_{12} are present. The temperature curves show no deviation between the three approaches at all. Moreover, a good accordance regarding the degradation of the austenitic volume fraction is observed. Taking a look at the stress evolution, no differences can be seen until the onset of the phase transformation around seven seconds of cooling, since a homogeneous, austenitic material is present up to this point. After that, only small deviations for the approach with harmonic effective material parameters are observed, which results in lower tensile stresses. Furthermore, the results of the SAMP approach and the arithmetic PH approach are close to each other due to the same averaging method, that is applied. It is well known that computing an arithmetic mean results in the most stiffest material response, often referred to as an upper bound. A respective lower bound could be given by a material

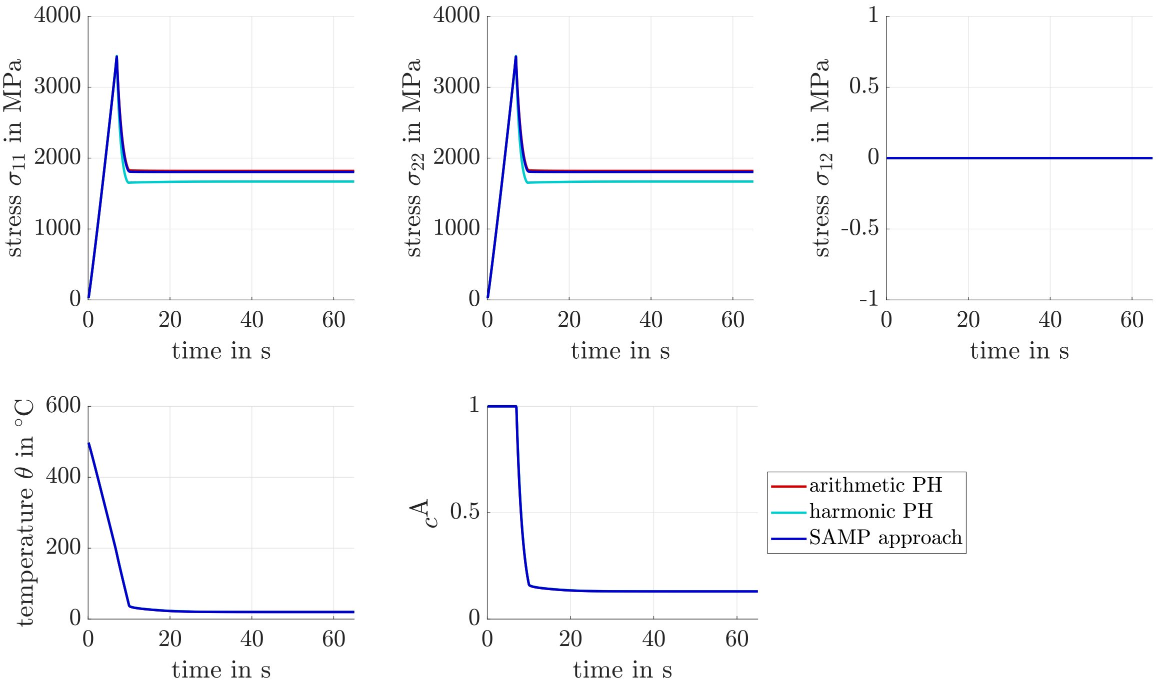

Figure 6.2: Case a - balance of energy. Stresses σ_{11}, σ_{22} and σ_{12} as well as temperature θ and austenitic phase c^{A} evolution on integration point level at point x of investigation, cf. Figure 6.1a.

model with full harmonic effective parameters. At this point, it should be emphasized again that harmonic averaging is not chosen for all material parameters in this work, because K_{tv} and K_{trip} are weighted by the martensitic volume fraction instead.

6.1.2 Case b - cooling boundary condition

As boundary conditions for case b, the displacement of the bottom nodes is fixed in x_2-direction, i.e., $u_2 = 0$, and the displacement of the left side is fixed in x_1-direction, i.e., $u_1 = 0$, see Figure 6.1b. On the top edge, the same linear cooling $\Delta\theta$ of $-480\,°\mathrm{C}$ is applied in ten seconds, while on the other bounds no heat flux occurs. As before, the temperature on the top edge is held constant until the temperature gradient vanishes in the specimen. Figure 6.3 shows that all approaches computing the effective material response behave similarly. The evolutions of the temperature and the austenitic phase fraction are the same as in case a. With respect to the stress evolution, the stress components σ_{11} and σ_{22} show the same qualitative behavior. Before the onset of the phase transformation, nearly no stresses evolve since the geometry can contract freely. The onset of the phase transformation around seven seconds of cooling evokes compressive stresses in the investigated point up to $\sigma_{11} = -150\,\mathrm{MPa}$ and $\sigma_{22} = -100\,\mathrm{MPa}$. The highest values are computed with the set of harmonic effective parameters, which exceed the previous values by roughly 33%. When the phase transformation starts also in the neighboring material points, a tensile stress peak appears which shows qualitatively the same differences between the three approaches, arithmetic PH, harmonic PH or SAMP approach. These deviations regarding the amplitude of tensile and compressive stresses balance out with ongoing cooling process. If the temperature gradient vanishes, no stresses are present in the specimen in

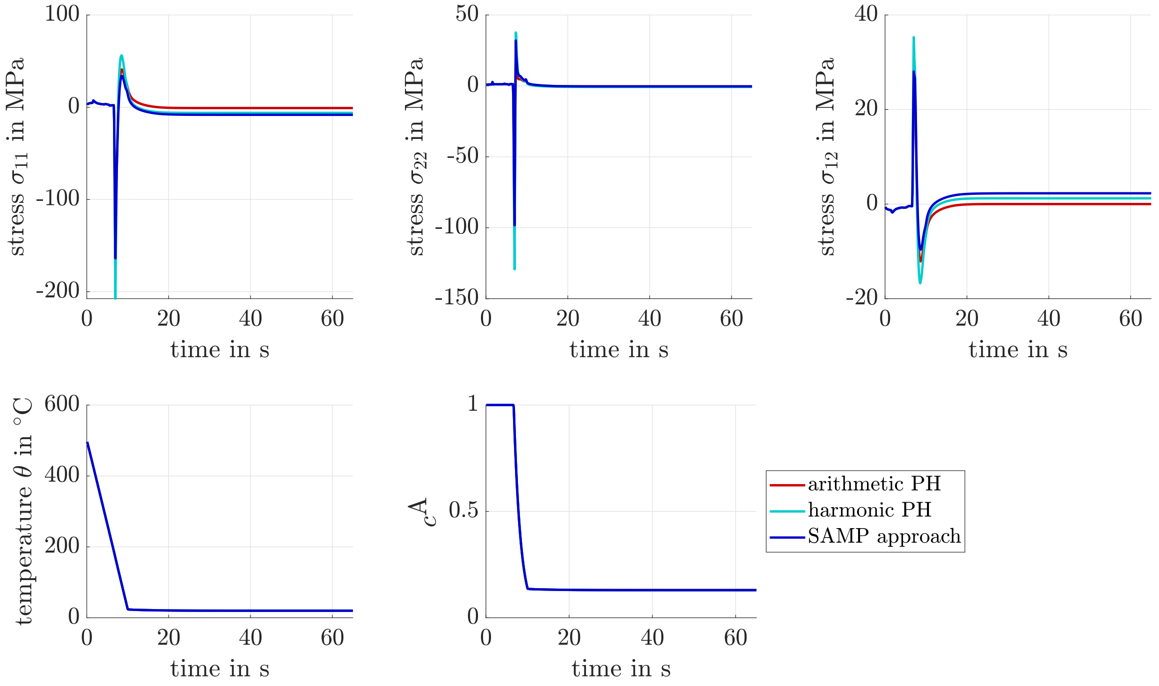

Figure 6.3: Case b - cooling boundary condition. Stresses σ_{11}, σ_{22} and σ_{12} as well as temperature θ and austenitic phase c^{A} on integration point level at point x of investigation, cf. Figure 6.1b.

the final state as expected. The latter holds also for the shear stress σ_{12}, for which a tensile stress peak is observed with the onset of phase transformation. When the cooling progresses, the compressive shear stresses occur, opposite to stresses σ_{11} and σ_{22}. In general it is observed that the arithmetic PH and SAMP approach behave very similar. Regarding σ_{11} and σ_{12}, the final stress values for the arithmetic PH material modeling are slightly higher or lower, respectively, that for the SAMP material model. Nevertheless, these deviations are quite small.

6.1.3 Case c - uniaxial tension

In a next step, the initial temperature of $\theta_0 = 500\,°\mathrm{C}$ is fixed for all nodes in the geometry of case c, see Figure 6.1c, to consider only the balance of momentum. The same displacement boundary conditions as for case b are applied, i.e., the displacement of the bottom nodes is fixed in x_2-direction, i.e., $u_2 = 0$, and the displacement of the left side is fixed in x_1-direction, i.e., $u_1 = 0$. The thermal cooling of the top edge is replaced by an uniaxial displacement $\Delta u_2 = 0.1\,\mathrm{mm}$, which represents an elongation of 1% of the initial length. This displacement is applied in ten seconds, afterwards the specimen is maintained in its configuration. Due to the temperature above the martensitic start temperature, no phase transformation occurs and all material models, PH or SAMP, describe the same response of the homogeneous austenitic material. The material can freely expand or contract due to the set boundary conditions, so that the stresses σ_{11} and σ_{12} are zero except numerical inaccuracies, see Figure 6.4. The stress distribution in second direction σ_{22} represents the yield behavior of the austenitic phase as expected, thus the elastic deformation is followed by plastification with prominent linear hardening. After the specimen is fully elongated, the stresses remain constant during the last 55 seconds of the computation.

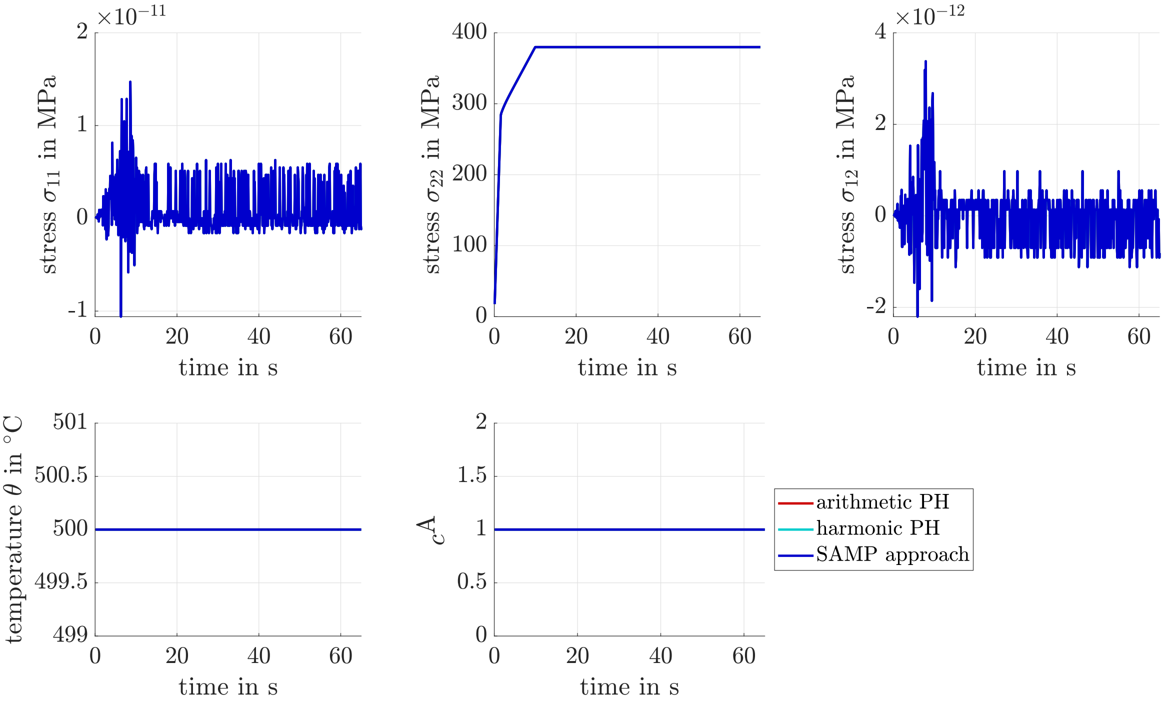

Figure 6.4: Case c - uniaxial tension. Stresses σ_{11}, σ_{22} and σ_{12} as well as temperature θ and austenitic phase c^{A} on integration point level at point x of investigation, cf. Figure 6.1c.

6.1.4 Case d - combination of cooling and uniaxial tension

Finally, the cooling and the uniaxial tension are combined, see Figure 6.1d. Regarding the displacement boundary conditions, the bottom of the geometry is fixed in x_2-direction, i.e., $u_2 = 0$, and the left side of the geometry is fixed in x_1-direction, i.e., $u_1 = 0$. On the top edge, a displacement of $\Delta u_2 = 0.1\,\mathrm{mm}$ in x_2-direction is applied, which resembles 1% elongation of the specimen. Furthermore, the top edge is exposed to a linear cooling from the initial temperature of $\theta_0 = 500\,°\mathrm{C}$ by $\Delta\theta = -480\,°\mathrm{C}$ in ten seconds. On all other edges, zero Neumann bounds are defined for the thermal degree of freedom. Subsequently, the displacement Δu_2 and the applied temperature change $\Delta\theta$ are held constant at the top edge, until the temperature gradient vanishes in the geometry. Still, only small deviations are found comparing the different single-scale approaches with each other, see Figure 6.5.

In comparison with previous boundary value problems, the results are qualitatively in accordance with the stress evolution due to the cooling in case b superimposed with the stresses following uniaxial tension in case c. In the beginning, before the phase transformation starts, the linear increase of stress component σ_{22} resembles case c. Stress components σ_{11} and σ_{12} show small tensile and compressive stress values due to the cooling, cf. Figure 6.3. With the onset of the phase transformation, a compressive stress peak is observed for stress components $\sigma_{11} \approx -150\,\mathrm{MPa}$. The high tensile stress value of $\sigma_{22} \approx 420\,\mathrm{MPa}$ is reduced to 270 MPa by the superimposed compressive stresses, since the martensitic phase transformation comes along with a volumetric expansion of the atomic lattice. With ongoing cooling and progression of the phase transformation in material points below the examined one, small tensile stresses are found regarding the stress component σ_{11}. At the same time, it holds for σ_{22} that the tensile stresses of $\approx 420\,\mathrm{MPa}$ are recovered. As before, in a final state the specimen shows zero stresses regarding σ_{11} and σ_{12}.

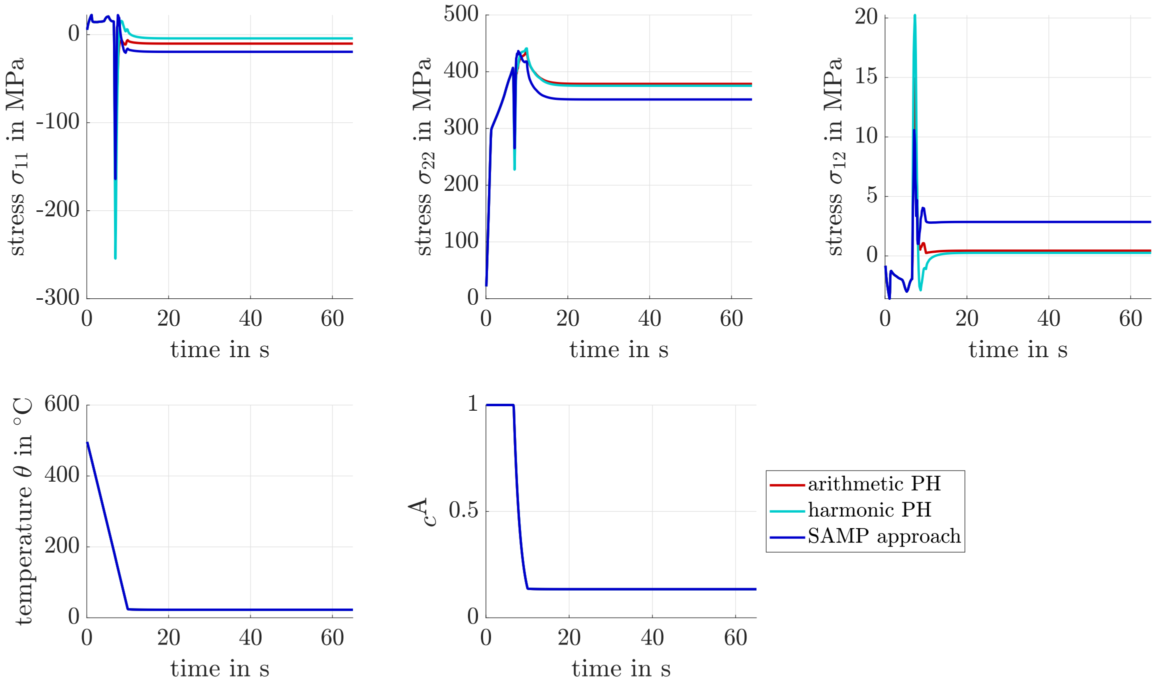

Figure 6.5: Case d - combination of cooling and uniaxial tension. Stresses σ_{11}, σ_{22} and σ_{12} as well as temperature θ and austenitic phase c^{A} on integration point level at point x of investigation, cf. Figure 6.1d.

The comparison of the three single-scale approaches shows that the descriptions of the macroscopic behavior are in good accordance. Summarizing, the harmonic material formulation shows highest magnitude concerning the stress peaks. Using arithmetic mean values for most parameters reduces the stress peaks compared to the calculation with harmonic effective parameters. Similar applies for the SAMP material model, which shows the same stress behavior in the beginning of the phase transformation, but at the end of the computation, the absolute stress values are slightly reduced compared to both previously discussed formulations. These strong similarities between the SAMP computation and the one with arithmetic parameters can be explained by the same averaging method, which weights either the parameters or the phase-specific stresses and tangent moduli by volume fractions. It can be concluded that the harmonic material formulation generally results in higher stresses than the other two approaches and, thus, in the following analysis the SAMP material modeling, presented in Section 5.5.2, is in focus. Its advantage compared to the arithmetic PH approach is that the phase-specific contributions are preserved during each computational step and thus, these can be investigated further.

6.2 Hot bulk forming of a cylindrical component

The first numerical example emphasized that a SAMP material model is well suited to carry out the investigation of cooling processes incorporating phase transformational effects. In the following, as a more complex geometry, a cylindrical specimen with eccentric hole is taken into account. The eccentricity is of special interest, since it evokes nonhomogeneous stress distributions inside the material as it is also the case for industrial components, see Simsir and Gür [169]. After a short introduction to the set-up of the experimental investigation, the boundary value problem is defined and a mesh density and time step size study is carried out. Afterwards, the numerical analysis of different cooling routes to evoke a targeted (residual) stress state inside the material is shown and the results regarding the stress distribution are discussed.

6.2.1 Experimental set-up of a hot bulk forming process

The experimental realization of a hot bulk forming process has been carried out at the Institute of Forming Technologies and Machines, Leibniz-University Hannover, see Behrens et al. [14; 15; 18; 19]. The process under consideration is the hot bulk forming process of the mentioned cylindrical specimen with eccentric hole, see Figure 6.6.

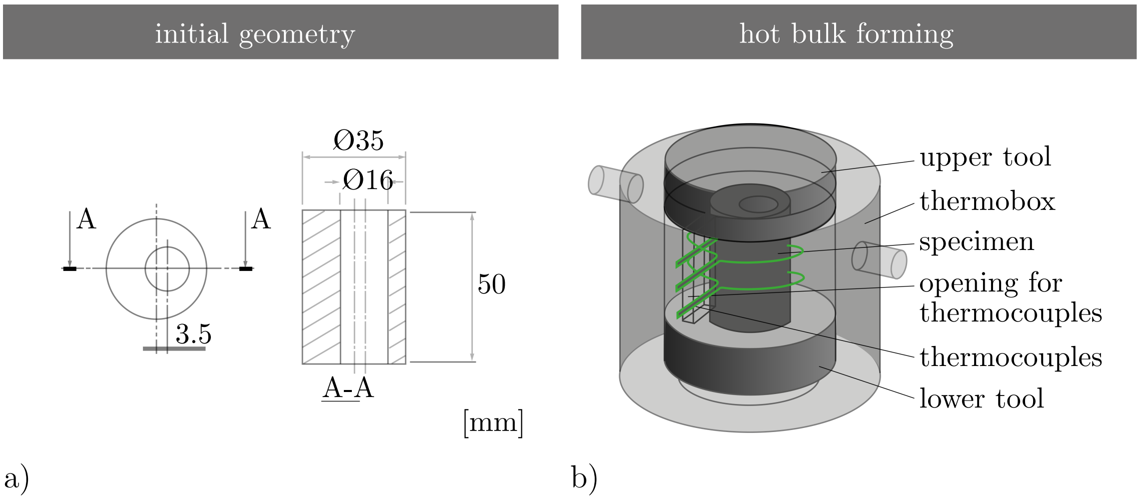

Figure 6.6: a) Dimension of the cylindrical specimen with eccentric hole and b) set-up of hot bulk forming process with thermobox, adapted from Behrens et al. [18].

This simple geometry serves for the development and evaluation of the finite element simulation tool. In a first process step, the specimen is heated to above 1000 °C in a thermobox with a suitable holding time to relax previous stresses inside the material. Thereby, a purely austenitic material is achieved which can be taken into account as nearly stress-free. In a second step, the component is upset using the forming simulator DYNSJ5590. The height is reduced from initially height of 50 mm to a height of 28 mm with a rate of 200 mm/s. The third step of hot bulk forming is the subsequent cooling, which is in focus of the following numerical analysis. Therefore, the specimen is removed from the thermobox and either cooled in water, by air or with application of a spray. Measuring points are defined on the surface of the specimen and connected to thermocouples, such that the temperature evolution is evaluated throughout the cooling. The process is schematically illustrated in Figure 6.7.

In case of spray cooling, a device with six circularly arranged independent nozzles is considered, which are two-substance nozzles of type XA PR 050 of Bete GmbH, cf. Figure 6.8. Thus, the spray is a mixture of water and air applied with a pressure of 0.04 MPa, resulting in a water flow rate of 0.2 l/s. For controlling the nozzles, solenoid valves are installed in front of the nozzles, which are regulated by the digital I/O module NI-9375 from National Instruments and programmed with the LabView software. The HTC (heat transfer coefficient) values are obtained by experimental and numerical comparison. That means, in a first step the cooling process is experimentally realized with a starting temperature of 1000 °C for a cylindrical specimen of height 50 mm and diameter 40 mm with six nozzles.

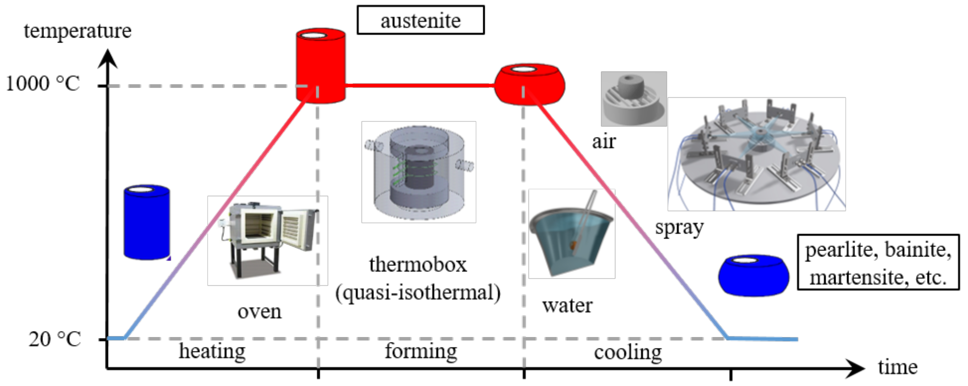

Figure 6.7: Schematic illustration of a hot bulk forming process of a cylindrical component with eccentric hole, which is at first heated, then upset and subsequently cooled, either by air, in water or with a spray, adapted from Uebing et al. [191].

During the cooling down to room temperature of 20 °C, the time-temperature-relation in depth of 3 mm in the front face is measured. In a second step, a numerical model is implemented in simufact.forming with varying HTC to fit the experimental data, until the method of the least squares between the calculated and experimental temperature-time curves achieves good agreement, see Behrens et al. [14; 15; 17; 18].

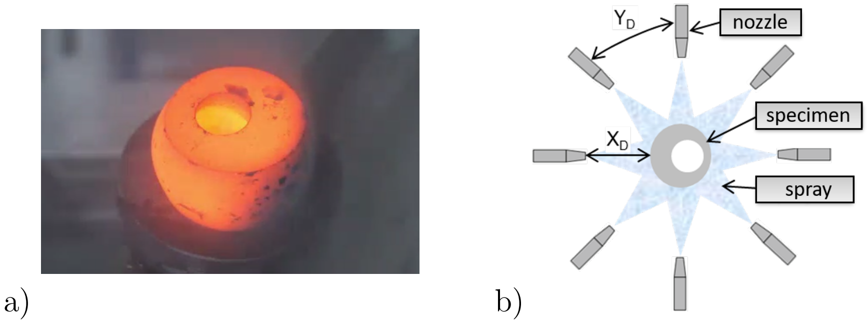

a) b)

Figure 6.8: a) Cylinderical specimen with eccentric hole exposed to a spray cooling in experiments at IFUM and b) schematic representation of a spray cooling device with eight nozzles. Therein, X_D denotes the distance between the specimen and a nozzle and Y_D is the distance between two nozzles.

6.2.2 Numerical investigation of the cooling step of hot bulk forming

The initial geometry for the hot bulk forming process, which is divided into heating, forming and cooling step, is provided in Figure 6.6a. Heating to above 1000 °C with a suitable holding time ensures a nearly stress-free, fully austenitic state of material 100Cr6, which is then upset. Thereby, the height is reduced by approximately 50%. In the last step, the deformed specimen is cooled down to room temperature. Therefore, different cooling media can be taken into account, for example cooling by air, cooling in water or the application of a spray with a spray cooling device. Different cooling routes can evoke different kinds of phase transformation and therewith decisive variations of the resulting stress distributions, which are examined numerically in the following. In absence of outer forces and moments and in case of an homogeneous temperature distribution over the component, the resulting stresses can be interpreted as macroscopic residual stresses (first type). The following numerical analysis focuses on the cooling step of hot bulk forming taking into account the SAMP material model presented in Section 5.5.2. The idea is to find a cooling route, which induces a predefined residual stress state in the material to positively influence the component's properties, i.e., compressive stresses in regions near the outer surface of the cylinder, which are able to prevent crack growth.

Boundary value problem

For the numerical analysis of the cooling of the considered cylindrical specimen with eccentricity, a two-dimensional slice, which is taken from the deformed cylindrical specimen before the cooling step, is taken into account. Its dimensions and displacement boundary conditions are provided in Figure 6.9 exploiting symmetry.

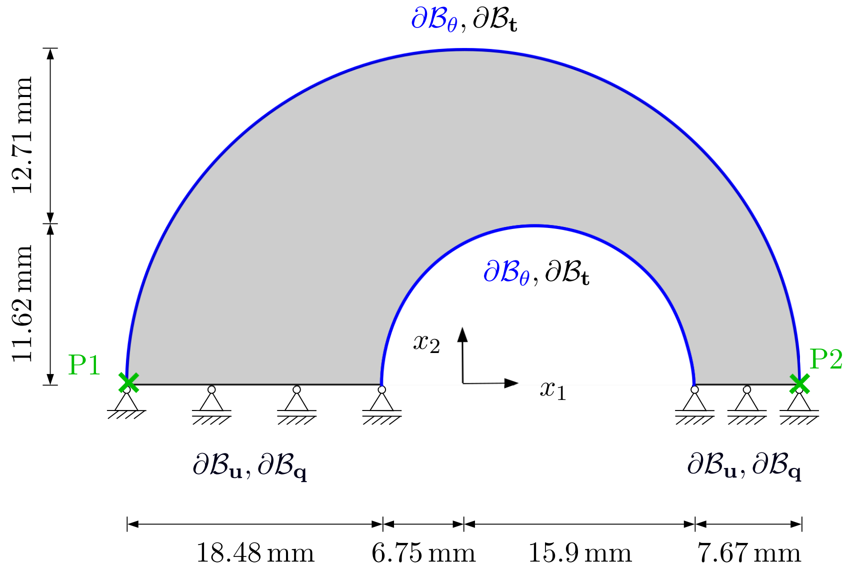

Figure 6.9: Two-dimensional slice taken from a cylindrical specimen with eccentric hole with its dimensions and displacement boundary conditions. The cooling is applied on the lateral surface, which is marked in blue. The marked points P1 and P2 are in focus of the investigation.

The cooling is applied on the lateral surface as Dirichlet type boundary conditions, marked in blue. In order to consider different cooling routes, such as cooling in water, by air or with a spray, the thermal boundary conditions are defined individually, see Section 6.2.4, Section 6.2.5 and Section 6.2.6, respectively. As a consequence of the eccentricity, the left side of the specimen as shown in Figure 6.9 is referred to as thick side while the right part is named thin side.

Plastic strains from hot bulk forming

Due to the focus of this work on the cooling process step, the forming history of the analyzed specimen has to be taken into account as a kind of initialization step. Based on macroscopic simulations done at the IFUM, LU Hannover, information regarding the accumulated plastic strains inside the cylindrical specimen is provided. The data can be processed and applied to the considered geometry at time $t = 0\,\mathrm{s}$, see Figure 6.10. In the following, this initialization step is referred to as offset.

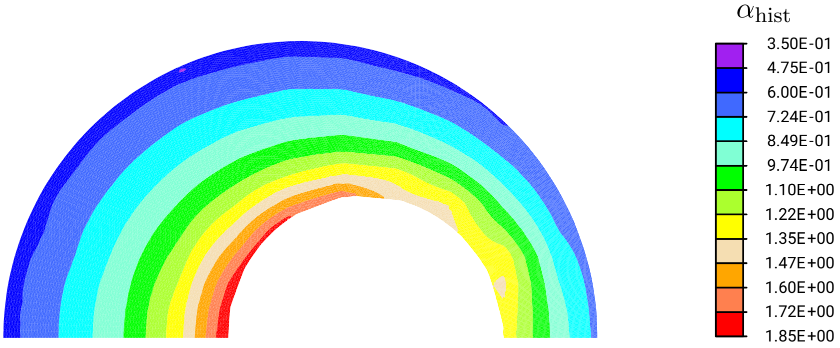

Figure 6.10: Exemplary accumulated plastic strains (offset) α_{hist} after hot bulk forming before the cooling for a two-dimensional slice taken from a cylindrical specimen.

6.2.3 Convergence study

The presented material model utilizes an adaptive split into five strain components, cf. Section 5.2. Therein, the plastic strain component and TRIP-strain component require an adequate time step size. Additionally, the rapid cooling applied on the lateral surface implies a temperature gradient, which has to be resolved accurately. Thus, a time step size and mesh density study has to be carried out. First, different discretizations are compared for a constant chosen time step size. Afterwards, a time stepping scheme is found that balances numerical costs and accuracy for the chosen mesh. The considered meshes and time step sizes are summarized in Table 6.1. With regard to the discretization, the different mesh sizes are sorted into three groups, namely “coarse“, “mediumänd “fine“. Exemplary, the coarse discretization 30 × 40 with 30 elements in radial and 40 elements in circumferential direction is plotted in Figure 6.11. For the purpose of comparison, the first cooling route, namely cooling in water, which is in detail described in the following Section 6.2.4, is utilized. For now, it is sufficient to know about the geometry, the considered SAMP material model, cf. Section 5.5.2, and that a cooling is applied on the lateral surface to execute the study. This fast, exponential cooling from above 1000 °C to room temperature of approximately 20 °C lasts for 80 seconds.

Table 6.1: Overview of the analyzed macroscopic discretizations (in radial and circumferential direction), which are sorted by size in groups “coarse“, “mediumänd “fine“, and the time step sizes.

macroscopic mesh elements radial	circumferential	name	time step size $\Delta t = 1\text{s}$	$\Delta t = 0.1\text{s}$	$\Delta t = 0.05\text{s}$	$\Delta t = 0.01\text{s}$
20	40	coarse	/	/	✓	/
30	40		/	✓	✓	/
20	60		/	✓	✓	/
40	80	medium	/	✓	✓	/
50	100		/	✓	✓	✓
70	140	fine	/	✓	✓	✓
100	200		/	✓	✓	✓

/ : diverged computation ✓ : converged computation

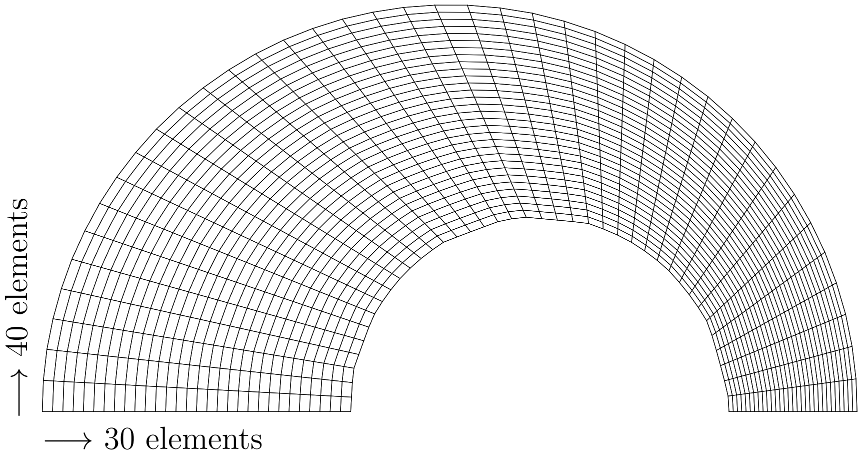

Figure 6.11: Exemplary mesh density for the coarse discretization 30 × 40 with 30 elements in radial and 40 elements in circumferential direction.

In a first attempt, the numerical computation is carried out for all defined meshes with a constant time step size of $\Delta t = 1\,\mathrm{s}$. The problems diverge directly during the first computational steps. Thus, a second time step size, $\Delta t = 0.1\,\mathrm{s}$ is of interest. Here, the coarsest mesh with 20×40 elements once again does not converge and is thus not considered in the following comparison. All other discretizations converge, but show small yet significant differences in numbers, as depicted in Figure 6.12 for σ_{11} and in Figure 6.13 for σ_{22} for times of $t = 15\,\mathrm{s}$, $t = 30\,\mathrm{s}$ and $t = 80\,\mathrm{s}$. Additionally, Figure 6.14 displays the respective stress components σ_{11} and σ_{22} along the x_1-axis for times of $t = 15\,\mathrm{s}$, $t = 30\,\mathrm{s}$ and $t = 80\,\mathrm{s}$. Therefore, the finest discretization with 100 elements in radial and 200 elements in circumferential direction is taken into account.

As can be seen in both Figures 6.12 and 6.13, the results converge, i.e., the differences between the stress results decrease with increasing number of elements. In order to substantiate this result with numbers, the σ_{11}- and σ_{22}-stress values at three points are compared at the same times. These points are located at $\mathrm{X}_1(-14|1)$, $\mathrm{X}_2(-2|18)$ and $\mathrm{X}_3(20|5)$, as illustrated in Figure 6.15. The finest mesh with 100×200 elements is used as a reference solution to determine the relative error as

$$err_{11}^{m,i} = \left| \frac{\sigma_{11}^{m,i} - \sigma_{11}^{100\times200,i}}{\sigma_{11}^{100\times200,i}} \right| \quad \text{and} \quad err_{22}^{m,i} = \left| \frac{\sigma_{22}^{m,i} - \sigma_{22}^{100\times200,i}}{\sigma_{22}^{100\times200,i}} \right| \tag{6.1}$$

with superscripts $i \in \{15\,\mathrm{s}, 30\,\mathrm{s}, 80\,\mathrm{s}\}$ giving the time and $m \in \{20 \times 60, 30 \times 40, 40 \times 80, 50 \times 100, 70 \times 140\}$ referring to the mesh density.

Figure 6.16a-c visualizes the results for $err_{11}^{m,i}$ and $err_{22}^{m,i}$ for all m and all i. Coarse meshes (20×60 and 30×40) show strong deviations from the reference solution with errors up to nearly 300 %. For the first medium sized discretization with 40×80 elements a smaller error is computed, but it is still greater than 10 % as can be seen for e.g. σ_{11} after $t = 80\,\mathrm{s}$ in Figure 6.16c. The medium sized mesh with 50×100 elements and the fine mesh with 70×140 elements show improved behavior. The error does not exceed approximately 6 %. One can conclude that both discretizations are suitable for further analysis of the problem at hand.

Another motivation to use sufficiently fine mesh densities is closely related to the definition of the FEM. Here, the investigated quantities are calculated at the integration points of

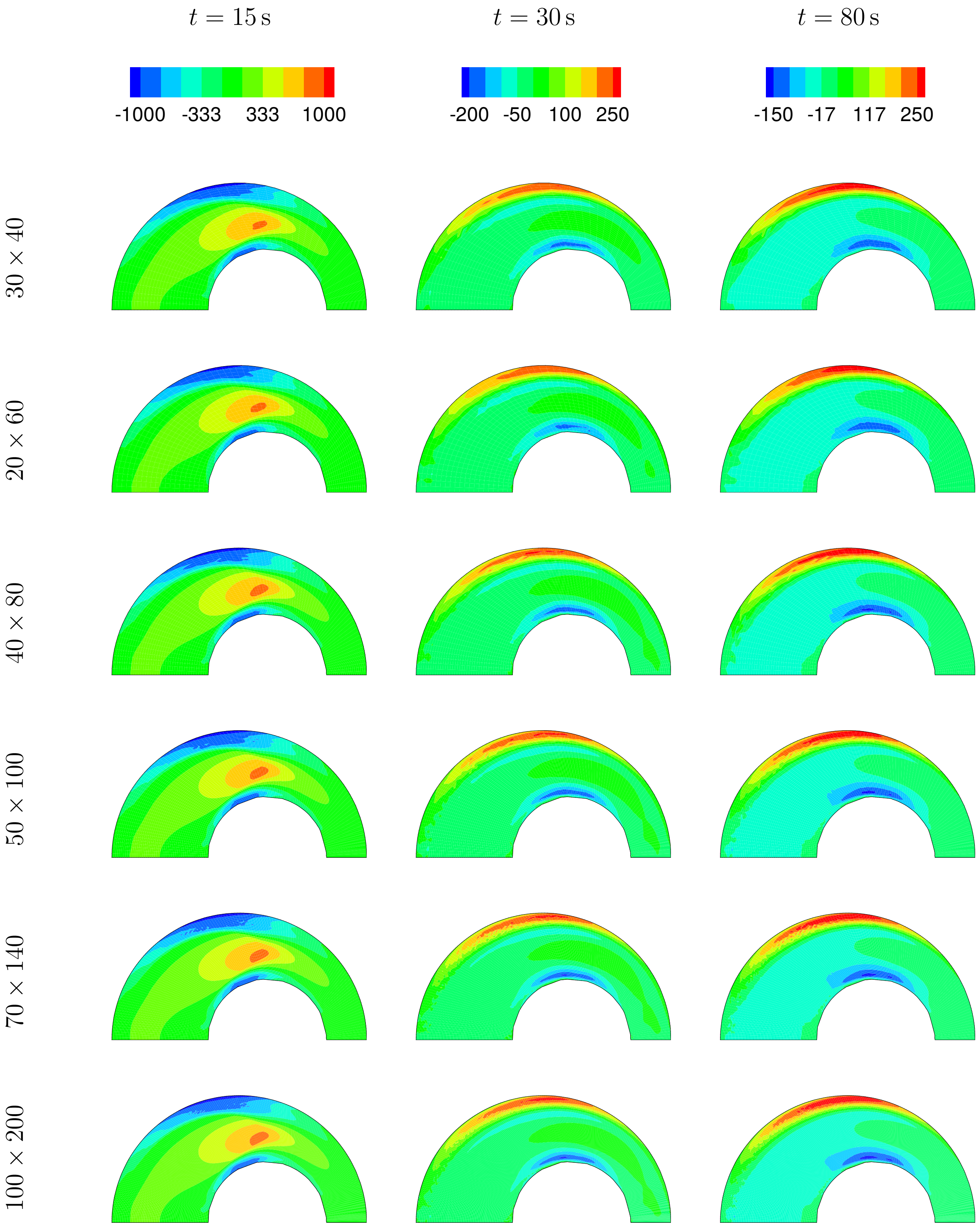

Figure 6.12: Comparison of different discretizations, namely with 30×40, 20×60, 40×80, 50×100, 70×140 and 100×200 elements, by means of stress component σ_{11} in MPa computed with time step size $\Delta t = 0.1\,\mathrm{s}$, after $t = 15\,\mathrm{s}$, $t = 30\,\mathrm{s}$ and $t = 80\,\mathrm{s}$.

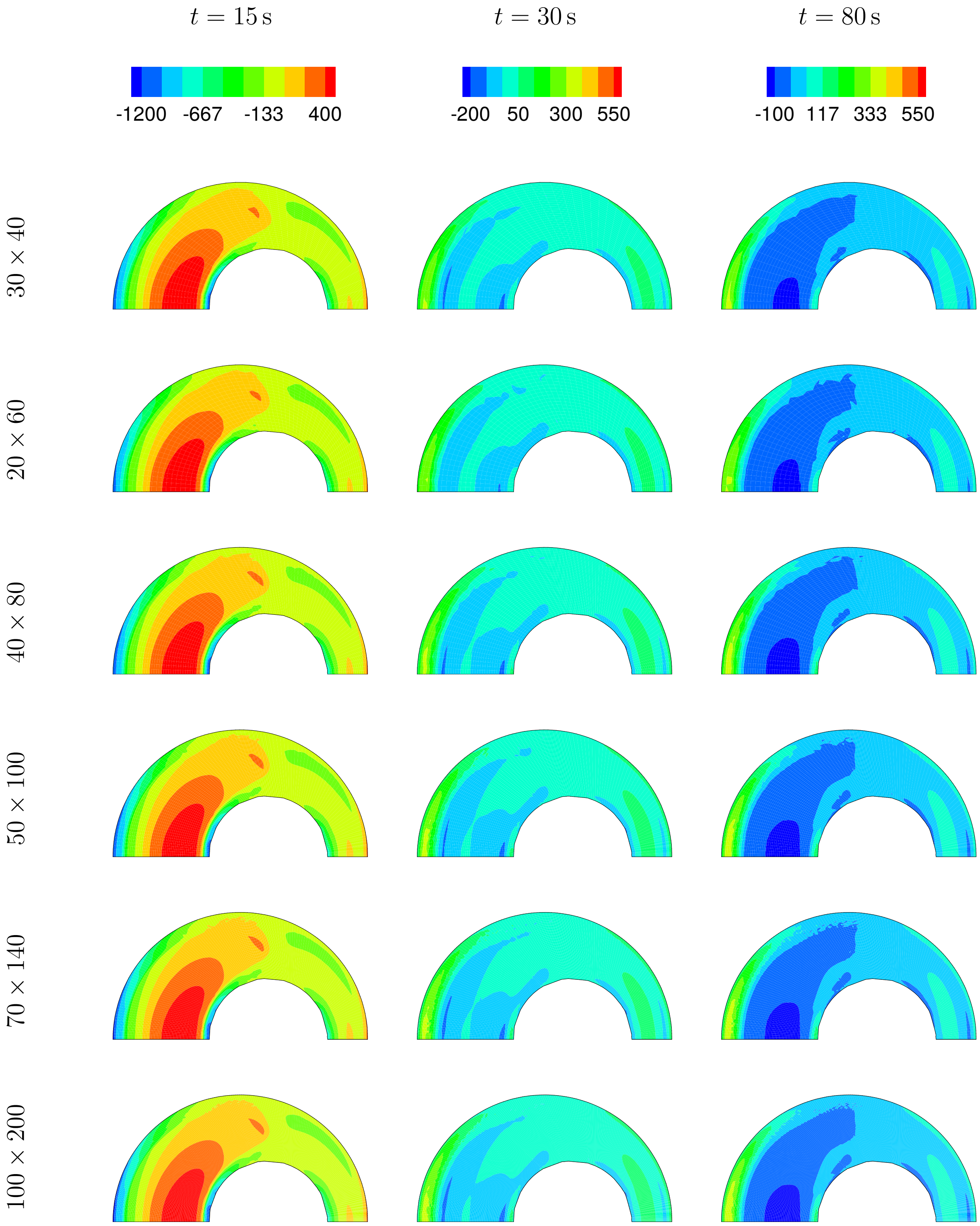

Figure 6.13: Comparison of different discretizations, namely with 30×40, 20×60, 40×80, 50×100, 70×140 and 100×200 elements, by means of stress component σ_{22} in MPa computed with time step size $\Delta t = 0.1\,\mathrm{s}$, after $t = 15\,\mathrm{s}$, $t = 30\,\mathrm{s}$ and $t = 80\,\mathrm{s}$.

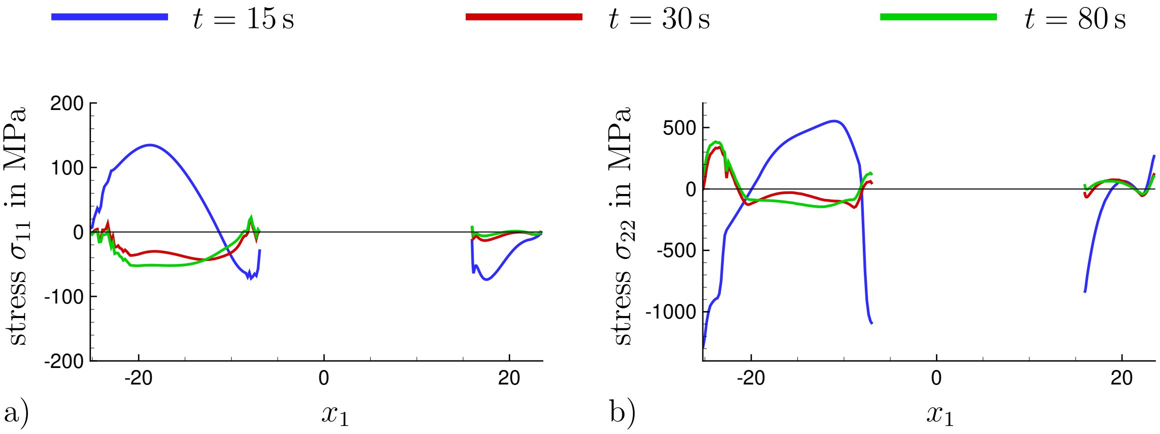

Figure 6.14: Stress components σ_{11} and σ_{22} along the x_1-axis for the finest discretization with 100 × 200 elements after $t = 15\,\mathrm{s}$, $t = 30\,\mathrm{s}$ and $t = 80\,\mathrm{s}$.

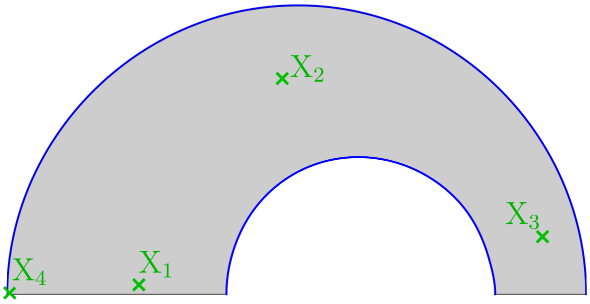

Figure 6.15: Location of the three points X_1, X_2 and X_3 used to evaluate the relative error, given in Equation 6.1, between different mesh densities. The integration point near the left corner, marked by X_4, is used to compare the evolution of different quantities over the cooling time.

an element and then the nodal values are extrapolated, in which context, the importance of a good discretization becomes especially apparent. This extrapolation provides room for inaccuracies and errors, which motivates a comparison of the calculations directly on integration point level. Thus, to confirm the thesis that discretizations with 50 × 100 or 70 × 140 elements are suitable, the evolution of different quantities during the complete cooling process on integration point level is investigated. To illustrate this, Figures 6.17 and 6.18 show the time evolution of the temperature θ, the martensitic volume fraction c^{M} and the stress components σ_{11} and σ_{22} in the integration point closest to the point X_4 marked in Figure 6.9.

As can be seen, the temperature evolution θ does not rely on the chosen discretization and shows only negligible minor to none deviations, since the point is very close to the outer surface, on which the temperature is set as boundary condition, cf. Figure 6.17a. As already mentioned during the motivation of the mesh density study, the temperature gradient must be resolved very adequately in the radial direction. It is found that a discretization with 20 elements in radial direction, i.e., 20 × 60, is not sufficient. Even 30 elements in combination with a coarse number of 40 elements in circumferential direction are not suitable, see the zoom in Figure 6.17b. Since the examined point is closer to the outer edge or, more precisely, closer to the outer corner for finer discretizations with many elements than for coarser meshes, these differences occur. In case of a high

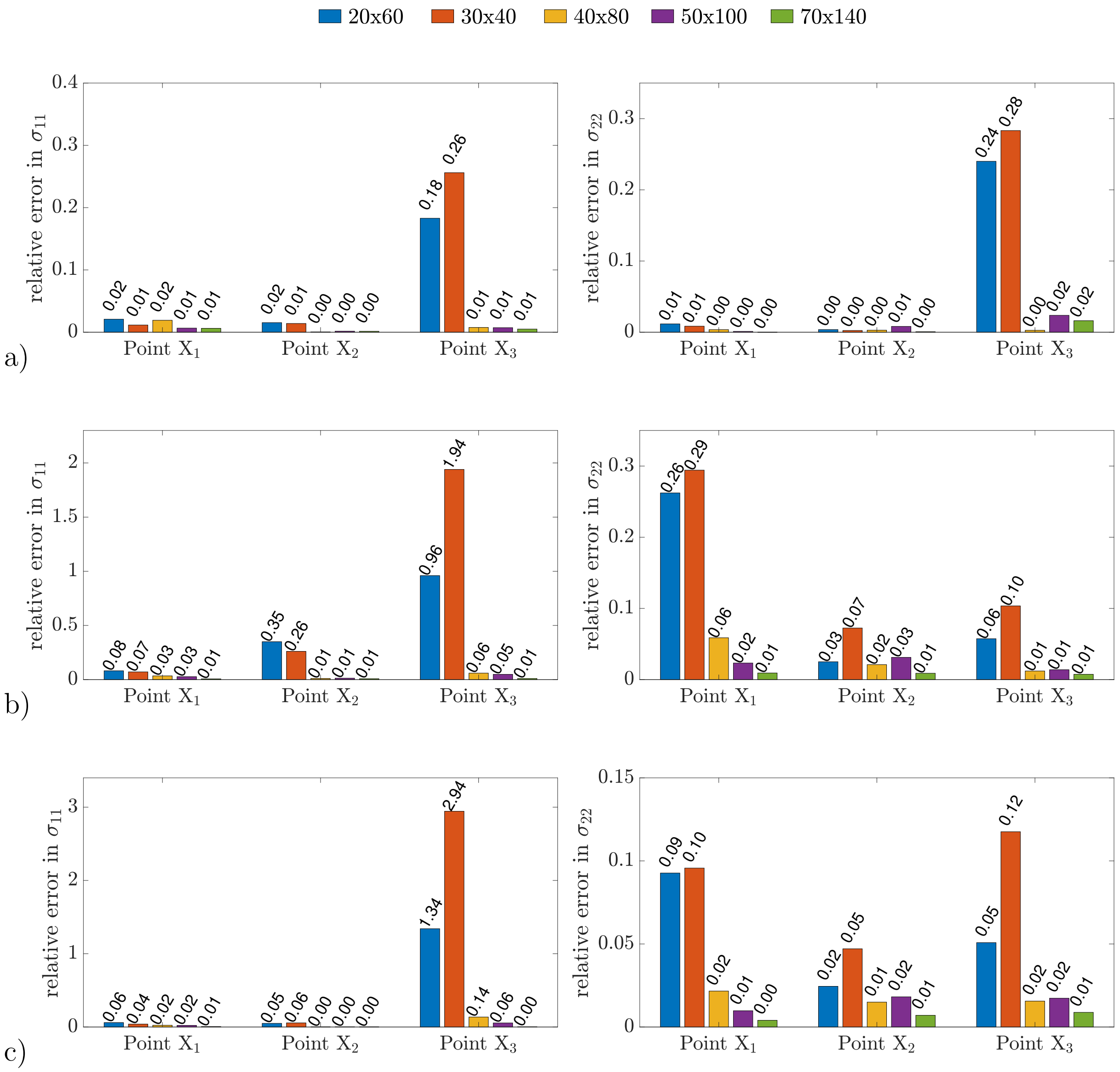

Figure 6.16: Relative error in σ_{11} and σ_{22} in relation to the finest mesh with 100×200 elements for three different points after a) $t = 15\,\mathrm{s}$, b) $t = 30\,\mathrm{s}$ and c) $t = 80\,\mathrm{s}$ for points X_1, X_2 and X_3, as marked in Figure 6.15.

number of elements in radial direction, the temperature in point X_4 decreases faster than for a less elements in radial direction, see Figure 6.17a. As a consequence, the onset of the austenite-to-martensite phase transformation is offset, cf. Figure 6.17b.

This, of course, influences the stress evolution as well, cf. Figure 6.18a and b. Regarding stress component σ_{11} in Figure 6.18a, oscillations are observed starting around $t = 10\,\mathrm{s}$. It holds that the coarser the mesh, the larger the amplitudes of the oscillations. For a coarse discretization the occurring zic-zac behavior is quite pronounced. Thus, mesh sizes with more elements are inevitable to depict the phase transformation precisely. It is found that the discretizations with 50 or more elements in radial direction show fitting stress curves. Therefore, the previous statement to chose a discretization with 50×100 elements or finer can be verified. Differences in stress component σ_{22} are quite small for these finer discretization, hence, the drawn conclusion can be acknowledged, cf. Figure 6.18b and c.

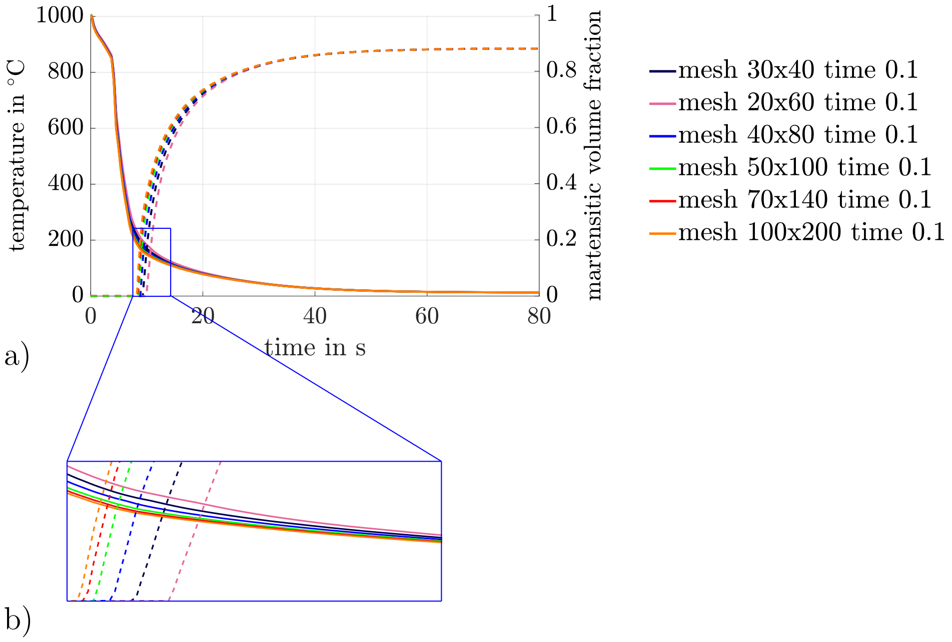

Figure 6.17: a) Evolution of temperature θ and martensitic volume fraction c^{M} over cooling time in the integration point nearest to the left corner, marked with X_4 in Figure 6.15, for different discretizations and b) with zoom in for $t \in [8\,\mathrm{s}, 15\,\mathrm{s}]$. Solid line depicts temperature, dashed line is martensitic volume fraction.

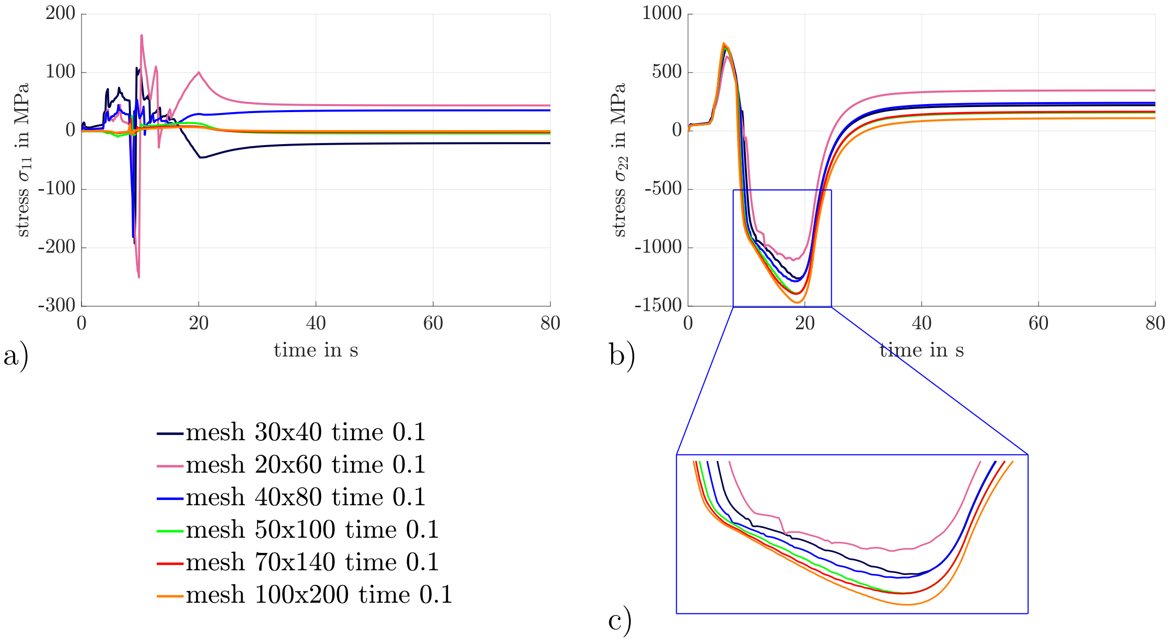

Figure 6.18: Evolution of stress components a) σ_{11} and b) σ_{22} over the cooling time in the integration point nearest to the left corner, marked with X_4 in Figure 6.15, for different discretizations and c) with zoom in for time $t \in [8\,\mathrm{s}, 25\,\mathrm{s}]$.

In addition to refine the discretization, the time step size could be adapted as well. As can be found in Table 6.1, the four coarsest meshes do not converge for a time step size of $\Delta t = 0.01\,\mathrm{s}$, although they give results for a five times larger time step size of $\Delta t = 0.05\,\mathrm{s}$. Thus, in the following they are disregarded. For the remaining meshes it holds that a finer time step size can improve the accuracy of the solution, e.g. for the medium mesh 50 × 100. At the same time, one observes that the reduced time step size has only small to none impact for a very fine discretization, as it holds for 100 × 200 elements, see Figure 6.19. As can be found, for a very good combination, balancing number of degrees of freedom and number of time steps with regard to ensuring accurate results, a mesh with 50 × 100 elements seems to be a good choice.

Furthermore, all the previous graphs show nearly none deviation in the cooling time before the onset of the phase transformation. Due to the speed of the diffusionless phase transformation to martensite, the transition is nearly finished after the first half of the cooling process. Thus, an adaptive time stepping scheme can be utilized, i.e., in the beginning and end of the cooling process, here for time intervals of $t \in [0\,\mathrm{s}, 8\,\mathrm{s}]$ and $t \in [40\,\mathrm{s}, 80\,\mathrm{s}]$, the time step size can be chosen as $\Delta t = 0.1\,\mathrm{s}$. During the phase transformation, the time step size is reduced to $\Delta t = 0.01\,\mathrm{s}$. In order to investigate different cooling routes, i.e., the cooling in air or with a spray, this time stepping scheme can be adopted accordingly. Considering spray cooling, that lasts for 500 seconds, the phase transformation mainly takes place between 25 s and 100 s. In contrast to that, cooling by air takes much more time, i.e., 5000 seconds. Therefore, a constant time step size is adequate, so that it holds

$$
\begin{aligned}
\Delta t_{\mathrm{air}}(t) &= 1\,\mathrm{s} = \mathrm{const} \quad 0\,\mathrm{s} \le t \le 5000\,\mathrm{s}\,, \\
\Delta t_{\mathrm{water}}(t) &= \begin{cases} 0.1\,\mathrm{s} & 0\,\mathrm{s} \le t < 8\,\mathrm{s} \\ 0.01\,\mathrm{s} & 8\,\mathrm{s} \le t < 40\,\mathrm{s} \\ 0.1\,\mathrm{s} & 40\,\mathrm{s} \le t \le 80\,\mathrm{s} \end{cases} , \\
\Delta t_{\mathrm{spray}}(t) &= \begin{cases} 0.1\,\mathrm{s} & 0\,\mathrm{s} \le t < 25\,\mathrm{s} \\ 0.01\,\mathrm{s} & 25\,\mathrm{s} \le t < 100\,\mathrm{s} \\ 0.1\,\mathrm{s} & 100\,\mathrm{s} \le t \le 500\,\mathrm{s} \end{cases} .
\end{aligned}
\tag{6.2}
$$

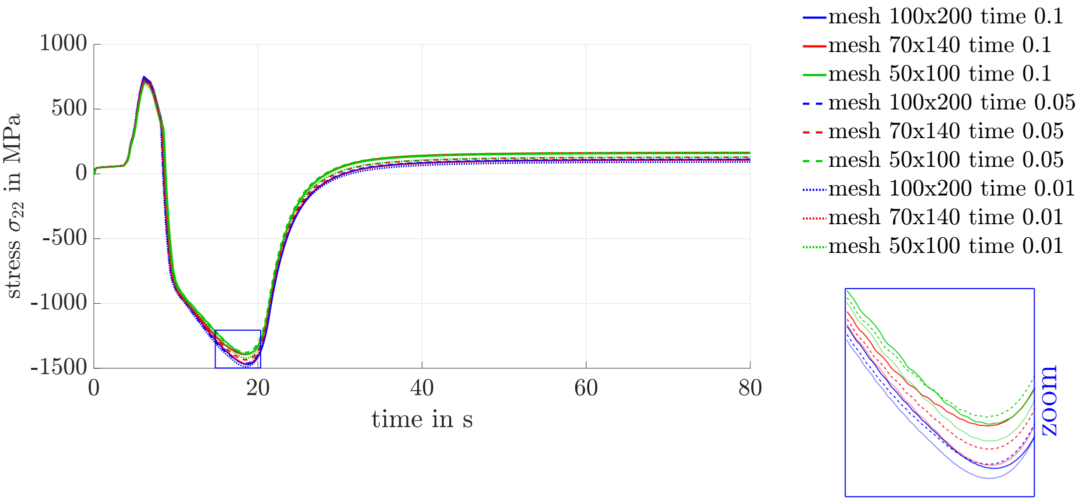

Figure 6.19: Influence of time step size $\Delta t \in \{0.1\,\mathrm{s}, 0.05\,\mathrm{s}, 0.01\,\mathrm{s}\}$ for meshes with 50×100, 70×140 and 100×200 elements, evaluated in the integration point nearest to the left corner, marked with X_4 in Figure 6.15.

6.2.4 Diffusionless cooling in water

Quenching of the deformed cylindrical specimen in water, the geometry is given in Figure 6.9, results in a diffusionless phase transformation from the initial purely austenitic material to a martensitic dominated microstructure. For this purpose, one thermal boundary condition is defined for each lateral surface, namely outer and inner lateral surface, cf. Figure 6.20, which shows the evolution of the temperature and the related martensitic volume fraction over time. Thus, for the final state at room temperature of approximately 20 °C, 87 % martensite and 13 % retained austenite are present, following Behrens et al. [15] and see the curve of c^{M} in Figure 6.20. The martensitic start temperature is considered for the Cr-alloyed steel as $\theta_{\mathrm{Ms}} = 185\,^\circ\mathrm{C}$, while the final temperature is room temperature $\theta_{\mathrm{RT}} = 20\,^\circ\mathrm{C}$. The complete cooling lasts for 80 seconds until a homogeneous temperature distribution is obtained. Note that this is important to achieve a separation of thermally evoked stresses from residual stresses.

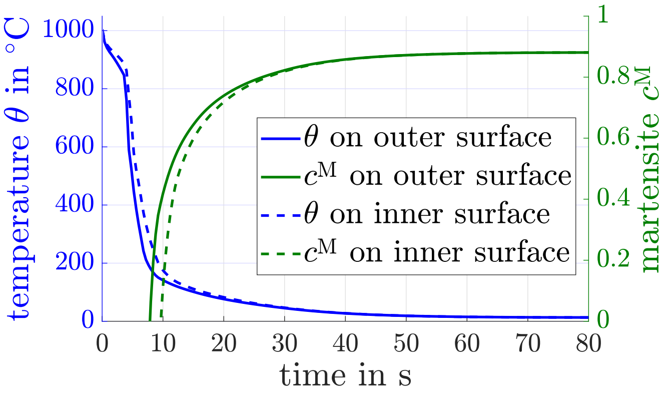

Figure 6.20: Thermal Dirichlet boundary conditions for cooling in water on outer (point P1, cf. Figure 6.9) and inner (point P2, cf. Figure 6.9) lateral surface with related martensitic volume fraction.

The resulting stress evolutions of stress component σ_{22} in points P1 and P2 are depicted over time in Figure 6.21 together with the evolution of temperature and martensitic volume fraction. For comparison, simulative results and experimental stress measurement, carried out at IFUM, see Behrens et al. [17], are given. Since the investigated points are located on the x_1-axis, the stress component σ_{22} can be interpreted as tangential stress σ_{tang}. [1.)] First, before the onset of the phase transformation, the cooling leads to thermal contraction of the specimen and thus, tensile tangential stresses are present in both points P1 and P2. If the temperature drops below the martensitic start temperature, the volumetric expansion of the atomic lattice, which is taken as 1 %, cf. Olle [133], leads to a superposition with high compressive stresses. Afterwards, when the phase transfor-

---

[1.)] In order to determine the tangential stresses in the component in a point $\boldsymbol{x}$, the stress tensor $\boldsymbol{\sigma}$ is rotated by rotation matrix $\boldsymbol{R}$, which is defined based on the angle α. This angle α rotates x_1-x_2-coordinate system to the x_1^*-x_2^*-coordinate system so that the x_1^*-axis points in direction of the position vector $\boldsymbol{x}$. The tangential stresses σ_{tang} are identified as entry σ_{22}^* in the rotated stress tensor $\boldsymbol{\sigma}^*$.

$$\bar{\boldsymbol{R}} = \begin{pmatrix} \cos(\alpha) & -\sin(\alpha) & 0 \\ \sin(\alpha) & \cos(\alpha) & 0 \\ 0 & 0 & 1 \end{pmatrix} , \quad \boldsymbol{\sigma}^* = \boldsymbol{R} \cdot \boldsymbol{\sigma} \cdot \boldsymbol{R}^{\mathrm{T}} .$$

mation starts in the bulk material, the sign of the stresses changes once more in the regions near the lateral surface. In the final state, tensile stresses are present in regions near the outer boundary. In comparison to the simulations carried out at IFUM using simufact.forming, the stress evolution shows good accordance, especially qualitatively. Furthermore, the experimentally measured stresses of about 216 MPa at P1 and 138 MPa at P2 are satisfactorily matched.

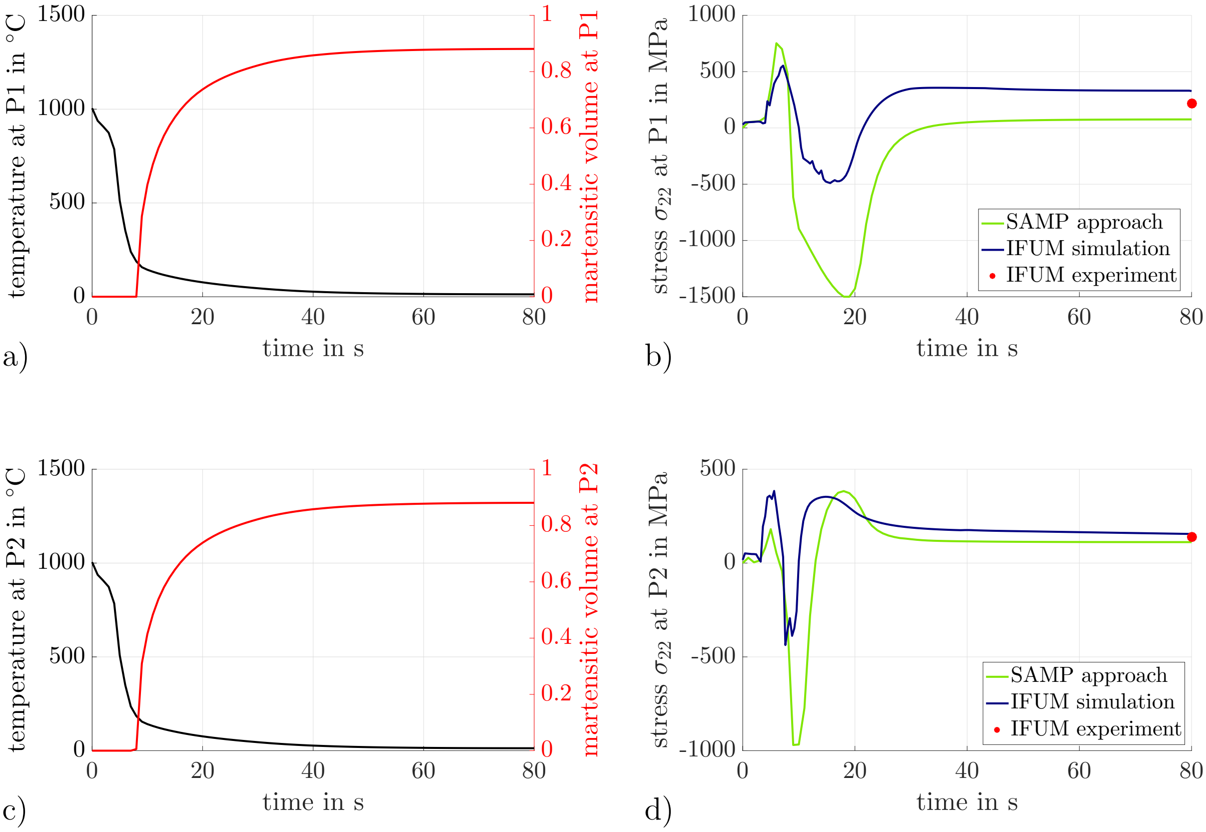

Figure 6.21: Water cooling - a) & c) Evolution of temperature θ in °C, martensitic volume fraction c^{M} and b) & d) tangential stresses σ_{tang} in MPa over cooling time in measuring points P1 and P2, respectively, as marked in Figure 6.9a. Simulations and experimental measurements carried out at IFUM are presented in Behrens et al. [17].

Figure 6.22 displays the temperature distribution θ, martensitic phase evolution c^{M} and tangential stress state σ_{tang} at different points in time. First, after eight seconds of time, the temperature is still higher than the martensitic start temperature and thus, the phase transformation has not started yet. The tangential stresses are nearly homogeneous, showing tensile stress values in regions near the outer bound on the thick side due to thermal contraction. The onset of the phase transformation in regions near the outer surface after ten seconds leads to an increase of the martensitic volume fractions at the outer lateral surface. This comes along with high compressive stress values, as already visualized in Figure 6.21 for the two measuring points on that surface. A few seconds later, after 15 seconds of cooling time, the temperature is below the martensitic start temperature in roughly 50 % of the cylindrical slice. Except of the bulk material on the left side of the geometry, the phase transformation takes place in almost the whole domain. On the thick side, high compressive stress values can be seen on the lateral surfaces, whereas the bulk material shows tensile stress values.

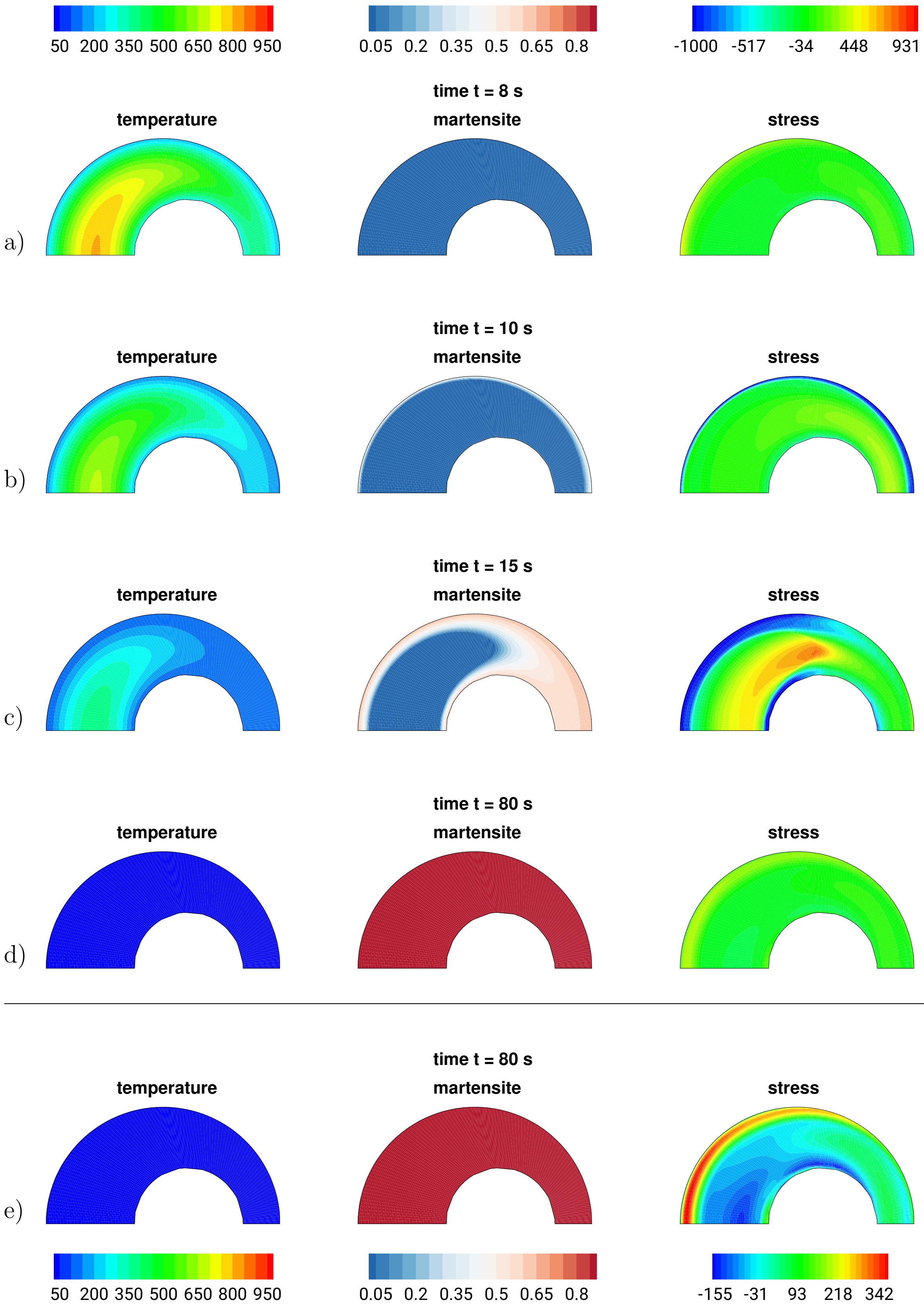

Figure 6.22: Water cooling - Evolution of temperature θ in °C, martensitic volume fraction c^{M} and tangential stresses σ_{tang} in MPa before a) $t = 8\,\mathrm{s}$, during b) $t = 10\,\mathrm{s}$ & c) $t = 15\,\mathrm{s}$ and at the end of the phase transformation d) $t = 80\,\mathrm{s}$ and with e) adapted scaling of the color legend for the final stress state.

In contrast to that, the bulk material already undergoes the phase transformation on the thin side of the geometry. As a consequence, the compressive stresses in regions near the surfaces are superimposed by tensile stresses, which arise as counterpart to compressive stresses in the bulk due to the martensitic volumetric expansion. In the final state, after 80 seconds, room temperature has been reached in the component and a homogeneous phase distribution with 13 % retained austenite and 87 % martensite has set. As emphasized by Figure 6.22e tensile stresses are present in regions near the lateral surface and in the bulk material opposed compressive stresses are observed.

6.2.5 Diffusion controlled cooling by air

Cooling by air takes much more time than quenching in water, i.e., 5000 seconds compared to 80 seconds. Thereby, a diffusion controlled phase transformation takes place, which is simulated with the JMAK equation, see Section 4.1.1. For the defined boundary value problem with changed thermal boundary conditions, as depicted in Figure 6.23, the phase transformation form austenite to pearlite has to be modeled as experimentally observed, cf. Behrens et al. [15]. Microstructural investigation shows that in the final state an almost complete transformation to pearlite has taken place. The volumetric expansion of the atomic lattice during the austenite-to-pearlite phase transformation is set to 0.1 %.

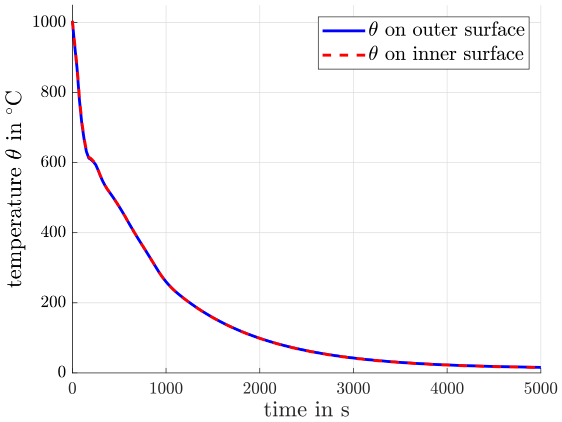

Figure 6.23: Cooling Dirichlet boundary conditions for cooling by air on outer (point P1, cf. Figure 6.9) and inner (point P2, cf. Figure 6.9) lateral surface.

In Figure 6.24 the phase, temperature and stress evolution are depicted for both points P1 and P2 in combination with experimental measurements and simulations carried out at IFUM. The results show that the fast phase transformation takes place around $t = 120\,\mathrm{s}$. As a consequence of this, the firstly occurring tensile stresses from thermal contraction are superimposed with compressive stresses, resulting in the compressive stress peak. As the cooling proceeds, a stress weakening is observed analogously to cooling in water. Thus, in the final state, tensile stresses are computed. This does not fit with the experimental measurements very well, which show compressive stresses in both points P1 and P2 at the end of the cooling by air. But, it is to be noticed that all values are very low of magnitude compared to the cooling in water. Thus, another cooling strategy should be tested to obtain the targeted compressive residual stresses in regions near the outer surface, that influence the component's properties positively.

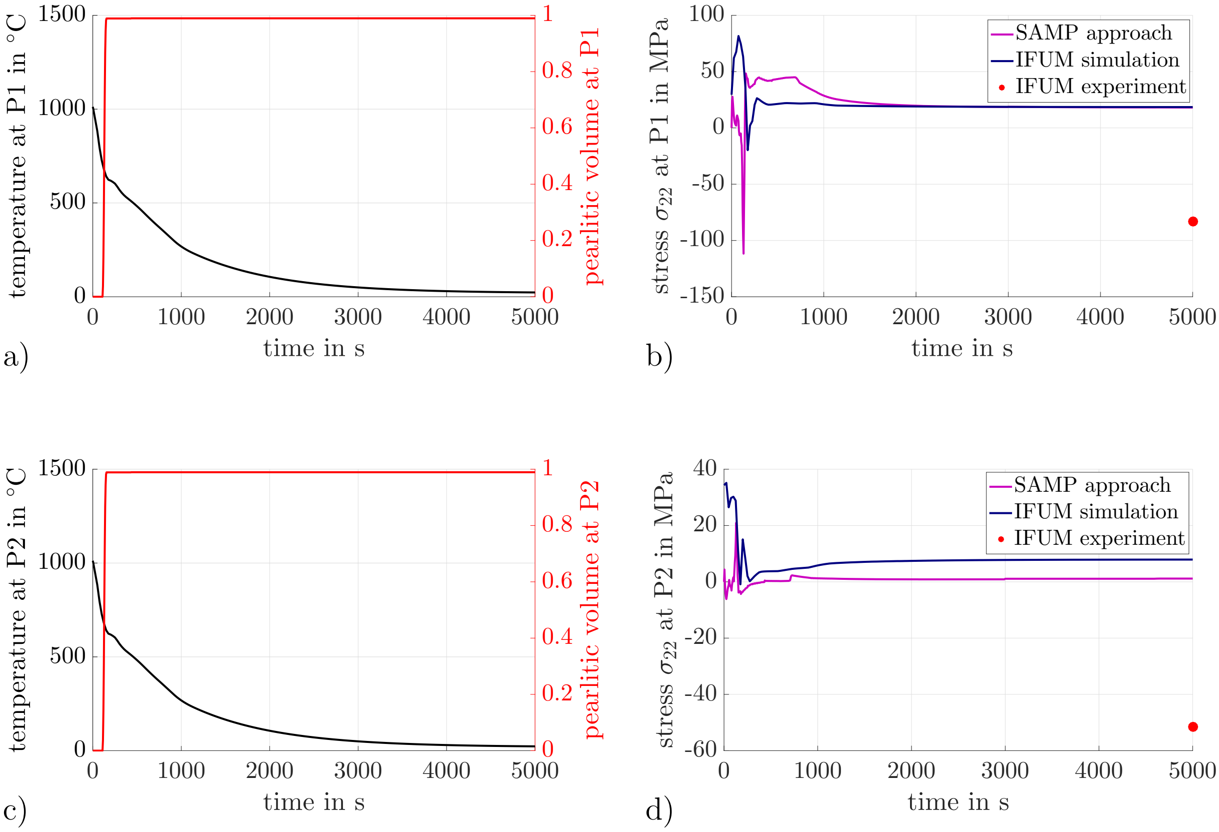

Figure 6.24: Air cooling - a) & c) Evolution of temperature θ in °C, pearlitic volume fraction c^{P} and b) & d) tangential stresses σ_{tang} in MPa over cooling time in measuring points P1 and P2, respectively as marked in Figure 6.9a. Simulations and experimental measurements carried out at IFUM are presented in Behrens et al. [17] and Behrens et al. [18].

In addition, Figure 6.25 displays the three quantities, c^{P}, θ and σ_{tang}, for the cylindrical slice for certain points in time, which are before $t = 105\,\mathrm{s}$ and after $t = 130\,\mathrm{s}$ the phase transformation and at the end of the cooling process $t = 5000\,\mathrm{s}$. The shown stress evolution is qualitatively in good accordance with the stresses resulting from cooling in water. Due to the slower cooling, the temperature gradient in the slice is pronounced and as a direct consequence, the phase transformation is accomplished in a shorter period of time and in a more homogeneous manner, which results in lower stress values, cf. Figure 6.25d.

6.2.6 Diffusionless cooling using a spray cooling device

Instead of cooling in water or by air, which are two examples of immersion cooling, the application of a spray as splash cooling is as third route taken into account. The utilization of a spray cooling device with six independent nozzles as it is shown in Figure 6.26, enables the temporal and spatial control of the cooling process, cf. Section 6.2.1. Here, a constant spray as mixture of water and air is applied with one active nozzle for about 300 seconds to the thick side of the geometry. Thus, the boundary conditions have to be adapted to suit the experiments.

Utilizing the proposed material model of Section 5, the computing time has to be adapted

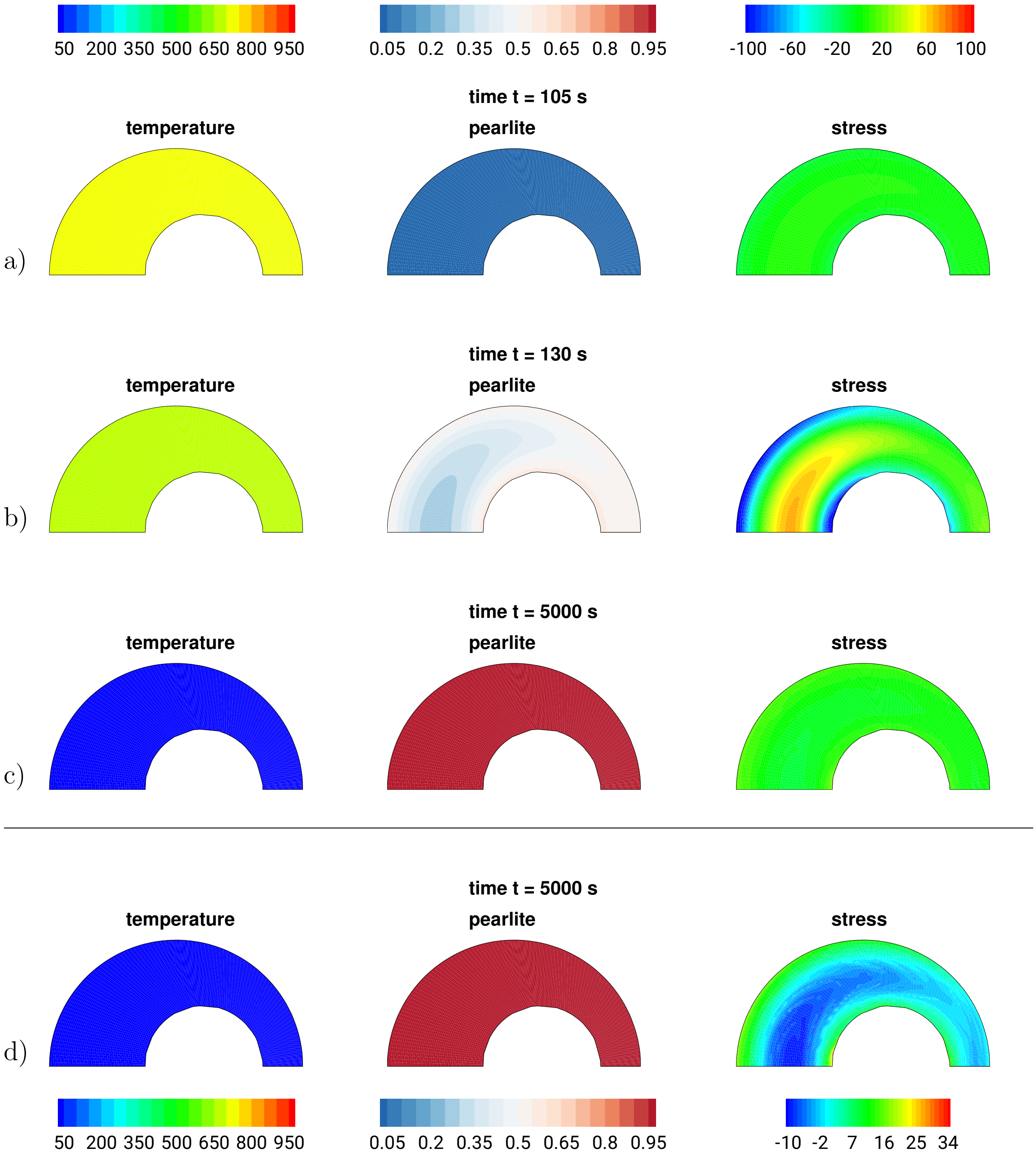

Figure 6.25: Air cooling - Evolution of temperature θ in °C, pearlitic volume fraction c^{P} and tangential stresses σ_{tang} in MPa before a) $t = 105\,\mathrm{s}$, during b) $t = 130\,\mathrm{s}$ and at the end of the phase transformation c) $t = 5000\,\mathrm{s}$ and with d) adapted scaling of the color legend for the final stress state.

as well, so that in the final state, a constant temperature in the whole cylindrical slice is obtained. Otherwise, it is not possible to distinguish, if either the temperature and/or the phase transformation evokes the stresses, and hence no residual stress state could be defined. Therefore, the computing time is extended to 500 seconds while the cooling still last for 300 seconds, see Figure 6.27. In order to account for the different cooling paths in dependence of the distance of the applied spray, the thermal boundary condition varies

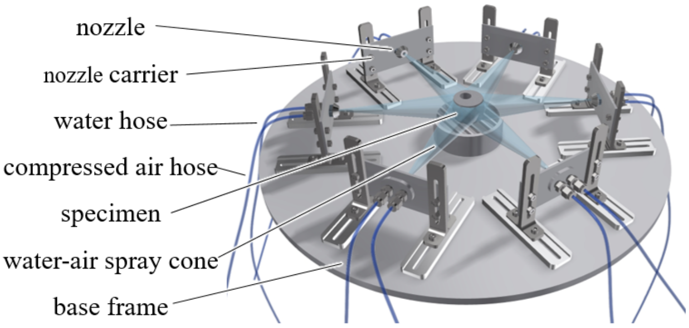

Figure 6.26: Spray cooling device with six independent nozzles, taken from BEHRENS ET AL. [18].

approximately all 10°, cf. Figure 6.28. The temperature evolution on the lateral surfaces in points P1 and P2 are given in Figure 6.27. The observed tangential stresses in points P1 and P2 are plotted in Figure 6.29 together with the simulative results obtained at IFUM using simufact.forming. As a consequence of the spray, a fast cooling in point P1 and a slower cooling in point P2 can be observed. Due to the heat conduction through the specimen's geometry from left to right, point P2 is cooled slower but still fast enough to undergo the austenite-to-martensite phase transformation until a homogeneous phase distribution is gained.

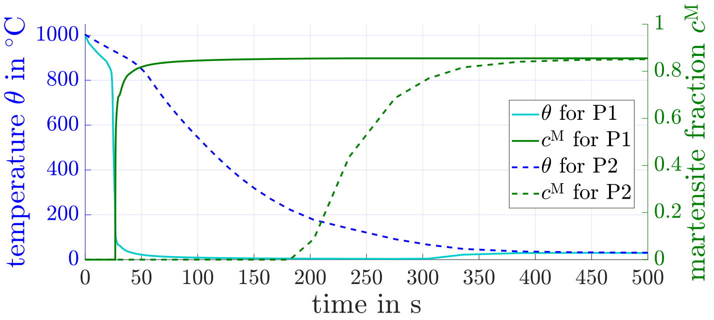

Figure 6.27: Thermal Dirichlet boundary conditions for cooling with a spray for sprayed region and on the opposite outer side

The resulting stress evolution in point P1 in Figure 6.29b shows that at first tensile stresses due to thermal contraction occur, compare cooling in water in Section 6.2.4. With heat conduction to the whole geometry and the onset of the phase transformation in the spray exposed region, the stress sign changes, and compressive stresses occur. These are weakened when the phase transformation starts in the bulk material of the thick side.

As the cooling proceeds, the stresses even change their sign again and tensile stresses occur, see also Figures 6.30 and 6.31. In the final state, cf. Figure 6.31e, compressive stresses are present in the region around P1, in which the spray cooling is applied. As depicted in Figure 6.29b, the stresses behave slightly different in point P2. As a consequence of the spray cooling applied to the thick side of the component, the right side undergoes the phase transformation much later. For P2 it holds that the martensitic phase starts to evolve after approximately 170 seconds of cooling time, see also Figure 6.27. The phase transformation occurs slower compared to the spray exposed part of the geometry. Influenced by the phase transformation of the bulk material, compressive stresses occur

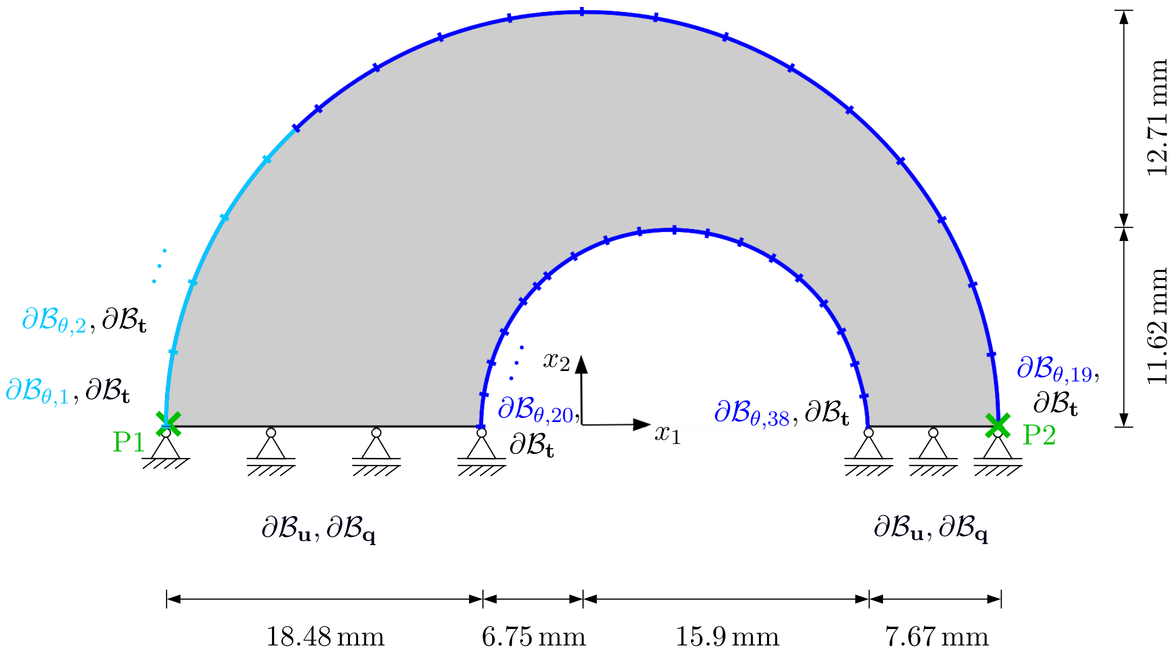

Figure 6.28: Two-dimensional slice taken from a cylindrical specimen with eccentric hole with its dimensions and adapted boundary conditions for spray cooling. The cooling is applied on the lateral surface, which is marked in dark and lighter blue. The marked points P1 and P2 are in focus of the investigation.

which are weakened between 200 and 300 seconds of cooling time. In the final state, compressive stresses are present. Therewith, the aimed for compressive stress state near the outer lateral surface is obtained. Experimental measurements show that this targeted residual stress state is a consequence of the changed cooling route. It has been proven that e.g. the evolving microstructure is the same as for the cooling in water and thus, this does not influence the out coming stress distribution.

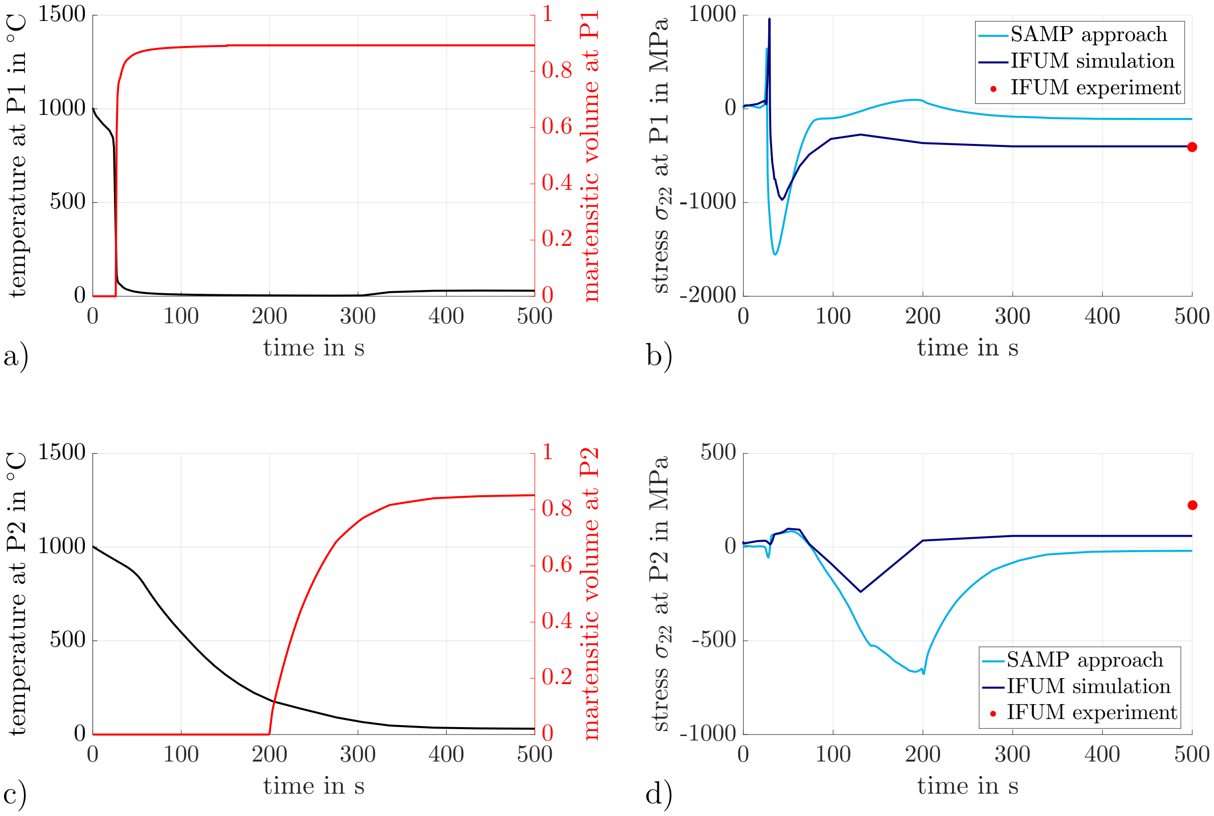

Figure 6.29: Spray cooling - a) & c) Evolution of temperature θ in °C, martensitic volume fraction c^{M} and b) & d) tangential stresses σ_{tang} in MPa over cooling time in measuring points P1 and P2, respectively as marked in Figure 6.28. Simulations and experimental measurements carried out at IFUM are presented in Behrens et al. [17] and Behrens et al. [18].

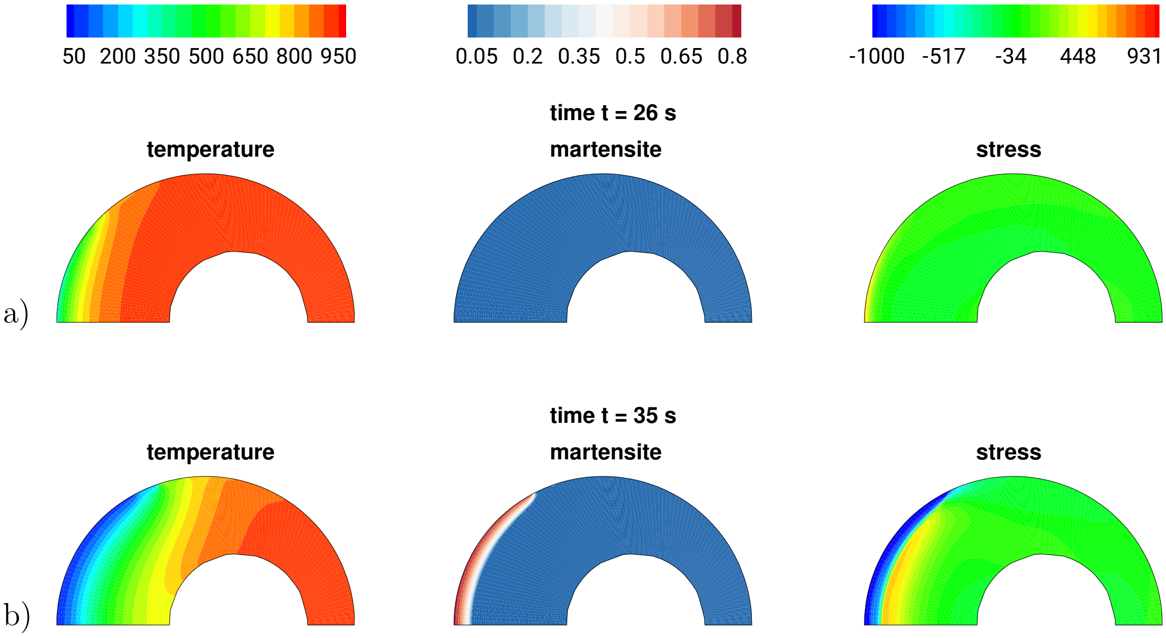

Figure 6.30: Spray cooling - Evolution of temperature θ in °C, martensitic volume fraction c^{M} and tangential stresses σ_{tang} in MPa before a) $t = 26\,\mathrm{s}$ and during b) $t = 35\,\mathrm{s}$ the phase transformation.

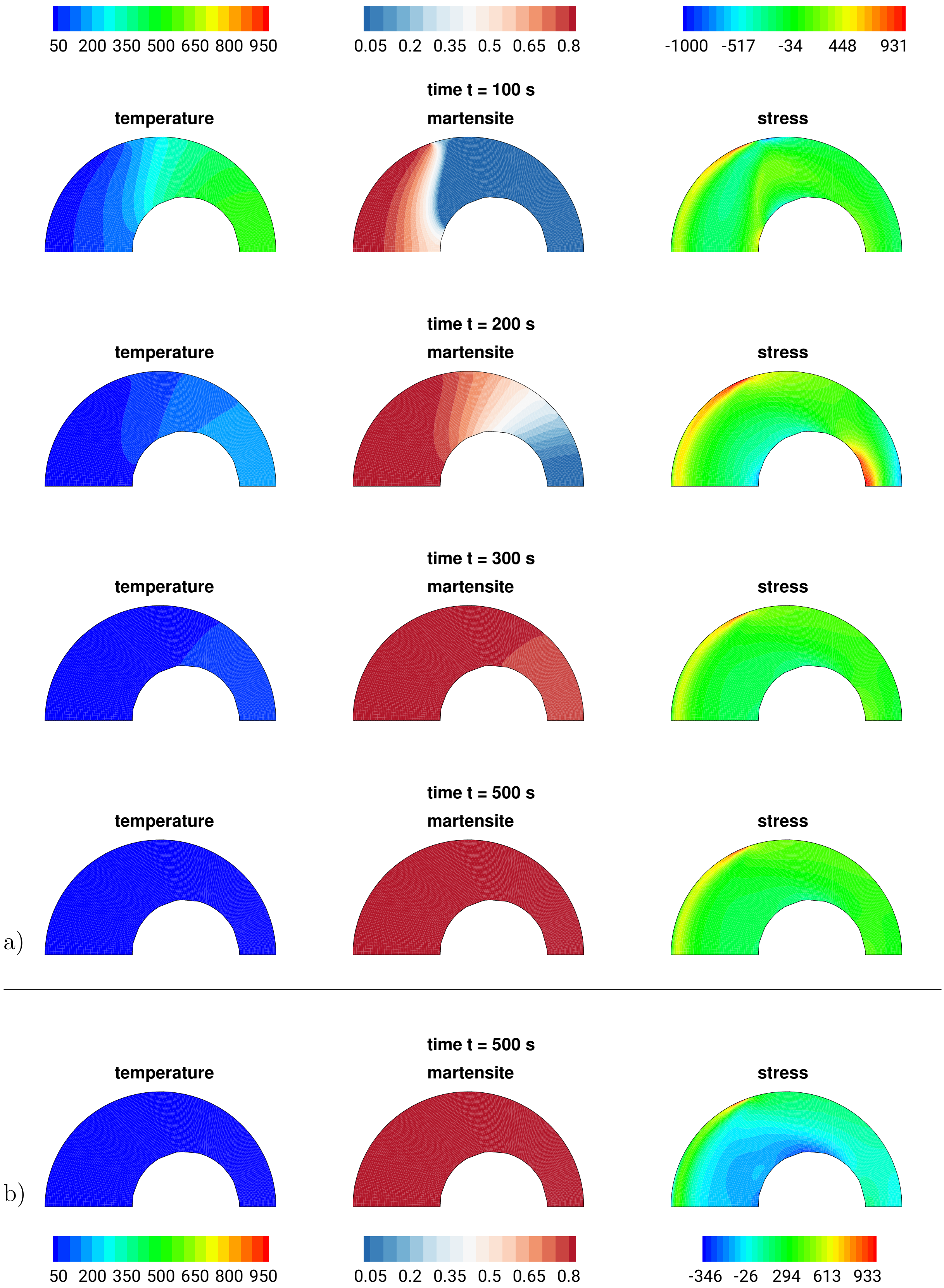

Figure 6.31: Spray cooling - Evolution of temperature θ in °C, martensitic volume fraction c^{M} and tangential stresses σ_{tang} in MPa during a) $t = 100\,\mathrm{s}$, b) $t = 200\,\mathrm{s}$ and c) $t = 300\,\mathrm{s}$ at the end d) $t = 500\,\mathrm{s}$ of the phase transformation, with e) adapted scaling of the color legend for the final stress state.

6.2.7 Surface elements for cooling in water

In the previous numerical analysis of cooling a cylindrical slice with eccentricity, a Dirichlet boundary condition has been utilized in order to apply the time-temperature relation of the specific cooling route on the surface. Instead of doing so, surface elements can be defined on the lateral surface, i.e., the cooled surface, to describe the heat flux over the boundary. Required input are the ambient temperature and the heat transfer coefficient (HTC) to the surrounding medium, water or air, which is highly dependent on the temperature. For the realization of the spray cooling, the HTC is characterized experimentally as described in Section 6.2.1. Exemplary, for the considered material 100Cr6, the HTC for water at approximately 20 °C is presented in Figure 6.32. In Appendix E, more information regarding the HTCs for the surrounding medium air or for application of a spray cooling are given.

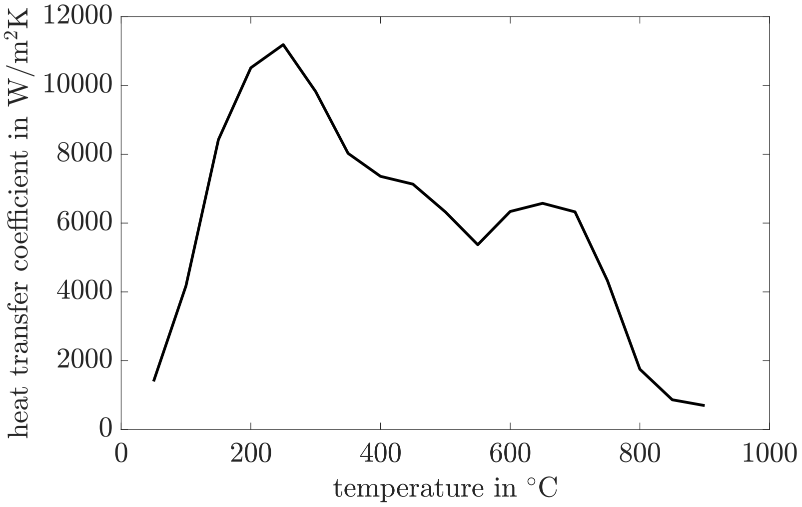

Figure 6.32: Heat transfer coefficient for cooling in water in W/m^{2}K, cf. BEHRENS ET AL. [17].

With this at hand, the numerical simulation of the boundary value problem defined in Figure 6.9a with surface element, i.e., Robin boundary conditions, instead of thermal Dirichlet boundary condition on the blue marked boundary $\partial \mathcal{B}_\theta$ is carried out. For simplicity, the different approaches are named “Dirichlet bc“[2.)], “Robin bcänd “IFUMïn the following, of which the latter are simulations carried out at IFUM using simufact.forming. In Figure 6.33, the stress evolution in the previously defined points P1 and P2 is depicted over cooling time for all three cases. Since the deviations in comparison to the “Robin bcßimulation are qualitatively different for both points, at first the focus lies on points P1.

In the beginning of the cooling up to $t =$ 5s, there is nearly no difference between the three simulations. Afterwards, the temperature drops faster for approaches “IFUMänd thus also “Dirichlet bccompared to the “Robin bcänalysis, see Figure 6.33a. Thus, the martensitic phase transformation is also switched on earlier for these two cases, cf. Figure 6.33b. As a consequence, the tensile stress peak due to the thermal contraction as well as the compressive stresses due to the volumetric expansion of the atomic lattice during the phase

---

[2.)] bc = boundary condition

transformation appear with a little offset for the “Robin bcäpproach, see Figure 6.33c. Furthermore, the compressive stresses around $t = 20\,\mathrm{s}$ are less in magnitude compared to the “Dirichlet bcßimulation and thus, the final stress value is higher and therewith closer to “IFUMßimulations as well as experimental measurements.

For point P2, all three simulations show nearly the same temperature evolution and hence only small deviations for the evolution of the martensitic phase fraction, see Figure 6.33b and d. Thus, the stress evolutions for “Dirichlet bcänd “Robin bcäre in very good accordance until the phase transformation in the bulk material is set on. Thereby, the “Robin bcßimulation results in much higher tensile stress values around $t = 20\,\mathrm{s}$, which are only slightly weakened until the end of the computation. Thus, the final stress value exceeds the two reference simulations as well as the experimental measurements clearly.

As shown by e.g. Medina-Juárez et al. [116], many numerical investigations overestimate tensile stresses and underestimate compressive stresses although the chosen HTCs fit experimental measurements quite well. The differences in the previously described results considering HTCs (“Robin bcänd “IFUM“) or Dirichlet boundary conditions (“Dirichlet bc“) to define the heat loss at the boundary are quite obvious. While the final results are close, the evolution over cooling time differs significantly. The red curve is at all times exceeded by the simulations using the proposed material model, either for boundary elements or thermal Dirichlet boundary conditions. The deviation in the temperature evolution for all three approaches, although small, leads to an error assimilation, first in the actual phase fractions and thereby also in the stresses.

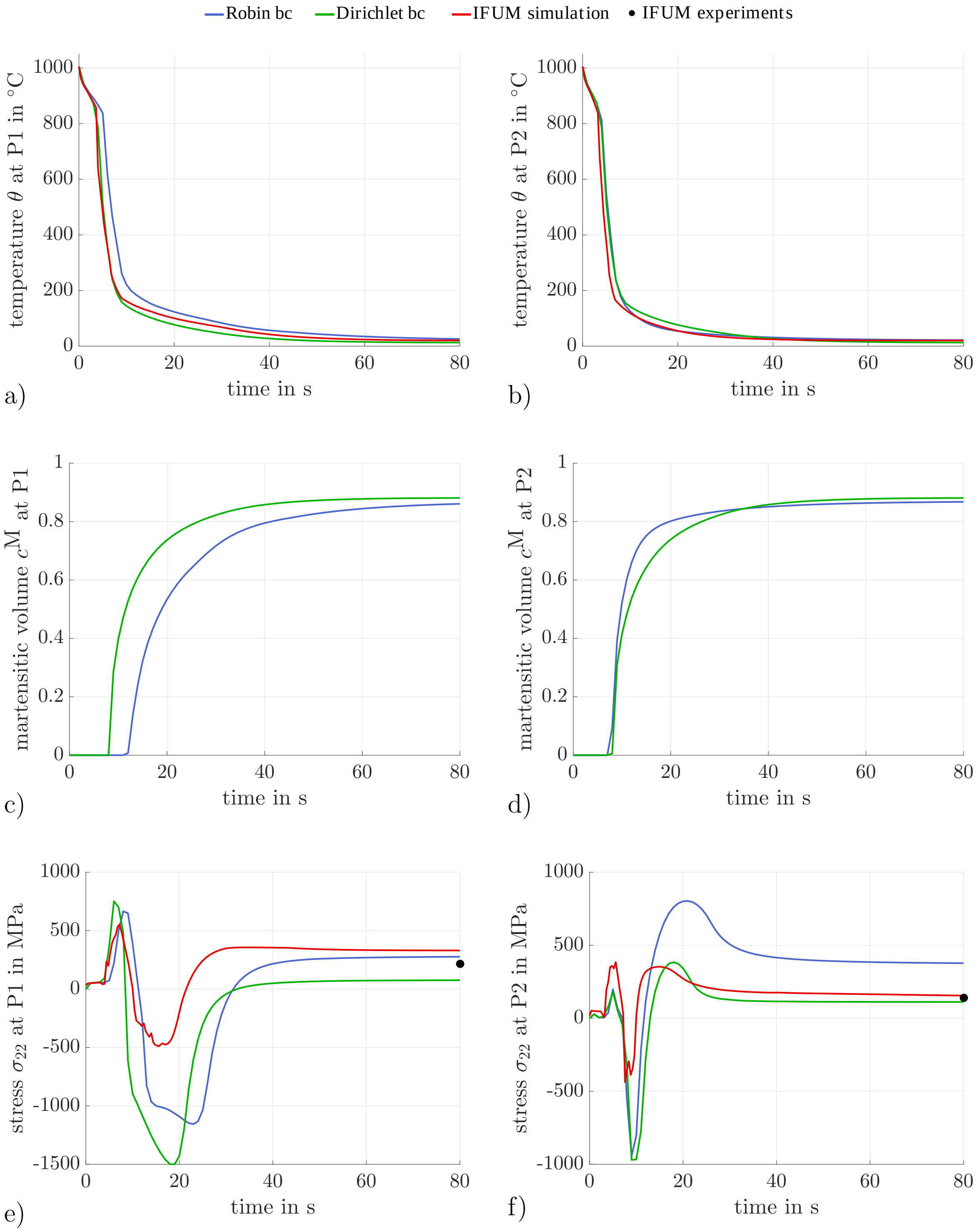

Figure 6.33: Water cooling - Results of simulation with Robin type boundary conditions (bc): temperature θ in °C in a) P1 and b) P2, martensitic phase c^{M} in c) P1 and d) P2, stress σ_{22} in MPa in e) P1 and f) P2 in comparison to the simulations carried out at IFUM, cf. Behrens et al. [17], and simulations with Dirichlet boundary conditions, see Section 6.2.4, as well as experimental measurements in the final state.

Similar findings hold for the application of surface element to depict the cooling by air or the application of a spray cooling device. Figure 6.34 displays the evolution of the temperature θ, the pearlitic volume fraction c^{P} and the stress component σ_{22} for the investigated points P1 and P2 for cooling by air. The simulations carried out utilizing surface elements are compared to previous computations, in which the temperature evolution on the lateral surface was defined as a Dirichlet boundary condition, and simulative analysis performed at IFUM. Moreover, the final values of experimental stress measurement are provided. Analogously to the cooling in water, one observes, surface elements to describe the heat flux over the boundary ("Robin bc") lead to a slower cooling of the component. Thereby, an offset in the evolution of the product phase is obtained. In both investigated points P1 and P2, the final stress values are quite higher than for the other two simulative examinations, namely the simulations carried out at IFUM ("IFUM") and the analysis with thermal Dirichlet boundary conditions ("Dirichlet bc").

In Figure 6.35, the different approaches ("Dirichlet bc", "Robin bcänd "IFUM") are compared for the spray cooling regarding the temperature θ, the martensitic volume fraction c^{M} and the stress component σ_{22}. Here, the deviations are quite pronounced. It seems that with the utilization of surface elements, the stresses are quite overestimated, supporting the thesis in Medina-Juárez et al. [116]. Even before the onset of the phase transformation, the tensile stress peak due to the thermal contraction of the specimen is higher than in the boundary value problem computed beforehand ("Dirichlet bc"). As a consequence, the compressive stress peak, when the phase transformation starts, is less in magnitude. When the bulk material transforms from austenite to martensite, the tangential stress shows high compressive stresses in point P1, which are not resolved until the end of the cooling process. On the thin side, to the right of the eccentricity, a qualitatively good agreement is shown for all three investigated quantities, θ, c^{M} and σ_{22}. However, the temperature flow through the slice is much slower when surface elements are used, see Figure 6.35a. As a result, the phase transformation starts later, around 340 seconds. Thus, the compressive stresses at P2 are lower and also offset. In the final state, however, there is again good agreement between all three simulations quantitatively.

The results of all three cooling routes show that surface elements can depict the evolution of the tangential stress in the specimen qualitatively but not quantitatively. In all three cases, an offset in the temperature evolution on the boundary is found, which influences the phase transformation and thereby also the stresses. Nevertheless, the application of surface elements possesses certain advantages. The HTC depend on the material and the cooling medium and have to be fitted by experimental measurements. After accomplishing this task, surface elements provide a good tool to describe the temperature evolution over the boundary quite more natural than it is done by Dirichlet boundary conditions. For example, in the case of water or air cooling, only one temperature evolution is given for the outer lateral surface and one for the inner lateral surface, while in the case of a spray, the lateral surfaces are divided into sections with the same boundary condition. Using surface elements, each boundary node in the finite element mesh can have a different temperature evolution than its neighboring nodes. This is particularly advantageous for larger geometries with complex boundary surfaces or for three-dimensional problems.

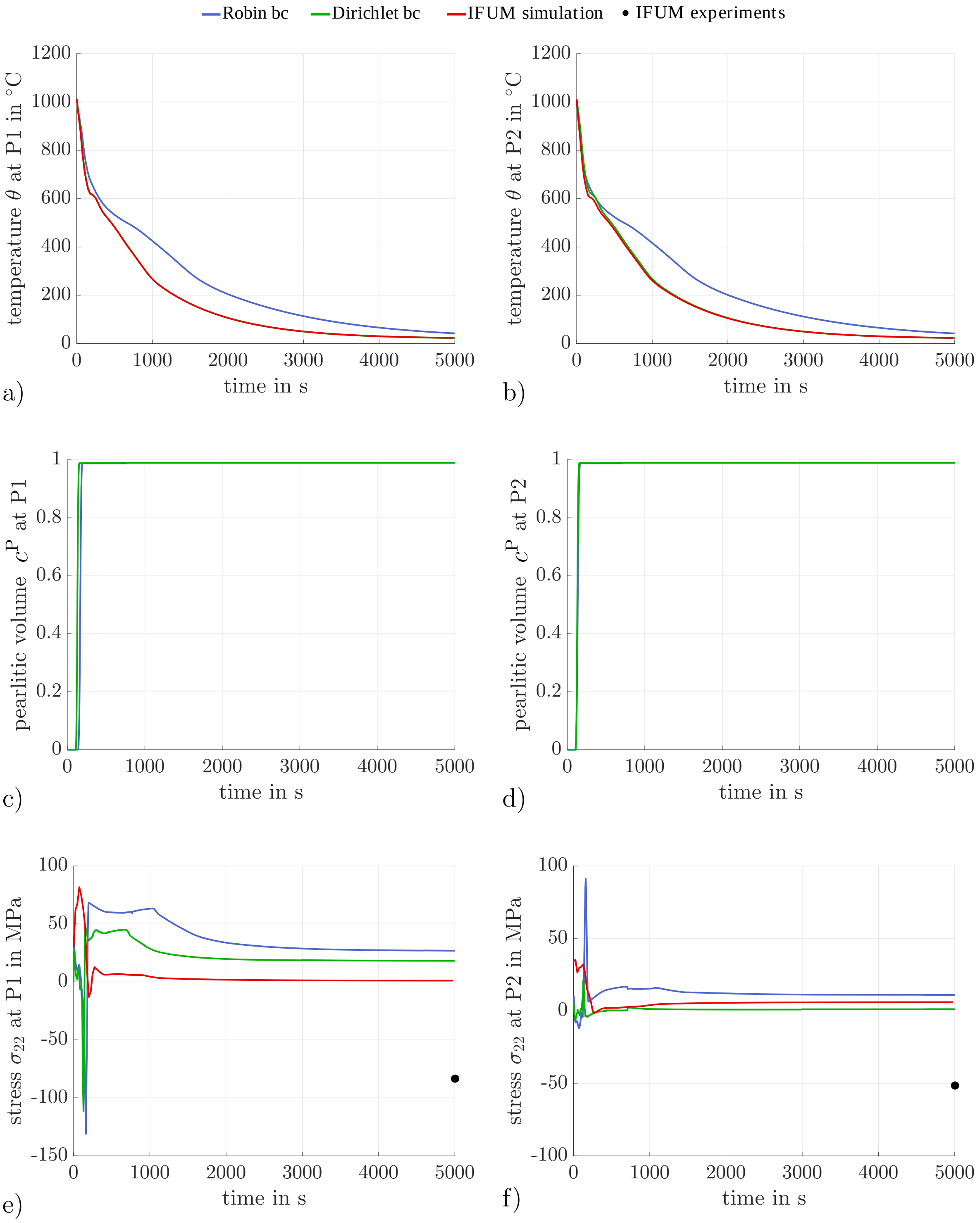

Figure 6.34: Air cooling - Results of simulation with Robin type boundary conditions (bc): temperature θ in °C in a) P1 and b) P2, pearlitic phase c^{P} in c) P1 and d) P2, stress σ_{22} in MPa in e) P1 and f) P2 in comparison to the simulations carried out at IFUM, cf. Behrens et al. [17], and simulations with Dirichlet boundary conditions, see Section 6.2.5, as well as experimental measurements in the final state. figs pearlitic

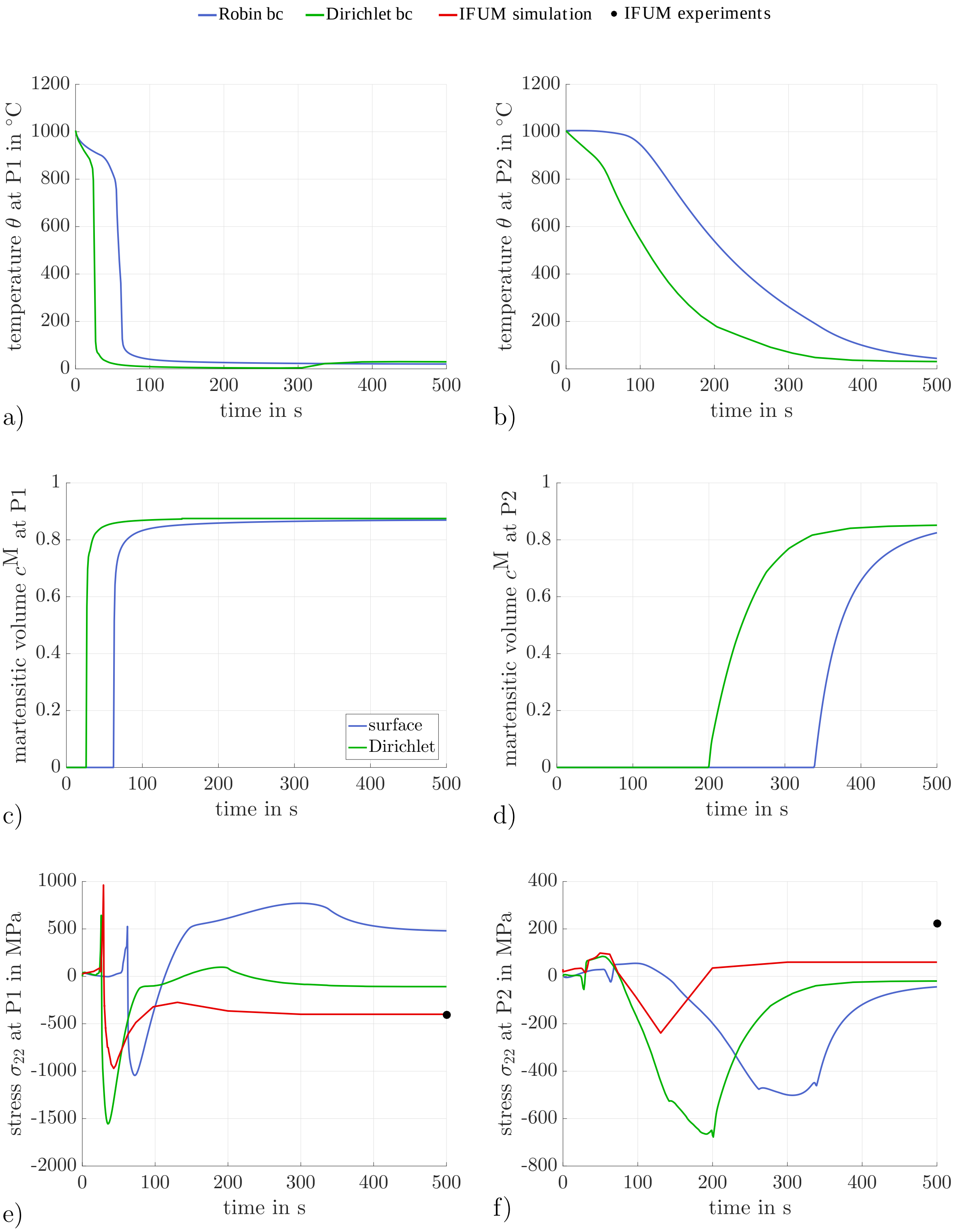

Figure 6.35: Spray cooling - Results of simulation with Robin type boundary conditions (bc): temperature θ in °C in a) P1 and b) P2, martensitic phase c^{M} in c) P1 and d) P2, stress σ_{22} in MPa in e) P1 and f) P2 in comparison to the simulations carried out at IFUM, cf. Behrens et al. [17], and simulations with Dirichlet boundary conditions, see Section 6.2.6, as well as experimental measurements in the final state.

6.3 Phase-specific contributions and the influence of TRIP strains

Many materials show microscopically heterogeneities or consist generally of different constituents, such as composite materials. These constituents, such as the phases austenite and martensite, for instance, differ significantly with respect to their properties. Each constituent possesses individual properties and contributes to the overall behavior, cf. Section 5.3. Martensite has a much higher yield strength than austenite, for instance. This motivates to investigate phase-specific stresses in austenite and martensite during the diffusionless cooling in water. Therefore, a cylindrical slice is cut from the undeformed cylindrical specimen, that is defined in Figure 6.6a. Its dimensions, displacement and thermal Dirichlet boundary conditions are defined in Figure 6.36.

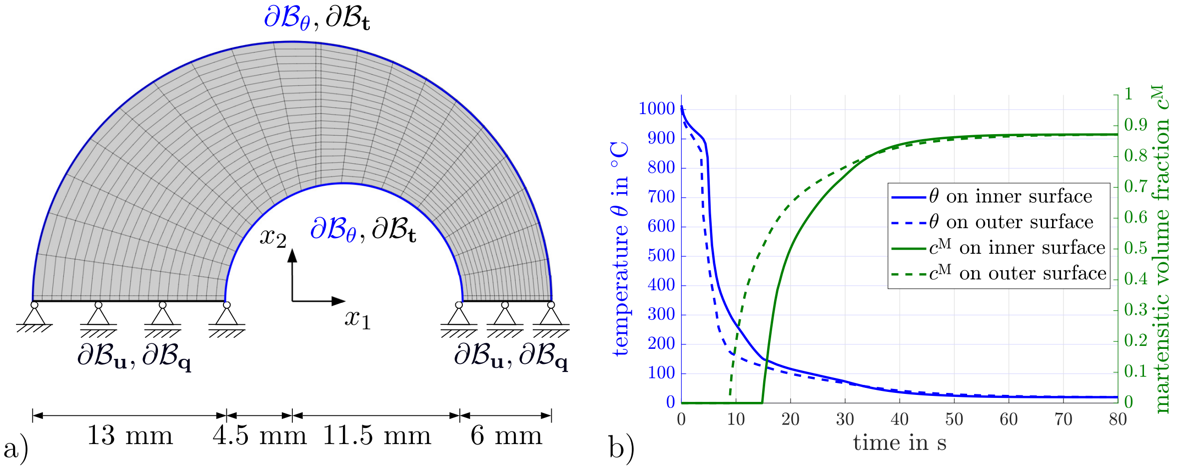

Figure 6.36: a) Geometry of the two-dimensional horizontal cross section of the undeformed cylindrical specimen with boundary definitions for finite element simulation. b) Temperature θ of outer and inner lateral surface of the cylinder over cooling time t, adapted from Uebing et al. [189].

The material model is based on the SAMP approach utilizing the additive split into the five strain parts, namely elastic, plastic, thermal, transformation volumetric and TRIP strains, see Table 5.5. One important difference is that the volumetric expansion of the atomic lattice has been taken into account as $K^\mathrm{M}_\mathrm{tv} = 2\%$. Another difference is that instead of the two-step linear interpolation scheme to determine the yield strength y and the linear hardening parameter h, a one-step linear interpolation scheme is applied to compute the material parameters y, Q_0, δ and h, which all contribute to the actual temperature dependent yield strength. Therefore the yield criterion is defined as

$$\phi = \sqrt{\frac{3}{2}} \| \operatorname{dev} \boldsymbol{\sigma} \| - h\alpha - Q_0(1 - \exp(-\delta\alpha)) - y \tag{6.3}$$

with the exponential hardening parameter δ and the material parameter Q_0, cf. Simo and Hughes [166], Mahnken et al. [110] and Uebing et al. [189]. The required parameters are fitted to phase-specific isothermal yield functions, provided by IFUM, LU Hannover, see Figure 5.4. The resulting stress distributions are compared to multi-scale investigations, that are in detail studied in Section 10.2 and in Uebing et al. [192]. Tangential stresses are in focus of the analysis, since they are known to be most relevant with respect to wear resistance or lifetime of the component.

Figure 6.37 shows the distribution of the temperature, the total tangential stresses and the phase-specific tangential stresses of austenite and martensite computed with the single-scale approach and a multi-scale method at certain points in time, i.e., with the beginning $t = 9\,\text{s}$, in the middle $t = 15\,\text{s}$ and at the end $t = 80\,\text{s}$ of the phase transformation.

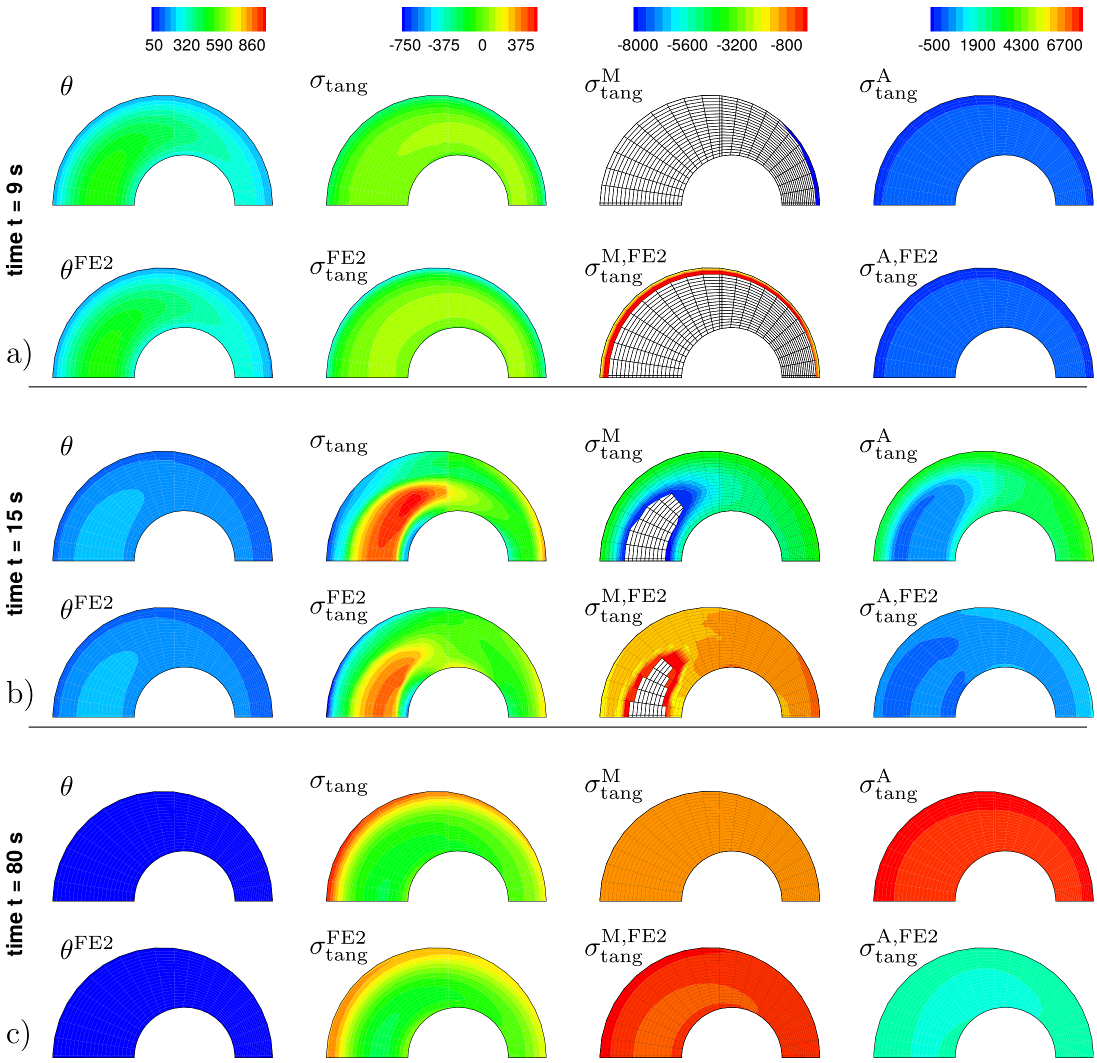

Figure 6.37: Temperature distribution θ and tangential stress distribution σ_{tang} and phase-specific tangential stresses in martensite and austenite for both computational approaches, $\sigma^{\text{M}}_{\text{tang}}$, $\sigma^{\text{A}}_{\text{tang}}$, in MPa after a) $t = 9\,\text{s}$, b) $t = 15\,\text{s}$ and c) $t = 80\,\text{s}$, adapted from Uebing et al. [189].

Regions, in which the temperature is higher than the martensitic start temperature, are blanked in the plot of the martensitic tangential stress $\sigma^{\text{M}}_{\text{tang}}$. Qualitatively, the single- and the multi-scale approach are in very good accordance. The temperature distributions θ and θ^{FE2} as well as the total tangential stresses σ_{tang} and $\sigma^{\text{FE2}}_{\text{tang}}$ coincide. First, the fast cooling results in tensile tangential stresses in regions near the outer lateral surface. There, the phase transformation occurs after $t = 9\,\text{s}$, so that these tensile stresses are superimposed with high compressive stresses due to the austenite-to-martensite phase transformation, see Figure 6.37a. With ongoing cooling, tensile stresses arise inside the bulk material of the thick side of the eccentricity to fulfill the equilibrium condition of residual stresses, see Figure 6.37b. If the phase transformation also starts in the bulk material, compressive tangential stresses are observed, which lead to tensile stresses in regions near the outer lateral surface in the final state, cf. Figure 6.37c.

In contrast to that, the phase-specific stress contributions show very different results for the single-scale and the multi-scale analysis. Taking a closer look at the evolution of the martensitic tangential stresses $\sigma^{\mathrm{M}}_{\mathrm{tang}}$ compared to $\sigma^{\mathrm{M,FE2}}_{\mathrm{tang}}$ compressive stresses arise in the material with the onset of phase transformation. After $t = 9\,\mathrm{s}$, the only region that undergoes phase transformation in the single-scale computation is on the outer lateral surface on the thin side. Here, values of $\sigma^{\mathrm{M}}_{\mathrm{tang}} \approx -8000\,\mathrm{MPa}$ are found, which are multiple times higher than the value of $\sigma^{\mathrm{M,FE2}}_{\mathrm{tang}} \approx -1200\,\mathrm{MPa}$. Moreover, it is found that the phase transformation in the multi-scale approach takes already place along the complete outer lateral surface. With ongoing cooling and related increase of the martensitic volume fraction, it is observed that the single-scale approach still computes much higher values for $\sigma^{\mathrm{M}}_{\mathrm{tang}}$ than the multi-scale model. In a final state, both computations result in nearly homogeneous values, but the single-scale computation still results in higher compressive stress values in martensite. Considering the austenitic phase-specific tangential stresses $\sigma^{\mathrm{A}}_{\mathrm{tang}}$ vs. $\sigma^{\mathrm{A,FE2}}_{\mathrm{tang}}$, compressive stresses are observed as a consequence of the thermal expansion. These fit quite well comparing the single-scale and the multi-scale approach. As more and more martensite forms, tensile stresses arise in the austenitic phase. In a final state, the distributions of $\sigma^{\mathrm{A}}_{\mathrm{tang}}$ and $\sigma^{\mathrm{A,FE2}}_{\mathrm{tang}}$ are nearly homogeneous. But analogously to the findings for $\sigma^{\mathrm{M}}_{\mathrm{tang}}$ and $\sigma^{\mathrm{M,FE2}}_{\mathrm{tang}}$, respectively, the single-scale approach shows much higher stresses than the multi-scale analysis. It is concluded that the single-scale approach does not lead to physical phase-specific stresses, since the values of $\sigma^{\mathrm{A}}_{\mathrm{tang}}$ and $\sigma^{\mathrm{M}}_{\mathrm{tang}}$ seem to be strongly overestimated compared to the yield stresses in Figure 5.4. This motivates to carry out further multi-scale analysis to investigate phase-specific stress contributions, cf. Section 10.

Additionally to the phase-specific analysis, the influence of the TRIP has been studied in Uebing et al. [189]. Therefore, the material parameter K_{trip} has been set to zero for the martensitic phase. Thereby, the decisive influence of the TRIP strains during austenite-to-martensite phase transformation with respect to the resulting (residual) stresses is shown, see Figure 6.38. In the middle of phase transformation, after $t = 12\,\mathrm{s}$, the computation without TRIP shows much higher stresses than the computations with TRIP than the multi-scale computation. Further analysis must consider a two-scale model including the TRIP effect to evaluate these differences.

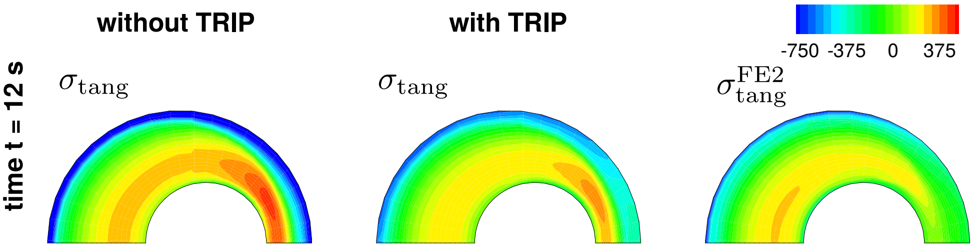

Figure 6.38: Tangential stress distribution σ_{tang} computed with the SAMP model with and without TRIP effects and tangential stresses computed with the two-scale approach, $\sigma^{\mathrm{FE2}}_{\mathrm{tang}}$ in MPa after $t = 12\,\mathrm{s}$, adapted from Uebing et al. [189].

7 Three-dimensional single-scale analysis of a thermo-mechanically coupled problem

The previous two-dimensional example of cooling a cylindrical specimen with eccentric hole could clearly suffer regarding accuracy due to the restriction to 2D, see Section 6.2. Although, the prescribed thermal Dirichlet boundary conditions applied on the lateral surface resemble the cooling over the boundary quite well, they do not take into account the cooling and heat flux, respectively, over the height of the component. Therefore, a three-dimensional extension of the boundary value problem should be analyzed to gain knowledge of the possible error by reduction to the two-dimensional case. For this purpose, at first the two-dimensional slice taken from the deformed cylindrical specimen as discussed in Section 6.2.2 is extended to 3D. Afterwards, an extruded three-dimensional cylindrical specimen is object to examination.

7.1 Cylindrical slice

For the first three-dimensional boundary value problem, the two-dimensional geometry is extruded to a height of 1 mm as shown in Figure 7.2a. In addition to the previously defined boundary conditions for static bearing, symmetry exploitation and cooling of the lateral surface, the bottom of the slice is fixed in third direction, i.e., $u_3 = 0$. In order to obtain comparable results to the two-dimensional case, the following analysis also evaluates the stress evolution in measuring points P1 and P2, as marked in Figures 7.2b and c.

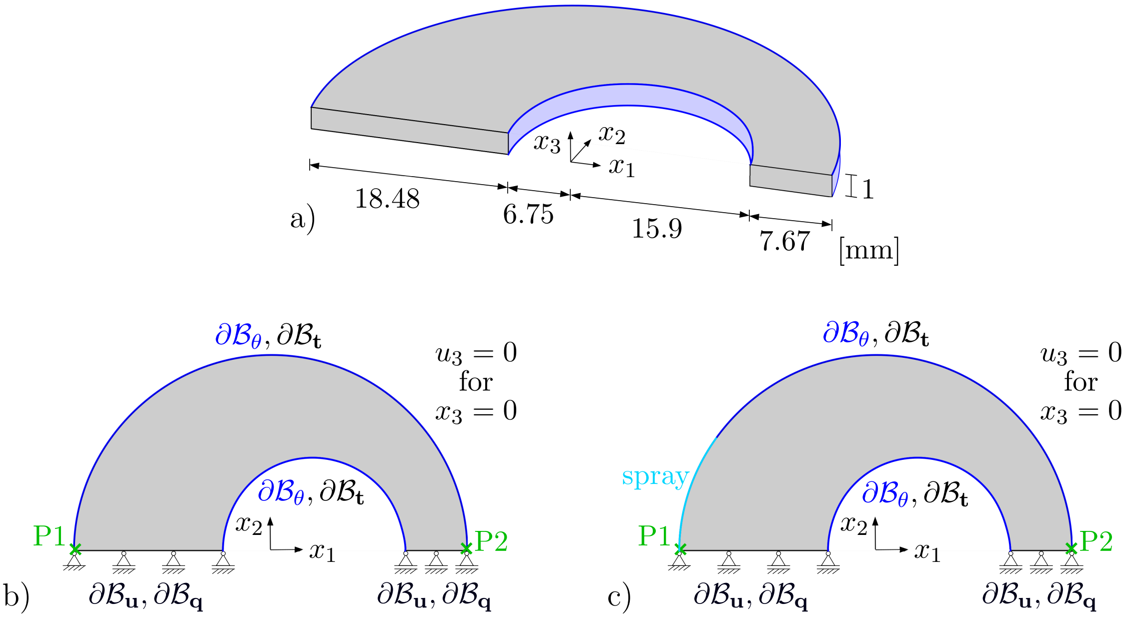

Figure 7.1: a) Geometry with dimensions and boundary conditions for cooling b) in water c) or with a spray.

Three-dimensional simulations of both cooling routes, namely in water or using a spray cooling device, confirm the previous findings of the two-dimensional analysis, compare Figures 7.2 and 7.3 with Figures 6.21 and 6.29. Looking closely at the tangential stress evolution in point P1 in case of spray cooling, the results seem to be more reasonable. Around 200 seconds of cooling time, the bulk material undergoes the phase transformation and the related volumetric expansion of the atomic lattice weakens the high compressive stresses in regions near the outer surface. In the two-dimensional analysis, even tensile stresses occurred. In contrast to that, the three-dimensional simulation is qualitatively equivalent, but the stresses remain compressive. Thereby, it can be clearly shown that the influence of the third direction during such cooling simulations is not negligible. Additionally, Figure 7.4 shows the stress component σ_{22} for the complete cylindrical slice after $t = 75\,\mathrm{s}$ and at the end of the process for $t = 500\,\mathrm{s}$. It is observed that the phase transformation passes through the geometry from the left to the right side. Thus, after $t = 75\,\mathrm{s}$, compressive stresses are present at the side, which is exposed to the spray. In the final state, these compressive stresses are weakened but still measurable.

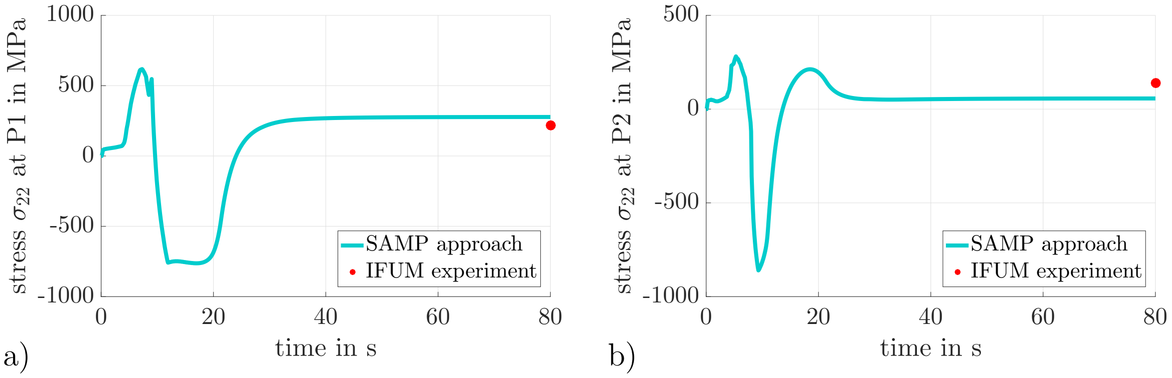

Figure 7.2: Water cooling - Tangential stress evolution σ_{22} in MPa over cooling time in measuring points a) P1 and b) P2 as marked in Figure 7.1b. The experimental measurements carried out at IFUM are presented in Behrens et al. [17].

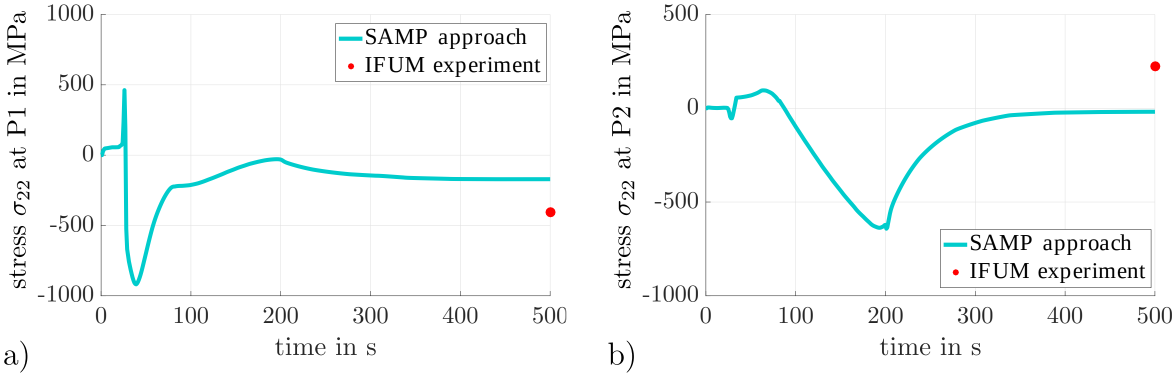

Figure 7.3: Spray - Tangential stress evolution σ_{22} in MPa over cooling time in measuring points a) P1 and b) P2 as marked in Figure 7.1c. The experimental measurements carried out at IFUM are presented in Behrens et al. [17] and Behrens et al. [18].

7.2 Full three-dimensional cylindrical specimen

As observed, the third direction is not negligible in analysis of hot bulk forming parts. Thus, the following analysis focuses on the influence of the heat flux over the component's height. Therefore, an extrusion of the previously considered geometry is taken into account with a height of 10 mm. It is to be noticed that the meshing is very coarse (10 × 20 × 10 elements) contradicting the mesh density study in Section 6.2.3 and hence, does not

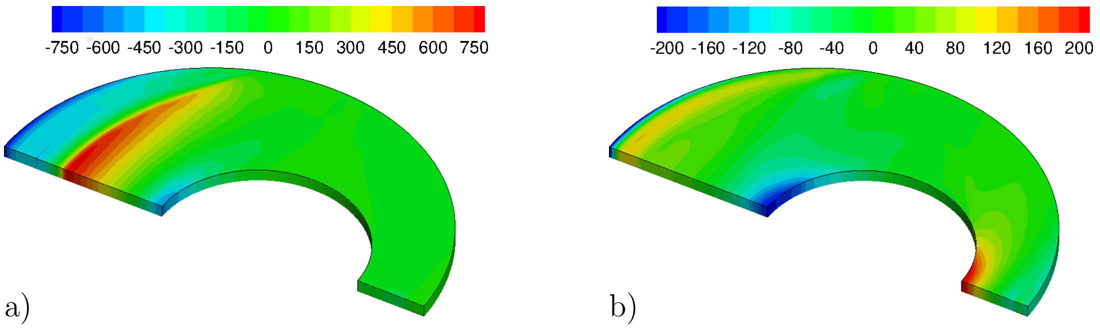

Figure 7.4: Spray cooling - Stresses σ_{22} in MPa after a) $t = 75\,\mathrm{s}$ and b) at the end of cooling after $t = 500\,\mathrm{s}$.

present the exact solution probably. An analogous study would be inevitable in case of detailed investigations of the material behavior, the evolving stresses and the associated change of the final component's properties. Furthermore, a component, that has been treated in hot bulk forming, i.e., here a reduction of height by approximately 50 %, should show bulging, which is also not considered. Moreover, no offset describing the plastification due to forming is taken into account. As thermal boundary condition representing the cooling in water, the same time-temperature relation for all nodes on the lateral surface is applied. Both assumptions serve as simplifications. Usually, one would expect that the inner lateral surface cools slower than the outer one, cf. Figure 6.20.

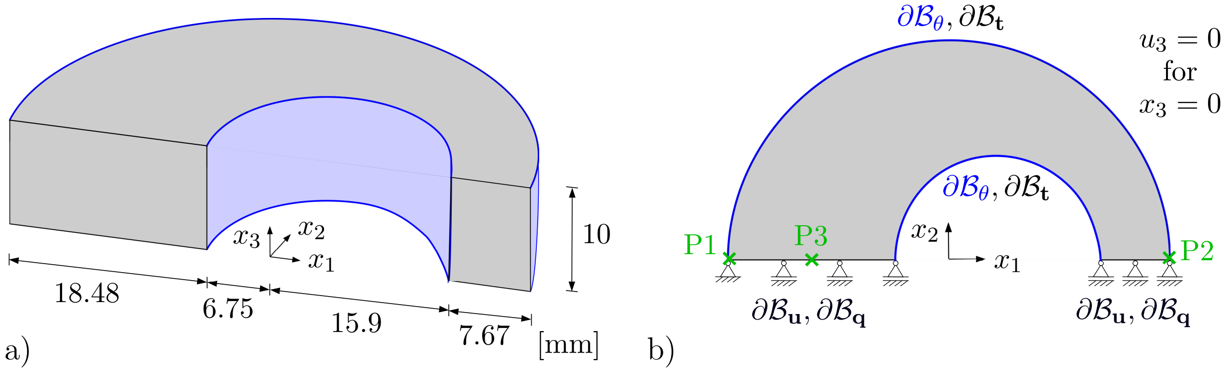

Figure 7.5: a) Extruded geometry with dimensions and b) boundary conditions for cooling in water utilized to represent the influence of the third dimension. Points P1, P2 and P3 are in focus of the investigation.

In Figure 7.6, the tangential stresses at times $t = 15\,\mathrm{s}$ and $t = 80\,\mathrm{s}$ are given. One can clearly see that the stresses are not constant with respect to their position in x_3-direction. This effect in connection to the real bulged geometry due to the previous forming step would even lead to more complex material behavior and stress profiles. Thus, it is inevitable to incorporate the effect of the third dimension into numerical tools to predict residual stresses and the component's behavior.

Additionally, different integration points are analyzed regarding their stress evolution over time. Therefore, three points are defined each, with x_1- and x_2-coordinate of points P1 and P2, but with different heights. The points are referred to as P1$_k$ and P2$_k$ with $k \in \{t, m, b\}$ with t and b referring to top and bottom of the component, respectively, and m abbreviating the middle height. Moreover, point P3 is located in the middle of the part of the geometry left of the eccentricity, see Figure 7.5a. For comparing the results over the component's height, points $P3_k$ with $k \in \{t, m, b\}$ are defined as previously described. The results regarding stress component σ_{22} are given in Figure 7.7. Since all examined points fulfill $x_2 = 0$, these stresses can be interpreted as tangential stresses. While the stress evolution at bottom and middle nodes are very similar for points P1 and P2, the stresses evolving in top points vary clearly. For instance, the curve of $P2_t$ fits qualitatively to $P2_b$ and $P2_m$ but differs quantitatively, such that in the final state an offset of approximately 150 MPa is observed. The stress evolution of $P1_t$ does not even behave in accordance to $P1_b$ and $P1_m$, its curve shows differences in quality and quantity. In point P3, top and middle nodes $P3_t$ and $P3_m$ show similarities, while curve $P3_b$ shows an offset of roughly 50 MPa.

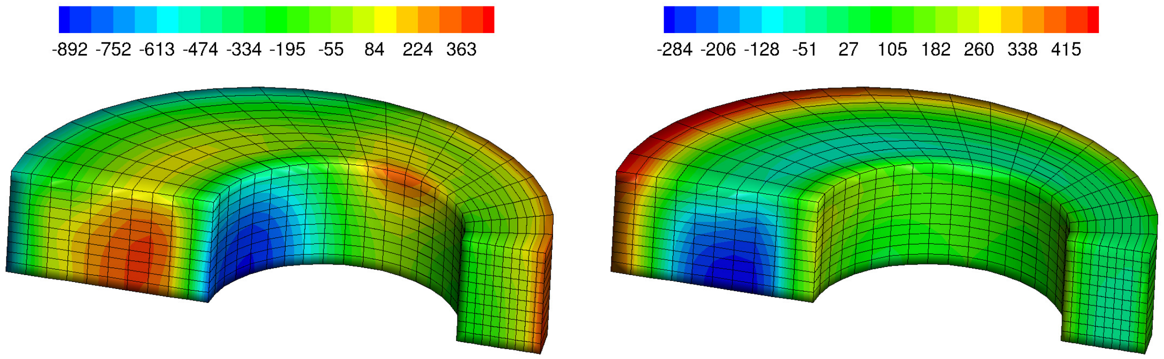

a) b)

Figure 7.6: Water cooling - Tangential stress distribution in MPa after a) $t = 15\,\mathrm{s}$ and b) $t = 80\,\mathrm{s}$ for the extruded three dimensional cylindrical component, which shows none constant stress values in third direction (height).

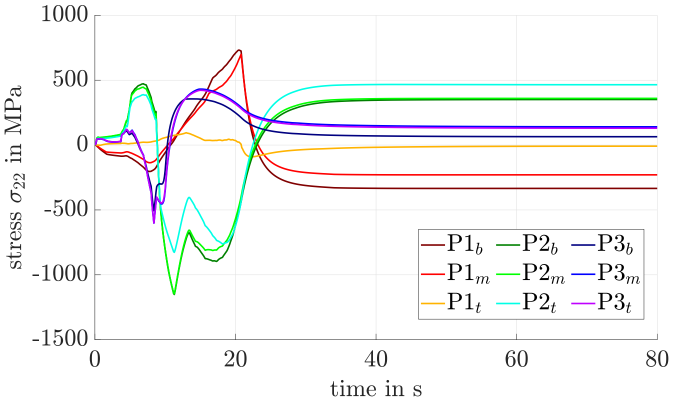

Figure 7.7: Water cooling - Evolution of stresses σ_{22} in MPa in Gauss points located at $P1_k$, $P2_k$ and $P3_k$ with $k \in \{t, m, b\}$.

8 Two-scale Finite Element Method: the FE^2 approach

In recent decades, the requirements for components and their materials have continued to increase. Materials such as conventional steel or aluminum do not meet the demands of industry anymore. Instead, artificial materials, complex alloy compositions as found in high-strength steels, composite materials or in general multiphase materials are to be considered. Current research focuses on different aspects to meet the various demands made by industry, as for example: sustainable materials to reduce waste; smart materials with the ability of self-healing or shape memory; nanomaterials to increase the component's strength e.g. in energy or mobility sectors; additive manufactured materials e.g. by 3D-printing to create new polymer filaments; or in general lightweighting materials applied e.g. in aerospace industry. One example of these materials are dual-phase steels, which are commonly used in the automotive industry. They are characterized by high ductility and stability at the same time. In those materials, the microscopic composition and its heterogeneous properties play an important role, because every constituent has an impact on the final material properties. In order to meet the increasing requirements of industrial applications, numerical simulation techniques are a valuable tool. With these, the material properties as well as the component's performance under complex load conditions can be tested efficiently. Due to the heterogeneity of the material's microstructure, it is useful to take into account its individual constituents in the model, for which purpose current research focuses on multi-scale simulation techniques.

Such a numerical simulation tool is the FE^2 method, which is also referred to as the direct micro-macro transition approach. Therein, a part of the microstructure, which is sufficiently large to reflect all microstrutural characteristics, is attached to each macroscopic material point. By application of suitable mathematical homogenization procedures, it is bridged between the scales. Thus, microscopic phenomena such as phase transformation or residual stresses of second and third type can be explicitly captured, while their influence on the macroscopic properties is determined as well. Fundamental works in the field of homogenization and multi-scale FE^2 method are e.g. SMIT [171], SUQUET [175], MOULINEC AND SUQUET [127], SMIT ET AL. [170], MIEHE ET AL. [121; 122], FEYEL [44], MICHEL ET AL. [118], TERADA ET AL. [182], FEYEL AND CHABOCHE [45], GEERS ET AL. [57] and SCHRÖDER [161; 162].

In case of thermo-mechanical coupled problems, it is infeasible to characterize the thermo-mechanical behavior of the considered material. Most materials show microscopic heterogeneities or consist generally of different phases, which must be taken into account individually. Each of these constituents contributes to the overall component's properties. Therefore, early works regard the mathematical homogenization of thermal properties of composite materials, see e.g. GERMAIN ET AL. [59] or ENE [35]. Asymptotic expansion methods are utilized to derive the macroscopic and microscopic equations by CHATZIGEORGIOUA ET AL. [26] in the regime of small strains, while in TEMIZER [178], the author proposed the asymptotic expansion for the first-order computational homogenization method, that was presented in TEMIZER AND WRIGGERS [179] for finite thermo-elasticity. One important result of the asymptotic expansion is that the macroscopic temperature can be taken as constant in the material point. Thus, the microscopic balance of linear momentum does not depend on the microscopic temperature fluctuations. This finding coincides with early results of WILLIS [200] that a isothermal microscopic problem is not an assumption but a direct consequence of the first-order homogenization. More recent works in the context of thermo-mechanically coupled multi-scale simulations are presented e.g. in Özdemir et al. [138; 139], where a nested solution algorithm for heat conduction problems was given and extended to the full thermo-mechanical coupling of heterogeneous materials. Barrogqueiro et al. [9] gave a summary on the theory and the application of multi-scale approaches for heat treatment in steels. Moreover, in Eden and Muntean [34] also the phase transformation is taken into account. Wicht et al. [199] applied a Fast Fourier transformation to solve for a fully coupled thermo-mechanical problem on two scales. Further recent publications on thermo-mechanically coupled multi-scale approaches and their applications are Monteiro et al. [125], Terada et al. [183], Fleischhauer et al. [53; 54], Sengupta et al. [164; 165] and Berthelsen and Menzel [20], among many others.

In the following, the basic principles of the homogenization theory and the definition of representative volume elements are introduced. Afterwards, the direct micro-macro transition approach consisting of a macroscopic and a microscopic boundary value problem is described and its numerical implementation is discussed. Furthermore, a microstructural material model based on the model presented in Section 5.5.2 is adapted for a multi-scale formulation.

8.1 Basics on homogenization theory

In general, the previously described single-scale Finite Element Method, (FEM) see Section 3, cannot resolve the microstructural heterogeneities or individual constituents of a material. Thus, it motivates a consideration of multiple scales in the numerical investigation, of which two are taken into account in most multi-scale approaches. Those scales are distinguished as macro-, meso-, micro- and nanoscale. Therein, the macroscale represents the component or total system, at the mesoscale the material is distinguished into different phases such as e.g. matrix and inclusion, while the microscale refers to individual grains and the nanoscale to single atoms. It should be noted that there are in general different definitions of these scales in literature. In this work, it is referred to an upper scale, the macroscale, and a lower scale, the microscale, so that the macroscale refers to the component's size of a few centimeters and the microscale refers to the size of micrometers to represent the grains in the microstructure.

A suitable *homogenization* scheme relates these two scales, as macroscopic quantities are determined by averaging their microscopic counterparts. Early analytical homogenization schemes for microstructures with discrete phases were proposed in Voigt [193] and Reuss [145], which base on the assumption of a constant stress or strain field throughout the material, respectively. These mean field approaches compute macroscopic quantities based on the individual phase fractions and their respective microscopic counterparts as an arithmetic or harmonic mean. One fundamental method has been given by Eshelby [39; 40] to determine an averaged strain field for an ellipsoidal inclusion in an infinite matrix. Based thereon, many analytical and semi-analytical approaches have been developed, such as the Mori-Tanaka scheme, the self-consistent method, the dilute distribution approach and the differential method, see Hashin and Shtrikman [72; 73; 74], Hill [79], Budiansky [23], Mori and Tanaka [126], Norris [131] and Hashin [71]. These methods are restricted to simple geometries of the inclusion material and show inaccuracies, when the difference between the quantity of the individual phases, which is to be homogenized, is quite large. Then, asymptotic expansion or fully numerical homogenization schemes are utilized, see e.g. SANCHEZ-PALENCIA [150], GUEDES AND KIKUCHI [64], FISH AND WAGIMAN [52], GHOSH ET AL. [60], TERADA AND KIKUCHI [181], TEMIZER AND ZOHDI [180] or GEERS ET AL. [58]. In order to apply a first-order homogenization scheme, the concept of the *separation of scales* has to be satisfied. It states that the typical length of macroscale L and the typical length on microscale l have to be distinctly different, i.e., $l \ll L$. As a consequence of the scale separation, the deformation gradient is considered constant in one material point. Its variation in that point and its environment is small and thus the gradient of the deformation is negligible. Different fundamental assumptions are made for the computation of the overall macroscopic material behavior by homogenization depending on microscopic quantities, which are summarized in the following.

The *concept of an ensemble* is an approach to describe the macroscopic material behavior of a micro-heterogeneous material. For a collection $\mathcal{S}$ of samples α of random microstructure and probability density p of a sample it has to hold for the considered material response $\mathcal{F}$ that

$$\bar{\mathcal{F}}(\boldsymbol{x}) = \int_{\mathcal{S}} \mathcal{F}(\boldsymbol{x}, \alpha)\, p(\alpha)\, \mathrm{d}\alpha\,, \tag{8.1}$$

in which $\bar{\mathcal{F}}$ is called the ensemble average. If the number of samples $\alpha \in \mathcal{S}$ is sufficiently large, the ensemble average approximates the effective overall material response well.

By replacing the ensemble average by a simple volume average over a sample or RVE $\mathcal{B}$ with volume V one obtains

$$\langle \mathcal{F}(\boldsymbol{x}, \alpha) \rangle = \frac{1}{|V|} \int_V \mathcal{F}(\boldsymbol{x} + \boldsymbol{y}, \alpha)\, \mathrm{d}\boldsymbol{y}\,, \tag{8.2}$$

which does not depend on the sample α and equals the ensemble average for $|V| \to \infty$. Then, it is again fulfilled that the volume average $\langle \mathcal{F}(\boldsymbol{x}, \alpha) \rangle$ is a good approximation of the effective material response. This is summarized by the *ergodic hypothesis* which states that every state which is available to the ensemble, is available to each sample in the ensemble as well.

Further aspects are *statistical homogeneity*, which is fulfilled if the ensemble average of material response $\mathcal{F}$ is invariant with respect to translation, and *statistical isotropy*, which in addition requires the ensemble average to be not only independent of the position of the coordinate system but also independent of its rotation.

One further important aspect in the framework of multi-scale analysis for the computation of the overall macroscopic behavior is the concept of a *representative volume element* (RVE). Such an RVE enables the modeling of each microscopic constituent as an individual continuum. In case of a periodic microstructure, a unit-cell serves as RVE, but most microstructures in engineering materials are non-periodic. The term *representative volume element* has been established in the 1960's by Hill, who also gave a first definition. Throughout the years, different statements regarding an RVE and its properties have been made, see ZEMAN [209], for instance by

- HILL [**78**]: An RVE has to be large enough to represent the micro-heterogeneous structure. It contains a sufficient number of inclusions to ensure that the effective material response is independent of the surface values of traction and displacement.

- Hashin [**70**]: An RVE is used as a model to determine effective properties on the macroscopic level. It hast to be large enough to contain a sufficient amount of information regarding the microscale but must be smaller than the macroscopic dimensions.

- Drugan and Willis [**33**]: An RVE is the smallest microscopic volume element possible to represent the macroscopic material response adequately.

- Ostoja-Starzewski [**137**]: An RVE is a unit cell in case of periodic microstructures or a volume element with a high number of microscopic characteristics to fulfill statistical homogeneity and the ergodic hypothesis.

- Stroeven et al. [**174**]: The size of an RVE depends on the considered material as well as on the structure sensitivity of the measured physical quantity.

The definition used here is that an RVE has to be large enough to reflect all micro-heterogeneous properties and characteristics, but it has to be smaller than the macroscopic dimensions, i.e., $l \ll d \ll L$ with d as dimension of the RVE. Furthermore, it has to hold that every choice of microstructure with same dimensions has to provide the same overall material response to be considered as an RVE.

8.2 Direct micro-macro transition approach

In case of non-linear material behavior, semi-analytical homogenization schemes are not considered a well suited option to determine the macroscopic material behavior. Instead, the direct micro-macro transition approach serves as powerful tool, which distinguishes between a macroscopic and a microscopic boundary value problem. On macroscopic level, the complete component is taken into account while on microscopic level, the material inhomogeneities, as e.g. inclusions, cracks or phases, are considered, so that the concept of separation of scales is fulfilled. A sketch of the general idea of the two-scale approach is depicted in Figure 8.1.

The macroscopic boundary value problem is discretized in terms of the classical FEM, but a sufficient phenomenological law to describe the material behavior in each macroscopic integration point is no longer required. Instead, a microscopic boundary value problem is attached in each macroscopic integration point, which is solved in every computational step. This means that it is no longer necessary to find a suitable macroscopic phenomenological material law, which is a significant advantage of the multi-scale computational approach. At the same time, however, this is associated with high numerical costs.

The *Hill-Mandel condition*, which is also called macro-homogeneity condition, states the energetic equivalence between the scales and is applied to bridge between micro- and macroscale. It is furthermore used to define microscopic boundary conditions based on macroscopic measures for the RVE. For the discussion of macroscopic and microscopic boundary value problems the following notation is introduced: macroscopic quantities are marked by $(\bar{\bullet})$ while the microscopic counterpart remains unmarked as $(\bullet)$.

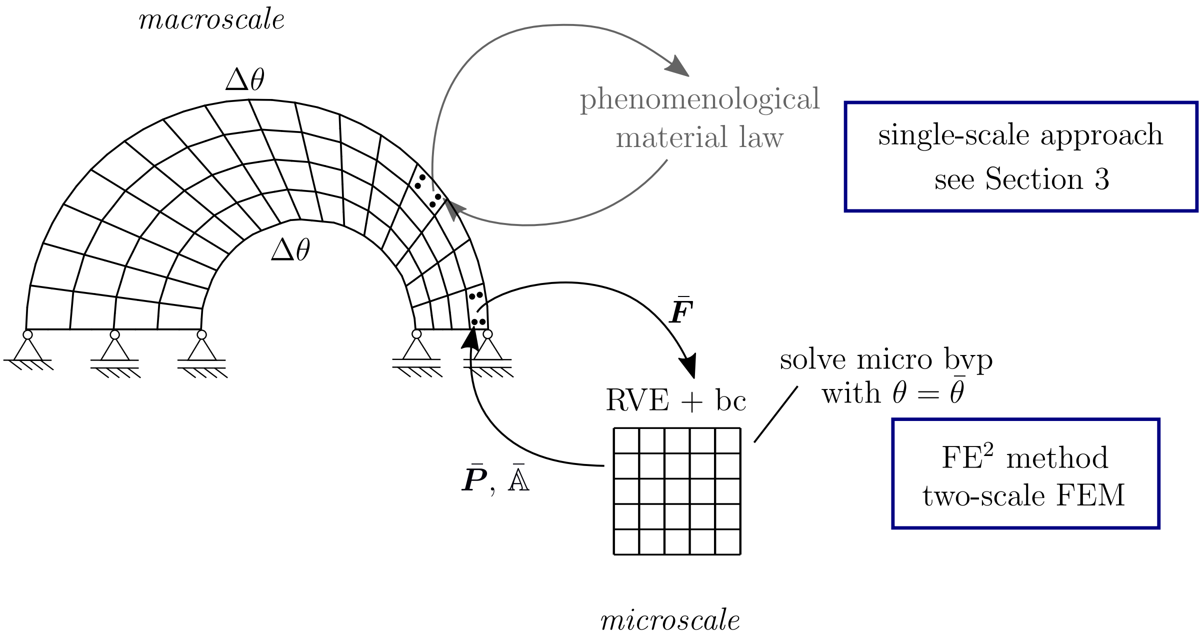

Figure 8.1: Idea of FE^2 method: Instead of considering a phenomenological material law directly on the macroscale, a microscopic boundary value problem is attached in every macroscopic integration point, to which the macroscopic deformation gradient $\bar{\boldsymbol{F}}$ is communicated. By homogenization, macroscopic stresses $\bar{\boldsymbol{P}}$ and tangent moduli $\bar{\mathbb{A}}$ are passed back to the macroscale after the microscopic boundary value problem (micro bvp) is solved. These are computed as suitable averages over microscopic quantities.

8.3 Boundary value problems on macroscale and microscale

On macroscopic level, the body of interest in reference configuration is denoted by $\bar{\mathcal{B}}_0 \in \mathbb{R}^3$. Each point is defined by its position vector $\bar{\boldsymbol{X}} \in \bar{\mathcal{B}}_0$, which is mapped onto the actual configuration $\bar{\boldsymbol{x}} \in \bar{\mathcal{B}}$ by the deformation map $\bar{\varphi}(\bar{\boldsymbol{X}}) : \bar{\mathcal{B}}_0 \to \bar{\mathcal{B}} \in \mathbb{R}^3$ with $\bar{\boldsymbol{X}} \mapsto \bar{\boldsymbol{x}}$. Neglecting acceleration terms, the balance of momentum reads

$$\mathrm{Div}_{\bar{\boldsymbol{X}}}\, \bar{\boldsymbol{P}} + \rho_0\, \bar{\boldsymbol{b}} = \boldsymbol{0} \tag{8.3}$$

with macroscopic body forces $\rho_0\, \bar{\boldsymbol{b}}$ and first Piola-Kirchhoff stresses $\bar{\boldsymbol{P}}$. Based on the balance of angular momentum, the relation $\bar{\boldsymbol{P}} \cdot \bar{\boldsymbol{F}}^{\mathrm{T}} = \bar{\boldsymbol{F}} \cdot \bar{\boldsymbol{P}}^{\mathrm{T}}$ has to be satisfied. The boundary conditions on the macroscopic continuum are given by

$$\bar{\boldsymbol{u}} = \bar{\boldsymbol{u}}_0 \quad \text{on} \quad \partial\bar{\mathcal{B}}_{0\boldsymbol{u}} \qquad \text{and} \qquad \bar{\boldsymbol{P}} \cdot \bar{\boldsymbol{N}} = \bar{\boldsymbol{t}}_0 \quad \text{on} \quad \partial\bar{\mathcal{B}}_{0\boldsymbol{t}} \tag{8.4}$$

with $\partial\bar{\mathcal{B}}_{0\boldsymbol{u}} \cup \partial\bar{\mathcal{B}}_{0\boldsymbol{t}} = \partial\bar{\mathcal{B}}_0$ and $\partial\bar{\mathcal{B}}_{0\boldsymbol{u}} \cap \partial\bar{\mathcal{B}}_{0\boldsymbol{t}} = \emptyset$.

On microscopic level, the micro-continuum is referred to as $\mathcal{B}_0 \in \mathbb{R}^3$ with position vector $\boldsymbol{X} \in \mathcal{B}_0$ in undeformed configuration. The deformation map to the actual configuration is defined as $\varphi(\boldsymbol{X}) : \mathcal{B}_0 \to \mathcal{B} \in \mathbb{R}^3$ with $\boldsymbol{X} \mapsto \boldsymbol{x}$, which relates $\boldsymbol{X}$ to the position vector in actual placement $\boldsymbol{x} \in \mathcal{B}$. Neglecting acceleration terms and body forces, the balance of momentum reads

$$\mathrm{Div}_{\boldsymbol{X}}\, \boldsymbol{P} = \boldsymbol{0} \tag{8.5}$$

with first Piola-Kirchhoff stresses $\boldsymbol{P}$, for which $\boldsymbol{P} \cdot \boldsymbol{F}^{\mathrm{T}} = \boldsymbol{F} \cdot \boldsymbol{P}^{\mathrm{T}}$ has to be fulfilled.

8.4 Relation of macroscopic quantities and its microscopic counterparts

This section provides details on the derivation of the macroscopic quantities and their respective microscopic counterparts. Therefore, an RVE $\mathcal{B}_0$ in reference configuration with boundary $\partial\mathcal{B}_0$ and volume V is considered. A hole inside and its boundary are denoted by $\mathcal{L}_0$ and $\partial\mathcal{L}_0$, respectively. In general, the volume average as measure of a microscopic quantity $(\bullet)$ on the macroscale is defined as

$$\langle(\bullet)\rangle = \frac{1}{V}\int_{\mathcal{B}_0} (\bullet)\,\mathrm{d}V\,. \tag{8.6}$$

Thus, for the Jacobian, i.e., the determinant of the macroscopic deformation gradient, it holds

$$\bar{J} = \langle J\rangle = \frac{1}{V}\int_{\mathcal{B}_0} J\mathrm{d}V = \frac{1}{V}\int_{\mathcal{B}} \mathrm{d}v = \frac{v}{V} \quad \text{with} \quad v = \int_{\mathcal{B}} \mathrm{d}v\,. \tag{8.7}$$

The volume average of the deformation gradient $\langle\boldsymbol{F}\rangle$ and the first Piola-Kirchhoff stress tensor $\langle\boldsymbol{P}\rangle$ are defined in terms of surface integrals over the boundaries of the RVE $\partial\mathcal{B}_0$ including the boundaries $\partial\mathcal{L}_0$ of the holes

$$\begin{aligned}\langle\boldsymbol{F}\rangle &= \frac{1}{V}\int_{\partial\mathcal{B}_0} \boldsymbol{x}\otimes\boldsymbol{N}\,\mathrm{d}A + \frac{1}{V}\int_{\partial\mathcal{L}_0} \boldsymbol{x}\otimes\boldsymbol{N}\,\mathrm{d}A\,,\\ \langle\boldsymbol{P}\rangle &= \frac{1}{V}\int_{\partial\mathcal{B}_0} \boldsymbol{t}_0\otimes\boldsymbol{X}\,\mathrm{d}A + \frac{1}{V}\int_{\partial\mathcal{L}_0} \boldsymbol{t}_0\otimes\boldsymbol{X}\,\mathrm{d}A\,.\end{aligned} \tag{8.8}$$

Thus, the macroscopic deformation gradient $\bar{\boldsymbol{F}}$ and the macroscopic first Piola-Kirchhoff stress tensor $\bar{\boldsymbol{P}}$ can be expressed as the volume average of the associated quantity corrected by the integral over the holes. By assuming that the RVE is a continuum without holes, this correction vanishes and one obtains

$$\bar{\boldsymbol{F}} = \frac{1}{V}\int_{\partial\mathcal{B}_0} \boldsymbol{x}\otimes\boldsymbol{N}\,\mathrm{d}A \quad \text{and} \quad \bar{\boldsymbol{P}} = \frac{1}{V}\int_{\partial\mathcal{B}_0} \boldsymbol{t}_0\otimes\boldsymbol{X}\,\mathrm{d}A\,, \tag{8.9}$$

see for instance also Schröder [161] or Schröder [162] for more details. An additive decomposition of the deformation gradient into a constant and a fluctuation part is introduced, i.e.,

$$\boldsymbol{F} = \bar{\boldsymbol{F}} + \tilde{\boldsymbol{F}}\,. \tag{8.10}$$

Inserting Equation (8.10) into the volume average in Equation $(8.9)_1$ results in the requirement for the volume average of the fluctuations to vanish. Since the macroscopic part $\bar{\boldsymbol{F}}$ is constant over the RVE, one can reformulate

$$\bar{\boldsymbol{F}} = \frac{1}{V}\int_{\mathcal{B}_0} \boldsymbol{F}\,\mathrm{d}V = \frac{1}{V}\int_{\mathcal{B}_0} (\bar{\boldsymbol{F}}+\tilde{\boldsymbol{F}})\,\mathrm{d}V = \bar{\boldsymbol{F}} + \frac{1}{V}\int_{\mathcal{B}_0} \tilde{\boldsymbol{F}}\,\mathrm{d}V\,, \tag{8.11}$$

which implies

$$\frac{1}{V}\int_{\mathcal{B}_0} \tilde{\boldsymbol{F}}\,\mathrm{d}V = 0\,. \tag{8.12}$$

The fluctuation part of deformation gradient $\tilde{\boldsymbol{F}} = \mathrm{Grad}_{\boldsymbol{X}}\,\tilde{\boldsymbol{u}}$ can be expressed in terms of the microscopic deformation field $\tilde{\boldsymbol{u}} = \boldsymbol{x} - \bar{\boldsymbol{F}}\cdot\boldsymbol{X}$. For the microscopic fluctuation part of the deformation field it holds $\frac{1}{V}\int_{\partial\mathcal{B}_0} \tilde{\boldsymbol{u}}\otimes\boldsymbol{N}\,\mathrm{d}A = 0$. Analogously, the first Piola-Kirchhoff stress tensor is decomposed into a constant and a fluctuation part by $\boldsymbol{P} = \bar{\boldsymbol{P}} + \tilde{\boldsymbol{P}}$, for which $\frac{1}{V}\int_{\mathcal{B}_0} \tilde{\boldsymbol{P}}\,\mathrm{d}V = 0$ holds, since one can derive

$$\bar{\boldsymbol{P}} = \frac{1}{V}\int_{\mathcal{B}_0} \boldsymbol{P}\,\mathrm{d}V = \frac{1}{V}\int_{\mathcal{B}_0} (\bar{\boldsymbol{P}} + \tilde{\boldsymbol{P}})\,\mathrm{d}V = \bar{\boldsymbol{P}} + \frac{1}{V}\int_{\mathcal{B}_0} \tilde{\boldsymbol{P}}\,\mathrm{d}V\,. \tag{8.13}$$

Thus, for the traction vector the decomposition results in the additive split $\boldsymbol{t}_0 = \boldsymbol{P}\cdot\boldsymbol{N} = (\bar{\boldsymbol{P}} + \tilde{\boldsymbol{P}})\cdot\boldsymbol{N} =: \bar{\boldsymbol{t}}_0 + \tilde{\boldsymbol{t}}_0$ with $\frac{1}{V}\int_{\partial\mathcal{B}_0} \tilde{\boldsymbol{t}}_0 \otimes \boldsymbol{X}\,\mathrm{d}A = \boldsymbol{0}$. In case of linearized strain theory, one can compute the macroscopic Cauchy stress by the volume average $\bar{\boldsymbol{\sigma}} = \frac{1}{V}\int_{\mathcal{B}_0} \boldsymbol{\sigma}\,\mathrm{d}V$.

8.5 Macro-homogeneity condition

The *Hill-Mandel condition* or macro-homogeneity-condition is utilized to describe the localization and the boundary conditions on the microscale. As it sets the energetic equivalence of the two scales, it states that the macroscopic stress power is equal to the volume average of the microscopic stress power. Thereby, it can be used to translate quantities from microscale to macroscale. For the regime of finite strains, it can be formulated as

$$\bar{\boldsymbol{P}} : \dot{\bar{\boldsymbol{F}}} = \frac{1}{V}\int_{\partial\mathcal{B}_0} \boldsymbol{t}_0 \cdot \dot{\boldsymbol{x}}\,\mathrm{d}A\,, \tag{8.14}$$

which can also be reformulated to

$$\bar{\boldsymbol{P}} : \dot{\bar{\boldsymbol{F}}} = \frac{1}{V}\int_{\mathcal{B}_0} \boldsymbol{P} : \dot{\boldsymbol{F}}\,\mathrm{d}V\,. \tag{8.15}$$

Hence, utilizing Equations (8.11) and (8.13) it is equivalent to

$$0 = \frac{1}{V}\int_{\mathcal{B}_0} \boldsymbol{P} : \dot{\boldsymbol{F}}\,\mathrm{d}V - \bar{\boldsymbol{P}} : \dot{\bar{\boldsymbol{F}}} = \int_{\mathcal{B}_0} (\boldsymbol{P} - \bar{\boldsymbol{P}}) : (\dot{\boldsymbol{F}} - \dot{\bar{\boldsymbol{F}}})\,\mathrm{d}V\,. \tag{8.16}$$

This condition is directly fulfilled for the assumptions of Reuss and Voigt, i.e., in case of constant stress over the RVE $\boldsymbol{P} = \bar{\boldsymbol{P}}\ \forall \boldsymbol{X} \in \mathcal{B}_0$ or constant deformation gradient over the RVE $\boldsymbol{F} = \bar{\boldsymbol{F}}\ \forall \boldsymbol{X} \in \mathcal{B}_0$. Based on the definition of the rate of deformation gradient on microscopic level $\dot{\boldsymbol{F}} = \mathrm{Grad}_{\boldsymbol{X}}\,\dot{\boldsymbol{x}}$ and the identity $\mathrm{Grad}_{\boldsymbol{X}}\,\boldsymbol{X} = \boldsymbol{I}$ it follows that

$$0 = \int_{\mathcal{B}_0} (\boldsymbol{P} - \bar{\boldsymbol{P}}) : (\dot{\boldsymbol{F}} - \dot{\bar{\boldsymbol{F}}})\,\mathrm{d}V = \int_{\mathcal{B}_0} (\boldsymbol{P} - \bar{\boldsymbol{P}}) : (\mathrm{Grad}_{\boldsymbol{X}}\,\dot{\boldsymbol{x}} - \dot{\bar{\boldsymbol{F}}}\cdot\mathrm{Grad}_{\boldsymbol{X}}\,\boldsymbol{X})\,\mathrm{d}V\,.$$

Further reformulations in index notations give

$$\begin{aligned}
0 &= \int_{\mathcal{B}_0} (P_{ij} - \bar{P}_{ij})(\dot{x}_{i,j} - \dot{\bar{\mathcal{F}}}_{ik}X_{k,j})\,\mathrm{d}V \\
&= \int_{\mathcal{B}_0} \big((P_{ij} - \bar{P}_{ij})(\dot{x}_i - \dot{\bar{\mathcal{F}}}_{ik}X_k)\big)_{,j}\,\mathrm{d}V - \int_{\mathcal{B}_0} \underbrace{(P_{ij} - \bar{P}_{ij})_{,j}}_{=0\,\text{for equilibrium}}(\dot{x}_i - \dot{\bar{\mathcal{F}}}_{ik}X_k)\,\mathrm{d}V \\
&= \int_{\partial\mathcal{B}_0} \big((P_{ij} - \bar{P}_{ij})(\dot{x}_i - \dot{\bar{\mathcal{F}}}_{ik}X_k)\big)N_j\,\mathrm{d}A \\
\Rightarrow 0 &= \int_{\partial\mathcal{B}_0} (\boldsymbol{t}_0 - \bar{\boldsymbol{P}}\cdot\boldsymbol{N})\cdot(\dot{\boldsymbol{x}} - \dot{\bar{\boldsymbol{F}}}\cdot\boldsymbol{X})\,\mathrm{d}A\,.
\end{aligned} \tag{8.17}$$

The boundary integral in Equation (8.17) is considered to the definition of suitable microscopic boundary conditions. In addition to the Reuss and Voigt condition, three types of microscopic boundary conditions can be defined. *Dirichlet type boundary conditions* are defined by $\boldsymbol{x} = \bar{\boldsymbol{F}} \cdot \boldsymbol{X} \; \forall \boldsymbol{X} \in \partial \mathcal{B}_0$ and, analogously, *Neumann type boundary conditions* are given as $\boldsymbol{t}_0 = \bar{\boldsymbol{P}} \cdot \boldsymbol{N} \; \forall \boldsymbol{X} \in \partial \mathcal{B}_0$. For the derivation of periodic boundary conditions, the boundary is decomposed into two disjunct associated parts by $\partial \mathcal{B}_0 = \partial \mathcal{B}_0^- \cup \partial \mathcal{B}_0^+$. For every point $\boldsymbol{X}^+ \in \partial \mathcal{B}_0^+$ an associated point $\boldsymbol{X}^- \in \partial \mathcal{B}_0^-$ exists with outward normals $\boldsymbol{N}^+ = -\boldsymbol{N}^-$, respectively, see Figure 8.2.

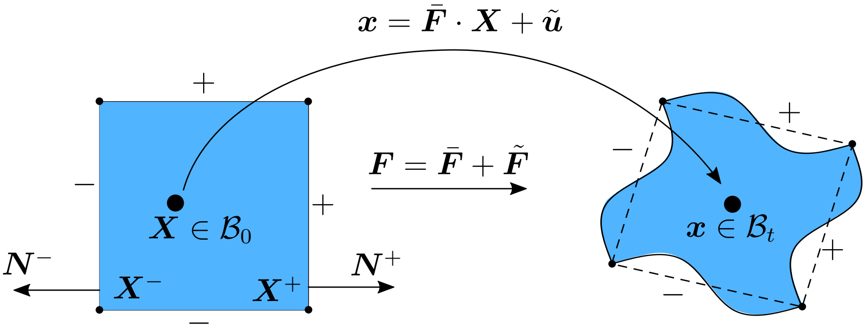

Figure 8.2: Application of periodic boundary conditions on the microscale.

With the above presented definition of the microscopic fluctuation field $\tilde{\boldsymbol{u}} = \boldsymbol{x} - \bar{\boldsymbol{F}} \cdot \boldsymbol{X}$, the macro-homogeneity condition appears as

$$0 = \int_{\partial \mathcal{B}_0} (\boldsymbol{t}_0 - \bar{\boldsymbol{P}} \cdot \boldsymbol{N}) : \tilde{\boldsymbol{u}} \, \mathrm{d}A = \int_{\partial \mathcal{B}_0^+} (\boldsymbol{t}_0^+ - \bar{\boldsymbol{P}} \cdot \boldsymbol{N}^+) : \tilde{\boldsymbol{u}}^+ \, \mathrm{d}A + \int_{\partial \mathcal{B}_0^-} (\boldsymbol{t}_0^- - \bar{\boldsymbol{P}} \cdot \boldsymbol{N}^-) : \tilde{\boldsymbol{u}}^- \, \mathrm{d}A \,, \tag{8.18}$$

which is valid in case of

$$\tilde{\boldsymbol{u}}^+ = \tilde{\boldsymbol{u}}^- \,, \quad \boldsymbol{t}_0^+ = -\boldsymbol{t}_0^- \,, \quad \text{and} \quad \boldsymbol{N}^- = -\boldsymbol{N}^+ \,. \tag{8.19}$$

Table 8.1 gives a summary on boundary conditions derived from Equation (8.14).

Table 8.1: Different types of microscopic boundary conditions (bc).

Reuss assumption	$\boldsymbol{P} = \bar{\boldsymbol{P}}$	$\forall \boldsymbol{X} \in \mathcal{B}_0$
Voigt assumption	$\dot{\boldsymbol{F}} = \dot{\bar{\boldsymbol{F}}}$	$\forall \boldsymbol{X} \in \mathcal{B}_0$
Dirichlet bc	$\boldsymbol{x} = \bar{\boldsymbol{F}} \cdot \boldsymbol{X}$	$\forall \boldsymbol{X} \in \partial \mathcal{B}_0$
Neumann bc	$\boldsymbol{t}_0 = \bar{\boldsymbol{P}} \cdot \boldsymbol{N}$	$\forall \boldsymbol{X} \in \partial \mathcal{B}_0$
periodic bc	$\tilde{\boldsymbol{u}} = \boldsymbol{x} - \bar{\boldsymbol{F}} \cdot \boldsymbol{X}$ $\tilde{\boldsymbol{u}}^+ = \tilde{\boldsymbol{u}}^-$ $\boldsymbol{t}_0^+ = -\boldsymbol{t}_0^-$	$\forall \boldsymbol{X}^+ \in \partial \mathcal{B}_0^+$ and $\boldsymbol{X}^- \in \partial \mathcal{B}_0^-$

8.6 Numerical implementation

In this section, aspects on the numerical implementation of the macroscopic and microscopic boundary value problems are discussed. The basics of the utilized FEM are given in Section 3, such that the focus here lies on the algorithmic consistent tangent moduli and the general variational formulation. The following remarks on the numerical implementation are based on Miehe et al. [121; 122], Miehe and Koch [120] and Schröder [162].

8.6.1 Macroscale

On the macroscopic level, the weak form of the balance of momentum is given as

$$\bar{G} = -\int_{\bar{\mathcal{B}}_0} \delta\bar{\boldsymbol{x}} \cdot (\mathrm{Div}_{\bar{\boldsymbol{X}}}\, \bar{\boldsymbol{P}} + \rho_0\, \bar{\boldsymbol{b}})\, \mathrm{d}V = 0\,, \tag{8.20}$$

which has to be zero in case of equilibrium. With the Gauss integral theorem and the relation $\delta\bar{\boldsymbol{x}} \cdot \mathrm{Div}_{\bar{\boldsymbol{X}}}\, \bar{\boldsymbol{P}} = \mathrm{Div}_{\bar{\boldsymbol{X}}}[\delta\bar{\boldsymbol{x}} \cdot \bar{\boldsymbol{P}}] - \underbrace{\mathrm{Grad}_{\bar{\boldsymbol{X}}}\, \delta\bar{\boldsymbol{x}}}_{\delta\bar{\boldsymbol{F}}} : \bar{\boldsymbol{P}}$ the weak form can be reformulated to

$$\bar{G} = \underbrace{\int_{\bar{\mathcal{B}}_0} \delta\bar{\boldsymbol{F}} : \bar{\boldsymbol{P}}\, \mathrm{d}V}_{\bar{G}^{\mathrm{int}}} - \underbrace{\left(\int_{\bar{\mathcal{B}}_0} \delta\bar{\boldsymbol{x}} \cdot \rho_0\, \bar{\boldsymbol{b}}\, \mathrm{d}V + \int_{\partial\bar{\mathcal{B}}_0} \delta\bar{\boldsymbol{x}} \cdot \bar{\boldsymbol{t}}_0\, \mathrm{d}A\right)}_{\bar{G}^{\mathrm{ext}}}\,. \tag{8.21}$$

The increment of the internal part $\bar{G}^{\mathrm{int}}$, which is inevitable to solve $\bar{G} = 0$ by a Newton-Raphson iteration scheme numerically, reads

$$\Delta\bar{G}^{\mathrm{int}} = \int_{\bar{\mathcal{B}}_0} \delta\bar{\boldsymbol{F}}^{\mathrm{T}} : \bar{\mathbb{A}} : \Delta\bar{\boldsymbol{F}}\, \mathrm{d}V\,. \tag{8.22}$$

Therein, $\bar{\mathbb{A}}$ denotes the macroscopic overall algorithmic consistent tangent moduli. They are defined as the partial derivative of the macroscopic first Piola-Kirchhoff stress tensor with respect to the macroscopic deformation gradient, i.e.,

$$\bar{\mathbb{A}} = \frac{\partial\bar{\boldsymbol{P}}}{\partial\bar{\boldsymbol{F}}}\,. \tag{8.23}$$

Thus, for the incremental formulation it holds that $\Delta\bar{\boldsymbol{P}} = \bar{\mathbb{A}} : \Delta\bar{\boldsymbol{F}}$. Since there is no explicit expression for $\bar{\boldsymbol{P}}$ in terms of $\bar{\boldsymbol{F}}$ in $\bar{\boldsymbol{P}} = \frac{1}{V}\int_{\mathcal{B}_0} \boldsymbol{P}(\boldsymbol{F})\, \mathrm{d}V$, a numerical computation is to be derived. For now it is assumed to know the macroscopic moduli $\bar{\mathbb{A}}$, which is in detail derived in Section 8.6.3.

For the numerical solution of Equation (8.20) via the classical finite element formulation, see also Section 3, field quantities are approximated in one finite element with isoparametric ansatz functions N^I. Thereby, the actual, virtual and incremental deformation within one finite element is given as

$$\bar{\boldsymbol{x}}(\boldsymbol{\xi}) = \sum_{I=1}^{n_{\mathrm{node}}} N_I(\boldsymbol{\xi})\bar{\boldsymbol{x}}_I\,, \quad \delta\bar{\boldsymbol{x}}(\boldsymbol{\xi}) = \sum_{I=1}^{n_{\mathrm{node}}} N_I(\boldsymbol{\xi})\delta\bar{\boldsymbol{d}}_I \quad \text{and} \quad \Delta\bar{\boldsymbol{x}}(\boldsymbol{\xi}) = \sum_{I=1}^{n_{\mathrm{node}}} N_I(\boldsymbol{\xi})\Delta\bar{\boldsymbol{d}}_I\,, \tag{8.24}$$

with $\bar{\boldsymbol{x}}_I = \bar{\boldsymbol{X}}_I + \bar{\boldsymbol{d}}_I$, the natural coordinates $\boldsymbol{\xi}$ in the isoparametric space and $\bar{\boldsymbol{d}}_I$, $\delta\bar{\boldsymbol{d}}_I$ and $\Delta\bar{\boldsymbol{d}}_I$ as actual, virtual and incremental nodal displacement vectors. The element B-matrix $\boldsymbol{B}^e$ consists of the partial derivatives of the ansatz functions with respect to the reference configuration. Therewith, the discretizations of the virtual and incremental deformation gradient for element e with element virtual and incremental displacement vector $\delta\bar{\boldsymbol{d}}^e$ and $\Delta\bar{\boldsymbol{d}}^e$, respectively, read

$$\delta\bar{\boldsymbol{F}} = \boldsymbol{B}^e\delta\bar{\boldsymbol{d}}^e \quad \text{and} \quad \Delta\bar{\boldsymbol{F}} = \boldsymbol{B}^e\Delta\bar{\boldsymbol{d}}^e\,. \tag{8.25}$$

As a consequence, the discrete counterpart to Equation (8.21) for one element $\bar{\mathcal{B}}_0^e$ is formulated as [3.)]

$$\bar{G}^e = \delta\bar{\boldsymbol{d}}^{e,\mathrm{T}} \underbrace{\left\{\int_{\bar{\mathcal{B}}_0^e} \boldsymbol{B}^{e,\mathrm{T}}\bar{\boldsymbol{P}}\,\mathrm{d}V - \int_{\bar{\mathcal{B}}_0^e} \boldsymbol{N}^{e,\mathrm{T}}\rho_0\,\bar{\boldsymbol{b}}\,\mathrm{d}V + \int_{\partial\bar{\mathcal{B}}_0^e} \boldsymbol{N}^{e,\mathrm{T}}\bar{\boldsymbol{t}}_0\,\mathrm{d}A\right\}}_{=:\bar{\boldsymbol{r}}^e}\,, \tag{8.26}$$

with $\boldsymbol{N}^e$ as matrix with the ansatz functions for the finite element. The vector $\bar{\boldsymbol{r}}^e$ is referred to as element right-hand side vector, analogously to the single-scale FEM. In parallel, the discrete counterpart of the increment $\Delta\bar{G}^{\mathrm{int}}$ in Equation (8.22) is given by

$$\Delta\bar{G}^{e,\mathrm{int}} = \delta\bar{\boldsymbol{d}}^{e,\mathrm{T}} \underbrace{\int_{\bar{\mathcal{B}}_0^e} \boldsymbol{B}^{e,\mathrm{T}}\,\bar{\mathbb{A}}\,\boldsymbol{B}^e\,\mathrm{d}V}_{=:\bar{\boldsymbol{k}}^e}\,\Delta\bar{\boldsymbol{d}}^e\,, \tag{8.27}$$

with $\bar{\boldsymbol{k}}^e$ as element stiffness matrix. By summation over all elements, i.e.,

$$\bar{G} = \sum_e \bar{G}^e \quad \text{and} \quad \Delta\bar{G} = \sum_e \Delta\bar{G}^{e,\mathrm{int}}\,, \tag{8.28}$$

and by utilizing classical assembling procedures the system of equation results in

$$\bar{G} + \Delta\bar{G} = \delta\bar{\boldsymbol{D}}^{\mathrm{T}}(\bar{\boldsymbol{K}}\,\Delta\bar{\boldsymbol{D}} + \bar{\boldsymbol{R}}) = 0\,, \tag{8.29}$$

which is to be solved with respect to the global incremental displacement vector $\Delta\bar{\boldsymbol{D}} = -\bar{\boldsymbol{K}}^{-1}\bar{\boldsymbol{R}}$. Therein, $\bar{\boldsymbol{K}}$ and $\bar{\boldsymbol{R}}$ denote the macroscopic global stiffness matrix and the macroscopic global residual vector.

8.6.2 Microscale

For the microscopic boundary value problem, the weak form of the balance of linear momentum without acceleration or inertia terms is derived as

$$G = -\int_{\mathcal{B}_0} \delta\boldsymbol{x}\cdot\mathrm{Div}_{\boldsymbol{X}}\,\boldsymbol{P}\,\mathrm{d}V = \int_{\mathcal{B}_0} \delta\tilde{\boldsymbol{F}} : \boldsymbol{P}\,\mathrm{d}V = 0\,. \tag{8.30}$$

The fluctuation part of the displacement field on microscopic level $\tilde{\boldsymbol{u}}$ is expressed with the microscopic displacement $\boldsymbol{x} = \bar{\boldsymbol{F}}\cdot\boldsymbol{X} + \tilde{\boldsymbol{u}}$. Thus, it holds for the virtual and incremental fluctuation part of the deformation gradient that

$$\delta\tilde{\boldsymbol{F}} = \mathrm{Grad}_{\boldsymbol{X}}\,\delta\tilde{\boldsymbol{u}} \quad \text{and} \quad \Delta\tilde{\boldsymbol{F}} = \mathrm{Grad}_{\boldsymbol{X}}\,\Delta\tilde{\boldsymbol{u}}\,. \tag{8.31}$$

The linearized form of Equation (8.30) results in

$$\Delta G = \int_{\mathcal{B}_0} \delta\boldsymbol{F}^{\mathrm{T}} : \mathbb{A} : \Delta\boldsymbol{F}\,\mathrm{d}V = \int_{\mathcal{B}_0} \delta\boldsymbol{F}^{\mathrm{T}} : \mathbb{A} : (\Delta\bar{\boldsymbol{F}} + \Delta\tilde{\boldsymbol{F}})\,\mathrm{d}V\,, \tag{8.32}$$

[3.)] For the discrete formulation of the problem tensorial quantities as the stress tenosr $\bar{\boldsymbol{P}}$, for instance, have to be replaced by matrices and vectors, respectively, which is not explicitly labeled.

with $\mathbb{A} := \partial_{\boldsymbol{F}} \boldsymbol{P}$ as the algorithmic consistent tangent moduli. Analogously to the macroscopic derivation, the actual, virtual and incremental fluctuations are discretized as

$$\tilde{\boldsymbol{u}}(\boldsymbol{\xi}) = \sum_{I=1}^{n_{\text{node}}} N_I(\boldsymbol{\xi}) \tilde{\boldsymbol{d}}_I \,, \quad \delta\tilde{\boldsymbol{u}}(\boldsymbol{\xi}) = \sum_{I=1}^{n_{\text{node}}} N_I(\boldsymbol{\xi}) \delta\tilde{\boldsymbol{d}}_I \quad \text{and} \quad \Delta\tilde{\boldsymbol{u}}(\boldsymbol{\xi}) = \sum_{I=1}^{n_{\text{node}}} N_I(\boldsymbol{\xi}) \Delta\tilde{\boldsymbol{d}}_I \,, \tag{8.33}$$

with the natural coordinates $\boldsymbol{\xi}$ in the isoparametric space and $\tilde{\boldsymbol{d}}_I$, $\tilde{\delta}\boldsymbol{d}_I$ and $\tilde{\Delta}\boldsymbol{d}_I$ as actual, virtual and incremental nodal fluctuation vectors. Based on the element B-matrix $\boldsymbol{B}^e$, which consists of the partial derivatives of the ansatz functions with respect to the reference configuration, the discretizations of the fluctuations of the virtual and incremental deformation gradient for element e result in

$$\delta\tilde{\boldsymbol{F}} = \boldsymbol{B}^e \delta\tilde{\boldsymbol{d}}^e \quad \text{and} \quad \Delta\tilde{\boldsymbol{F}} = \boldsymbol{B}^e \Delta\tilde{\boldsymbol{d}}^e \,. \tag{8.34}$$

Therein, $\delta\tilde{\boldsymbol{d}}^e$ and $\Delta\tilde{\boldsymbol{d}}^e$ denote the element's virtual and incremental fluctuation vectors. As a consequence, the discrete counterparts of Equations (8.30) and (8.32) for one element $\bar{\mathcal{B}}_0^e$ are derived as

$$\begin{aligned} G^e &= \delta\tilde{\boldsymbol{d}}^{e,\mathrm{T}} \int_{\mathcal{B}_0^e} \boldsymbol{B}^{e,\mathrm{T}} \boldsymbol{P} \, \mathrm{dV} \,, \\ \Delta G^e &= \delta\tilde{\boldsymbol{d}}^{e,\mathrm{T}} \underbrace{\int_{\mathcal{B}_0^e} \boldsymbol{B}^{e,\mathrm{T}} \mathbb{A} \, \mathrm{d}V}_{=:\boldsymbol{l}^e} \Delta\bar{\boldsymbol{F}} + \delta\tilde{\boldsymbol{d}}^{e,\mathrm{T}} \underbrace{\int_{\mathcal{B}_0^e} \boldsymbol{B}^{e,\mathrm{T}} \mathbb{A} \boldsymbol{B}^e \, \mathrm{d}V}_{=:\boldsymbol{k}^e} \,. \end{aligned} \tag{8.35}$$

The first integral is identified as matrix $\boldsymbol{l}^e$, that represents the sensivity of the tangent moduli on the finite elements, and the second integral is defined as microscopic element stiffness matrix $\boldsymbol{k}^e$. The summation overall elements

$$G = \sum_e G^e \quad \text{and} \quad \Delta G = \sum_e \Delta G^{e,\text{int}} \,, \tag{8.36}$$

in combination with assemblation

$$\boldsymbol{K} = \mathop{\mathsf{A}}_{\mathrm{e}\,=\,1}^{n_{\text{ele}}} \int_{\mathcal{B}_0^e} \boldsymbol{B}^{e,\mathrm{T}} \, \mathbb{A} \, \boldsymbol{B}^e \, \mathrm{d}V \,, \quad \boldsymbol{L} = \mathop{\mathsf{A}}_{\mathrm{e}\,=\,1}^{n_{\text{ele}}} \int_{\mathcal{B}_0^e} \boldsymbol{B}^{e,\mathrm{T}} \, \mathbb{A} \, \mathrm{d}V \quad \text{and} \quad \boldsymbol{R} = \mathop{\mathsf{A}}_{\mathrm{e}\,=\,1}^{n_{\text{ele}}} \int_{\mathcal{B}_0^e} \boldsymbol{B}^{\mathrm{T}} \boldsymbol{P} \, \mathrm{d}V \tag{8.37}$$

results in the system of equations $G + \Delta G = 0$, which is to be solved with an iterative Newton-Raphson scheme

$$\delta\tilde{\boldsymbol{D}}^{\mathrm{T}} (\boldsymbol{K} \, \Delta\tilde{\boldsymbol{D}} + \boldsymbol{L} \, \Delta\bar{\boldsymbol{F}} + \boldsymbol{R}) = 0 \,. \tag{8.38}$$

Therein, $\boldsymbol{K}$ denotes the microscopic global stiffness matrix and $\boldsymbol{L}$ is the general right hand side which takes into account the sensitivity of the moduli of the individual finite element. Furthermore, $\boldsymbol{R}$ is the assembled residual vector. The system of equations is solved with respect to the incremental fluctuation field as a consequence of an incremental macroscopic deformation gradient

$$\Delta\tilde{\boldsymbol{D}} = -\boldsymbol{K}^{-1} \boldsymbol{L} \Delta\bar{\boldsymbol{F}} \,. \tag{8.39}$$

During the solution of the microscopic boundary value problem, it holds that the incremental macroscopic deformation gradient is zero, i.e., $\Delta\bar{\boldsymbol{F}} = \boldsymbol{0}$ which simplifies the Equation (8.38) to $\delta\tilde{\boldsymbol{D}}^{\mathrm{T}} (\boldsymbol{K} \, \Delta\tilde{\boldsymbol{D}} + \boldsymbol{R}) = 0$. If the microscopic boundary value problem is solved and convergence is obtained, it holds that the residual vanishes, i.e., $\boldsymbol{R} = \boldsymbol{0}$.

8.6.3 Algorithmic consistent tangent moduli

The macroscopic algorithmic tangent moduli in Equation (8.23) cannot be derived analytical, as previously stated. For its numerical computation, the relation $\boldsymbol{P} = \mathbb{A} : \boldsymbol{F}$ and the split of the deformation gradient into $\boldsymbol{F} = \bar{\boldsymbol{F}} + \tilde{\boldsymbol{F}}$ is utilized, i.e.,

$$\begin{aligned}\bar{\mathbb{A}} &= \frac{\partial\big(\frac{1}{V}\int_{\mathcal{B}_0}\boldsymbol{P}\,\mathrm{d}V\big)}{\partial\bar{\boldsymbol{F}}} = \frac{1}{V}\int_{\mathcal{B}_0}\frac{\partial\boldsymbol{P}}{\partial\bar{\boldsymbol{F}}}\,\mathrm{d}V = \frac{1}{V}\int_{\mathcal{B}_0}\frac{\partial\mathbb{A}:(\bar{\boldsymbol{F}}+\tilde{\boldsymbol{F}})}{\partial\bar{\boldsymbol{F}}}\,\mathrm{d}V \\ &= \frac{1}{V}\int_{\mathcal{B}_0}\mathbb{A}\,\mathrm{d}V + \frac{1}{V}\int_{\mathcal{B}_0}\mathbb{A}:\frac{\partial\tilde{\boldsymbol{F}}}{\partial\bar{\boldsymbol{F}}}\,\mathrm{d}V\,. \qquad (8.40)\end{aligned}$$

Considering the discretization in Equation $(8.34)_2$ and a discrete formulation on element level, the second term in Equation (8.40) can be reformulated to

$$\frac{1}{V}\sum_e\underbrace{\int_{\mathcal{B}_0^e}\mathbb{A}\,\boldsymbol{B}^e\,\mathrm{d}V}_{=\boldsymbol{l}^{e,\mathrm{T}}}\,\frac{\partial\Delta\tilde{\boldsymbol{d}}^e}{\partial\bar{\boldsymbol{F}}}\,. \qquad (8.41)$$

If $\mathbb{A}$ is symmetric, the transposed matrix $\boldsymbol{l}^{e,\mathrm{T}}$ can be identified. With the solution of the microscopic boundary value problem in Equation (8.39) and by application of an assembling procedure, the macroscopic algorithmic tangent moduli is derived as

$$\bar{\mathbb{A}} = \frac{1}{V}\int_{\mathcal{B}_0}\mathbb{A}\,\mathrm{d}V - \frac{1}{V}\boldsymbol{L}^{\mathrm{T}}\boldsymbol{K}^{-1}\boldsymbol{L}\,. \qquad (8.42)$$

The derivation of the multi-scale model has been carried out for finite strains. In this work, analyses in the regimes of small strains are done, for which the fundamental equations are summarized in Table 8.2.

Table 8.2: Important relations for the FE^2 method in the linearized theory of small strains.

macroscopic balance of linear momentum	$\mathrm{div}\,\bar{\boldsymbol{\sigma}} + \rho_0\bar{\boldsymbol{b}} = \boldsymbol{0}$ with $\bar{\boldsymbol{\sigma}} = \bar{\boldsymbol{\sigma}}^{\mathrm{T}}$
microscopic balance of linear momentum	$\mathrm{div}\,\boldsymbol{\sigma} = \boldsymbol{0}$ with $\boldsymbol{\sigma} = \boldsymbol{\sigma}^{\mathrm{T}}$
macroscopic strain	$\bar{\boldsymbol{\varepsilon}} = \frac{1}{V}\int_{\partial\mathcal{B}_0}\boldsymbol{u}\otimes\boldsymbol{n}\,\mathrm{d}a$
macroscopic stress	$\bar{\boldsymbol{\sigma}} = \frac{1}{V}\int_{\partial\mathcal{B}_0}\boldsymbol{t}\otimes\boldsymbol{x}\,\mathrm{d}a$
Hill condition	$\bar{\boldsymbol{\sigma}}:\dot{\bar{\boldsymbol{\varepsilon}}} = \frac{1}{V}\int_{\mathcal{B}_0}\boldsymbol{\sigma}:\dot{\boldsymbol{\varepsilon}}\,\mathrm{d}v$
microscopic periodic boundary conditions	$\dot{\tilde{\boldsymbol{u}}} = \dot{\boldsymbol{u}} - \dot{\bar{\boldsymbol{\varepsilon}}}\cdot\boldsymbol{x}$ $\tilde{\boldsymbol{u}}^+ = \tilde{\boldsymbol{u}}^- \quad \forall\boldsymbol{x}^+\in\partial\mathcal{B}_0^+$ and $\boldsymbol{x}^-\in\partial\mathcal{B}_0^-$ $\boldsymbol{t}_0^+ = -\boldsymbol{t}_0^-$
macroscopic consistent tangent	$\bar{\mathbb{C}} = \frac{1}{V}\int_{\mathcal{B}_0}\mathbb{C}\,\mathrm{d}v - \frac{1}{V}\boldsymbol{L}^{\mathrm{T}}\boldsymbol{K}\boldsymbol{L}$

8.7 Two-scale thermo-mechanical material model

When a micromechanically driven approach in the framework of a finite element analysis is aimed for, it is helpful to choose a multi-scale computational method. Therefore, material models are required to describe the behavior of the individual phases or materials in the heterogeneous microstructure. Here, a microscopic material model is defined, which bases on the single-scale material description on the macroscale, for details see Section 5.5.2. Therein, the linearized theory of small strains is taken into account for the formulation of the macro- and microscopic boundary value problems.

In order to set up the macroscopic boundary value problem, a body $\bar{\mathcal{B}} \in \mathbb{R}^3$ and a thermo-mechanical coupling are considered. That is, the balance of momentum in absence of outer forces $\operatorname{div} \bar{\boldsymbol{\sigma}} = \boldsymbol{0}$ and the balance of energy neglecting heat sources and the heat flux $\bar{\rho}\,\dot{\bar{e}} - \bar{\boldsymbol{\sigma}} : \dot{\bar{\boldsymbol{\varepsilon}}} = 0$ are solved analogously to the single-scale approach. The balance of angular momentum is implicitly considered, i.e., the Cauchy stress tensor $\bar{\boldsymbol{\sigma}}$ is symmetric, $\bar{\boldsymbol{\sigma}}^{\mathrm{T}} = \bar{\boldsymbol{\sigma}}$. Further quantities therein are the macroscopic density $\bar{\rho}$, the rate of the macroscopic specific internal energy $\dot{\bar{e}}$ and the rate of the macroscopic strains $\dot{\bar{\boldsymbol{\varepsilon}}}$. Moreover, to complete the definition of the thermo-mechanically coupled macroscopic boundary value problem, mechanical and thermal boundary conditions are required, which are defined as

$$\begin{aligned} \bar{\boldsymbol{u}} &= \bar{\boldsymbol{u}}_0 \quad \text{on} \quad \partial\bar{\mathcal{B}}_{\boldsymbol{u}}\,, & & & \bar{\boldsymbol{\sigma}} \cdot \bar{\boldsymbol{n}} &= \bar{\boldsymbol{t}} \quad \text{on} \quad \partial\bar{\mathcal{B}}_{\boldsymbol{t}}\,, \\ \bar{\theta} &= \bar{\theta}_0 \quad \text{on} \quad \partial\bar{\mathcal{B}}_{\theta} & & \text{and} & \bar{\boldsymbol{q}} \cdot \bar{\boldsymbol{n}} &= \bar{q}_0 \quad \text{on} \quad \partial\bar{\mathcal{B}}_{\boldsymbol{q}}\,. \end{aligned} \tag{8.43}$$

These have to satisfy

$$\begin{aligned} \partial\bar{\mathcal{B}}_{\boldsymbol{u}} \cup \partial\bar{\mathcal{B}}_{\boldsymbol{t}} &= \partial\bar{\mathcal{B}}\,, & & & \partial\bar{\mathcal{B}}_{\boldsymbol{u}} \cap \partial\bar{\mathcal{B}}_{\boldsymbol{t}} &= \emptyset\,, \\ \partial\bar{\mathcal{B}}_{\theta} \cup \partial\bar{\mathcal{B}}_{\boldsymbol{q}} &= \partial\bar{\mathcal{B}} & & \text{and} & \partial\bar{\mathcal{B}}_{\theta} \cap \partial\bar{\mathcal{B}}_{\boldsymbol{q}} &= \emptyset\,. \end{aligned} \tag{8.44}$$

Instead of directly computing the tangent moduli and the stresses by means of a suitable material model, a microscopic boundary value problem is associated with every macroscopic integration point. Therefore, an RVE is taken into account as microscopic continuum $\mathcal{B} \in \mathbb{R}^3$ following the given definition. Here, the domain is chosen in form of a unit square. Assuming a constant temperature in each macroscopic integration point for one computational time step, an isothermal material model is formulated solving the microscopic balance of linear momentum $\operatorname{div} \boldsymbol{\sigma} = \boldsymbol{0}$. Therein, the microscopic balance of angular momentum ensures the symmetry of the microscopic stress tensor, i.e., $\boldsymbol{\sigma}^{\mathrm{T}} = \boldsymbol{\sigma}$. On this minor scale, a material model to compute the microscopic stresses and tangent moduli is required. Analogously to the single-scale material model, an additive split of the total strains into elastic, plastic, thermal, transformation volumetric and transformation induced plasticity (TRIP) strain is defined, see Equation (5.11). For the derivation of the material model, the actual time step is denoted by t_{n+1} and the last time step as t_n, respectively.

As an initialization step, the accumulated plastic strains α_{hist} (offset), which are taken from the forming simulations, are applied to the macroscopic continuum at time $t = 0\,\text{s}$ and passed to the microscale as a constant value in each integration point, cf. Section 6.2.2. Then, the following steps, which are summarized in Table 8.3, are carried out at every time step t_{n+1}. In addition to the macroscopic total strains $\bar{\boldsymbol{\varepsilon}}_{n+1}$, the macroscopically computed temperature is passed onto the microscale. In order to achieve numerical stability, the temperature of last time step $\bar{\theta}_n$ is considered as a state variable θ_{n+1}. Based thereon, the actual volume fractions of the product phases are determined. Therefore, the Koistinen-Marburger differential equation is utilized to compute the actual martensitic volume fraction in case of a diffusionless austenite-to-martensite phase transformation, see Section 4.1.2. If a diffusion controlled phase transformation from e.g. austenite to pearlite occurs, the Johnson-Mehl-Avrami-Kolmogorov (JMAK) equation is considered instead, see Section 4.1.1. The remaining volume fraction of the parent phase can be defined by balancing, since the sum of all phases present has to equal one, cf. Equation (5.18).

According to the computed volume fractions of austenite and martensite, or austenite and pearlite, respectively, the phase transformation is depicted in the RVE. Initially at time $t = 0\,\mathrm{s}$, all elements have been austenitic. Now, at time t_{n+1}, a certain number of elements is switched from austenite to martensite or pearlite. As many elements are switched, until their volume in relation to the RVE size reflects the calculated volume fraction of the product phase. This means exemplary for the diffusionless phase transformation to martensite that the ratio of the volume of the martensitically chosen elements V_{M} to the volume of the RVE V equals the total martensitic volume fraction c^{M}, i.e., $c^{\mathrm{M}} = \frac{V_{\mathrm{M}}}{V}$. Different possibilities to choose martensitic or pearlitic elements can be thought of, which are in detail studied in Section 9. With the switch from austentite to martensite or pearlite, the accumulated plastic strains are set to zero, since by undergoing a phase transformation the shearing of the atomic lattice comes along with a relaxation.

Furthermore, the temperature θ_{n+1} serves as an input parameter in the interpolation of thermal, elastic and phase transformational material parameters such as κ, μ, k, c_ρ, α_{T}, K_{trip} and K_{tv}, see Section 5.3. These are the bulk and shear modulus κ and μ, the heat conduction coefficient k, the product of the density and specific heat capacity abbreviated as c_ρ and the heat expansion coefficient α_{T}. Furthermore, K_{trip} and K_{tv} are coefficients to compute the TRIP strains and the transformation volumetric strains. The yield strength y_{n+1} and the linear hardening parameter h_{n+1} also depend on the accumulated plastic strains of the last time step α_n in addition to the temperature θ_{n+1}.

The respective single-scale formulas of the elastic, plastic, thermal and transformation volumetric strain parts are adopted from the macroscopic formulation straightforwardly, but with respect to the TRIP strains, small adaptions are inevitable. By definition following Leblond [99] for a macroscopic material description, the TRIP strains base on the deviatoric part of the stresses and the change in the volume fraction $\Delta c^{\mathrm{M}}_{n+1}$ or $\Delta c^{\mathrm{P}}_{n+1}$, respectively, cf. Equation (5.14). The overall martensitic or pearlitic volume fraction in the RVE increases from time step to time step, while in one microscopic integration point, there is either 100 % austenite or 100 % martensite (pearlite). As a consequence, it is inevitable to consider macroscopic quantities for the computation of the TRIP strains such as the macroscopic deviatoric part of the stresses $\operatorname{dev} \bar{\boldsymbol{\sigma}}_n$. Applying a radial return algorithm enables to determine the microscopic tangent moduli $\mathbb{C}_{n+1}$ and stresses $\boldsymbol{\sigma}_{n+1}$.

Based thereon, the macroscopic stresses $\bar{\boldsymbol{\sigma}}$ and the macroscopic algorithmic consistent tangent moduli $\bar{\mathbb{A}}$ are finally computed by homogenization following Equations (8.6) and (8.42). For the formulation of the thermo-mechanical coupling terms on the macroscale, κ as mechanical and k, c_ρ and α_{T} as thermal material parameters have to be averaged as well, i.e.,

$$\langle(\bullet)\rangle = \frac{1}{V}\int_V (\bullet)\ \mathrm{d}V \quad \text{for } (\bullet) \in \{\kappa, k, c_\rho, \alpha_\mathrm{T}\}\,. \tag{8.45}$$

Table 8.3: Material modeling at time step t_{n+1} computing phase specific stresses and material tangent, which are averaged for effective stresses and tangent moduli. Exemplary algorithm for the diffusionless phase transformation from austenite to martensite.

```
$t = 0\,\mathrm{s}$ initialize history of accumulated plastic strains resulting from hot bulk
         forming if necessary, see Section 6.2.2

(I) Get temperature $\theta_{n+1} = \bar{\theta}_n$ and total strains $\bar{\boldsymbol{\varepsilon}}_{n+1}$ from macroscale
(II) Compute martensitic volume fraction
    $c^{\mathrm{M}}_{n+1}(\theta_{n+1}) = \begin{cases} 1 - \exp\left(-\frac{\theta_{\mathrm{Ms}}-\bar{\theta}_n}{\theta_{\mathrm{M0}}}\right) & \text{for } \theta_{n+1} \le \theta_{\mathrm{Ms}} \\ 0 & \text{else} \end{cases}$
    and saturation function $f_{n+1}(c^{\mathrm{M}}_{n+1}) = (2 - c^{\mathrm{M}}_{n+1})c^{\mathrm{M}}_{n+1}$ with $f'_{n+1}(c^{\mathrm{M}}_{n+1}) = 2(1 - c^{\mathrm{M}}_{n+1})$
(III) Choose elements $e_{\mathrm{M}}$ with volume $V_{\mathrm{M}}$ to represent martensite
        such that it holds $\frac{V_{\mathrm{M}}}{V} = c^{\mathrm{M}}$ with $V$ as volume of the RVE and $V_{\mathrm{M}} = \sum_{e_{\mathrm{M}}} V_{e_{\mathrm{M}}}$
        (for different RVE definitions see Section 9)
(IV) Get history values of accumulated plastic strains $\alpha_n$, plastic strains $\boldsymbol{\varepsilon}^{\mathrm{p}}_n$,
    TRIP strains $\boldsymbol{\varepsilon}^{\mathrm{trip}}_n$ and martensitic volume fraction $c^{\mathrm{M}}_n$
(V) Interpolate material parameters $\kappa, \mu, k, c_\rho, \alpha_{\mathrm{T}}, K_{\mathrm{trip}}, K_{\mathrm{tv}}$ for $\theta_{n+1}$, see Section 5.3
(VI) Compute thermal strains $\boldsymbol{\varepsilon}^{\mathrm{tv}}_{n+1} = \frac{1}{3}K_{\mathrm{tv}}\mathbf{1}$
    and transformation volumetric strains $\boldsymbol{\varepsilon}^{\theta}_{n+1} = \alpha_{\mathrm{T}}(\theta_{n+1} - \theta_0)\mathbf{1}$
(VII) Compute elastic trial strains $\boldsymbol{\varepsilon}^{\mathrm{e,trial}}_{n+1} = \boldsymbol{\varepsilon}_{n+1} - \boldsymbol{\varepsilon}^{\mathrm{p}}_n - \boldsymbol{\varepsilon}^{\mathrm{trip}}_n - \boldsymbol{\varepsilon}^{\mathrm{tv}}_{n+1} - \boldsymbol{\varepsilon}^{\theta}_{n+1}$
    and deviatoric trial stresses $\operatorname{dev}\boldsymbol{\sigma}^{\mathrm{trial}}_{n+1} = 2\mu \operatorname{dev}\boldsymbol{\varepsilon}^{\mathrm{e,trial}}_{n+1}$
    and deviatoric trial tangent $\mathbb{C}^{\mathrm{trial}}_{n+1} = \frac{2\mu}{\gamma}\mathbb{P}$ with $\mathbb{P} = \mathbb{I} - \frac{1}{3}\mathbf{1} \otimes \mathbf{1}$
          with $\gamma = 1 + 3\mu\, K_{\mathrm{trip}} f'(c^{\mathrm{M}}_{n+1})\Delta c^{\mathrm{M}}_{n+1}$ and $\Delta c^{\mathrm{M}}_{n+1} = c^{\mathrm{M}}_{n+1} - c^{\mathrm{M}}_n$
(VIII) Compute yield stress $y_{n+1}(\theta_{n+1}, \alpha_n)$ by two-step interpolation scheme, see Section 5.3
(IX) Compute yield criterion $\Phi^{\mathrm{trial}}_{n+1} = \|\operatorname{dev}\boldsymbol{\sigma}^{\mathrm{trial}}_{n+1}\| - \sqrt{\frac{2}{3}}y_{n+1}$
    if $\Phi^{\mathrm{trial}}_{n+1} \le 0$ then
        $\alpha_{n+1} = \alpha_n$, $\boldsymbol{\varepsilon}^{\mathrm{p}}_{n+1} = \boldsymbol{\varepsilon}^{\mathrm{p}}_n$, $\boldsymbol{\varepsilon}^{\mathrm{trip}}_{n+1} = \boldsymbol{\varepsilon}^{\mathrm{trip}}_n$
        $\operatorname{dev}\boldsymbol{\sigma}_{n+1} = \operatorname{dev}\boldsymbol{\sigma}^{\mathrm{trial}}_{n+1}$, $\mathbb{C}_{n+1} = \mathbb{C}^{\mathrm{trial}}_{n+1}$
    else radial return algorithm
        (i) Solve residuum function
            $r(\Delta\lambda) = \frac{\|\operatorname{dev}\boldsymbol{\sigma}^{\mathrm{trial}}_{n+1}\| - 2\mu\Delta\lambda}{\gamma} - \sqrt{\frac{2}{3}}y_{n+1} = 0$
        (ii) Update $\alpha_{n+1} = \alpha_n + \sqrt{\frac{2}{3}}\Delta\lambda_{n+1}$,  $\boldsymbol{\varepsilon}^{\mathrm{p}}_{n+1} = \boldsymbol{\varepsilon}^{\mathrm{p}}_n + \Delta\lambda_{n+1}\boldsymbol{n}_{n+1}$
        (iii) Update deviatoric stresses $\operatorname{dev}\boldsymbol{\sigma}_{n+1} = \frac{1}{\gamma}\left(\operatorname{dev}\boldsymbol{\sigma}^{\mathrm{trial}}_{n+1} - 2\mu\Delta\lambda_{n+1}\boldsymbol{n}_{n+1}\right)$
        (iv) Compute tangent moduli with Jacobian $J(\Delta\lambda) = \partial r(\Delta\lambda)/\partial\Delta\lambda$
            $\mathbb{C}_{n+1} = \frac{2\mu}{\gamma}\mathbb{P} - \Delta\lambda\frac{(2\mu)^2}{\gamma}\frac{1}{\|\operatorname{dev}\boldsymbol{\sigma}^{\mathrm{trial}}_{n+1}\|}(\mathbb{P} - \boldsymbol{n}_{n+1} \otimes \boldsymbol{n}_{n+1}) + \left(\frac{2\mu}{\gamma}\right)^2\frac{1}{J}\boldsymbol{n}_{n+1} \otimes \boldsymbol{n}_{n+1}$
(X) Update TRIP strains $\boldsymbol{\varepsilon}^{\mathrm{trip}}_{n+1} = \boldsymbol{\varepsilon}^{\mathrm{trip}}_n + \frac{3}{2}K_{\mathrm{trip}} \operatorname{dev}\bar{\boldsymbol{\sigma}}_n f'_{n+1}(c^{\mathrm{M}}_{n+1})\Delta c^{\mathrm{M}}_{n+1}$
    and elastic strains $\boldsymbol{\varepsilon}^{\mathrm{e}}_{n+1} = \boldsymbol{\varepsilon}_{n+1} - \boldsymbol{\varepsilon}^{\mathrm{p}}_{n+1} - \boldsymbol{\varepsilon}^{\mathrm{trip}}_{n+1} - \boldsymbol{\varepsilon}^{\mathrm{tv}}_{n+1} - \boldsymbol{\varepsilon}^{\theta}_{n+1}$
(XI) Add volumetric stresses $\boldsymbol{\sigma}_{n+1} = \operatorname{dev}\boldsymbol{\sigma}_{n+1} + \kappa \operatorname{tr}\boldsymbol{\varepsilon}^{\mathrm{e}}_{n+1}\mathbf{1}$
    and volumetric tangent $\mathbb{C}_{n+1} = \mathbb{C}_{n+1} + \kappa\mathbf{1} \otimes \mathbf{1}$
```

8.8 Quadratic measure of microscopic fluctuations

By definition it holds that the volume average of the microscopic fluctuations of the stresses equals zero in FE^2 methods, i.e.,

$$\langle \tilde{\boldsymbol{\sigma}} \rangle = 0 \quad \text{with} \quad \tilde{\boldsymbol{\sigma}} = \boldsymbol{\sigma} - \bar{\boldsymbol{\sigma}} \,. \tag{8.46}$$

However, it can be helpful to have a measure of the microscopic stress fluctuations on the macroscopic scale. Therewith, the influence of the microscopic fluctuation on the macroscopic stresses can be displayed and evaluated on the macroscale. As a consequence, it enables to analyze the impact of the microscopic fluctuations on the macroscopic properties of the component, such as strength or durability and provides an efficient tool to assess engineering usability. Thereby, it is possible to resolve the origin of the evolving macroscopic stresses, which are a consequence of cooling and a superimposed phase transformation.

Hence, quadratic measures are defined for the stress components based on the proposal in e.g. Uebing et al. [192]. In the following derivation, the position vector $\bar{\boldsymbol{x}}$ refers to the macroscopic actual coordinates of the integration point, for which the measure is to be determined. The RVE with volume V is attached to this integration point. The macroscopic $\bar{\boldsymbol{x}}_1$-$\bar{\boldsymbol{x}}_2$-coordinate system is rotated around an angle α, so that the $\bar{\boldsymbol{x}}_1^*$-axis of the rotated $\bar{\boldsymbol{x}}_1^*$-$\bar{\boldsymbol{x}}_2^*$-coordinate system points in direction of the position vector $\bar{\boldsymbol{x}}$, see Figure 8.3.

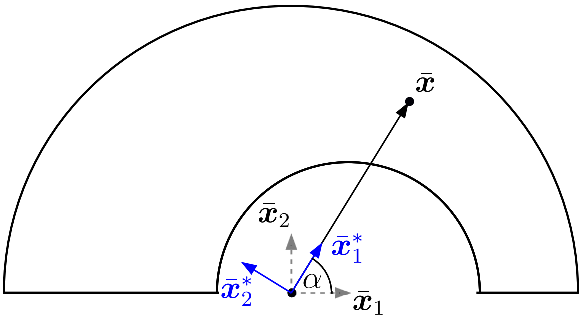

Figure 8.3: Considering the macroscopic position vector $\bar{\boldsymbol{x}}$, the $\bar{\boldsymbol{x}}_1$-$\bar{\boldsymbol{x}}_2$-coordinate system is rotated around angle α. The $\bar{\boldsymbol{x}}_1^*$-axis of the resulting $\bar{\boldsymbol{x}}_1^*$-$\bar{\boldsymbol{x}}_2^*$-coordinate system points in direction $\bar{\boldsymbol{x}}$.

The related rotation matrix $\bar{\boldsymbol{R}}$ in the $\bar{\boldsymbol{x}}_1$-$\bar{\boldsymbol{x}}_2$-plane is given by

$$\bar{\boldsymbol{R}} = \begin{pmatrix} \cos(\alpha) & -\sin(\alpha) & 0 \\ \sin(\alpha) & \cos(\alpha) & 0 \\ 0 & 0 & 1 \end{pmatrix} . \tag{8.47}$$

It is passed onto the microscale, where it is a constant quantity for the RVE. Given the microscopic stress tensor $\boldsymbol{\sigma}$, it can be rotated according to the macroscopic angle α by

$$\boldsymbol{\sigma}^* = \bar{\boldsymbol{R}} \cdot \boldsymbol{\sigma} \cdot \bar{\boldsymbol{R}}^{\mathrm{T}} \,. \tag{8.48}$$

For the fluctuation part of the microscopic stresses one computes with $\tilde{\boldsymbol{\sigma}} = \boldsymbol{\sigma} - \bar{\boldsymbol{\sigma}}$

$$\tilde{\boldsymbol{\sigma}}^* = \bar{\boldsymbol{R}} \cdot \tilde{\boldsymbol{\sigma}} \cdot \bar{\boldsymbol{R}}^{\mathrm{T}} = \bar{\boldsymbol{R}} \cdot (\boldsymbol{\sigma} - \bar{\boldsymbol{\sigma}}) \cdot \bar{\boldsymbol{R}}^{\mathrm{T}} = \bar{\boldsymbol{R}} \cdot \boldsymbol{\sigma} \cdot \bar{\boldsymbol{R}}^{\mathrm{T}} - \bar{\boldsymbol{R}} \cdot \bar{\boldsymbol{\sigma}} \cdot \bar{\boldsymbol{R}}^{\mathrm{T}} \,. \tag{8.49}$$

Therein, the tangential part of the fluctuations of the stresses are identified as the stress component $\tilde{\sigma}_{\text{tang}} = \tilde{\sigma}^*_{22}$. Its quadratic measure $\|\tilde{\sigma}_{\text{tang}}\|^V_{\mathcal{L}^2}$ is defined as

$$\|\tilde{\sigma}_{\text{tang}}\|^V_{\mathcal{L}^2} = \sqrt{\langle \tilde{\sigma}^2_{\text{tang}} \rangle} \quad \text{with} \ \langle \tilde{\sigma}^2_{\text{tang}} \rangle = \frac{1}{V} \int \tilde{\sigma}^2_{\text{tang}} \, \mathrm{d}V \, . \tag{8.50}$$

Therein, the $\mathcal{L}^2$-norm is defined as $\|(\bullet)\|_{\mathcal{L}^2} = \left(\int (\bullet)^2 \, \mathrm{d}V \right)^{\frac{1}{2}}$ and a modified version is given by $\|(\bullet)\|^V_{\mathcal{L}^2} = \left(\frac{1}{V} \int (\bullet)^2 \, \mathrm{d}V \right)^{\frac{1}{2}}$, which takes into account the volume of the RVE.

9 Microstructural analysis

As stated in Section 4.2, residual stresses can be classified by the scale, they act on, cf. MACHERAUCH ET AL. [108]. The differentiation into macroscopic (first type) and microscopic (second and third type) residual stresses motivates a two-scale analysis in order to resolve microscopic phenomena such as the phase transformation directly on the lower scale. Therefore, the two-scale direct micro-macro transition approach shall be utilized. In a first step, different schemes to depict the austenite-to-martensite phase transformation on the microlevel during quenching are compared and evaluated with respect to the macroscopic and microscopic stress evolution. Different aspects as the importance of individual grain orientations or phase-specific stress contributions can be investigated.

9.1 Evolution schemes of martensite on the level of a representative volume element (RVE)

In a two-scale Finite Element Method (FEM), a microscopic boundary value problem is solved in every macroscopic integration point instead of direct computation of the material behavior, as described in Section 8. The underlying microscopic boundary value problem consists of a representative volume element (RVE) with a suitable material model and appropriate boundary conditions, see Section 8.7. Here, periodic boundary conditions on an isothermal problem are applied. Based on the temperature θ, the martensitic volume fraction c^{M} is determined utilizing the Koistinen-Marburger differential equation, see Equation (4.4). In case of fast cooling, i.e., diffusionless phase transformation, the initial purely austenitic RVE has to switch elements to martensite to fulfill the computed phase distributions of austenite and martensite, respectively. For this purpose, the here analyzed martensitic evolution strategies can be taken into account as a selection of a large number of alternatives. A circular inclusion, a diagonal structure, an arbitrary switch and a grain structure are considered. It holds that all types of martensitic evolution are defined for an RVE with the same dimension and the same discretization, i.e., a structured mesh with 4-noded linear quadrilaterals. Based on experimental measurements, the final volume fractions are always set to 87 % martensite and 13 % retained austenite. These RVEs with the respective evolution strategies are to be evaluated in terms of the stress evolution on both scales. By comparison, the advantages and disadvantages of the different representations are found.

Circular evolution One of the most intuitive evolution strategies is the growth of a circular martensitic inclusion in an austenitic matrix, cf. UEBING ET AL. [188]. Therefore, the computed martensitic volume fraction c^{M} is related to the radius r of the centered circular inclusion. For every finite element n, the distance $|d_n| = |S_n - S|$ between the element's midpoint S_n and the midpoint S of the RVE is computed. If that distance is greater than the radius of the inclusion, i.e., $|d_n| > r$, the element stays austenitic. If that distance is smaller than or equal to the radius of the inclusion, i.e., $|d_n| \leq r$, the element is switched to martensite. Therein, the radius r is determined based on the actual volume fraction of martensite c^{M} as $r = \sqrt{V\, c^{\mathrm{M}}/\pi}$, which is equivalent to $\pi\, r^2 = c^{\mathrm{M}} V \approx V_{\mathrm{M}}$ with V_{M} as volume of all martensitic elements and V as total volume of the RVE. The schematic representation of such a circular evolution strategy is given in Figure 9.1, which also depicts the approximated martensitic volume V_{M}. It is important to keep in mind that for high percentages of martensite, the circular inclusion exceeds the RVE bounds, and thus, those volume fractions cannot be depicted accurately.

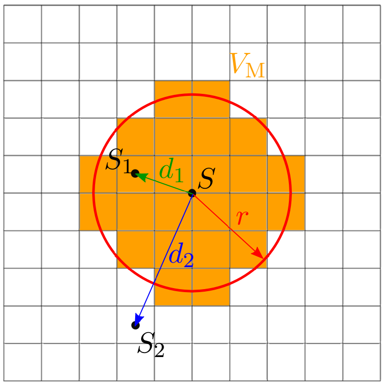

$|d_1| \leq r \quad \Rightarrow \quad$ martensite

$|d_2| > r \quad \Rightarrow \quad$ austenite

Figure 9.1: Schematic illustration of a circular inclusion for product phase in parent phase matrix, here applied to the austenite-to-martensite phase transformation. Martensitic elements approximate the martensitic volume fraction by V_M.

Diagonal structure A second pattern for representation of the austenite-to-martensite phase transformation is a very technical one, inspired by the known formation of martensitic as plate or lath martensite. The regular mesh is divided into subsections of 5×5 elements, which form a unit and are interpreted as a grain. Each of these grains is assigned one main axis or orientation of $\{-45°, 0°, 45°, 90°\}$ to determine the switching order of the elements to martensite, cf. Figure 9.2. Accordingly, several of these subdivisions have the central vertical or horizontal row of elements as their principal axis, while others are oriented along one of the two diagonals.

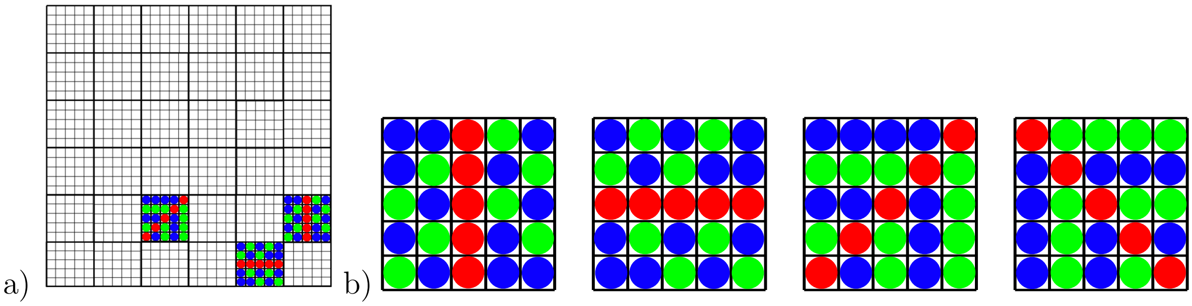

Figure 9.2: a) RVE with subunits, that depict grains, and the associated finite element mesh. b) Schematic representation of the phase transformation using a diagonal structure in one of those grains. At first, red elements switch to martensite, then the green ones and latest the blue elements depending on the actual martensitic volume fraction.

Taking the partitioning of the RVE into grains or subunits into account, the choice of orientation per subunit is done arbitrarily. Furthermore, the numbering of the grains in the microstructure is also coincidental. The amount of grains to be set to martensite depends on the martensitic volume fraction c^M, which is determined with the Koistinen-Marburger equation, see Equation (4.4). Thus, the transformation is implemented as given in Figure 9.2b: in a first step, elements along the main axis, i.e., the middle element row or the diagonal (red) of all grains switch to martensite according to the actual martensitic volume fraction. Starting from this main axis, in a second step, martensitic needles are formed at an angle of 45° (green). In a last step, so many of the remaining elements (blue) are switched until the computed volume fraction is reached. Since the RVE is discretized by 30 × 30 elements, 36 (6 × 6) of these grain structures can be found.

This switching order red→green→blue holds for the complete RVE and is not interpreted grain-wise. The later would mean that all 25 finite elements of one grain are switched by the rule red→green→blue, before the red elements of a second grain are considered to be martensite. Instead, all red marked elements in the complete RVE are switched to martensite according to the actual martensitic volume fraction before the first green element is set to martensite.

Arbitrary switch Another method to depict the austenite-to-martensite phase transformation on microscopic level is an arbitrary element-wise switch, see also UEBING ET AL. [190]. Therefore, so many elements are switched to martensite until their volume V_{M} related to the RVE size V approximates the computed actual martensitic volume fraction c^{M} closely. There is no recognizable pattern for the order of the element switch, but this order is fixed so that all microstructures (in different integration points) behave in the same way according to the temperature. In order to study the influence of the randomness on the martensitic evolution, different permutations are considered, which are referred to as cases 1 to 4. The final phase distributions consisting of 87% martensite and 13% retained austenite are given in Figure 9.3 indicating martensite in red and austenite in white.

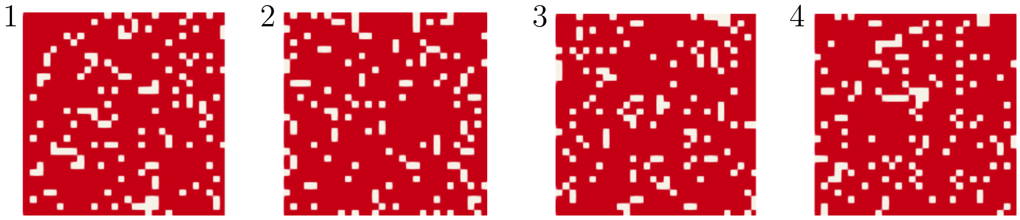

Figure 9.3: Four different final microstructures - case 1 to case 4 - of martensite (red) and retained austenite (white) using an arbitrary switching scheme, adopted from UEBING ET AL. [190].

Grain structure A fourth scheme relies on an experimental reconstruction of the initial austenitic grains, see Figure 9.4. With the open source software NEPER [129], which is helpful for the polycrystal construction and its meshing, an equivalent microstructure consisting of a given number of grains is built, see Figure 9.5. This number can randomly be chosen, so that if the number of grains is equal to the number of elements in the mesh, the arbitrary switch is restored. The phase transformation is described in such a way that element by element and one grain after the other grain switches, whereby the grain order is random and arbitrary. But again, this order is the same for every representative volume element in each macroscopic integration point.

However, the prescribed RVEs built from NEPER [129], which are shown in Figure 9.5, do not possess periodic grains at the edges, although periodic displacement boundary conditions are applied. Thus, a small C-code is used to obtain such grain structures, see Figure 9.6. Input variables are the number of grains, the number of finite elements per edge of the RVE as well as four key numbers, which are used to produce the Voronoi tessellation, see Appendix F.

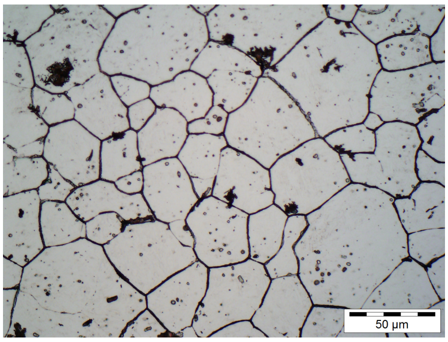

Figure 9.4: Reconstruction of austenitic grains provided by IFUM.

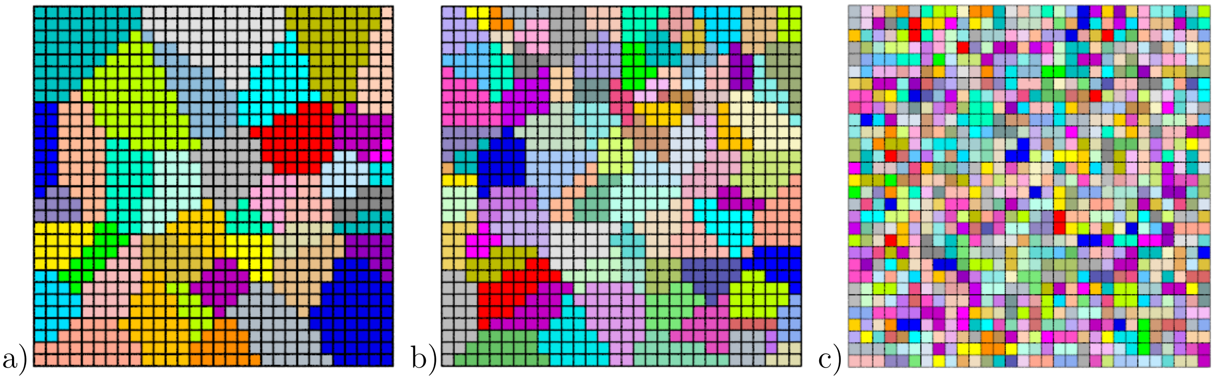

Figure 9.5: Different microstructures constructed with Neper [129] with a) 40 grains, b) 90 grains and c) 900 grains and discretized with 30 × 30 finite elements, such that the 900 grains reproduce the arbitrary switch.

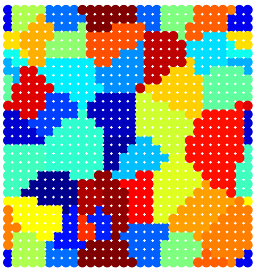

Figure 9.6: RVE with periodic grain structure along the boundary, built up with a small C-code, which is given in Appendix F. The number of grains equals 40, the mesh density is 30 × 30 finite elements.

9.2 Two-scale boundary value problem

In order to compare the previously defined evolution strategies to depict the austenite-to-martensite phase transformation on the microscale, the following two-dimensional boundary value problem is taken into account. On the macroscale, a cut of a circular geometry made from the Cr-alloyed steel 100Cr6 with eccentric hole is considered with an angle $\alpha = 5°$. It is defined with an outer radius of $r = 17.5\,\text{mm}$ and a hole radius of $r_h = 8\,\text{mm}$ with an eccentricity of 3.5 mm, see Figure 9.7. It is evident that no radial symmetry exists, but it is assumed for simplification. Thus, in addition to static support, displacement boundary conditions are applied along both cutting edges, i.e., it holds $\bar{u}_{\text{tang}} = 0\,\text{mm}$. Starting with the initial temperature of 1005 °C, the cooling following the temperature evolution presented in Figure 6.20 is applied to the lateral surface. As a consequence, a diffusionless phase transformation from austenite to martensite as discussed in previous sections and examples is evoked. The geometry is discretized with $\overline{30}$[4.)] elements in radial direction, following the suggestion in Uebing et al. [191], and one element concerning the slice's height. During the phase transformation, the initial time step width of $\Delta t = 0.1\,\text{s}$ is reduced to $\Delta t = 0.01\,\text{s}$ or even to $\Delta t = 0.025\,\text{s}$, if necessary.

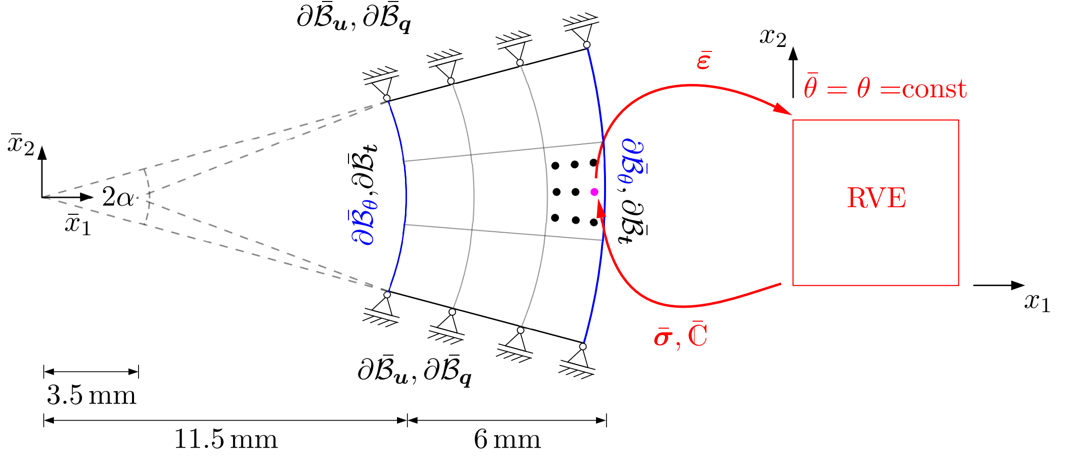

Figure 9.7: Two-scale boundary value problem for the comparison of different schemes for the austenite-to-martensite phase transformation. The results are compared regarding the violet marked integration point.

In order to compare the prescribed possibilities to depict the phase transformation on the microscale, namely with a circular martensitic inclusion, a diagonal structure, an arbitrary switch or a grain structure, the following set-up is chosen. The RVE is defined as a square with the size of 0.01 mm × 0.01 mm and discretized with a structured mesh of 30 × 30 linear quadrilateral elements. A mesh density study is provided in Uebing et al. [191], see also Section 10.1. Periodic boundary conditions are applied in all cases for the displacement. Thereby, all four computations utilizing the given RVE types should show same behavior, before the cooling evokes a martensitic phase transformation.

9.3 Macroscopic and microscopic analysis

In this section, the different strategies to depict the martensitic evolution on RVE level are compared. Therefore, the evolution of macroscopic as well as microscopic stresses or strains and phase fractions are in focus. For the evaluation of the results, pictographs are introduced for the different kinds of RVEs, see Figure 9.8.

9.3.1 Circular inclusion

The advantage of simplicity for realization of the martensitic evolution as circular inclusion in an austenitic matrix clearly comes along with certain decisive disadvantages

---

[4.)] In order to distinguish between the macroscopic and microscopic discretizations, an overline $(\overline{\bullet})$ marks macroscopic mesh sizes. The microscopic mesh densities remain unmarked.

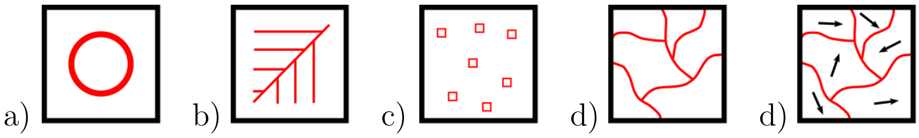

Figure 9.8: Pictographs of the different types of RVEs, that are a) a circular inclusion, b) the diagonal structure, c) the arbitrary switch and d) the grain structure, e) for which grain orientations will be defined in Section 9.4.

as observed in Figures 9.9, 9.10 and 9.11. Therein, different macroscopic mesh densities are considered, which deviates from previous definition of $\overline{30}$ elements in radial and one element in circumferential direction. For a first analysis, the number of elements in radial direction is set to ten, but is later refined up to $\overline{50}$ elements. Each legend gives further information regarding the macroscopic and microscopic discretization: the first number refers to the macroscopic mesh density, e.g. $\overline{10} \times \overline{1}$, i.e., ten elements in radial direction and one element in circumferential direction on macroscale; the second number describes the microscopic discretization, e.g. 20×20, i.e., 20 elements in x_1- and 20 elements in x_2-direction in the RVE. Since the distance between the midpoint of an element and the center of the RVE is evaluated, whether the element switches to martensite or stays austenitic, the martensitic phase growth rotational symmetric. The evolution of the martensitic volume fraction is not smooth but resembles a stair case function, since either no elements or at least four elements or more are switched in one computational step, see Figure 9.9. This inaccurate and coarse depiction of the phase fraction is also reflected on the microscale. The coarsest microscopic mesh with 20×20 elements leads more to a diamond shaped martensitic nucleus than a circular one. Moreover, it is obvious that for high percentages of martensite, which are experimentally observed, it is disadvantageous that the radius of the circular inclusion exceeds the boundary of the RVE. Thus, high martensitic phase fractions cannot be depicted precisely, independent of refinements of the microscopic discretization.

The evolution of the macroscopic tangential stresses $\bar{\sigma}_{\text{tang}}$ in the analyzed integration point shows first tensile stresses due to thermal contraction, cf. Figure 9.10a. These tensile stresses are superimposed with high compressive stresses by the increase of the martensitic volume fraction, which is accompanied by the volumetric expansion of the atomic lattice. The investigated integration point is located near the outer surface of the specimen and hence, undergoes the phase transformation earlier than the bulk material. Thus, as the cooling progresses and martensite starts to evolve in the bulk material, the region near the outer surface of the material shows tensile stresses once more, which are not resolved until the end of cooling. Figure 9.10b shows the stress component σ_{22} in relation to the previously depicted phase evolution on microscopic level. The microscopic results are evaluated for one integration point lying on the $\bar{x}_1$-axis, and thus, can be interpreted as microscopic tangential stresses. One can see that with onset of the phase transformation around $t = 8.6\,\text{s}$, compressive stresses arise in the martensitic elements, which are due to the volumetric expansion during the phase transformation. As a consequence, the austenitic matrix undergoes tensile stresses to ensure equilibrium. As the phase transition progresses, see $t = 10\,\text{s}$, $t = 15\,\text{s}$ or $t = 30\,\text{s}$, i.e., with the growth of the nucleus, the inner part shows tensile stresses and the newly switched martensitic area near the boundary of the nucleus shows compressive stresses.

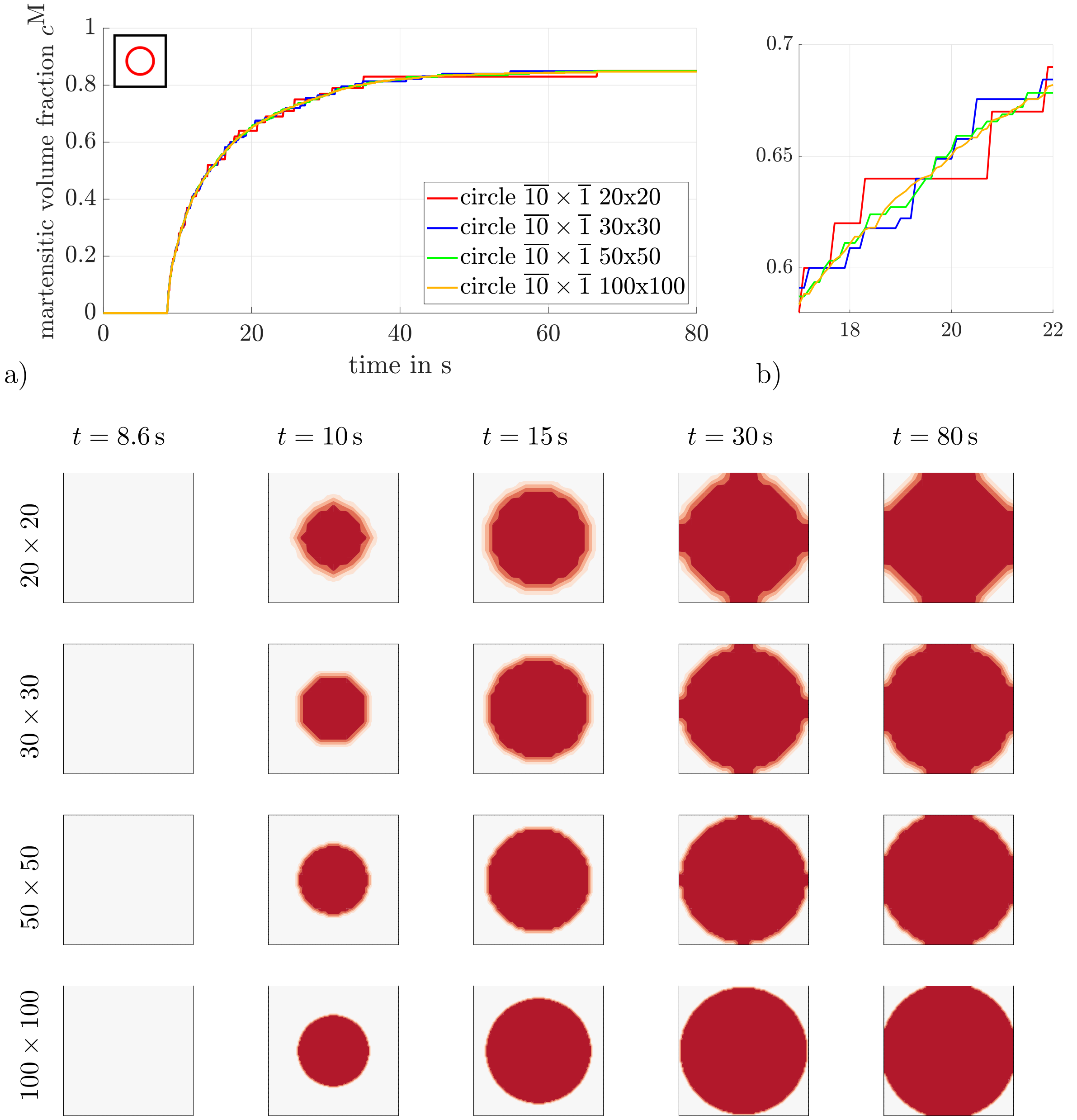

Figure 9.9: a) Evolution of martensitic phase fraction c^{M} in one integration point, marked in Figure 9.7, with b) zoom to compare different microscopic discretizations (20×20, 30×30, 50×50 and 100×100 elements) with a circular martensitic nucleus in an austenitic matrix. In addition, c) microscopic results regarding the evolution of the martensitic nucleus for the different discretizations at certain points in time.

As observed in Figure 9.11, the number of macroscopic elements in radial direction has no influence on the stress evolution. For a fixed microscopic mesh density of 50×50 elements, all four computations, either with $\overline{10}\times\overline{1}$, $\overline{20}\times\overline{1}$, $\overline{30}\times\overline{1}$ or $\overline{50}\times\overline{1}$ macroscopic elements, are in good accordance with respect to the evolution of the macroscopic tangential stress $\bar{\sigma}_{\mathrm{tang}}$ and show only small deviation.

The considered microscopic discretization results in strong oscillation, even if 50×50 microscopic elements are used, see Figure 9.10. In order to avoid these unwanted oscillation as well as the stair-case phenomenon regarding the phase evolution and to obtain

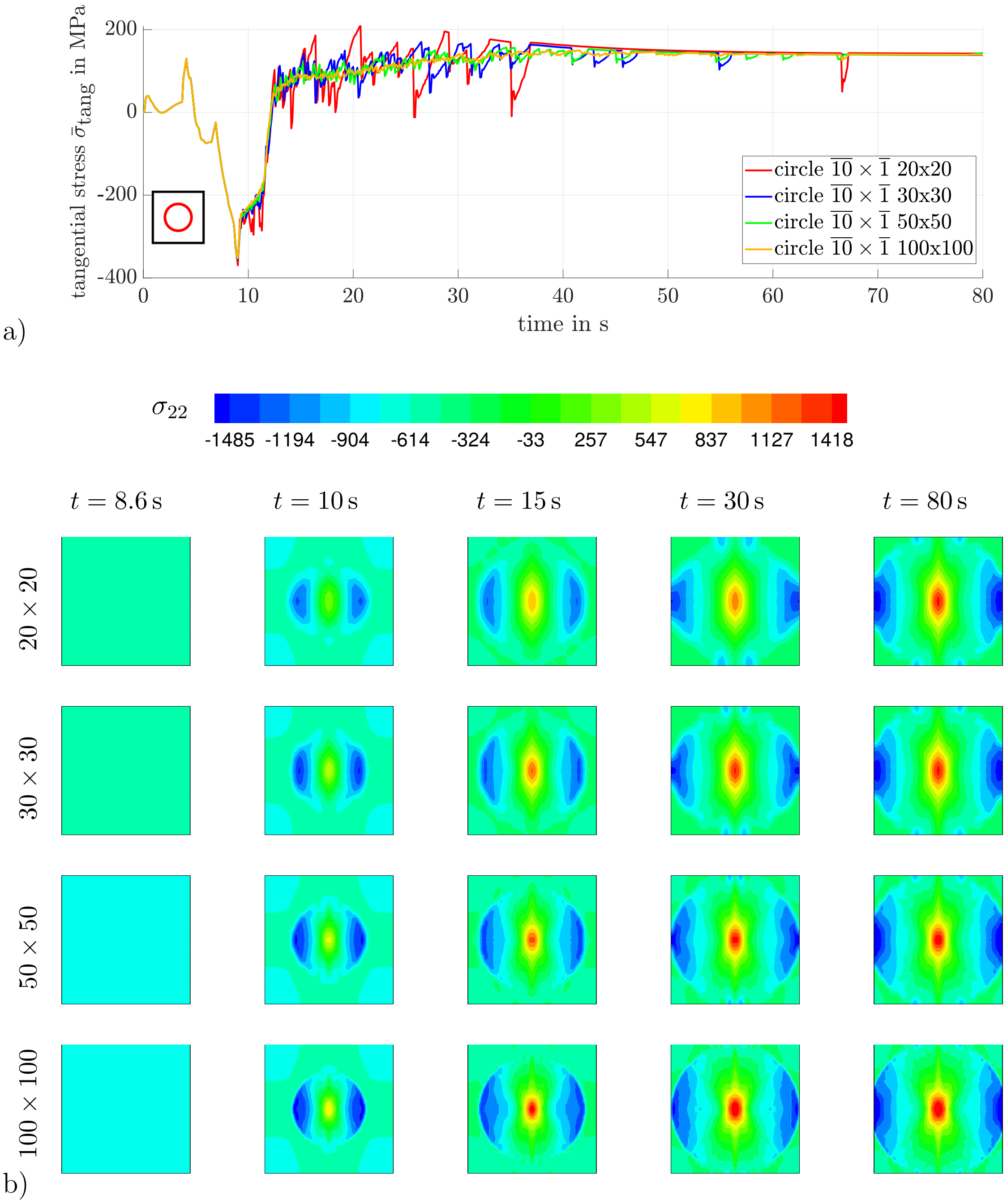

Figure 9.10: a) Evolution of macroscopic tangential stress $\bar{\sigma}_{\text{tang}}$ in MPa to compare different microscopic discretizations (20×20, 30×30, 50×50 and 100×100 elements) with a circular martensitic nucleus in an austenitic matrix and b) microscopic stress results showing component σ_{22} in MPa for the different discretizations at certain points in time.

a smoother curve for c^{M} or $\bar{\sigma}_{\text{tang}}$, a very fine microscopic discretization with at least 100 elements in each direction is inevitable. But thereby, the numerical costs of FE^2 computations for more complex boundary value problems on macroscopic level get out of hand, see Figure 9.12, which compares the computational time of one time step during the phase transformation as well as the total computational time. The consumed time of the computation with a fine discretization with 100×100 elements compared to a microstructure with 30×30 elements is 15 times as high. The additional time and numerical effort is not reasonable.

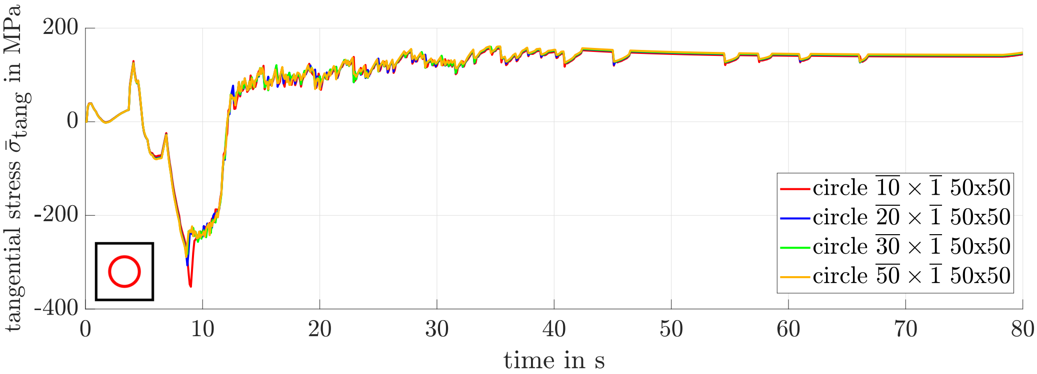

Figure 9.11: Evolution of macroscopic tangential stress $\bar{\sigma}_{\text{tang}}$ to compare different macroscopic mesh refinements with $\overline{10}$, $\overline{20}$, $\overline{30}$ or $\overline{50}$ elements in radial direction taking into account an RVE discretized with 50×50 elements with a circular martensitic nucleus in an austenitic matrix.

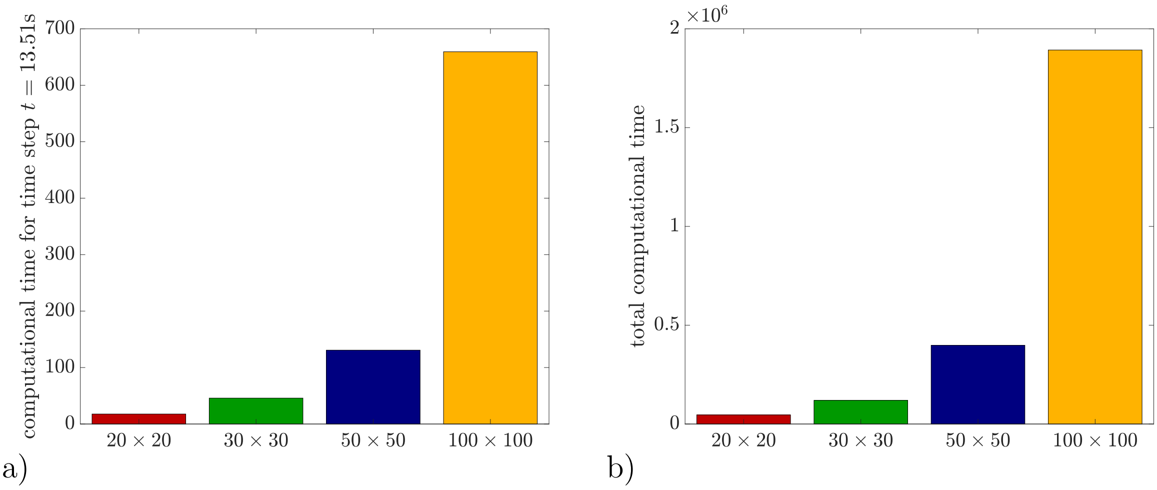

Figure 9.12: Comparison of computational time in seconds for different microscopic discretizations (20×20, 30×30, 50×50 and 100×100 elements) for a macroscopic mesh density of $\overline{10} \times \overline{1}$ elements.

9.3.2 Diagonal structure and arbitrary switch

Applying the diagonal structure or an arbitrary switch to describe the phase transformation from austenite to martensite gives6 qualitatively and quantitatively the same results regarding exemplary the martensitic volume fraction c^{M} and the macroscopic tangential stress evolution $\bar{\sigma}_{\text{tang}}$, cf. Figures 9.13 and 9.14. For the analyzed macroscopic integration point near the outer surface of the specimen, the development of the martensitic phase is modeled concordantly, cf. Figure 9.13a. On the minor scale, the complex switch pattern following the principle of the diagonal structure, is observed, while the arbitrary switch does not follow any design template, see Figure 9.13b. In relation, the microscopic stress component σ_{22} deviates slightly comparing the diagonal structure to the arbitrary switch, of which all four cases give very close results. The connected martensitic elements in the RVE using a diagonal structure show more pronounced compressive stresses than the RVEs with an arbitrary switching scheme, see Figure 9.14b. Moreover, that difference is also found as small deviations in the macroscopic tangential stresses $\bar{\sigma}_{\text{tang}}$. For instance, taking into account the stresses after a cooling time of ten seconds, $\bar{\sigma}_{\text{tang}}$ in case of a diagonal structure does not reflect such a high compressive stress peak as it is true for the four cases of the arbitrary switch. Taking a close look on the microscopic stress distribution in the RVEs, one finds small areas with prominent compressive stress values surrounded by lower compressive stresses. It holds for the diagonally structured RVE that these values are higher compared to the RVEs using an arbitrary switch. This results in the given macroscopic material response, which is computed by the volume averaging over the RVE, that the macroscopic tangential stresses $\bar{\sigma}_{\mathrm{tang}}$ are lower than for any case of an arbitrary switch at $t = 10\,\mathrm{s}$.

As more and more of the elements are switched representing the increasing martensitic volume fraction, complex phase and stress pattern form for both different evolution strategies. Concerning the microscopic stress component σ_{22} at $t = 10\,\mathrm{s}$ or $t = 15\,\mathrm{s}$, differences between the RVEs become visible, although the macroscopic averages for $\bar{\sigma}_{\mathrm{tang}}$ are overall in good accordance. At $t = 15\,\mathrm{s}$, the diagonally structured RVE shows more and higher tensile stress peaks compared to the four cases of the arbitrary switch. For the latter, clear differences between the RVEs are also observable. “Case 1änd “case 2ßeem to be more similar to the diagonally structured RVE than “case 3ör “case 4“. But, overall, the macroscopic tangential stress evolution for the four cases of arbitrary switch fits quite well. Around $t = 12\,\mathrm{s}$, the macroscopic compressive stresses are reduced and finally result in a tensile stress value around 120 MPa, which is in good fit with previous computations, see Figure 9.11. In the final state, the microstructure with the diagonal pattern shows complex interaction of tensile as well as compressive stress peaks, which are reduced in an arbitrary switching scheme. In order to analyze the mutual influence of neighboring elements during transformation, RVEs with grain structures are utilized in the following.

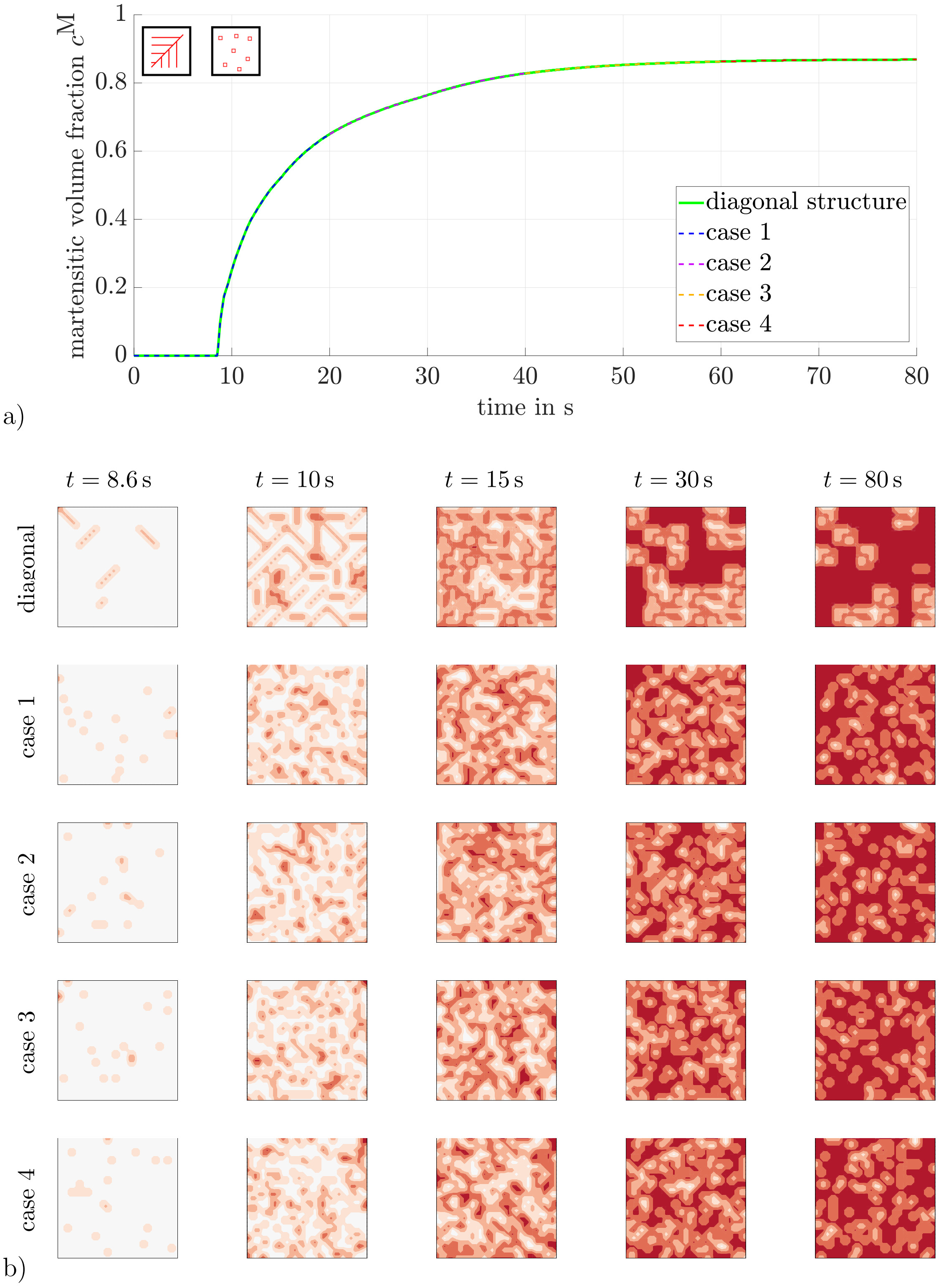

Figure 9.13: a) Evolution of martensitic volume fraction c^M in one integration point, marked in Figure 9.7, to compare different arbitrary switching schemes and the diagonally structured RVE and b) microscopic results regarding the evolution of martensite for the different schemes at certain points in time.

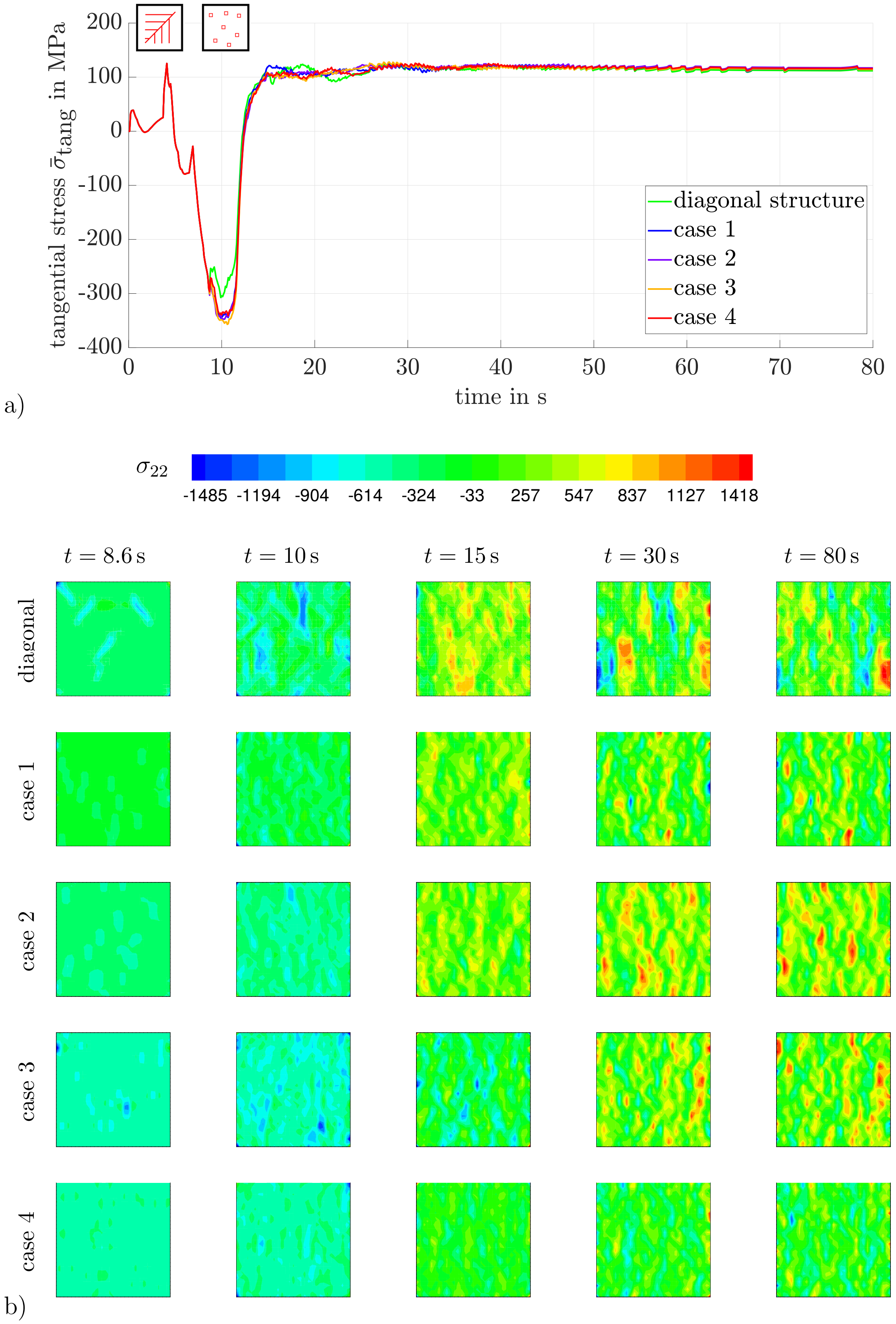

Figure 9.14: a) Evolution of macroscopic tangential stress $\bar{\sigma}_{\text{tang}}$ in MPa in one integration point, marked in Figure 9.7, to compare different arbitrary switching schemes and the diagonally structured RVE and b) microscopic stress results showing component σ_{22} in MPa for the different schemes at certain points in time.

9.3.3 Grain structure

The resulting macroscopic tangential stress $\bar{\sigma}_{\mathrm{tang}}$ and martensitic volume fraction c^{M} in case of taking into account microstructures consisting of a different number of grains, namely 40, 90 or 900, are shown in Figures 9.15 and 9.16.

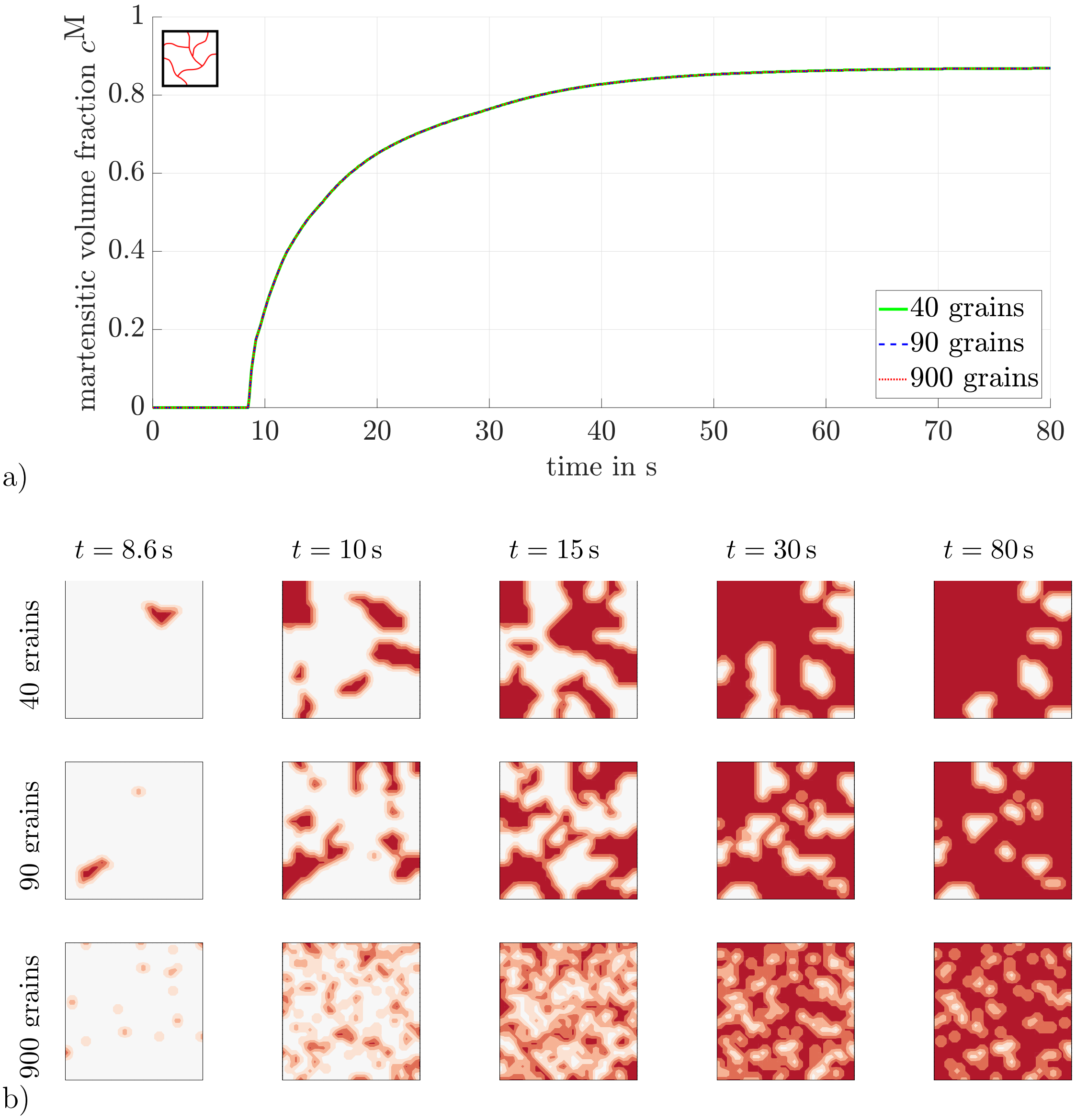

Figure 9.15: a) Evolution of martensitic phase fraction c^{M} in one integration point, marked in Figure 9.7, to compare different microscopic RVEs with 40, 90 or 900 grains and b) microscopic results regarding the martensitic evolution (red) in an austenitic matrix (white) for the different microstructures at certain points in time.

The macroscopic tangential stress evolution qualitatively fits the previously analyzed computations with RVEs based on a circular inclusion, a diagonal structure or an arbitrary switch. If the number of grains equals the number of microscopic elements, i.e., 900 grains and elements, the arbitrary switch is restored, as expected. Reducing the number of grains to a tenth, in this case 90 grains, effects the observed stress behavior during the phase transformation process. The differences are even more prominent in case of a microstructure with 40 grains, see Figure 9.16. Here, the final stress value exceeds the computations with RVEs taking into account 90 or 900 grains by approximately 25 MPa, see Figure 9.16a. It is found that the grain size has impact on the evolving stresses, i.e., if the phase transformation happens grain by grain, neighboring elements influence their volumetric expansion mutually and as a consequence also the stress evolution. The term grain by grain means that all elements of a first grain are switched before the first element of a second grain is considered as martensite. The quotient of the volume of all martensitic elements V_{M} and the volume of the RVE V has to be in accordance with the computed martensitic volume fraction c^{M}, independent to which grain the individual element belongs to.

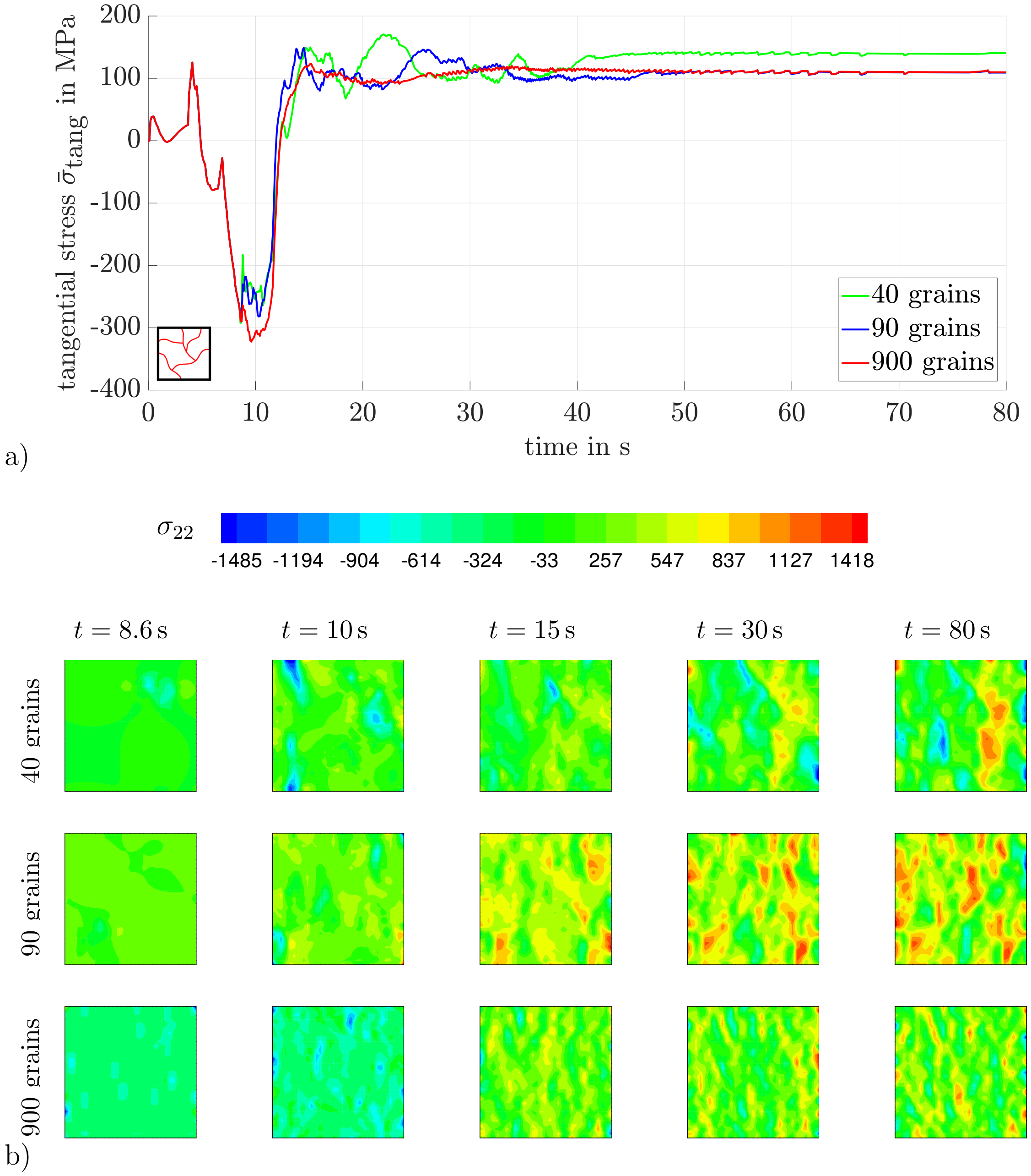

Figure 9.16: a) Evolution of macroscopic tangential stress $\bar{\sigma}_{\mathrm{tang}}$ in MPa in one integration point, marked in Figure 9.7, to compare different RVEs with 40, 90 or 900 grains and b) microscopic stress results showing component σ_{22} in MPa for the different microstructures at certain points in time.

If a microscopic element switches to martensite, compressive stresses occur inside due to the volumetric expansion of the atomic lattice. This can be observed for time $t = 8.6\,\mathrm{s}$ or $t = 10\,\mathrm{s}$. With ongoing cooling and the related phase transformation, the microstructure with 40 grains shows tensile stresses in regions of retained austenite and compressive stresses in newly switched martensitic elements. This observation is not as clear in case of microstructures with 90 grains anymore, for which mostly tensile stress peaks are visible. But, these cannot be directly related to areas of retained austenite. Considering the circular nucleus as an RVE with only one grain, this postulation can be verified that the differences between the micro- and macroscopic results are caused by the refinement or coarsening, respectively, of the grain structure. As shown in Figure 9.11, the final stress value lies around 150 MPa and, hence, exceeds the computations with RVEs based on 40, 90 or 900 grains.

In a next step, the impact of the switching order of the grains and its influence on the macroscopic stress component $\bar{\sigma}_{\mathrm{tang}}$ is in focus. Therefore, an RVE with 900 finite elements and 40 grains is taken into account, which grain size resembles most the restored austenitic grain structure in Figure 9.4. The microstructure with periodic grains is built up by Voronoi tessellation, recall Appendix F and see Figures 9.6 and 9.17.

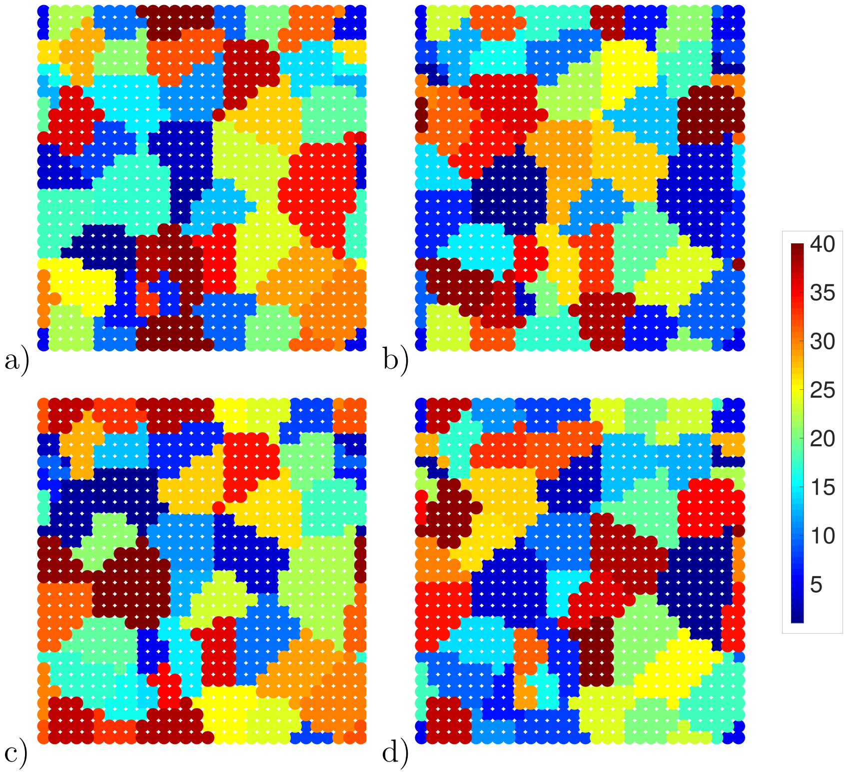

Figure 9.17: a) Periodic microstructure with b) & c) & d) three adapted switching orders for one Voronoi tessellation indicated by color. The phase transformation starts in blue grains and ends in red ones.

To apply the austenite-to-martensite phase transformation, the grains are randomly numbered, such that grain number 1 (blue) is the first to switch while grain number 40 (red) is the last one. Once more it is emphasized that inside one grain, the calculated martensitic volume fraction determines, if an element switches or not. The volume of all martensitic elements V_{M} in relation to the volume of the RVE V has to match c^{M}, i.e., not all elements of one grain have to switch at the same time. One can summarize this description for the phase transformation by an “element by element and grain by grainrrule. Naturally it is to be noticed that in case of retained austenite, not all grains will be switched to martensite. In the following analysis, four switching orders are taken into account, to which it is referred to as “random 1, “random 2, “random 3 and “random 4, respectively.

For comparison, the evolution of different macroscopic quantities are taken into account in the marked macroscopic integration point near the outer left surface, cf. Figure 9.7. These quantities are stress components $\bar{\sigma}_{11}$, $\bar{\sigma}_{22}$, $\bar{\sigma}_{33}$ and $\bar{\sigma}_{12}$, the norm of the deviatoric part of the stresses $\|\operatorname{dev}\bar{\boldsymbol{\sigma}}\|$, the homogenized accumulated plastic strains $\langle\varepsilon_{\mathrm{eq}}\rangle$ and the strain components $\bar{\varepsilon}_{11}$, $\bar{\varepsilon}_{22}$, $\bar{\varepsilon}_{33}$ and $\bar{\varepsilon}_{12}$, cf. Figures 9.18 to 9.20.

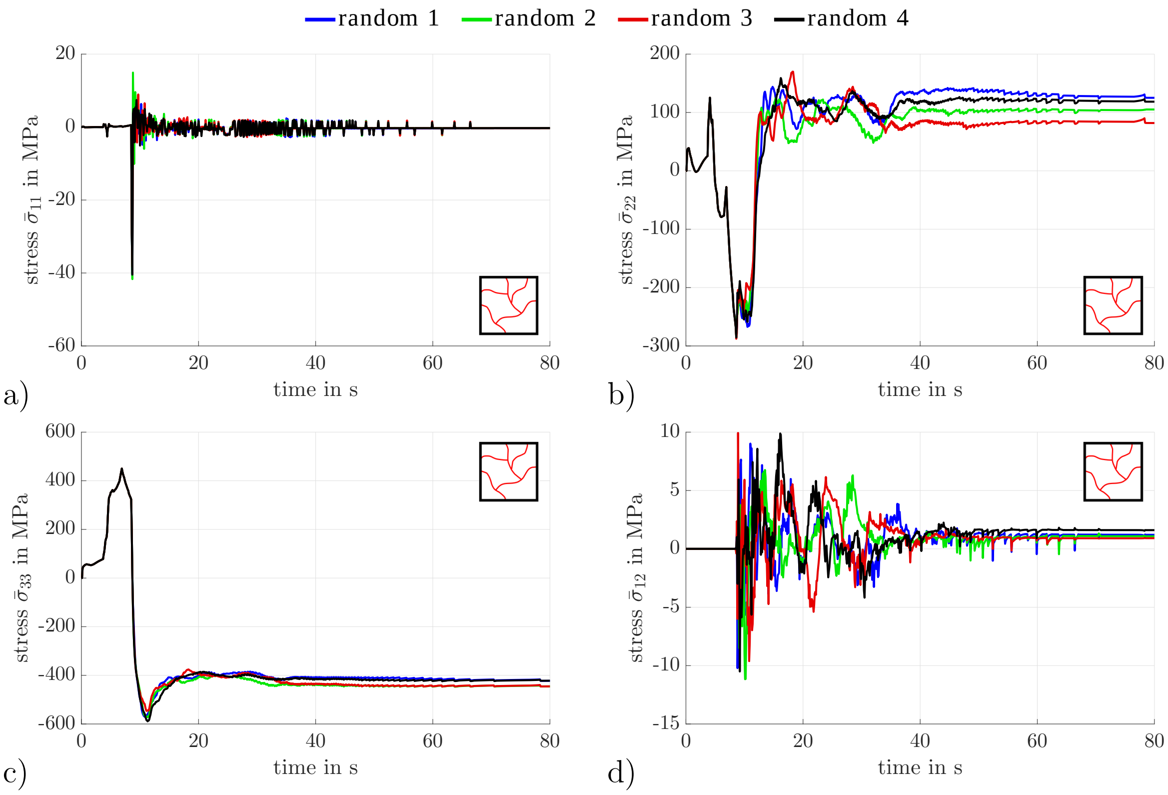

Figure 9.18: Comparison of cases “random 1, “random 2, “random 3 and “random 4, i.e., different switching orders for one grain structure obtained by Voronoi tessellation, regarding stress components a) $\bar{\sigma}_{11}$, b) $\bar{\sigma}_{22}$, c) $\bar{\sigma}_{33}$ and d) $\bar{\sigma}_{12}$.

The axial stresses $\bar{\sigma}_{11}$ for all six computations are close to zero, except during start of the phase transformation, see Figure 9.18a. Then, a compressive stress peak is present as expected due to the volumetric expansion of the atomic lattice. Similar is true for component $\bar{\sigma}_{12}$ in Figure 9.18d, which both can be taken as negligible due to the small absolute values. As can bes seen in Figure 9.18b, the evolution of the tangential stresses $\bar{\sigma}_{22}$ varies quite distinctively for the different RVEs with start of the phase transformation. Before, as long as the material is homogeneous, the results fit well. With increase of the martensitic volume fraction, the evolution of stress component $\bar{\sigma}_{22}$ seems nearly arbitrary. The final tangential stress value ranges from 80 MPa to 120 MPa. It is not possible to establish a relation between the microscopic switching order and the resulting macroscopic stress. One can only assume that with an increased number of microstructures, it is highly likely that a Gaussian distribution of the final values will be obtained. Microstructural experimental analyses and final stress measurements could give an insight on the quality of the computed data in order to assess the numerical simulation results. Similar findings are also true for the out of plane stress $\bar{\sigma}_{33}$ in Figure 9.18c.

In Figure 9.19a, the norm of the deviatoric part of the macroscopic stress $\|\operatorname{dev}\bar{\boldsymbol{\sigma}}\|$ is depicted, which combines all previously considered stress components into one scalar quantity. Initially, the material is stress-free due to the heating step of the hot bulk forming, such that it holds $\|\operatorname{dev}\bar{\boldsymbol{\sigma}}\| = 0\,\text{MPa}$ at time $t = 0\,\text{s}$. By cooling of the component over the lateral surface, stresses evolve up to $\|\operatorname{dev}\bar{\boldsymbol{\sigma}}\| \approx 400\,\text{MPa}$ at time $t \approx 18\,\text{s}$. With onset of the phase transformation, the atomic lattice relaxes and the inner stresses can be resolved, such that it holds $\|\operatorname{dev}\bar{\boldsymbol{\sigma}}\| \approx 150\,\text{MPa}$. In parallel, the homogenized accumulated plastic strains $\langle\varepsilon_{\text{eq}}\rangle$ increase to a value around 0.025 until martensite starts to form, cf. Figure 9.19b. At this point, the microscopic accumulated plastic strains are set to zero in an element that switches to martensite. Further cooling does not result in plastification of the martensitic material, since the yield stress is much higher compared to the austenitic yield stress at same temperature and accumulated plastic strain state. Thus, as the cooling time progresses, more and more microscopic elements switch to martensite and the homogenized accumulated plastic strains $\langle\varepsilon_{\text{eq}}\rangle$ are overall reduced by the homogenization scheme.

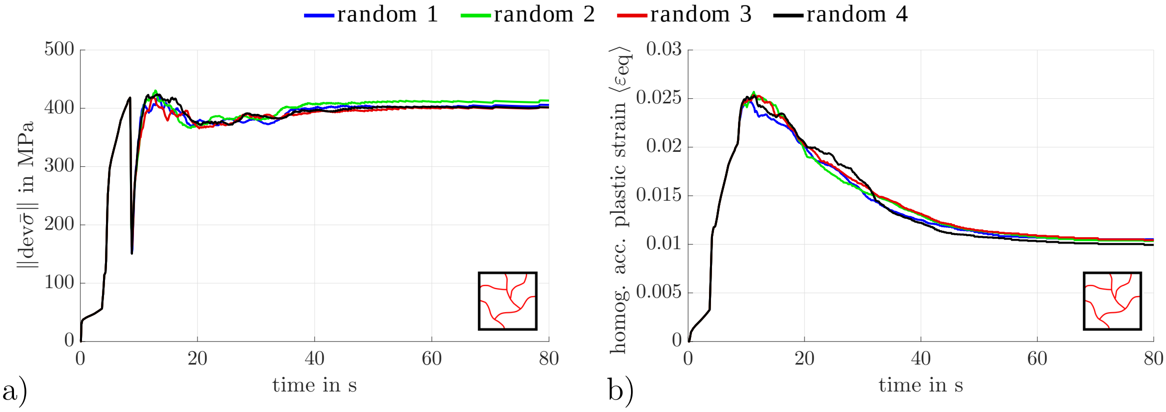

Figure 9.19: Comparison of cases “random 1, “random 2, “random 3 and “random 4, i.e., different switching orders for one grain structure obtained by Voronoi tessellation, regarding a) the norm of the deviatoric part of the stresses $\|\operatorname{dev}\bar{\boldsymbol{\sigma}}\|$ in MPa and b) the homogenized accumulated plastic strains $\langle\varepsilon_{\text{eq}}\rangle$.

In Figure 9.20a and b, the macroscopic strain components $\bar{\varepsilon}_{11}$ and $\bar{\varepsilon}_{22}$ are depicted over cooling. Due to the defined displacement boundary conditions, thermal shrinking can be observed before the phase transformation starts. With martensite formation, the component $\bar{\varepsilon}_{11}$ is reduced in absolute values from ≈ -0.03 to ≈ -0.015 as a consequence of the volumetric expansion of the atomic lattice while the strain component $\bar{\varepsilon}_{22}$ resembles a constant value of ≈ -0.02 due to the defined displacement boundary conditions. As the assumption of plane strain is made, it holds for the macroscopic strain component in third direction $\bar{\varepsilon}_{33} = 0$, cf. Figure 9.20c. Similar is true for the macroscopic shear strains $\bar{\varepsilon}_{12}$, which is also equal to zero throughout the cooling process except numerical inaccuracies, see Figure 9.20d.

In addition to the order of the grains, focus is now on different grain structures and the influence on the resulting macroscopic quantities. Therefore, eight additional Voronoi

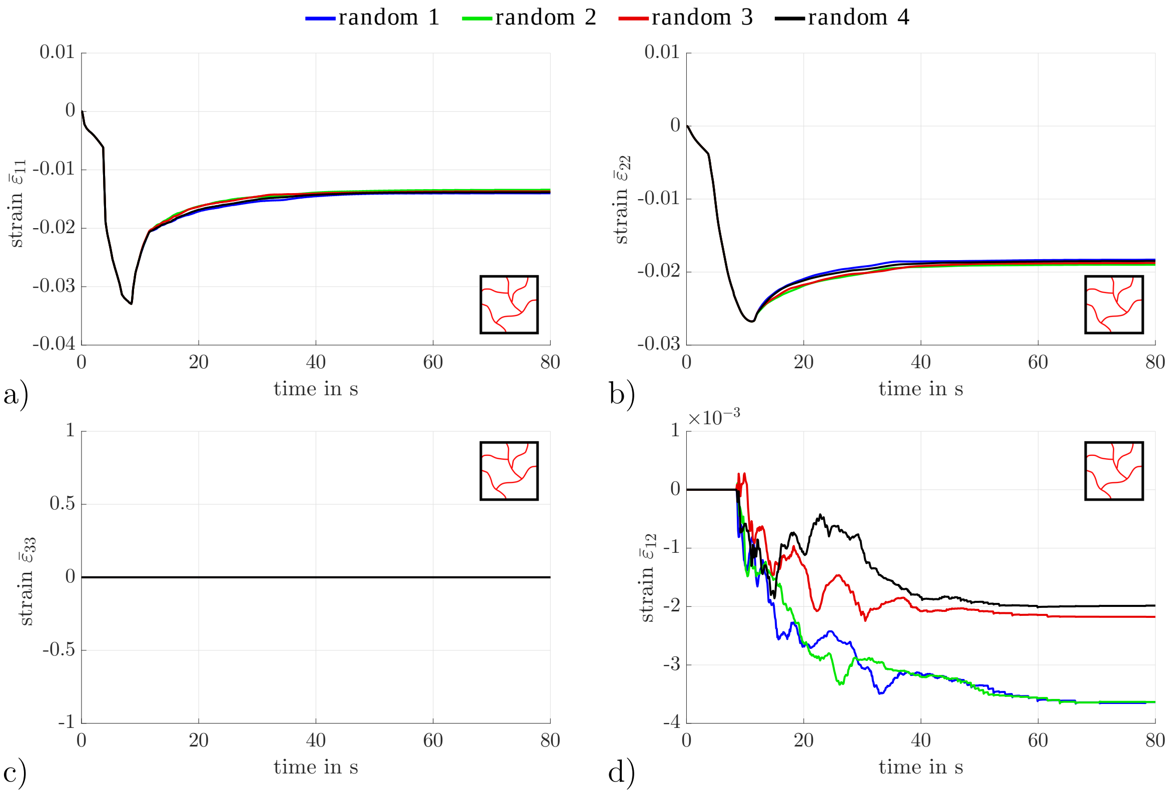

Figure 9.20: Comparison of cases “random 1, “random 2, “random 3 and “random 4, i.e., different switching orders for one grain structure obtained by Voronoi tessellation, regarding strain components a) $\bar{\varepsilon}_{11}$, b) $\bar{\varepsilon}_{22}$, c) $\bar{\varepsilon}_{33}$ and d) $\bar{\varepsilon}_{12}$.

tessellations are carried out with different initial seeding. Thereby, in total nine RVEs are obtained with 900 finite elements and 40 grains, which are compared in the following. As shown in Figure 9.21, the results for the RVEs based on different Voronoi tessellations are in good accordance with previous findings regarding the macroscopic stress component $\bar{\sigma}_{22}$, strain component $\bar{\varepsilon}_{22}$, the norm of the deviatoric part of the stresses $\|\,\mathrm{dev}\,\bar{\boldsymbol{\sigma}}\|$ and the homogenized accumulated plastic strains $\langle \varepsilon_{\mathrm{eq}} \rangle$.

Analogously to the analysis with respect to the grain order, quantitative deviations are visible but qualitative accordance is achieved. Taking a closer look at stress component $\bar{\sigma}_{22}$, differences especially during the phase transformation are present, but they equal out until a final value around $100\,\mathrm{MPa} \pm 20\,\mathrm{MPa}$. Thus, the different Voronoi tessellations do not show a significant effect in addition to the switching order of the grains. The thesis, that with a higher number of RVEs a Gaussian distribution of the final stress values is obtained, is supported.

Figures 9.22 and 9.23 show the evolution of the microscopic stresses σ_{22} in comparison to the martensitic volume fraction c^{M} for all considered nine Voronoi tessellations. In case, the temperature is lower than the martensitic start temperature, the austenite-to-martensite phase transformation starts, i.e., at $t = 8.6\,\mathrm{s}$. Then, martensite starts to form in the first element of the first grain of each RVE, or at maximum in two different grains, if the first grain consists of only few finite elements. As observed before, the martensitic islands are connected to compressive stresses as a consequence of the volumetric expansion of the atomic lattice. This phenomenon is also observable after ten seconds of cooling. Afterwards, when more and more grains in each RVE undergo the phase transformation,

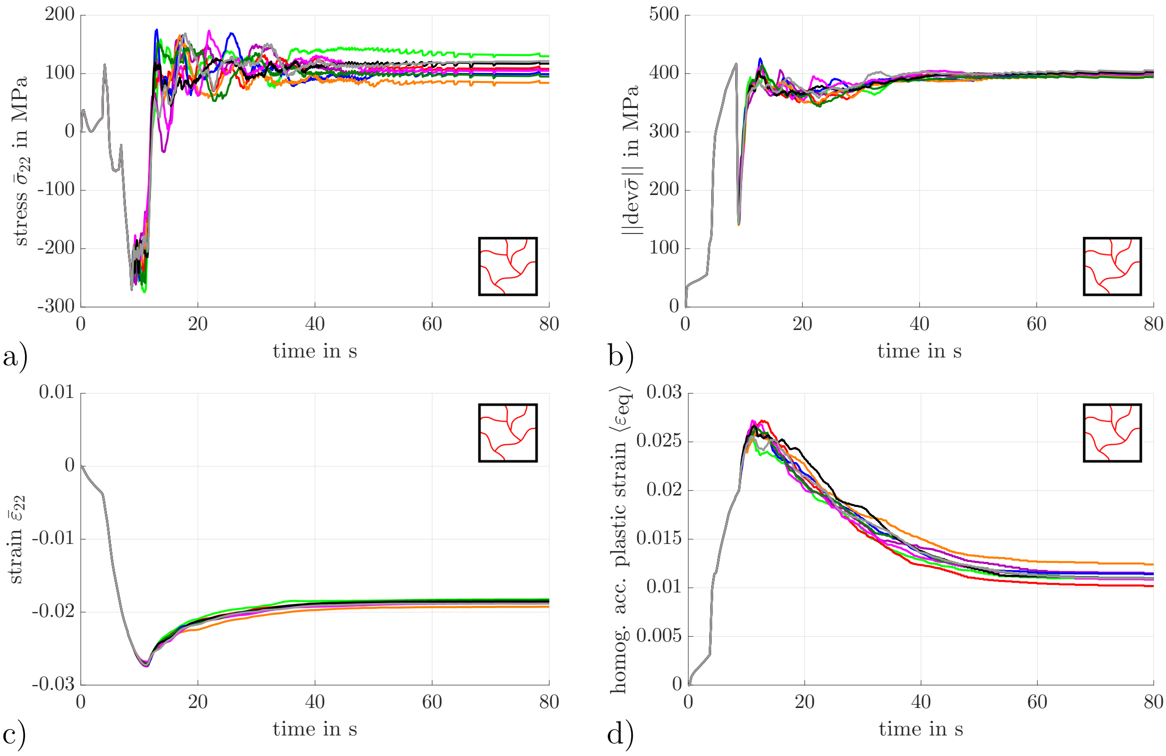

Figure 9.21: Comparison of different Voronoi tessellations regarding macroscopic quantities a) $\bar{\sigma}_{22}$, b) $\|\operatorname{dev}\bar{\boldsymbol{\sigma}}\|$, c) $\bar{\varepsilon}_{22}$ and d) $\langle\varepsilon_{\text{eq}}\rangle$.

the stress pattern becomes much more complex. A high number of tensile as well as compressive stress peaks can be found in each RVE. It is not possible to directly relate such peaks to the phase present. In a final state, all nine RVEs show complex stress patterns, which are similar to each other but at the same time also individually formed, see Figure 9.23c.

At this point it can be summarized that an RVE with a circular inclusion describes the stiffest material behavior of all approaches. Furthermore, the numerical and temporal effort is relatively high in this case. The artificial grains, which were conceived as part of the diagonal structure, do not show any differences compared to an arbitrary switch of the elements, which does not justify the effort to create such an RVE. The arbitrary switch is equivalent to providing the same number of grains as finite elements in the RVE. In order to investigate the influence of this number of grains, as well as to include the experimentally determined austenitic grains, RVEs with grain structures seem to give good results. Depending on the number of grains, effects on the macroscopic stresses in the component are shown, especially during the phase transformation. The order of switching the grains as well as the choice of different grain structures of the same type result in almost no changes. In general, however, it can be said that the macroscopic stress curves agree very well with those of an arbitrary switch. Due to the fact that the grain structure mostly resembles the austenitic grains and the RVE with an arbitrary switch can be implemented with the small effort, even if it is not physically based, these two microstructures are in focus for multi-scale analyses of hot bulk forming in the following Section 10.

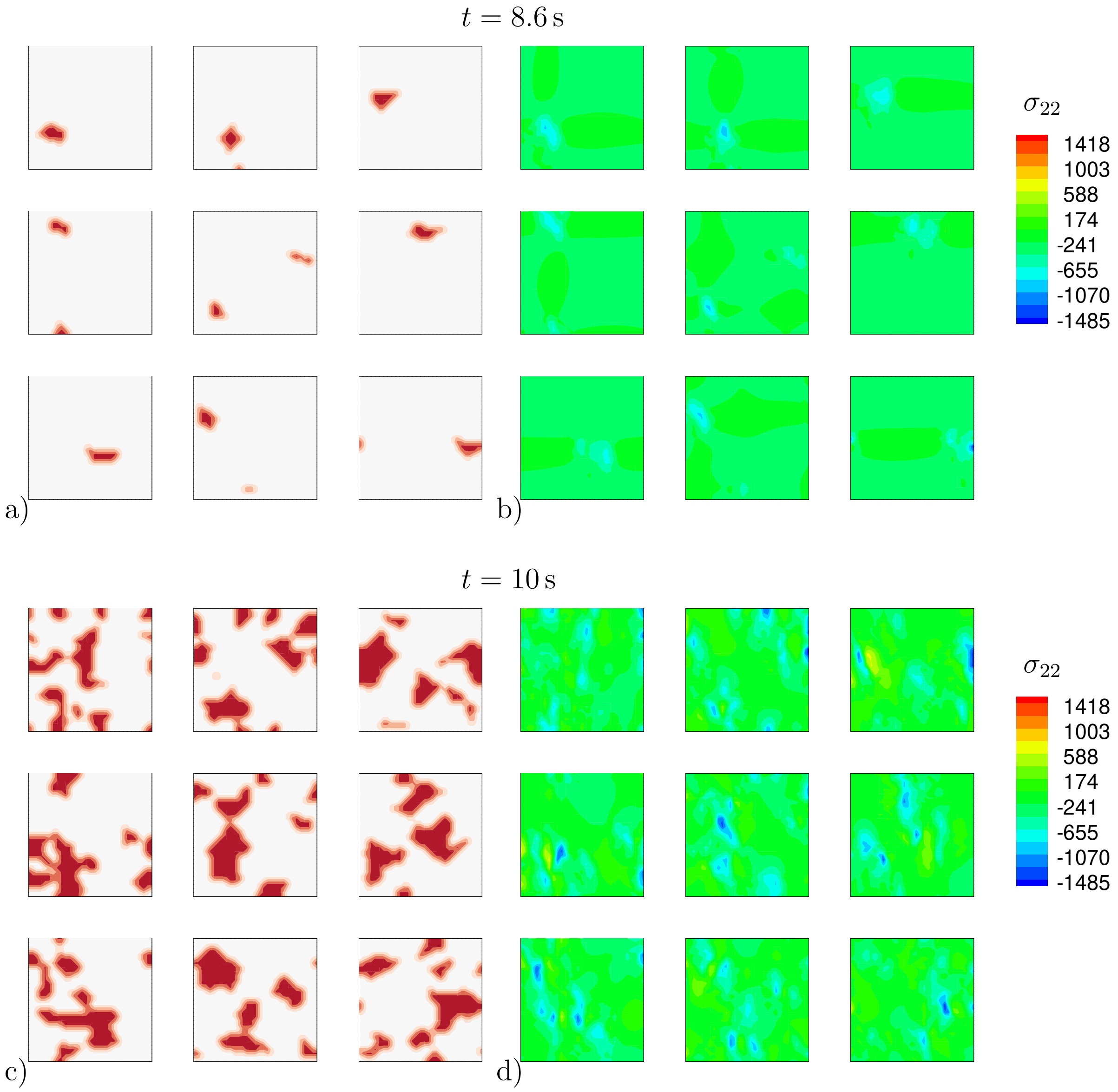

Figure 9.22: Comparison of nine different Voronoi tessellations, regarding a) & c) the martensitic volume fraction c^{M} (red) in an austenitic matrix (white) and b) & d) the microscopic stress component σ_{22} in MPa at certain points in time $t = 8.6\,\mathrm{s}$ and $t = 10\,\mathrm{s}$.

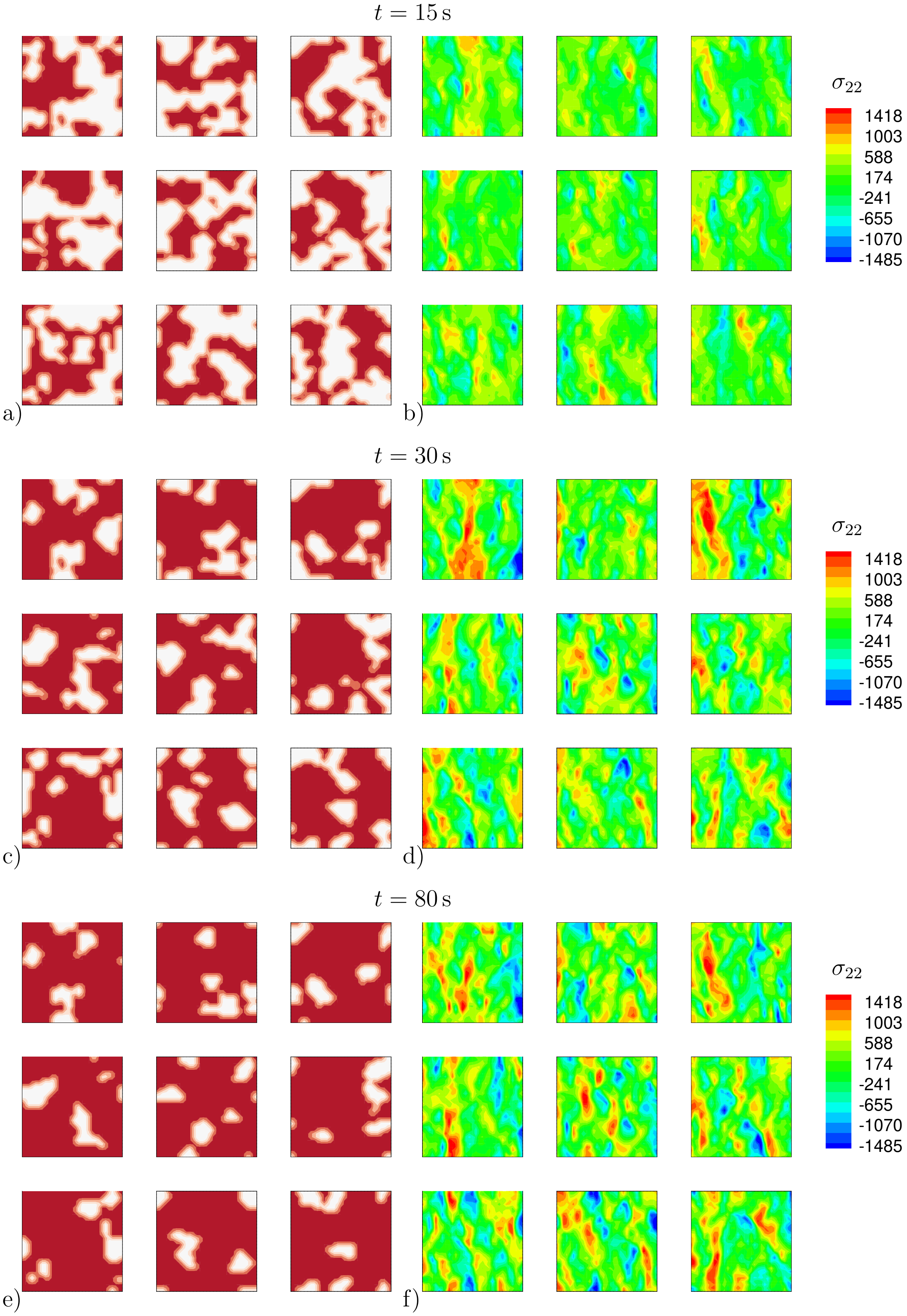

Figure 9.23: Comparison of nine different Voronoi tessellations, regarding a) & c) & e) the martensitic volume fraction c^{M} (red) in an austenitic matrix (white) and b) & d) & f) the microscopic stress component σ_{22} in MPa at certain points in time $t = 15\,\mathrm{s}$, $t = 30\,\mathrm{s}$ and $t = 80\,\mathrm{s}$.

9.3.4 Phase specific analysis

The previously presented results regarding macroscopic stresses and strains are based on a homogenization scheme, and hence, represent an effective material behavior of the phases present. The posed boundary value problem of cooling the cut of a cylindrical specimen takes into account two phases, austenite and martensite, as stated in Section 6.2.4. These phases have different material properties, for instance, martensite possesses higher strength and lower ductility compared to austenite. Recalling back to Section 5.3, in which phase-specific material parameters have been interpolated depending on the temperature as well as the accumulated plastic strains, it is obvious that martensite has higher yield strength than austenite, for instance. These and other phase-specific characteristics motivate to distinguish into phase-specific contributions regarding e.g. the stress components. Figure 9.24 shows the stress and strain evolution for the RVEs “random 1tto “random 4 divided into phase-specific components.

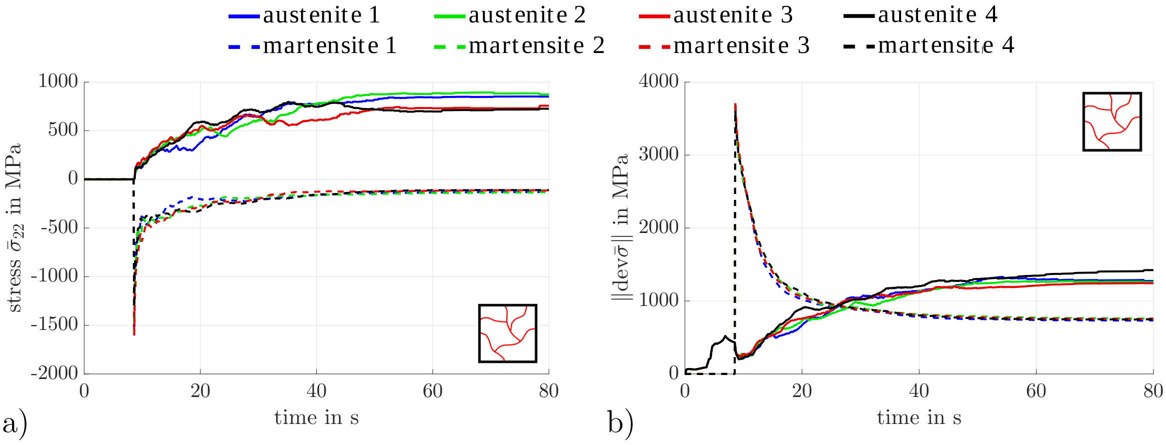

Figure 9.24: Phase-specific contributions compared for cases “random 1, “random 2, “random 3 and “random 4, i.e., different switching orders for one grain structure obtained by Voronoi tessellation, regarding a) stress component $\bar{\sigma}_{22}$ and b) the norm of the deviatoric part of the stresses $\|\operatorname{dev}\bar{\boldsymbol{\sigma}}\|$.

At first, tensile stresses are observed in a homogeneous austenitic material as a consequence of the thermal contraction. When the austenite-to-martensite phase transformation starts, the volumetric expansion of the unit cell leads to high compressive stress values for $\bar{\sigma}_{22}$ in the martensitic phase, cf. Figure 9.24a. As can be observed in Figure 9.24b, austenite possesses lower yield strength and hence, the norm of the deviatoric part of the stresses is much smaller than for martensite. As more and more elements of an RVE switch to martensite, the value of about 1700 MPa of the norm of the deviatoric part of the stresses after eight seconds of cooling is reduced to finally 500 MPa. This can be explained by the reset of the accumulated plastic strains in case an element is first switched to martensite. It follows the assumption that the atomic lattice relaxes by the phase transformation.

9.4 Non-uniform volumetric expansion in terms of Bain groups

As experimental observations prove, the shearing of the atomic lattice during the phase transformation of face-centered cubic to body-centered tetragonal unit cells is complex. The up to now considered homogeneous volumetric expansion in every principle direction is a strong simplification, cf. BHATTACHARYA [22] or SCHOOF [158] among many others. Thus, in order to study the influence of a non-uniform volumetric strain, an individual orientation is set for each grain. These orientation functions are obtained utilizing a geodesic dome, cf. FULLER [55]. The term comes from the science of measuring and understanding the earth's figure (geodesy), in which the subdivision into triangles plays a decisive role. In general, such a dome is a convex irregular polyhedron which satisfies Euler's polyhedron theorem. This states that the sum of the number of vertices n_v and the number of faces n_f minus the number of edges n_e must equal two, i.e.,

$$n_v + n_f - n_e = 2\,. \tag{9.1}$$

To construct a geodesic dome, one usually starts with a dodecahedron or an icosahedron as a base. A dodecahedron consists of twelve congruent regular pentagons as faces, 30 edges of equal length and 20 corners, in each of which three pentagons meet, while an icosahedron consists of 20 congruent equilateral triangles as faces, which are connected with 30 edges of equal length and twelve corners, in each of which five triangles meet. Such an icosahedron already has an approximately spherical shape, which is due to the five meeting faces per corner. However, to further approximate this construction of a sphere, the 20 triangles are divided into smaller triangles, which in turn are congruent and equilateral. Based on this subdivision, it is no longer true that five faces meet per corner. To enforce this would violate the assumption of perfectly equal triangles. In connection with the subdivision into smaller triangles one speaks of frequencies. For a geodesic dome of frequency 2, one subdivides each triangular surface into 4 smaller triangles, see Figure 9.25. This results in a dome with 80 faces and 42 corners. For a dome of frequency 3, each initial face is divided into 9 smaller triangles, and for frequency 4, even into 16.

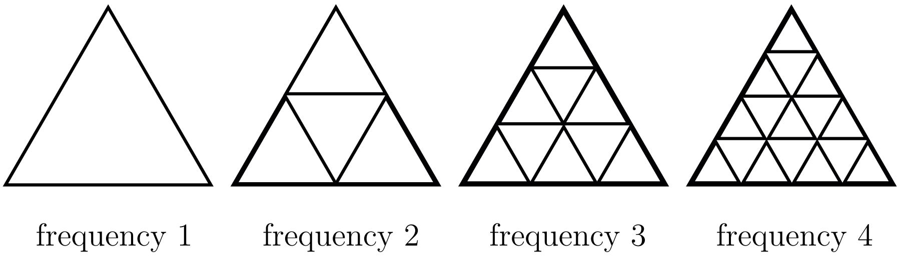

Figure 9.25: Subdivision of the triangles of a geodesic dome.

Based on these so formed spherical triangular grids, the required orientation distribution functions are defined. The orientation direction is uniquely determined by a vector from the center of the sphere to the corners. As a consequence, a geodesic dome of frequency 2 stands for 42 orientations, a dome of frequency 3 already stands for 92 orientations and a dome of frequency 4 even features 162 different orientations. Two normal vectors are assigned to each of these constructed vectors. These groups of three vectors each then describe the spatial orientation of a grain uniquely. Figure 9.26 displays a geodesic dome with its orientation distribution functions of frequency 2 and 3, respectively.

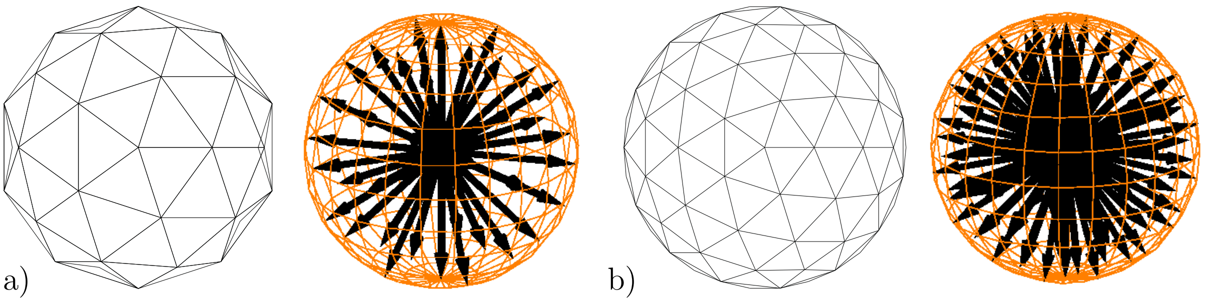

Figure 9.26: Geodesic dome a) with frequency 2 and b) frequency 3 and the respective resulting orientation distribution functions, taken from Kurzhöfer [96].

Since the idea is to take 40 grains in the microscopic structure into account, a geodesic dome of frequency 2 with 42 orientations satisfies the requirement of at least 40 unique orientations. Based on a grain identifier, the orientation is set. The volumetric expansion of the atomic lattice, which is taken as 1 % for the considered Cr-alloyed steel 100Cr6, is in the following not homogeneously distributed in the three principle directions, but it weights the volumetric expansion based on the specific orientation distribution function, see also Kurzhöfer et al. [97], Schröder et al. [163] and Labusch et al. [98]. Therefore, the homogeneous transformation volumetric strain, see Equation (5.12), is transformed to a Bain strain. Therein, the volumetric expansion of the unit cell is kept as $K_{\mathrm{tv}} = 1\,\%$ but a preferred direction is defined. In this preferred direction, the cubic unit cell elongates more than in the other two, so that a rectangular unit cell is obtained, see Figure 9.27.

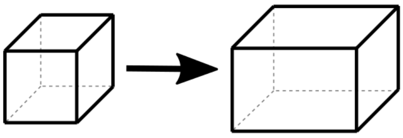

Figure 9.27: According to Bain and Dunkirk [7] and Bain and Griffiths [8], the austenitic unit cell expands during phase transformation to martensite. The expansion shows one preferred direction oriented along the principle axis, here schematically sketched for the first variant in x_1-direction.

The associated Bain strain is chosen as

$$\boldsymbol{\varepsilon}_{\mathrm{tv}} = \begin{pmatrix} 0.005 & & \\ & 0.00248448 & \\ & & 0.00248448 \end{pmatrix} . \tag{9.2}$$

The triad of vectors $\boldsymbol{g}_i^k$ with $i = 1, 2, 3$, which consists of the orientation direction and the associated normal vectors, defines the spatial orientation of the grain k. Therefore, the first normal vector $\boldsymbol{g}_2^k$ associated to the orientation vector $\boldsymbol{g}_1^k$ is freely chosen with the restriction that $\boldsymbol{g}_2^k$ is orthogonal to $\boldsymbol{g}_1^k$ and normalized. Then, the second normal vector $\boldsymbol{g}_3^k$ is computed as the crossproduct of the first two vectors, i.e., $\boldsymbol{g}_3^k = \boldsymbol{g}_1^k \times \boldsymbol{g}_2^k$. These three vectors are a dual base to the euclidean base system $\boldsymbol{e}_i$ with $i = 1, 2, 3$. The dual base is obtained as rotation by the euclidean base with the related rotation matrix $\boldsymbol{Q}$ given by

$$\boldsymbol{Q}^k = \sum_{i=1}^{3} \boldsymbol{g}_i^k \otimes \boldsymbol{e}_i = \boldsymbol{g}_1^k \otimes \boldsymbol{e}_1 + \boldsymbol{g}_2^k \otimes \boldsymbol{e}_2 + \boldsymbol{g}_3^k \otimes \boldsymbol{e}_3 \,. \tag{9.3}$$

This rotation matrix is applied to the Bain strain in Equation (9.2) to arrange the preferred direction associated to the orientation direction $\boldsymbol{g}_1^k$ as

$$\boldsymbol{\varepsilon}_{\mathrm{tv}}^{k,*} = \boldsymbol{Q}^k \cdot \boldsymbol{\varepsilon}_{\mathrm{tv}} \cdot \boldsymbol{Q}^{k,\mathrm{T}} \, . \tag{9.4}$$

Evaluating the stress and strain evolution over the cooling time in comparison to previous results with a homogeneous transformation volumetric strain shows that a homogeneous volumetric strain overestimates the different quantities perceptibly, cf. Figure 9.28. Therein, the results of Section 9.3.3 applying a homogeneous volumetric strain are referred to as “homogeneous“while the evolutions taking the decisive grain orientations into account are named “Bain“. The number refers to the switching order, cf. Figure 9.17.

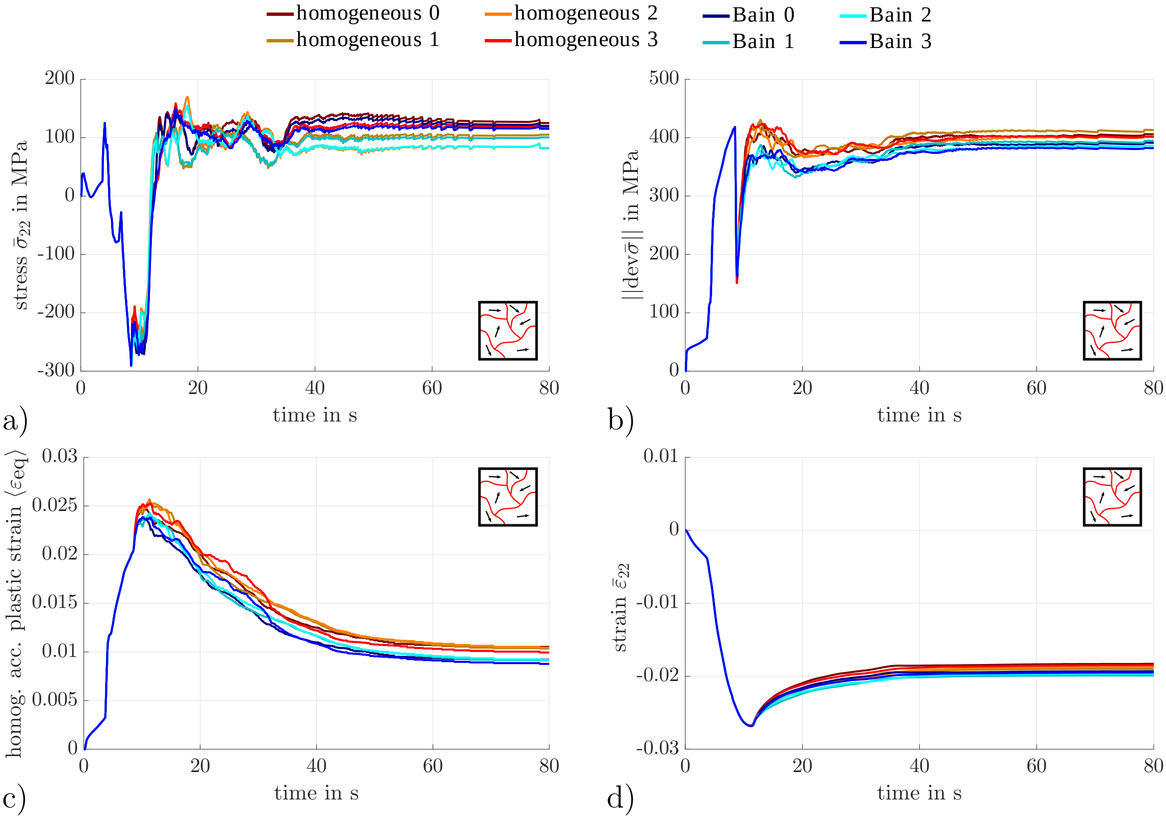

Figure 9.28: Comparison of cases “homogeneous 0tto “homogeneous 3“without decisive grain orientation to the same RVEs with a defined grain orientation “Bain 0tto “Bain 3 regarding the macroscopic quantities a) $\bar{\sigma}_{22}$, b) $\| \operatorname{dev} \bar{\boldsymbol{\sigma}} \|$, c) $\langle \varepsilon_{\mathrm{eq}} \rangle$ and d) $\bar{\varepsilon}_{22}$.

10 Two-scale analysis of hot bulk forming process

As already found in Section 6.2, hot bulk forming processes evoke complex residual stress distributions inside a component. These previously investigated macroscopic residual stresses (of first type) are highly influenced by microscopic residual stresses (of second and third type). However, microscopic quantities cannot be resolved explicitly in single-scale simulations, which motivates to carry out a two-scale analysis of such a hot bulk forming process. Therefore, focus lies on the cylindrical specimen, which was subject to several experimental investigations to determine its microscopic characteristics such as e.g. the volume fractions of the phases present, cf. Behrens et al. [14; 15; 17; 18; 19]. One advantage is the simplicity of the geometry; at the same time, the cylinder's eccentricity makes it a good substitute for a complex component in engineering applications. For instance, gear wheels or crankshafts as hot bulk forming parts are subjected to high tensile loadings at the teeth in tangential direction. As a consequence, the tangential stresses are in focus of the following investigations. Therefore, thermo-mechanically coupled two-dimensional boundary value problems are defined to investigate the evolution of the macroscopic and microscopic residual stress distributions inside the component, which result from the cooling and the related phase transformation. The considered cooling medium water evokes a diffusionless phase transformation from austenite to martensite, which is taken into account in an isothermal microscopic material model. In order to model the stresses accurately, the mesh density and the time step width must be chosen thoughtfully, cf. Section 6.2.3. Thus, at first, a simplified material model is taken into account, in which the transformation induced plasticity (TRIP) strains are neglected, to compare different mesh discretizations on both scales. The results have already been published in Uebing et al. [191]. Afterwards, the microscopic stress evolution and the influence of the microscopic stress fluctuations on the macroscopic residual stress distribution are discussed as already presented in Uebing et al. [192]. In course of that second analysis, transformation induced plasticity has also not been taken into account. Additionally, since an undeformed geometry of the cylindrical specimen is subject of the analysis, no accumulated plastic strains from the forming are applied as offset in the initialization step. Finally, a two-scale boundary value problem with the material model given in Section 8.7, i.e., considering TRIP strains and the accumulated plastic strains of the forming history, is investigated with respect to the stress evolution on both scales. The examined two-dimensional slice is therefore a cut out of the deformed cylinder.

10.1 Two-scale mesh density study

For an accurate description of the macro- and microscopic stress evolution in the hot bulk forming component it is inevitable to carry out a mesh density and time step size study. Therefore, the two-dimensional slice of the undeformed cylindrical specimen made from Cr-alloyed steel 100Cr6 is taken into account, which dimensions are already depicted in Figure 6.6. The heating and forming step of the hot bulk forming process prior to the simulated cooling step are maintained. The outer radius equals 17.5 mm, the radius of the hole, which is shifted by $e = 3.5\,\mathrm{mm}$ in the positive direction of the $\bar{x}_1$-axis, equals 8 mm. To reduce the complexity and as a consequence the computational effort, only two parts of the axial section are considered on the macroscale, see Figure 10.1. The angle α is chosen as $5\,^{\circ}$, so that the dimensions are sufficiently large to achieve convergent results but still small enough to get overall short computation times. The two resulting sections, that are taken into account on the macroscale, are referred to as thick and thin side, respectively, based on thickness of the material between the eccentricity and the outer surface. At first, the mesh density study on both scales is carried out, for which a constant time step size of $\Delta t = 0.1\,\mathrm{s}$ is chosen.

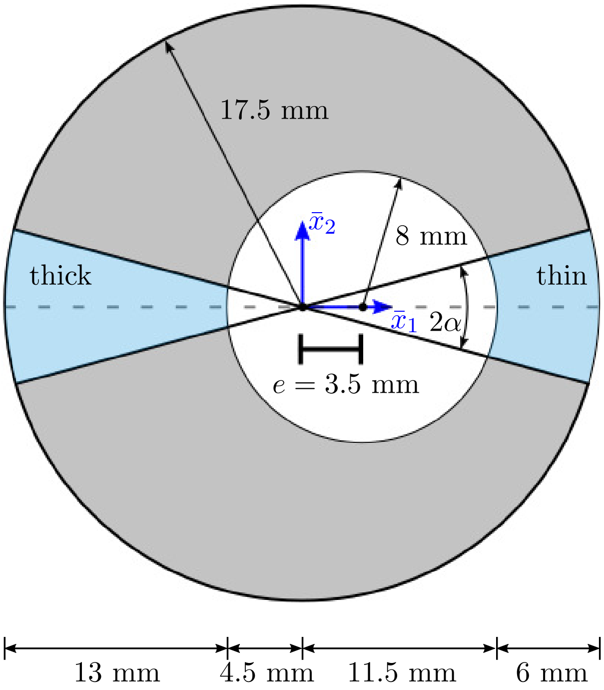

Figure 10.1: Geometry to analyze the cooling of the lateral surface of a cylinder inducing phase transformation and therewith resulting in residual stresses, adapted from UEBING ET AL. [191].

Figure 10.2 displays the resulting geometries with their dimensions and boundary conditions. Since these small sections are cut out from the cylindrical slice, displacement boundary conditions are applied on both cutting edges, i.e., the nodes on $\partial\bar{\mathcal{B}}_{\boldsymbol{u}}$ are fixed in orthogonal direction to the cutting edge. Thereby, radial symmetry is ensured, which serves as another simplification, since the cylinder does not possess radial symmetry due to its eccentricity. Furthermore, Dirichlet boundary conditions are applied on $\partial\bar{\mathcal{B}}_{\theta}$ to describe the temperature evolution on the lateral surface. It is assumed that the heat flux through the cutting edges is negligible small and, thus, it is set $\bar{q}_0 = 0$ on $\partial\bar{\mathcal{B}}_{\boldsymbol{q}}$. Since there are no outer forces or moments applied, it holds that the resulting stress distribution can be interpreted as residual stresses. Furthermore, due to the choice of the cut geometries, they are symmetric around the $\bar{x}_1$-axis, along which the stress component in $\bar{x}_2$-direction $\bar{\sigma}_{22}$ can be interpreted as tangential stress.

In terms of a two-scale finite element analysis, the material model in each macroscopic integration point is replaced by a microscopic boundary value problem. As depicted in Figure 10.2, a representative volume element (RVE) with a structured mesh is taken into account. On the minor scale, the material model presented in Section 8.7 is considered with neglecting TRIP strains and the offset, which initializes the accumulated plastic strains due to the forming step of the hot bulk forming process. As a consequence, only the subsequent cooling step from above 1000 °C to room temperature $\theta_{\mathrm{RT}} \approx 20\,^{\circ}\mathrm{C}$ is mod-

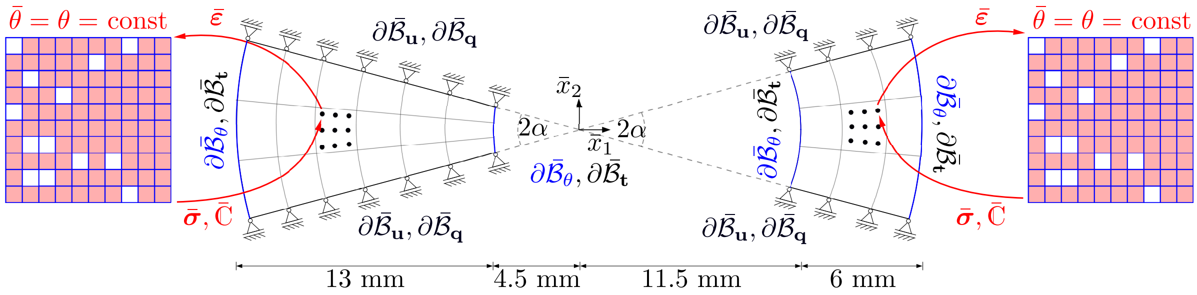

Figure 10.2: Two macroscopic boundary value problems are analyzed, depicting thick and thin cylindrical section with shown Dirichlet boundary $\partial\bar{\mathcal{B}}_{\boldsymbol{u}}$, $\partial\bar{\mathcal{B}}_\theta$ and Neumann boundary $\partial\bar{\mathcal{B}}_{\boldsymbol{t}}$, $\partial\bar{\mathcal{B}}_{\boldsymbol{q}}$. Cooling over the lateral surface $\partial\bar{\mathcal{B}}_\theta$ (blue), the microscopic mesh with final phase distribution, martensite in red and austenite in white, are shown, adapted from Uebing et al. [191].

eled. For the description of the austenite-to-martensite phase transformation in the RVE, different evolution strategies are compared in Section 9. Here, the arbitrary switch is taken into account with a final volume fractions of 87 % martensite and 13 % retained austenite obtained by cooling in water. The martensitic start temperature equals $\theta_{\text{Ms}} = 185\,°\text{C}$ for the considered material 100Cr6. For the following study, the volumetric expansion of the face-centered cubic austenitic unit cell to the body-centered tetragonal martensitic unit cell is chosen as $K_{\text{tv}} = 2\,\%$, which deviates from prior specification. For the numerical investigation of both two-scale boundary value problems quadratic quadrilateral elements with nine nodes are chosen as macroscopic finite element, while on the microscale linear quadrilateral elements with four nodes are considered. In Table 10.1, the different macroscopic and microscopic discretizations are summarized, and abbreviations for compact notation are introduced. Therein, the number of elements in tangential direction on the macroscale is set to a constant value of $\overline{5}$, since a refinement does not alter the results, cf. Uebing et al. [191]. On the microscale, the austenite-to-martensite phase transformation is depicted with an arbitrary switching scheme, as introduced in Section 9.

In order to evaluate the different mesh densities, the focus lies on the tangential stresses, which are known to have a decisive influence on the final component's properties. Due to the choice of the geometry of the boundary value problems, the stress component $\bar{\sigma}_{22}$ is taken into account in the integration points located along the $\bar{x}_1$-axis. Macroscopically coarse meshes $\overline{10}$ do not show adequate results. Independent of the microscopic mesh size, unreasonable stress distributions are found, and thus, finer mesh sizes with $\overline{20}$ or $\overline{30}$ macroscopic elements, $\overline{\text{M}}$ and $\overline{\text{F}}$, respectively, are taken into account. Figures10.3 and 10.4 display the tangential stress component $\bar{\sigma}_{22}$ after $t = 20\,\text{s}$ of cooling, that is in the middle of phase transformation. The stress curves for macroscopically medium and fine discretizations in combination with microscopically coarse, medium and fine mesh sizes are examined. It is found, that an RVE with 100 elements does not lead to reasonable results, since strong oscillations occur, see $\overline{\text{M}}\text{C}$ and $\overline{\text{F}}\text{C}$. The thick side boundary value problem shows less oscillations in case of the $\overline{\text{M}}\text{M}$ or $\overline{\text{F}}\text{M}$ discretizations, but that does not hold for the thin side boundary value problem. To obtain sufficiently smooth stress behavior, a microscopically fine discretization is inevitable to use. The computations with $\overline{\text{M}}\text{F}$ and $\overline{\text{F}}\text{F}$ both lead to reasonable results regarding $\bar{\sigma}_{22}$, which are confirmed when considering finer mesh sizes such as $\overline{\text{FF}}$ or $\overline{\mathbb{F}}$ on the macroscale, see Uebing et al. [191].

Table 10.1: Overview of the analyzed combination of macroscopic and microscopic discretization and explanation of the used abbreviation, adapted from Uebing et al. [191].

macroscopic mesh			microscopic mesh			
elements		abbreviation	elements		abbreviation	notation
width	height		width	height		
$\overline{10}$	$\overline{5}$	coarse $\overline{\text{C}}$	10 20 30	10 20 30	coarse C medium M fine F	$\overline{\text{C}}$C $\overline{\text{C}}$M $\overline{\text{C}}$F
$\overline{20}$	$\overline{5}$	medium $\overline{\text{M}}$	10 20 30	10 20 30	coarse C medium M fine F	$\overline{\text{M}}$C $\overline{\text{M}}$M $\overline{\text{M}}$F
$\overline{30}$	$\overline{5}$	fine $\overline{\text{F}}$	10 20 30	10 20 30	coarse C medium M fine F	$\overline{\text{F}}$C $\overline{\text{F}}$M $\overline{\text{F}}$F
$\overline{40}$	$\overline{5}$	$\overline{\text{FF}}$	30	30	fine F	$\overline{\text{FF}}$F
$\overline{50}$	$\overline{5}$	$\overline{\mathbb{F}}$	30	30	fine F	$\overline{\mathbb{F}}$F

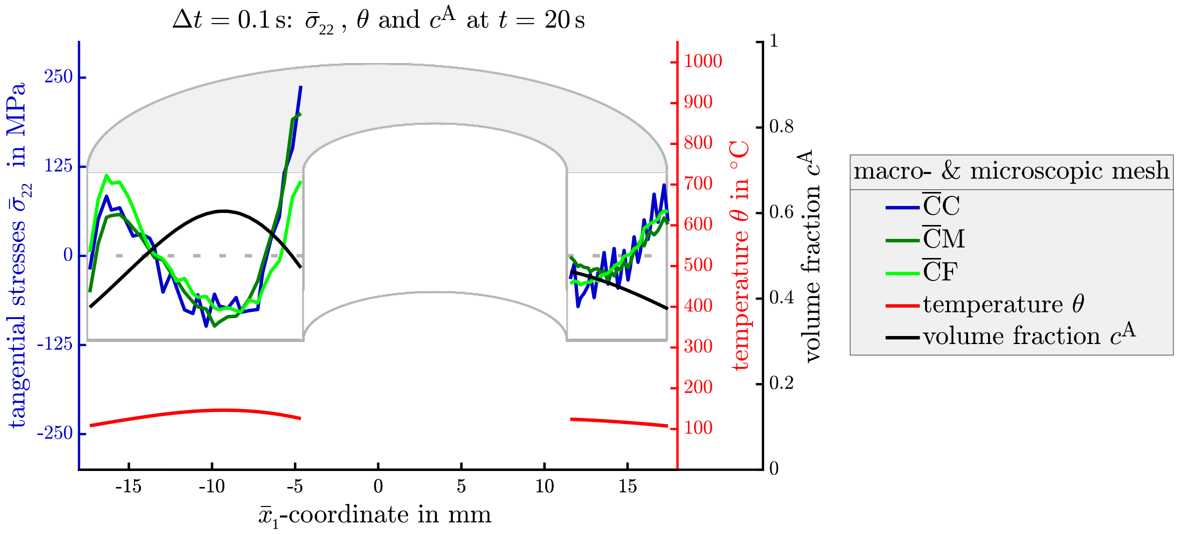

Figure 10.3: Tangential stresses $\bar{\sigma}_{22}$ for the $\bar{x}_1$-axis at $\bar{x}_2 = 0$ and $t = 20\,\text{s}$ for macroscopically coarse discretization $\overline{\text{C}}$ and different microscopic meshes using time step size $\Delta t = 0.1\,\text{s}$, adapted from Uebing et al. [191].

In addition, the refinement of the time step size Δt is investigated. The previously utilized time step size of $\Delta t = 0.1\,\text{s}$ is reduced to $\Delta t = 0.05\,\text{s}$ and $\Delta t = 0.01\,\text{s}$, respectively, during phase transformation, which takes mostly place between $t = 8\,\text{s}$ and $t = 40\,\text{s}$. Figures 10.5 and 10.6 depict the stress component $\bar{\sigma}_{22}$ along the $\bar{x}_1$-axis after $t = 20\,\text{s}$ for discretizations $\overline{\text{M}}$F and $\overline{\text{F}}$F, respectively. It is shown that a refinement of the time step size improves the results in case of a medium sized mesh on both scales. For a macroscopic discretization $\overline{\text{M}}$ and a microscopic fine mesh F, the stress curves fit very well for all time stepping schemes. Only small deviations can be seen for the refinement of the time step size to $\Delta t = 0.5\,\mathrm{s}$. Thus, overall it is seems most reasonable to chose the time step size according to Equation (6.2) as

$$\Delta t_{\mathrm{water}}(t) = \begin{cases} 0.1\,\mathrm{s} & 0\,\mathrm{s} \le t < 8\,\mathrm{s} \\ 0.01\,\mathrm{s} & 8\,\mathrm{s} \le t < 40\,\mathrm{s} \\ 0.1\,\mathrm{s} & 40\,\mathrm{s} \le t \le 80\,\mathrm{s} \end{cases} \quad . \tag{10.1}$$

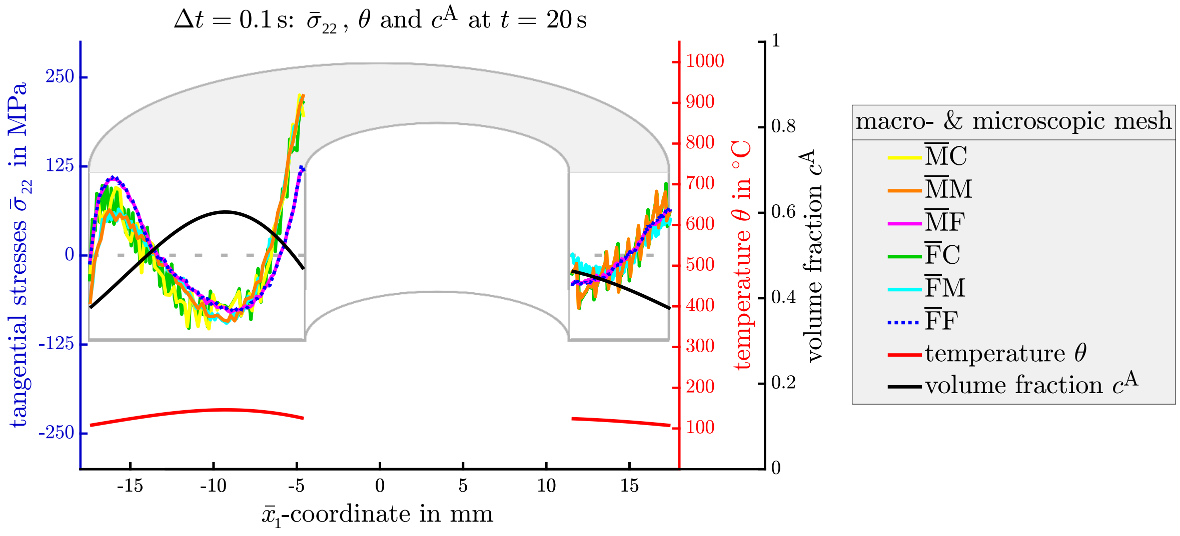
$\Delta t = 0.1\,\mathrm{s}$: $\bar{\sigma}_{22}$, θ and c^{A} at $t = 20\,\mathrm{s}$

Figure 10.4: Tangential stresses $\bar{\sigma}_{22}$ for the $\bar{x}_1$-axis at $\bar{x}_2 = 0$ and $t = 20\,\mathrm{s}$ for the discretization $\overline{\mathrm{M}}$ and $\overline{\mathrm{F}}$ of the macroscopic BVP and different microscopic meshes using time step size $\Delta t = 0.1\,\mathrm{s}$, adapted from Uebing et al. [191].

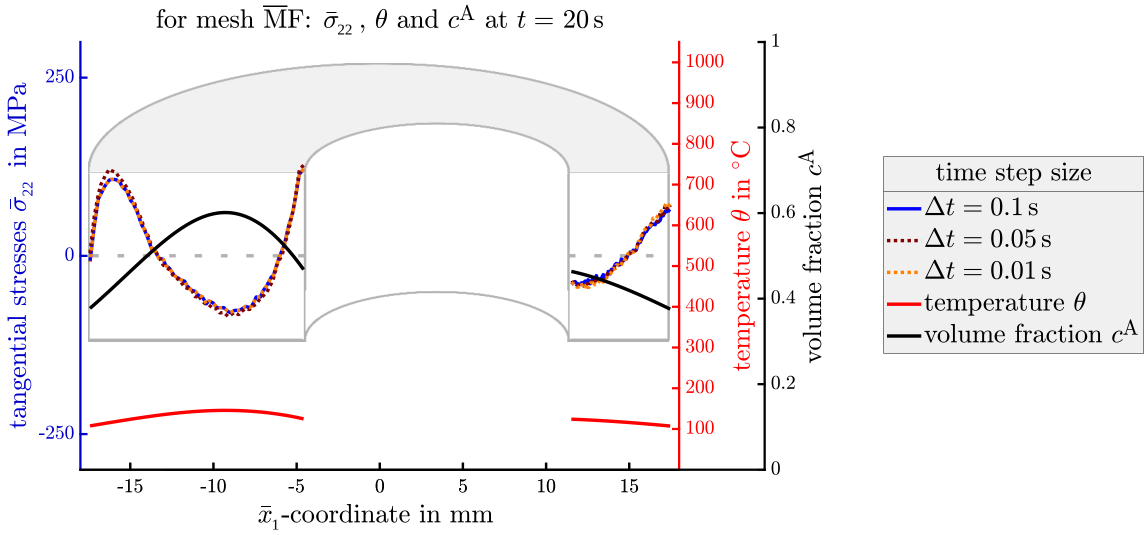
for mesh $\overline{\mathrm{M}}$F: $\bar{\sigma}_{22}$, θ and c^{A} at $t = 20\,\mathrm{s}$

Figure 10.5: Tangential stresses $\bar{\sigma}_{22}$ for the $\bar{x}_1$-axis at $\bar{x}_2 = 0$ and $t = 20\,\mathrm{s}$ for the discretization $\overline{\mathrm{M}}$F and different time step sizes of $\Delta t \in \{0.1\,\mathrm{s}, 0.05\,\mathrm{s}, 0.01\,\mathrm{s}\}$, adapted from Uebing et al. [191].

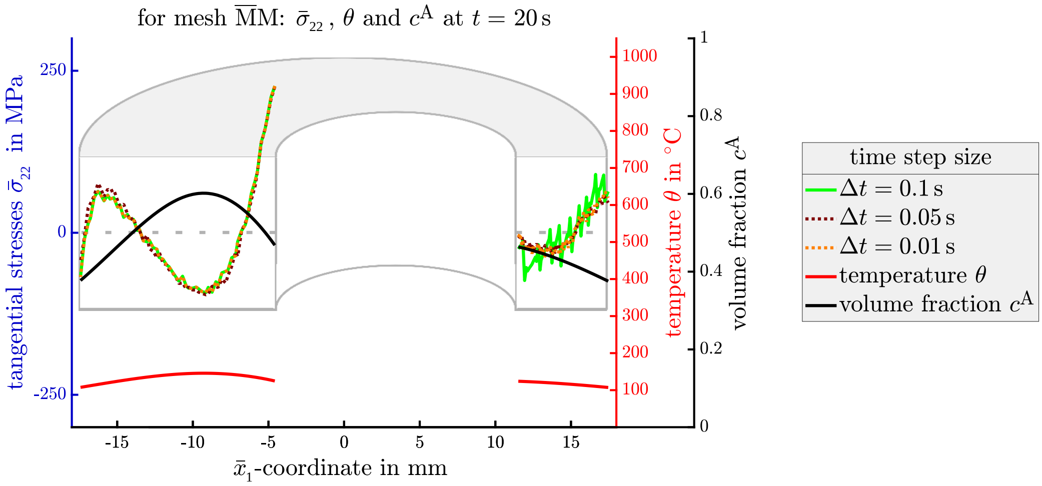

Figure 10.6: Tangential stresses $\bar{\sigma}_{22}$ for the $\bar{x}_1$-axis at $\bar{x}_2 = 0$ and $t = 20\,\text{s}$ for the discretization $\overline{\text{M}}$M and different time step sizes of $\Delta t \in \{0.1\,\text{s}, 0.05\,\text{s}, 0.01\,\text{s}\}$, adapted from Uebing et al. [191].

10.2 Microscopic stress analysis

Based on the mesh density study, it is aimed at the microscopic stress analysis in the hot bulk forming cylindrical specimen, which is treated in the same manufacturing process, that has already been introduced in Section 6.2.1 and for which the mesh density and time step size has been studied in the previous Section 10.1. Therefore, a two-dimensional slice of the undeformed cylindrical specimen is taken into account, exploiting symmetry conditions, see Figure 10.7. Therein, the dimension of the macroscopic geometry as well as the displacement and temperature bound for the thermo-elasto-plastic modeling are depicted. For the discretization, $\overline{20}$ quadrilateral elements with nine nodes in radial direction are chosen, according to the previously carried out study. The offset of the forming history, which is applied in an initialization step, see Section 8.7, as well as the influence of the TRIP are neglected. On the microscale, the RVE consists of 30×30 four noded finite elements, which corresponds to the discretization F. Moreover, a constant temperature is considered in each RVE, since it is attached to one macroscopic material point. Here, also an arbitrary switching scheme is applied to describe the phase transformation on the microscopic level.

In focus of the analysis are three regions of the macroscopic geometry, which are marked as I, II and III, and to which a local refinement of the macroscopic mesh is applied. Furthermore, three points of each of these regions are of special interest, which are marked with the symbols □, ▽ and △, respectively. In a first study, the austenite-to-martensite phase transformation is investigated on the microscopic scale and related to the macroscopic temperature distribution in the cylindrical slice, see Figures 10.8 and 10.9. If the temperature is higher than the martensitic start temperature of $\theta_{\text{Ms}} = 185\,°\text{C}$, the material is fully austenitic. The phase transformation takes place for temperatures lower than θ_{Ms} as seen in Section 6.2 for a similar geometry in a single-scale analysis. Then, the martensitic volume fraction starts to increase in regions near the outer lateral surface in point △ before $t = 9\,\text{s}$ in case of cooling in water, so that Figure 10.8a depicts a significant amount of martensitic elements. In regions near the inner lateral surface as in point □, the onset

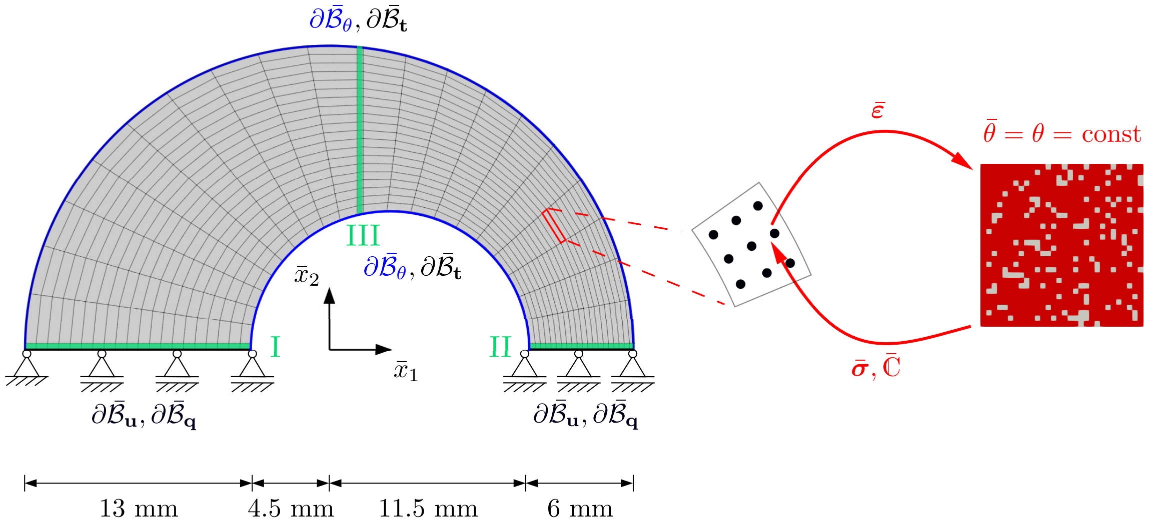

Figure 10.7: Two-scale boundary value problem to numerically simulate the cooling process. A two-dimensional slice of the cylindrical specimen in combination with two-dimensional boundary value problems to depict the austenite-to-martensite transformation is considered. On the macroscale, the boundary conditions $u_2 = 0$ on $\partial\bar{\mathcal{B}}_{\boldsymbol{u}}$, $\bar{q}_0 = 0$ on $\partial\bar{\mathcal{B}}_{\boldsymbol{q}}$, $\bar{\boldsymbol{t}} = 0$ on $\partial\bar{\mathcal{B}}_{\boldsymbol{t}}$ and $\bar{\theta}$ on $\partial\bar{\mathcal{B}}_\theta$ as given in Figure 6.20 are applied. The final phase distribution is given on the microscale with austenite in gray and martensite in red. Regions I, II and III with microscopic investigation points are marked in green, adapted from UEBING ET AL. [192].

of the phase transformation occurs later than at the outer lateral surface, since the inner surface is cooled slower than the outer one. Thus, after $t = 9\,\text{s}$, no martensite is present in these regions, while after $t = 12\,\text{s}$ the austenite-to-martensite phase transformation has already set in, cf. Figure 10.8b.

With ongoing cooling over the lateral surface, the temperature in the bulk material, marked as point $\triangledown$, also steps below the martensitic start temperature, so that the phase transformations is initiated. Here, the bulk material at the thin side of the eccentricity, i.e., in region II, cools faster as a consequence of a faster heat conduction to the middle of the region compared to the cuts I and III. But, after $t = 20\,\text{s}$, the martensitic formation is far advanced in every marked point $\square$, $\triangledown$ and $\triangle$ in each region I, II and III, cf. Figure 10.9a. In a final state after $t = 80\,\text{s}$, the cylindrical specimen is cooled down to room temperature of approximately $\theta_{\text{RT}} = 20\,°\text{C}$, and in every investigated macroscopic integration point 87 % martensite and 13 % retained austenite are observed, see Figure 10.9b.

As already discussed in Sections 4.1 and 9, the austenite-to-martensite phase transformation comes along with a volumetric expansion of the atomic lattice, which is taken as $K_{\text{tm}} = 2\,\%$ in this examination. Thereby, newly switched martensitic elements are known to show compressive stresses. For carrying out a first microscopic stress analysis, the pressure term $p = \frac{1}{3}\,\text{tr}\,\tilde{\boldsymbol{\sigma}}$ is taken into account. Figure 10.10 relates the distribution of this pressure term to the martensitic volume fraction at certain times during the cooling process for point $\triangle$ in region III. With the onset of the phase transformation, compressive stresses occur in the martensitic elements as found before, cf. Figure 10.10a. As more and more martensite forms, these compressive stresses evoke tensile stresses in the austenitic regions in between, which is a direct consequence of the interaction with neighboring expanding finite elements see Figures 10.10b and 10.10c. In a final state, high compressive pressure values up to $p = -1500\,\text{MPa}$ are observed in several martensitic elements, while

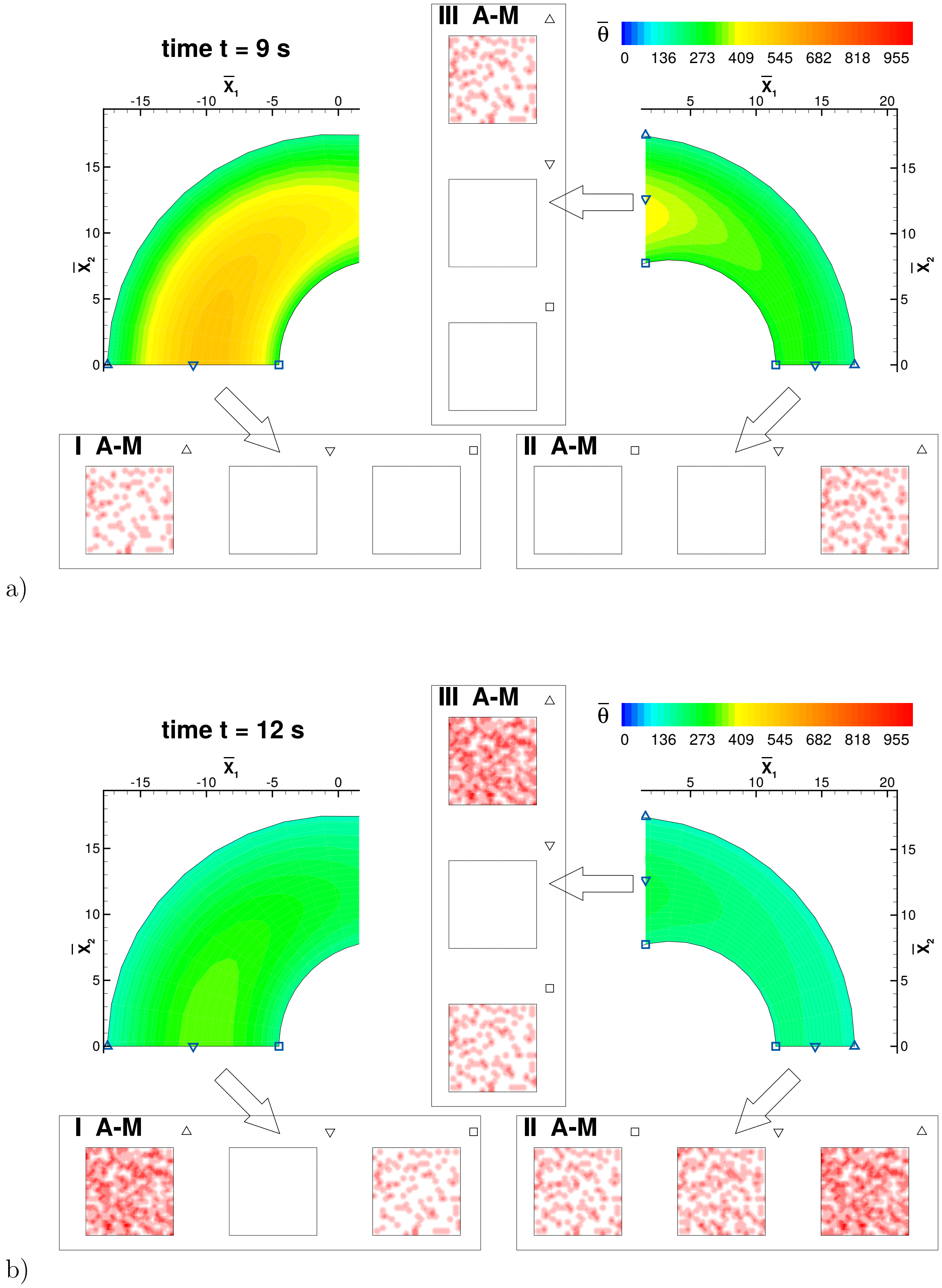

Figure 10.8: Macroscopic temperature $\bar{\theta}$ in °C and microscopic phase fractions of austenite (white) and martensite (red) after a) $t = 9\,\text{s}$ and b) $t = 12\,\text{s}$, adapted from Uebing et al. [192].

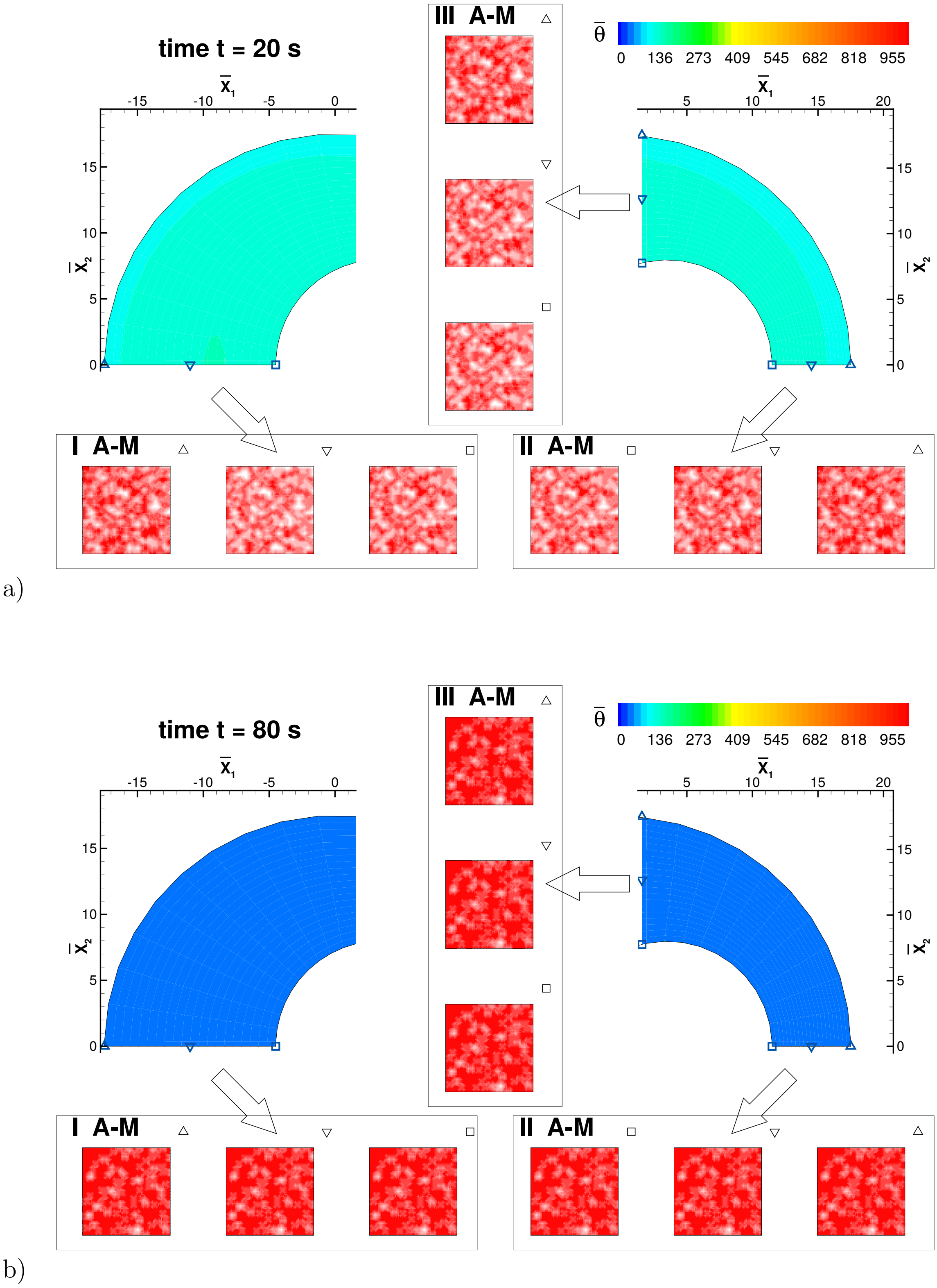

Figure 10.9: Macroscopic temperature $\bar{\theta}$ in °C and microscopic phase fractions of austenite (white) and martensite (red) after a) $t = 20\,\mathrm{s}$ and b) $t = 80\,\mathrm{s}$, adapted from Uebing et al. [192].

the regions of retained austenite show tensile pressure values of up to $p = 1500\,\mathrm{MPa}$, cf Figure 10.10d.

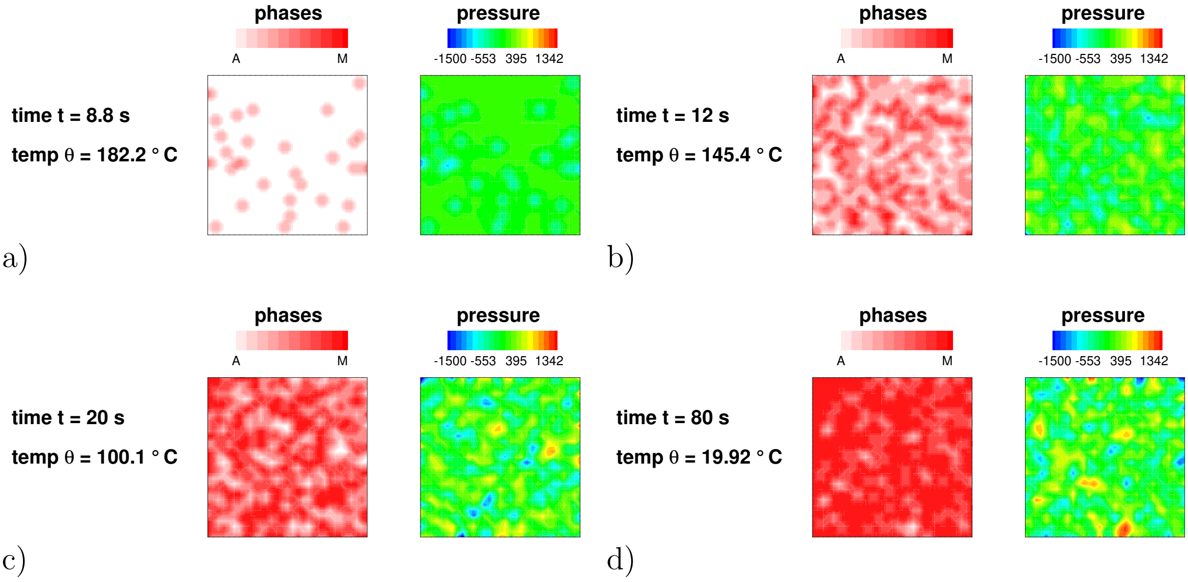

Figure 10.10: Evolution of microscopic phase transformation and relation to stress evolution in MPa on the RVE attached to region III point △ after a) $t = 8.8\,\mathrm{s}$ at the beginning of the martensitic transformation, b) $t = 12\,\mathrm{s}$, c) $t = 20\,\mathrm{s}$ and d) $t = 80\,\mathrm{s}$, adapted from Uebing et al. [192].

In Section 8.8, quadratic measures are defined, which are utilized to investigate the influence of the microscopic fluctuations on the macroscale. Next to the previously defined quadratic measure of the tangential stress fluctuations $||\tilde{\sigma}_{\mathrm{tang}}||^V_{\mathcal{L}^2}$, the quadratic measure of the deviatoric part of the microscopic stress fluctuations, the quadratic measure of the pressure term or the quadratic measure of single components of the microscopic stress fluctuations are taken into account. These are defined in accordance with Equation (8.50) as

$$\begin{aligned} ||p||^V_{\mathcal{L}^2} &= \sqrt{\langle p^2 \rangle} \quad \text{with} \quad \langle p^2 \rangle = \frac{1}{V}\int (\frac{1}{3}\,\mathrm{tr}\,\tilde{\boldsymbol{\sigma}})^2\,\mathrm{d}V\,, \\ ||\tilde{\sigma}_{11}||^V_{\mathcal{L}^2} &= \sqrt{\langle \tilde{\sigma}^2_{11} \rangle} \quad \text{with} \quad \langle \tilde{\sigma}^2_{11} \rangle = \frac{1}{V}\int (\sigma_{11} - \bar{\sigma}_{11})^2\,\mathrm{d}V\,, \\ ||(\mathrm{dev}\,\tilde{\boldsymbol{\sigma}})_{11}||^V_{\mathcal{L}^2} &= \sqrt{\langle (\mathrm{dev}\,\tilde{\boldsymbol{\sigma}})_{11}{}^2 \rangle} \quad \text{with} \quad \langle (\mathrm{dev}\,\tilde{\boldsymbol{\sigma}})_{11}{}^2 \rangle = \frac{1}{V}\int (\mathrm{dev}\,\tilde{\boldsymbol{\sigma}})_{11}{}^2\,\mathrm{d}V\,. \end{aligned} \tag{10.2}$$

Figure 10.11 displays the results for these four quadratic measures $||p||^V_{\mathcal{L}^2}$, $||\tilde{\sigma}_{11}||^V_{\mathcal{L}^2}$, $||(\mathrm{dev}\,\tilde{\sigma})_{11}||^V_{\mathcal{L}^2}$ and $||\tilde{\sigma}_{\mathrm{tang}}||^V_{\mathcal{L}^2}$ at four different stages of phase transformation. Before the phase transformation starts, all four measures are equal to zero, since no stresses are evoked on microscopic level, because the temperature is a constant state variable in every RVE. Shortly after the onset of phase transformation at $t = 9\,\mathrm{s}$, the first differences between the four measures become obvious, which are even more accessible after $t = 12\,\mathrm{s}$. The quadratic measure of the pressure $||p||^V_{\mathcal{L}^2}$ shows values of around $1500\,\mathrm{MPa}$ in regions near the outer lateral surface, which is higher than the computed values of $1200 - 1300\,\mathrm{MPa}$ for $||\tilde{\sigma}_{11}||^V_{\mathcal{L}^2}$ or $||\tilde{\sigma}_{\mathrm{tang}}||^V_{\mathcal{L}^2}$. The measure of the deviatoric part of the fluctuations $||(\mathrm{dev}\,\tilde{\sigma})_{11}||^V_{\mathcal{L}^2}$ is the smallest with values around $500\,\mathrm{MPa}$ in regions near the outer lateral surface, since the austenite-to-martensite phase transformation is characterized only by the volumetric expansion. If more and more martensite forms, the different quadratic measures show nearly homogeneous values after $t = 20\,\mathrm{s}$. This is also true at the end of the cooling process after $t = 80\,\mathrm{s}$. At this point, it still holds that the values of $\|p\|^V_{\mathcal{L}^2}$ exceed the values of $\|\tilde{\sigma}_{11}\|^V_{\mathcal{L}^2}$ and $\|\tilde{\sigma}_{\mathrm{tang}}\|^V_{\mathcal{L}^2}$, which are higher than $\|(\operatorname{dev}\tilde{\sigma})_{11}\|^V_{\mathcal{L}^2}$. But overall, it is found that all four quadratic measures show qualitatively the same behavior.

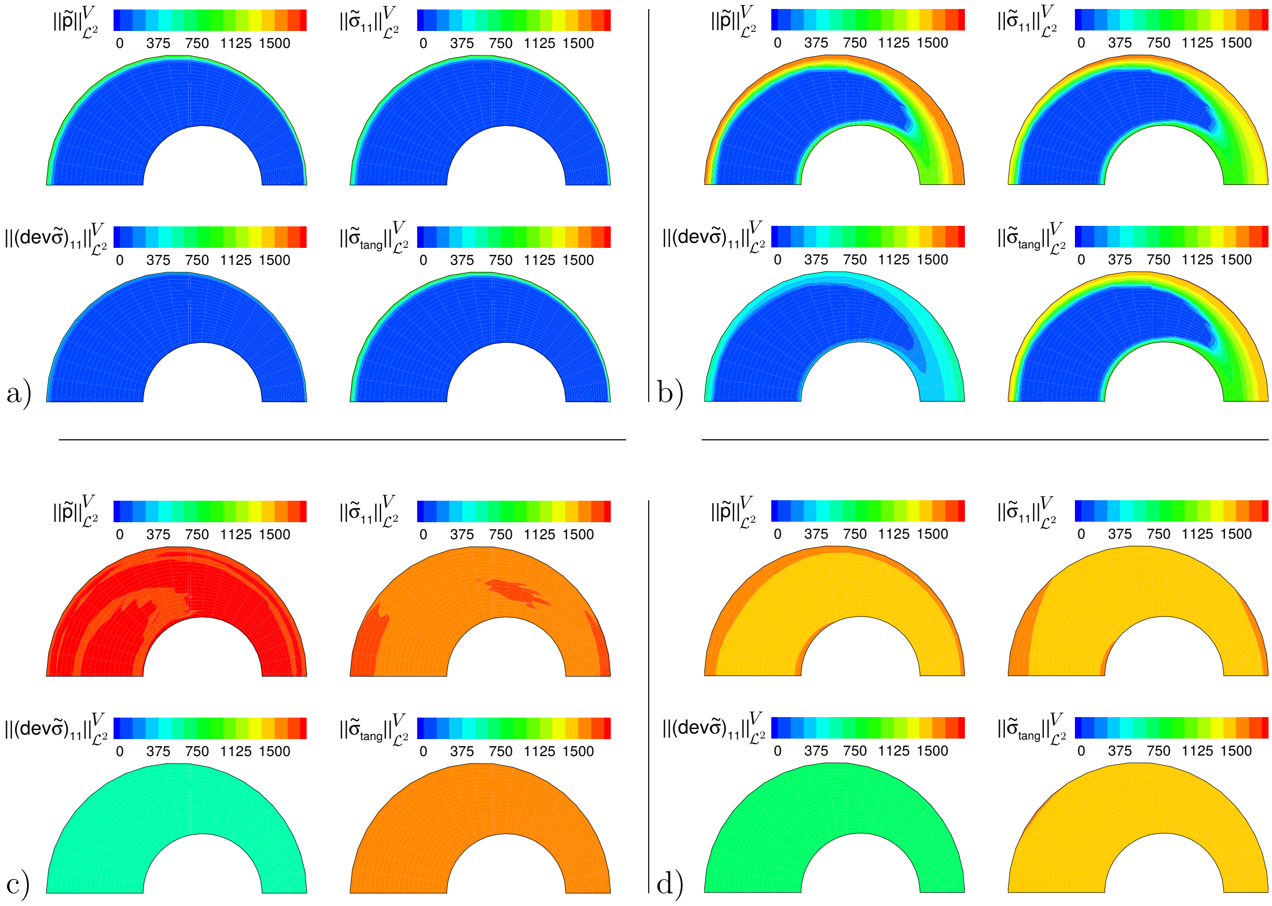

Figure 10.11: Macroscopic measures, namely $\|p\|^V_{\mathcal{L}^2}$, $\|\tilde{\sigma}_{11}\|^V_{\mathcal{L}^2}$, $\|(\operatorname{dev}\tilde{\sigma})_{11}\|^V_{\mathcal{L}^2}$ and $\|\tilde{\sigma}_{\mathrm{tang}}\|^V_{\mathcal{L}^2}$ in MPa after a) $t = 9\,\mathrm{s}$, b) $t = 12\,\mathrm{s}$, c) $t = 20\,\mathrm{s}$ and d) $t = 80\,\mathrm{s}$, adapted from Uebing et al. [192].

These quadratic measures can be used to evaluate the amount of the microscopic stress fluctuations on the macroscale. Nevertheless, they are still a smeared quantity by definition. Thus, it is of interest to investigate the microscopic stress evolution on the RVE directly. As before, no outer forces or moments are present, so that the evolving stresses can be interpreted as residual stress. It holds that the macroscopic stress represents the residual stresses of first type, while the microscopic stress fluctuations resemble the sum of the residual stresses of second and third type. Occurring stress peaks, either compressive or tensile, can influence the component's properties immensely, but, a purely macroscopic analysis or evaluation could lead to absolutely lower macroscopic stress values. As a consequence of the homogenization, these microscopic stress peaks would not be depicted in the macroscopic result although they are quite important as they could lead to e.g. microscopic crack initiation. For this reason it is inevitable to know of these stress peaks to make profound statements regarding the component's properties and its behavior.

Hence, in the following analysis, the microscopic tangential stress fluctuations $\tilde{\sigma}_{\text{tang}}$ are compared to their macroscopic quadratic measure $\|\tilde{\sigma}_{\text{tang}}\|^V_{\mathcal{L}^2}$. As stated previously, microscopic stresses occur with the onset of the austenite-to-martensite phase transformation. As depicted in Figures 10.12, 10.13 and 10.14, the martensite formation, which is in details analyzed in Figures 10.8 and 10.9, comes along with the evocation of microscopic stresses. In martensitic elements compressive stresses arise, which are surrounded by regions showing less compressive or tensile stress values. In the beginning of the phase transformation in regions near the outer lateral surface in point $\triangle$, the quadratic measure $\|\tilde{\sigma}_{\text{tang}}\|^V_{\mathcal{L}^2}$ differs from zero, see Figure 10.12, so that it can be concluded that the macroscopic measure displays the microscopic residual stresses (second and third type) on the component level.

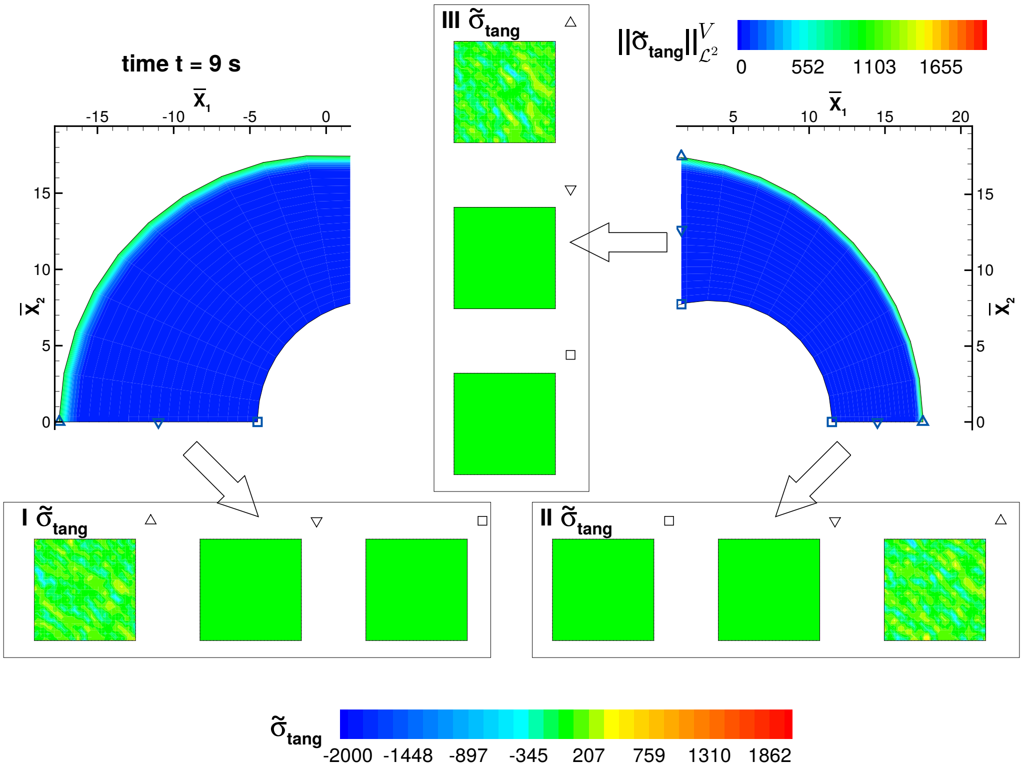

Figure 10.12: Tangential part of stress fluctuations $\tilde{\sigma}_{\text{tang}}$ in MPa on microscale and their quadratic measure $\|\tilde{\sigma}_{\text{tang}}\|^V_{\mathcal{L}^2}$ in MPa on the macroscale after $t = 9\,\text{s}$, adapted from UEBING ET AL. [192].

With ongoing cooling after $t = 12\,\text{s}$ or $t = 20\,\text{s}$, microscopically complex stress patterns are found consisting of compressive as well as tensile stress peaks, cf. Figures 10.13 and 10.14a. In accordance, the value of the quadratic measure increases in regions undergoing the phase transformation. As more and more elements switch from austenite to martensite, the stress evolutions in all points $\square$, $\bigtriangledown$ and $\triangle$ become more and more alike and thus, the quadratic measure shows a nearly homogeneous stress distribution. As expected, the final state after $t = 80\,\text{s}$ shows almost no deviations in the microscopic tangential stress distribution $\tilde{\sigma}_{\text{tang}}$ and as a consequence, the quadratic measure $\|\tilde{\sigma}_{\text{tang}}\|^V_{\mathcal{L}^2}$ is also almost entirely homogeneous, see Figure 10.14b. This is observed as expected, since the microstructure of the whole component is at room temperature and consists of the same phase fractions of austenite and martensite in the final state.

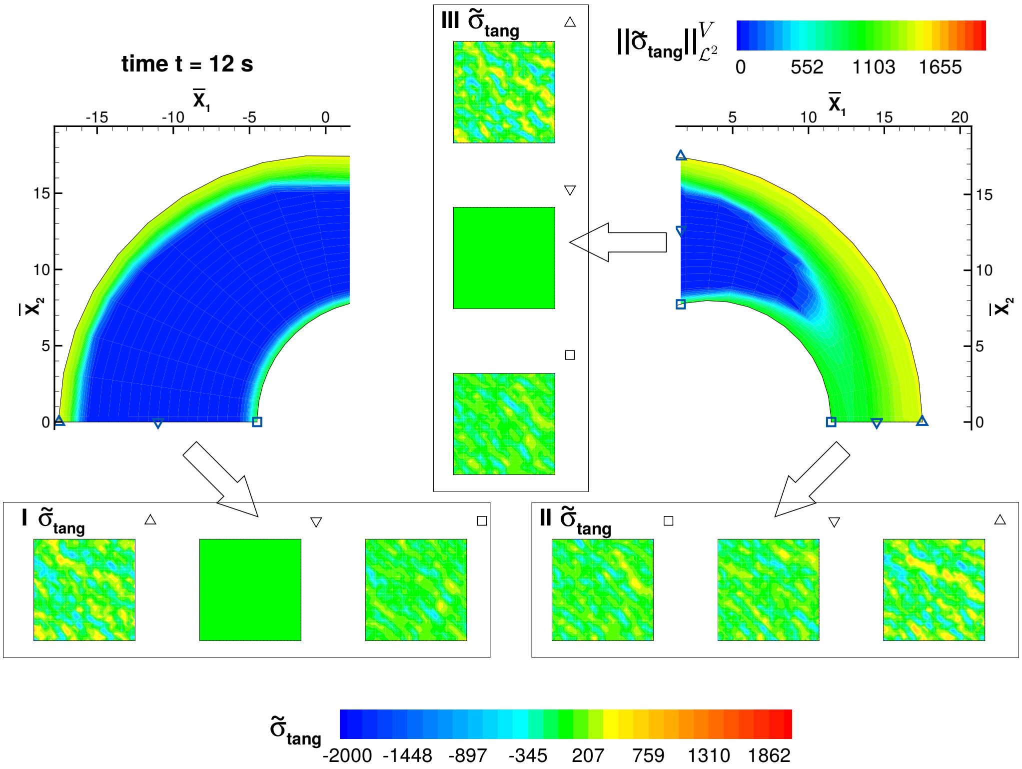

Figure 10.13: Tangential part of stress fluctuations $\tilde{\sigma}_{\text{tang}}$ in MPa on microscale and their quadratic measure $\|\tilde{\sigma}_{\text{tang}}\|^V_{\mathcal{L}^2}$ in MPa on the macroscale after $t = 12\,\text{s}$, adapted from Uebing et al. [192].

In a last step, the quadratic measure $\|\tilde{\sigma}_{\text{tang}}\|^V_{\mathcal{L}^2}$, which represents the microscopic residual stresses on the macroscale, is compared to the macroscopic residual stresses $\bar{\sigma}_{\text{tang}}$. As shown in Figure 10.15a, the fast cooling evokes tensile stresses in regions near the lateral surface for $\bar{\sigma}_{\text{tang}}$ due to the thermal contraction. At this point $t = 5\,\text{s}$, the phase transformation is not initiated and thus, the microscopic residual stresses, measured by $\|\tilde{\sigma}_{\text{tang}}\|^V_{\mathcal{L}^2}$, is equal to zero.

When the austenite-to-martensite phase transformation starts, the stresses $\bar{\sigma}_{\text{tang}}$ change their sign in the regions near the outer lateral surface, cf. Figure 10.15b. There, compressive stresses occur, which are a consequence of superposition of the tensile stresses due to thermal contraction and high compressive stress fluctuations due to the volumetric expansion of the unit cell during the lattice shearing. These high compressive microscopic residual stress values are indicated by the high values of the quadratic measure $\|\tilde{\sigma}_{\text{tang}}\|^V_{\mathcal{L}^2}$ in regions near the outer lateral surface, see also Figure 10.15c. In Figure 10.16 the macroscopic tangential residual stresses $\bar{\sigma}_{\text{tang}}$ and the quadratic measure of the microscopic tangential residual stresses $\|\tilde{\sigma}_{\text{tang}}\|^V_{\mathcal{L}^2}$ are compared with different color scaling in the final state. Thereby, differences in the measure $\|\tilde{\sigma}_{\text{tang}}\|^V_{\mathcal{L}^2}$ are found, i.e., the residual stresses left of the eccentricity are higher than on the right side. It is obvious, that the microscopic and macroscopic residual stress plots do not fit qualitatively. On macroscale tensile stresses are found in regions near the outer surface, while the bulk material shows compressive stress values. This observations is in good accordance with previously carried out single-scale computations of the cooling of a hot bulk formed part in water, see Section 6.2.4.

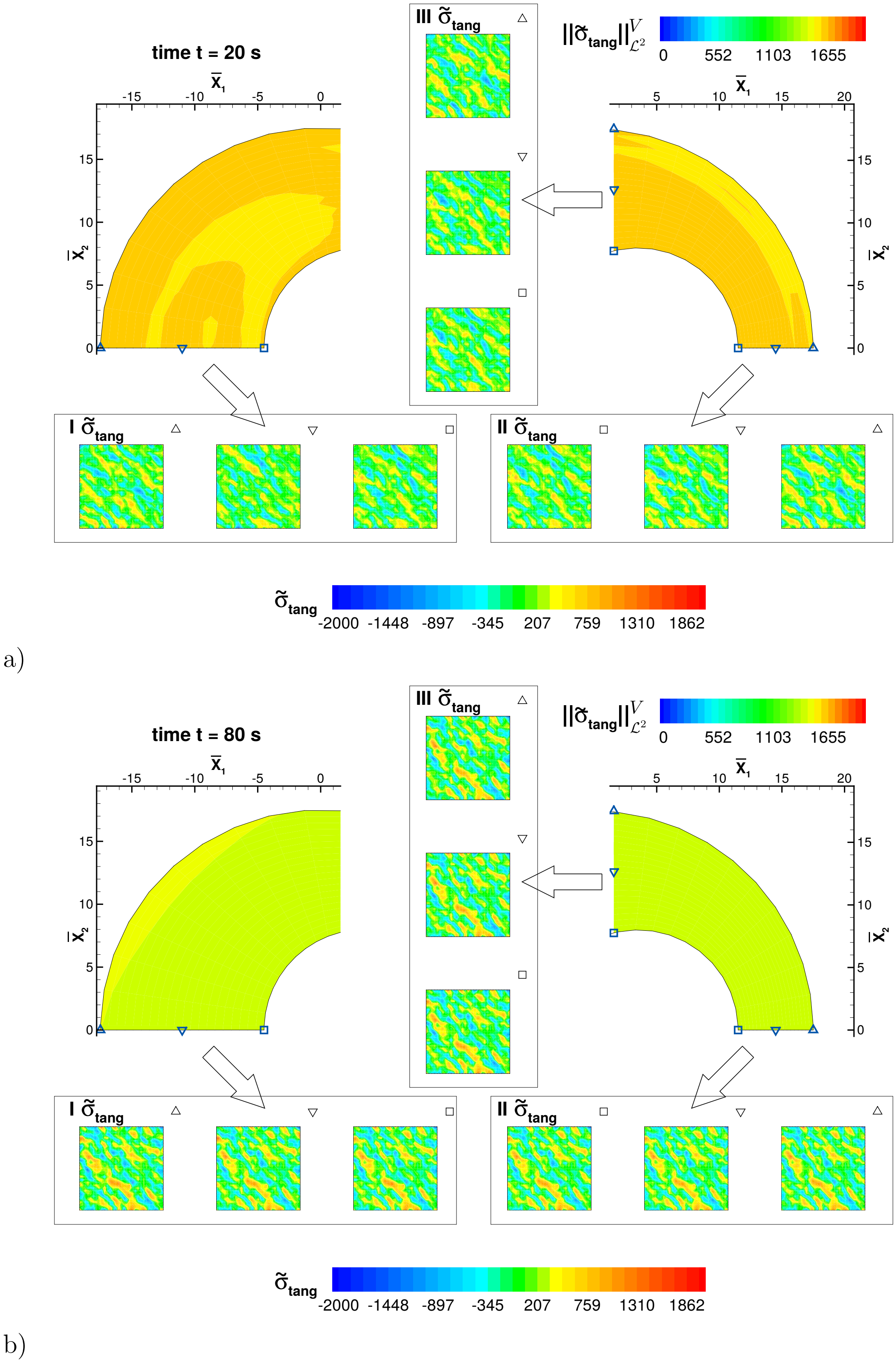

Figure 10.14: Tangential part of stress fluctuations $\tilde{\sigma}_{\text{tang}}$ in MPa on microscale and their quadratic measure $\|\tilde{\sigma}_{\text{tang}}\|^V_{\mathcal{L}^2}$ in MPa on the macroscale after a) $t = 20\,\text{s}$ and b) $t = 80\,\text{s}$, adapted from Uebing et al. [192].

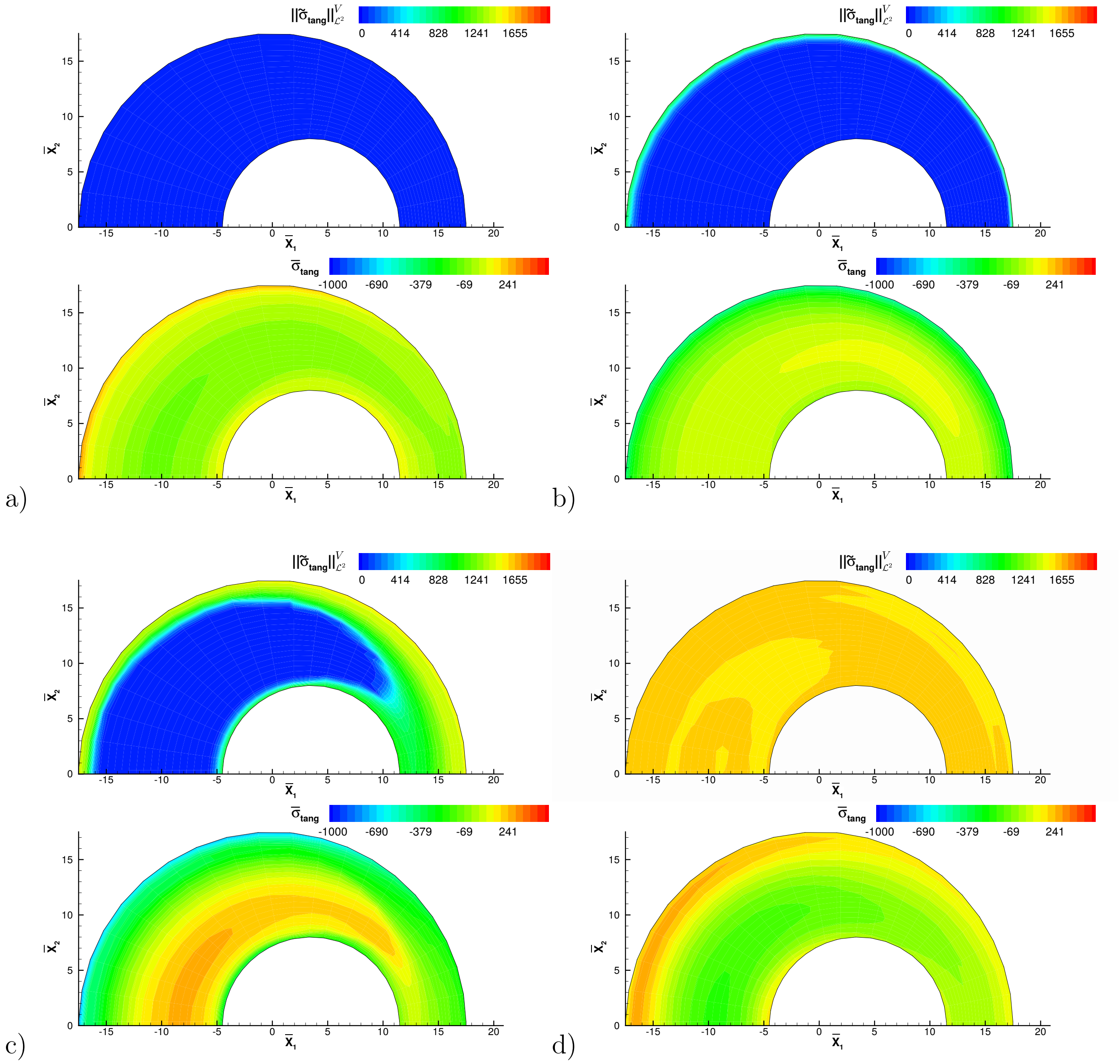

Figure 10.15: Tangential residual stresses of first type $\bar{\sigma}_{\text{tang}}$ in MPa and macroscopic measure of microscopic tangential residual stresses $||\tilde{\sigma}_{\text{tang}}||^V_{\mathcal{L}^2}$ in MPa after a) $t = 5\,\text{s}$, b) $t = 9\,\text{s}$, c) $t = 12\,\text{s}$ and d) $t = 20\,\text{s}$, adapted from Uebing et al. [192].

In contrast to that, the microscopic (residual) stress fluctuations do not seem to relate on their associated macroscopic position. At the end of the cooling, when the material consists of the same amount of austenite and martensite in every macroscopic integration point, a nearly homogeneous distribution of the quadratic measure is obtained.

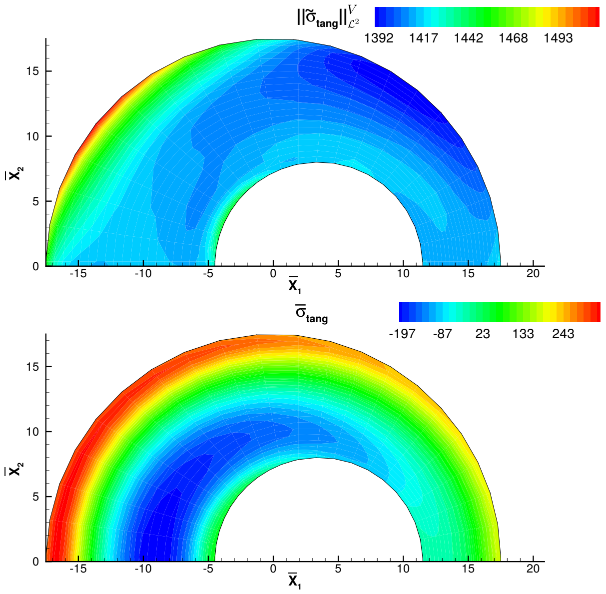

Figure 10.16: Tangential residual stresses of first type $\bar{\sigma}_{\mathrm{tang}}$ in MPa and macroscopic measure of microscopic tangential residual stresses $\|\tilde{\sigma}_{\mathrm{tang}}\|^V_{\mathcal{L}^2}$ in MPa after $t = 80\,\mathrm{s}$, adapted from UEBING ET AL. [192].

10.3 Microscopic stress analysis including TRIP strains

Based on the previous results and the results of Section 9, a two-scale analysis of the hot bulk forming of a cylindrical specimen with eccentric hole made from the Cr-alloyed steel 100Cr6 is carried out. In Section 6, the according two-dimensional single-scale boundary value problem for cooling with different media has already been defined, cf. e.g. Figures 6.9 and 6.20. In contrast to the mesh density study in Section 10.1 and the microscopic stress analysis in Section 10.2, the cylindrical slice is cut from the deformed cylindrical specimen. The geometry presented in Section 6.2 is now to be considered as the macroscopic boundary value problem. Moreover, the displacement boundary conditions as well as the thermal boundary conditions describing fast cooling in water over the lateral surface of the specimen are adopted. Unfortunately, the mesh size study in Section 6.2.3 has shown that at least 5000 finite elements are necessary to obtain reasonable results on the macroscopic level. This high number of degrees of freedom in combination with a microscopic boundary value problem based on a representative volume element (RVE), that also has a sufficient high number of microscopic elements, leads to high computational costs and very long computation times. Thus, it is inevitable to find a possibility to reduce the numerical complexity of the macroscopic boundary value problem.

Therefore, the following procedure can be applied: In a first step, the single-scale analysis is carried out, see Section 6. During the calculation, the displacement in second direction $\bar{u}_{2,\mathrm{original}}$ is stored along the red dashed line for every computational step, see Figure 10.17a. In a second step, the geometry is trimmed to the area beneath that dashed line. The stored displacement $\bar{u}_{2,\mathrm{original}}$ serves as an additional displacement boundary condition, that provides information regarding the cut of material behavior in a single-scale analysis of the cylindrical segment, see Figure 10.17b. In a final step, a two-scale analysis on the reduced cylindrical segment is carried out, for which the two-scale boundary value problem is defined in Figure 10.18. Thereby, the number of macroscopic elements is reduced to 300 finite elements (50 radial × 6 tangential), which resembles only 6 % of the initial mesh with 5000 finite elements that is 50 elements in radial direction and 100 elements in circumferential direction.

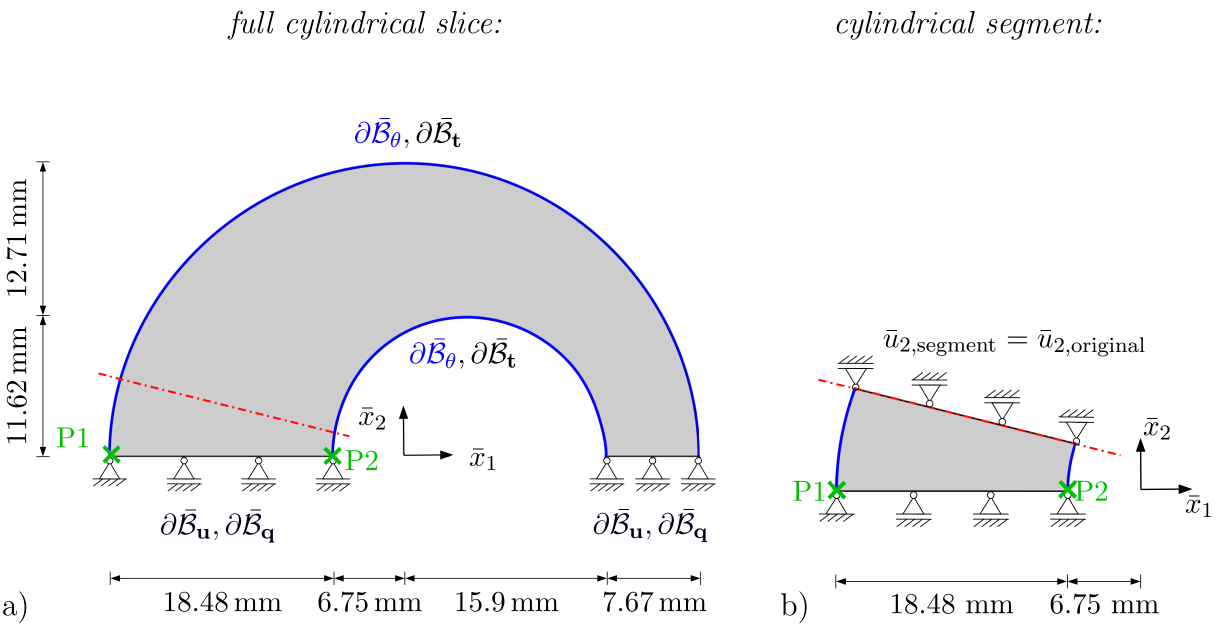

Figure 10.17: Geometries of two boundary value problems: a) A cylindrical slice with the given dimensions and boundary conditions is cooled over the lateral surface. During the calculation the displacement in second direction $\bar{u}_{2,\text{original}}$ is stored along the red dashed line for every computational step. b) A segment of the cylindrical specimen is considered with an additional boundary condition along the red dashed line $\bar{u}_{2,\text{segment}} = \bar{u}_{2,\text{original}}$.

On the microscopic level, two types of evolution strategies to depict the phase transformation are taken into account. As stated before, the fast cooling in water over the lateral surface results in a diffusionless phase transformation from austenite to martensite. This is considered either with an arbitrary switch or with a grain structure on the microscale. For the latter the different grain orientations are taken into account in terms of rotated Bain groups, cf. Section 9.4, which lead to nonuniform volumetric expansions of the atomic lattice.

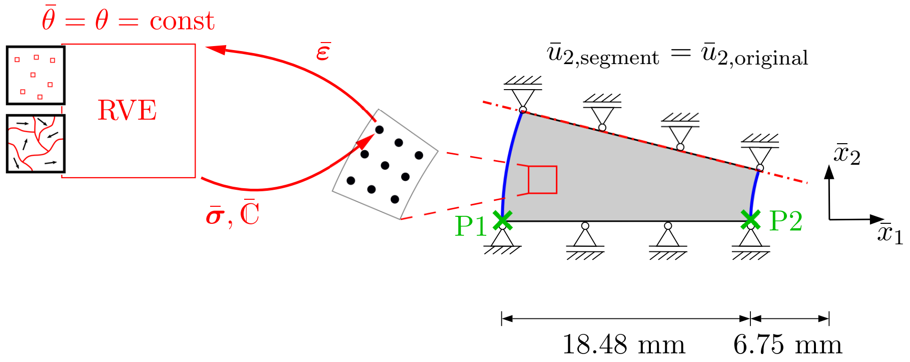

Figure 10.18: Two-scale boundary value problem with additional boundary condition along the red dashed line on the macroscale. The RVE on microscopic level is chosen either as RVE with an arbitrary switch or with a grain structure considering individual orientations as defined in Figures 9.3 or 9.6.

10.3.1 Macroscopic and microscopic stress analysis

At first, macroscopic results of the single-scale boundary value problem, the segmented boundary value problem in a single-scale analysis and the two-scale boundary value problem of the cylindrical segment taking into account either an RVE with an arbitrary switch or a grain structure with individual grain orientations are compared. Therefore, the stress evolutions in different macroscopic integration points over the complete cooling time are taken into account, which are marked in Figure 10.18 as points P1 and P2.

As shown in Figure 10.19, the different boundary value problems lead to small deviations regarding the macroscopic tangential stresses $\bar{\sigma}_{22} = \bar{\sigma}_{\text{tang}}$ in both points P1 and P2. The stress evolutions in both points for the full and the segmented single-scale boundary value problems fit very well. Regarding point P1, the tensile and compressive stress peaks of $\approx 750\,\text{MPa}$ and $-1350\,\text{MPa}$ are nearly of the same level and the final stress value of $100\,\text{MPa}$ coincides. Hence, the way to obtain the segmentation is assumed to be a simplified but good method. The segmented two-scale boundary value problem with the RVE utilizing the arbitrary switch results in a slightly less pronounced compressive stress peak of $-1000\,\text{MPa}$ around $t = 18\,\text{s}$. Taking into account a grain structure with 40 grains leads to the highest compressive stress around $-800\,\text{MPa}$. This offset propagates in the individual stress curves, so that the final values of both multi-scale calculations exceed the single-scale results. At the end of the cooling at time $t = 80\,\text{s}$, these respective stress values are $\bar{\sigma}_{22} = 300\,\text{MPa}$ in case of the arbitrary switch and $\bar{\sigma}_{22} = 400\,\text{MPa}$ in case of the grain structure.

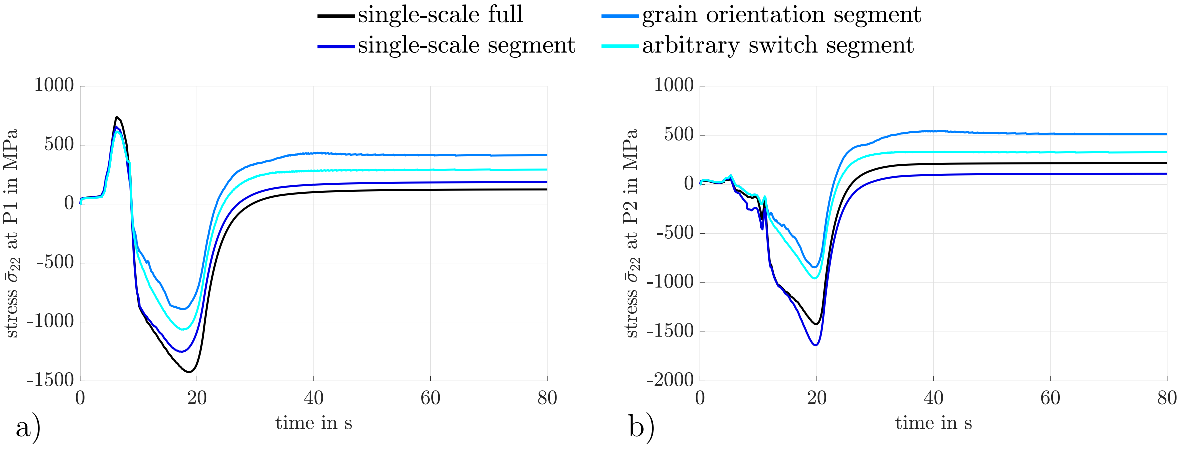

Figure 10.19: Comparison of the evolution of the stress component $\bar{\sigma}_{22}$ in MPa in two different macroscopic integration points located near a) P1 and b) P2 for the full single-scale boundary value problem, the segmented single-scale boundary value problem and the segmented two-scale boundary value problem.

For point P2 a qualitatively similar stress evolution is observed. With the onset of the phase transformation in regions near the lateral surface, where the points of interest are located, macroscopic compressive stresses arise. Here, the compressive stress peak is the smallest for the multi-scale approach utilizing the RVE with the grain structure, $\bar{\sigma}_{22} = -800\,\text{MPa}$, and largest for the segmented single-scale model, $\bar{\sigma}_{22} = -1600\,\text{MPa}$. Again, this difference remains throughout the cooling process. In the final state, both single-scale approaches and the multi-scale approach with the arbitrary switch fit quite well. The final stress value lies between $\bar{\sigma}_{22} = 100\,\text{MPa}$ to $200\,\text{MPa}$. In case of the multi-scale investigation with the RVE utilizing the grain structure, these values are significantly exceeded. Nevertheless, both single-scale approaches and the two-scale approach with the RVE utilizing the arbitrary switch are qualitatively in good accordance with respect to the macroscopic stress evolution. It can be concluded that the macroscopic quantities are close enough for the purpose of carrying out a microscopic analysis in terms of a two-scale approach. Therewith, information regarding the phase transformation and related microscopic stresses are gained. Regarding the computation with individual grain orientations, it is confirmed that the grain size impacts the final stresses. These findings are in good agreement with previous investigations in Section 9.4. However, it is important to examine other methods of obtaining the segment. In this approach, only the displacement in $\bar{x}_2$-direction is applied along the red dashed-line and the temperature evolution or the displacement in $\bar{x}_1$-direction is neglected. Taking into account both could lead to improved results and should be considered in further studies.

Figures 10.20 and 10.21 depict the macroscopic tangential stress $\bar{\sigma}_{\text{tang}}$ and the microscopic stress component σ_{22} in relation to the phase evolution for the RVE evaluated in the integration point nearest the left lower corner, marked as P1 in Figure 10.19. The upper plot always refers to an RVE with arbitrary switch while the lower one shows the results of a microstructure consisting of 40 grains with respective grain orientation. Before the onset of the phase transformation, both computations give the same results. On the left lateral surface, which cools fastest, macroscopic tensile stresses of approximately 700 MPa are observed as a consequence of thermal contraction. In both RVEs, the according homogeneous stress values for σ_{22} are found, cf. Figure 10.20a. With the onset of the phase transformation, the stress distributions in both RVEs are not homogeneous any more, see Figure 10.20b and c. In case of an arbitrary switch, elements considered to be martensite show compressive stresses due to the volume change of the unit cell and in the austenitic matrix, resultant tensile stresses are observed. In case of a grain structure, three prominent martensitic grains start to form, which evoke tensile stresses in the surrounding austenitic material. Since the macroscopic stresses are computed by homogenization of the microscopic stresses, the region near the outer lateral surface shows compressive stress values on the macrolevel for both boundary value problems.

After 15 seconds of cooling, in the middle of the phase transformation, stresses of -750 MPa are observed in regions near the left and right lateral surface for the RVE with the arbitrary switch, see Figure 10.21a. In case of the RVE with the grain structure, that value at the right lateral surface, $\bar{\sigma}_{\text{tang}} \approx -400$ MPa is clearly larger, what fits the observation in Figure 10.19. When the phase transformation proceeds to the bulk material, the macroscopic compressive stresses are weakened and tensile stresses in regions near the lateral surface occur, see Figure 10.21b and c. For the computations utilizing the arbitrary switch, theses stress values are less compared to the RVE with the grain structure. On the microscale, both RVEs show complex stress states with compressive and tensile stress peaks, which can roughly be mapped onto the occurring martensitic or austenitic regions. At the end of the cooling process, the macroscopic tangential stress distribution shows tensile stresses near the lateral surface and compressive stress values in the bulk material, which is in accordance with the full single-scale computation, see Section 6.2.4. The RVE with the grain structure evokes higher macroscopic tensile stress values in the component than the RVE utilizing the arbitrary switch.

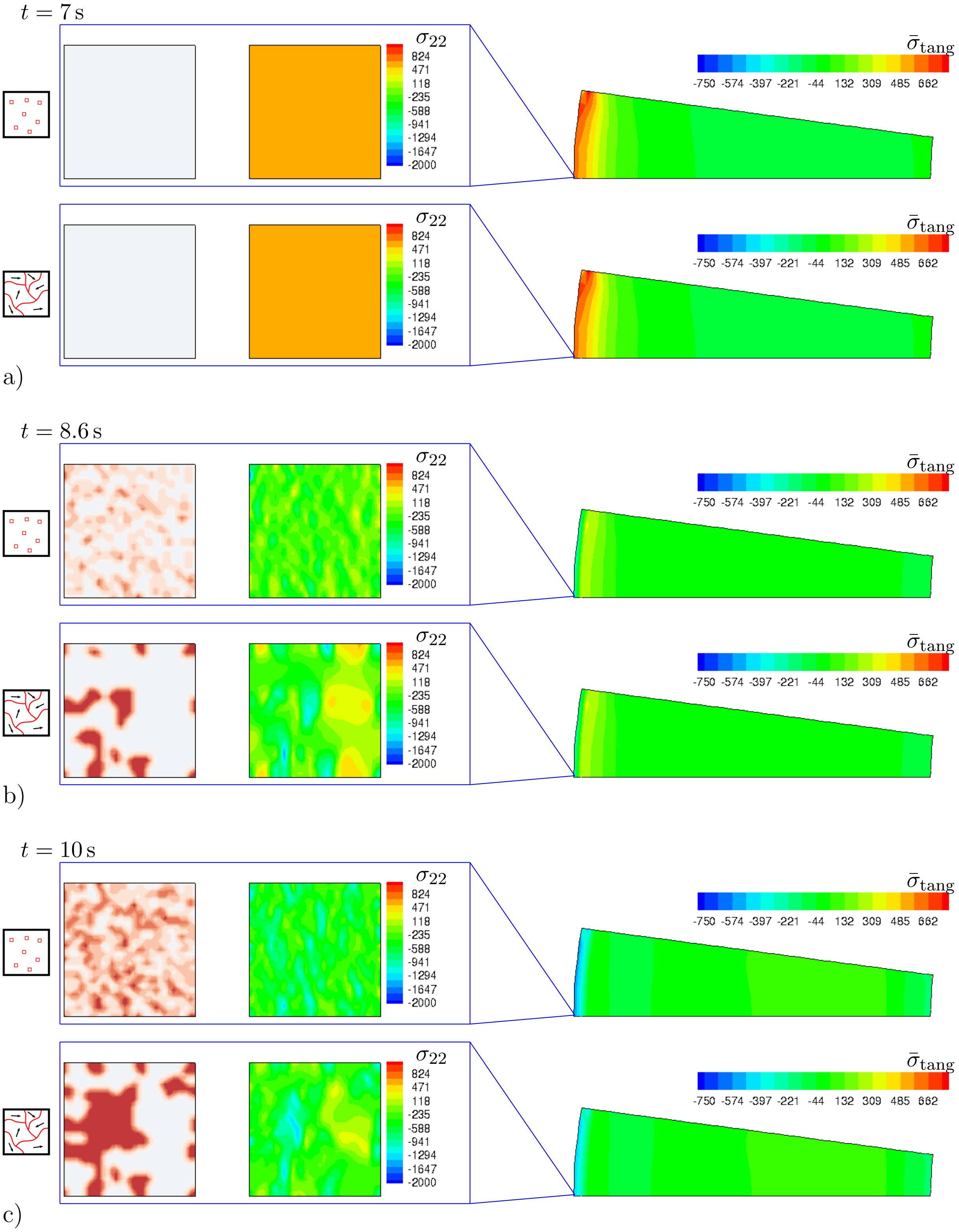

Figure 10.20: Macroscopic tangential stress $\bar{\sigma}_{\mathrm{tang}}$ in MPa and microscopic stress σ_{22} in MPa related to the phase evolution computed with two different RVEs, namely an arbitrary switch or a grain structure with different grain orientations at certain points in time a) $t = 7\,\mathrm{s}$, b) $t = 8.6\,\mathrm{s}$ and c) $t = 10\,\mathrm{s}$.

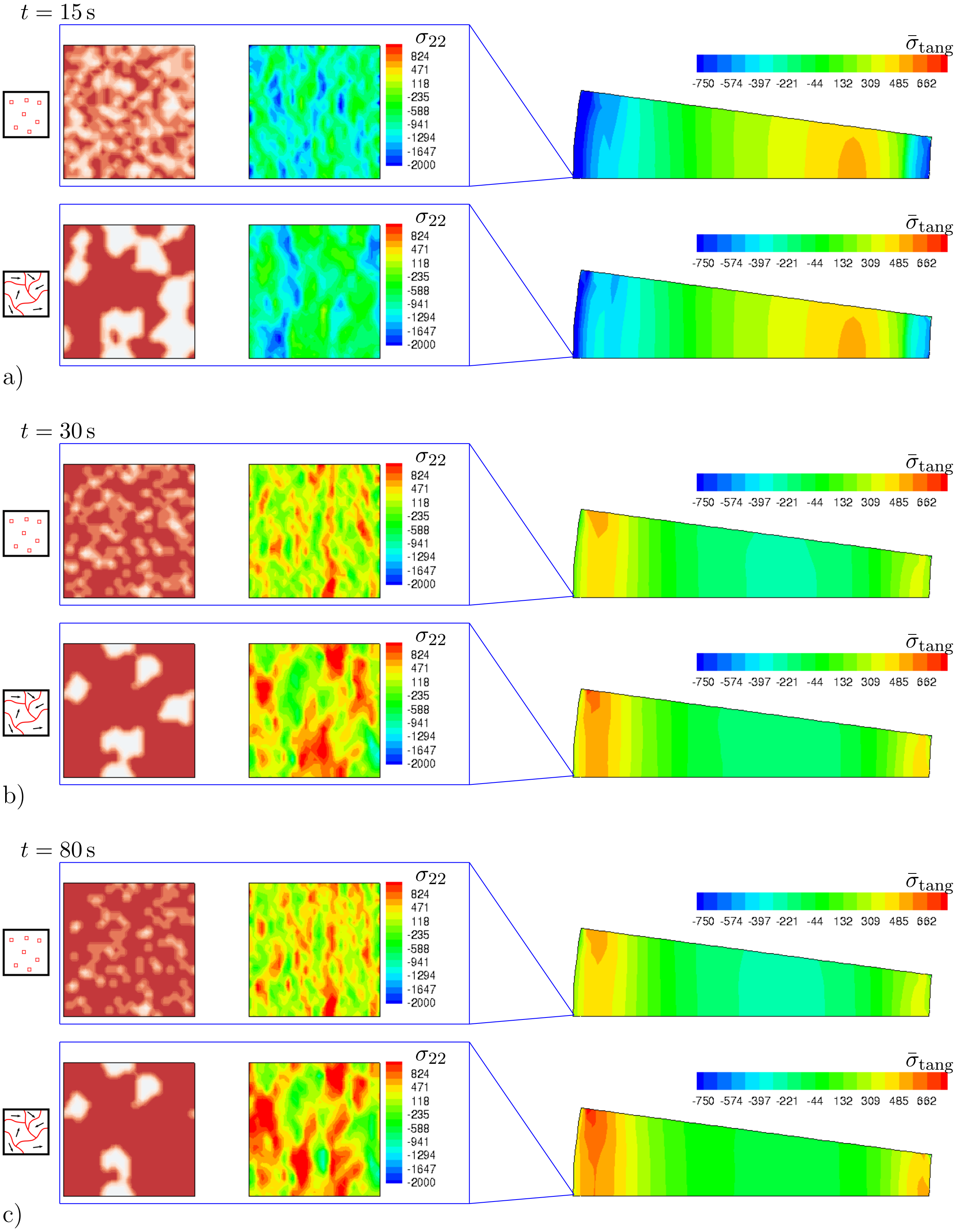

Figure 10.21: Macroscopic tangential stress $\bar{\sigma}_{\mathrm{tang}}$ in MPa and microscopic stress σ_{22} in MPa related to the phase evolution computed with two different RVEs, namely an arbitrary switch or a grain structure with different grain orientations at certain points in time a) $t = 15\,\mathrm{s}$, b) $t = 30\,\mathrm{s}$ and c) $t = 80\,\mathrm{s}$.

The stress evolution on different scales has been object of the analysis. In absence of outer forces and moments and since there is no temperature gradient in the final component's state, these stresses can be interpreted as residual stresses. With regard to the color legend in Figure 10.21c, one finds prominent differences between macroscale and microscale. On the upper scale, the stresses $\bar{\sigma}_{\text{tang}}$ are in a range from $-750\,\text{MPa}$ to $+750\,\text{MPa}$. On the lower scale, the color legend ranges from $-2000\,\text{MPa}$ to $+1000\,\text{MPa}$. Thus, high microscopic residual stress peaks, neither tensile nor compressive ones, are not predictable in single-scale investigations, although they are eminently significant with respect to the component's properties. Such high microstresses can induce microscopic cracks or promote the crack growth, especially if tensile residual stresses are present. Thereby, the component's strength can be reduced and the service-life shortened. For that reason, the targeted induction of predefined residual states is subject to current research, i.e., the induction of compressive residual stresses in regions near the outer surface. Adopting the cooling route, e.g. by application of a spray cooling, cf. Section 6.2.6, leads to compressive stresses in regions near the outer lateral surface, which is known to influence the component's behavior positively. Moreover, the microscopic residual stress distribution is also altered, see e.g. HELLEBRAND ET AL. [76].

10.3.2 Quadratic measure of microscopic fluctuations

Multi-scale methods enable the analysis of macroscopic and microscopic residual stresses in the component and the RVE, respectively, see Section 10.3.1. In addition, a representation of the microscopic stresses on the macroscale is of interest in the following. Therefore, the quadratic measures of the microscopic stress fluctuations are taken into account as defined in Section 8.8, which allow to study the influence of the microscopic fluctuations on the macroscopic stresses. At this point it is emphasized once more that it is unavoidable to define a quadratic measure, since the volume average of the microscopic stress fluctuations $\tilde{\boldsymbol{\sigma}}$ is zero by definition, i.e., $\langle \tilde{\boldsymbol{\sigma}} \rangle = 0$. However, a main disadvantage of such a quadratic measure is that information concerning the stress sign is lost. That means that due to the even exponent, it is no longer possible to deduce on the macroscale whether tensile or compressive stresses are present on the microscale. Here, the quadratic measure of the microscopic tangential part of the stress fluctuations $\|\tilde{\sigma}_{\text{tang}}\|^{V}_{\mathcal{L}^2}$ is evaluated in the following, cf. Equation (8.50). The results at certain points in time are depicted in Figure 10.22. Therein, the quadratic measure $\|\tilde{\sigma}_{\text{tang}}\|^{V}_{\mathcal{L}^2}$ is investigated for both the RVE considering an arbitrary switch and the RVE with a grain structure.

Before the phase transformation starts, the fluctuations $\tilde{\sigma}_{\text{tang}}$ and their quadratic measure $\|\tilde{\sigma}_{\text{tang}}\|^{V}_{\mathcal{L}^2}$ are zero as expected, cf. Figure 10.22a. Observed macroscopic and microscopic stresses, as depicted in Figure 10.20a, are hence of thermal nature. When the region near the outer lateral surface is cooled below the martensitic start temperature, i.e., the austenite-to-martensite phase transformation is switched on, this does not hold anymore. On the microscale, one observes a non-homogeneous microstructure consisting of austenite and martensite for both type of RVEs (arbitrary or grain structure), cf. Figures 9.13 and 9.15. The related microscopic tangential stress fluctuations show a combination of tensile and compressive stress values. The latter are due to several elements switching to martensite and the related volumetric expansion of the atomic lattice. For the RVE with the grain structure, these regions are only few but larger and more pronounced as it is the case for the RVE with an arbitrary switch, see Figure 10.22b. On the macroscale, first differences regarding the evolution of the quadratic measure $||\tilde{\sigma}_{\text{tang}}||^V_{\mathcal{L}^2}$ can be noticed at time $t = 8.6\,\text{s}$, comparing the two evolution strategies. For an arbitrary switch, a higher maximum value of $||\tilde{\sigma}_{\text{tang}}||^V_{\mathcal{L}^2} \approx 700\,\text{MPa}$ is computed, while the grain structure results in a reduced maximum value of $||\tilde{\sigma}_{\text{tang}}||^V_{\mathcal{L}^2} \approx 375\,\text{MPa}$. Please note that each macroscopic plot has its own, individual color legend. This difference on the macrolevel continues to accumulate, so that after ten seconds of cooling maximum values of $||\tilde{\sigma}_{\text{tang}}||^V_{\mathcal{L}^2} \approx 1300\,\text{MPa}$ and $||\tilde{\sigma}_{\text{tang}}||^V_{\mathcal{L}^2} \approx 500\,\text{MPa}$, respectively, are found, cf. Figure 10.22c. At this time, both RVEs show qualitatively the same behavior as in Figure 10.22b, resulting in a mix of regions with tensile and regions with compressive stresses. The progress of the phase transformation leads to increasing values for the quadratic measure in regions close to the lateral surface in both computations. But, it can be observed that after 15 seconds of cooling the RVE with the arbitrary switch yields values about twice as large as the RVE with the grain structure, see Figure 10.22d. At a lateral state of cooling after $t = 30\,\text{s}$, the phase transformations also take place in the bulk of the component, so that the values of the quadratic measure for the RVEs differ by a factor of 1.5, approximately, cf. Figure 10.22d. The macropscopic deviations, although slightly weakened, do not resolve until end of cooling, see Figure 10.22e.

This study shows that the grain structure on the microscale has an influence on the resulting microscopic stresses and microscopic residual stresses, respectively, which further influence their macroscopic counterparts. While both martensitic evolution strategies describe nearly the same macroscopic stress response for $\bar{\sigma}_{\text{tang}}$, significant discrepancies are seen in the evaluation of the quadratic measure of the microscopic fluctuation of the tangential stresses. To interpret this, it is best to look at the definition of the stress fluctuations given in Section 8, i.e., $\tilde{\boldsymbol{\sigma}} = \boldsymbol{\sigma} - \bar{\boldsymbol{\sigma}}$, which is equivalent to $\boldsymbol{\sigma} = \tilde{\boldsymbol{\sigma}} + \bar{\boldsymbol{\sigma}}$. Accordingly, the influence of the fluctuations on the stresses is larger for an RVE with the arbitrary switch than for an RVE with the grain structure. Conversely, for the latter it must be true that the influence of the homogeneous part is greater than for an RVE with the arbitrary switch. Section 9.3.3 already showed that the number of grains in the microstructure has an effect on the resulting macroscopic stresses. A higher number of grains is equivalent to a finer grain size, as is the case for the RVE with the arbitrary switch. The RVE with the grain structure is based on 40 grains, which is therefore interpreted as RVE with coarse grain size. Thus, the almost double values of the quadratic measure for RVEs with fine grain size compared to the coarse grain size proof the influence of the grain size on the phase transformation and the associated stress development. Such an effect of the initial austenitic grain size with respect to the phase transformation is also evident in HEINZE ET AL. [75], KLAPROTH AND VOLLERTSEN [90], CELADA-CASERO ET AL. [25] and BEHRENS ET AL. [16].

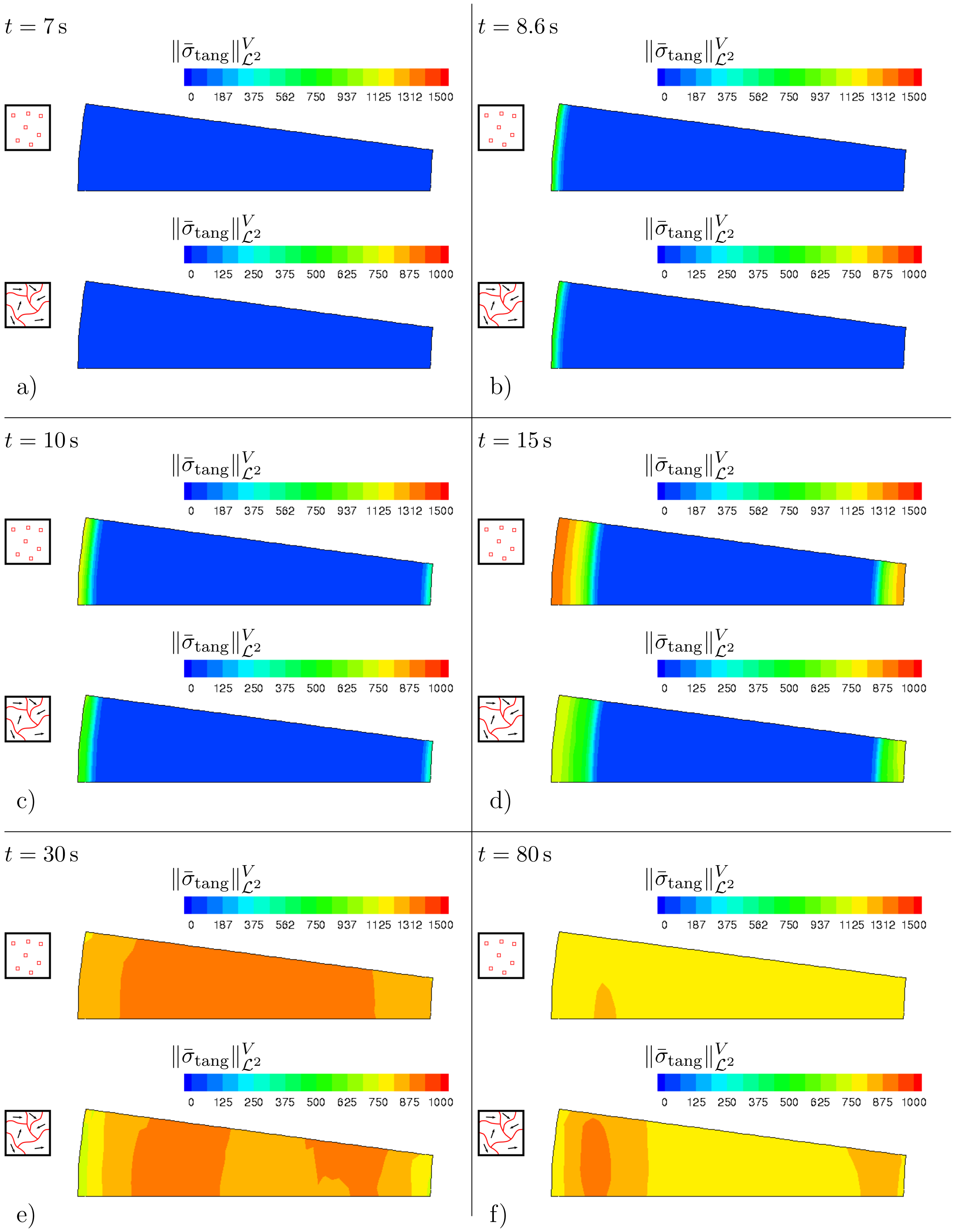

Figure 10.22: Macroscopic quadratic measures of tangential stress fluctuations $\|\tilde{\sigma}_{\text{tang}}\|$ in MPa and microscopic tangential stress fluctuations $\tilde{\sigma}_{\text{tang}}$ in MPa computed with two different RVEs, namely an arbitrary switch or a grain structure with different grain orientations at certain points in time a) $t = 7\,\text{s}$, b) $t = 8.6\,\text{s}$, c) $t = 10\,\text{s}$, d) $t = 15\,\text{s}$, e) $t = 30\,\text{s}$ and f) $t = 80\,\text{s}$.

11 Conclusion and Outlook

This doctoral thesis focused on the numerical investigation of the development of residual stresses in hot bulk forming parts. Therefore, particularly the third process step of hot bulk forming, which is the cooling of the heated and formed specimen, was of interest. Different cooling routes were applied to insert varying residual stress profiles in a specimen. Thus, targeted cooling led to predefined residual stress distributions in the component. In order to carry out a numerical analysis of these cooling procedures, material models were set up in terms of the Finite Element Method.

Thus, this work started with an introduction to the basic principles of continuum mechanics, which are the kinematics, the concept of stress and the balance principles. Afterwards the idea of the Finite Element Method was outlined, which was utilized in order to solve a boundary value problem. In this context, the discretization of the geometry, the formulation of the weak form as well as its linearization and the assemblation of the algebraic set of equations were discussed. The later was solved with an iterative Newton-Raphson scheme. In order to investigate thermo-mechanically coupled problems, surface finite elements, which can be used to describe the heat flux at the surface of the geometry, were introduced. Based on the considered material and the temperature path, different phases can occur, which show specific material properties. For the determination of these phase-specific material properties, interpolation schemes were required, which depend either on the temperature or on the temperature and the accumulated plastic strains. In a next step, a thermo-mechanically coupled constitutive material model was derived taking into account three different approaches to compute the effective material behavior. Here, either the phase-specific material parameters were directly averaged or the phase-specific stresses and moduli were determined, which were then averaged subsequently. This average based on the individual volume fractions of the occurring phases and hence, it was inevitable to depict these volume fractions accurately. Thus, for the numerical description of the actual volume fractions, the Johnson-Mehl-Avrami-Kolmogorov equation for diffusion controlled (e.g. pearlite) and the Koistinen-Marburger differential equation for a diffusionless (e.g. martensite) phase transformation were presented. Since phase transformations are one origin to evoke residual stresses, these were defined and the three different types of residual stresses were characterized based on the scale, they act on. Furthermore, the microscopic phase transformations from an initially austenitic phase to different product phases, here martensite or pearlite, depending on the cooling route, were incorporated in the single-scale material model. Therefore, an additive split of the total strains into five different parts, namely elastic, plastic, thermal, transformation volumetric and transformation induced plasticity strains was taken into account.

A first numerical investigation compared the different effective material models. It is found that the “semi-analytical multi-phasemmaterial model, which averages phase specific stresses and tangent moduli, differs from a material model utilizing harmonic effective parameters, but is in good accordance with that one using arithmetically averaged parameters. However, these both approaches do not enable to distinguish into phase-specific contributions, i.e., types of residual stresses, and thus, the “semi-analytical multi-phasemmodel seems most suitable for the incorporation of phase transformational effects. Therewith, the cooling of a cylindrical specimen with eccentricity was considered. A mesh density and time step size study was carried out, so that it was possible to balance numerical costs and accuracy. It is found that the temperature gradient as well as the phase transformation require a fine but not overdone discretization. Then, different cooling media, which are water or air or the application of a spray cooling, were considered and the respective influence on the resulting macroscopic stress distribution was analyzed. While cooling by air led to overall small residual stress values in the material, cooling in water evoked tensile residual stresses in regions near the outer surface. This contradicted the aim for compressive stresses in regions near the outer surface to improve the component's properties in case of tensile loading. The compressive residual stress in regions near the outer surface was achieved by applying a spray cooling on the thick side of the specimen, which resulted in the targeted compressive stress state in the spray exposed region. Both, cooling in water and with the spray, led to the same amount of martensite in the austenitic parent phase in the microstructure. Hence, it is evident that the residual stress state in a hot bulk forming component is effected by the change of the cooling route and not by direct microstructural modifications. Furthermore, the realization of surface elements to describe the cooling over the component's boundary serves as practical tool to describe the cooling without having to know the exact temperature evolution initially. Once the heat transfer coefficients have been determined for the material to be investigated and the chosen ambient medium, various geometries can be analyzed. A previous experimental realization and measurement of the temperature profile are then no longer required. This provides a fast, cost-saving and efficient method to evaluate different cooling routes with regard to the resulting stress distributions. It is shown that including TRIP effects is an important factor to describe the stress evolution due to the austenite-to-martensite phase transformation accurately. The extrusion of the cylindrical slice to a three-dimensional boundary value problem showed the relevance of the third dimension, because it also took into account the heat flow over the component's height. It is found that thereby, the cooling progresses slower to the bulk, which also effects the stress evolution in regions near the outer surface with a delay compared to the two-dimensional results. As a consequence, the analyzed stress curves fit experimental measurements and the predicted behavior quite well. In connection with surface elements this three-dimensional realization provides a great numerical tool to investigate the cooling of hot bulk forming parts with highly complex geometries and divers cooling media in future work.

These single-scale finite element analyses provided information on stress developments at the component level and could be evaluated as residual stresses in the final state. Macroscopic residual stresses (first type) are caused by microscopic phenomena and the resulting microscopic residual stresses (second and third type). For the purpose of analyzing these microscopic residual stresses, two-scale finite element computations were used to resolve the microscale. In order to find a suitable RVE to represent the austenite-to-martensite phase transformation, a simplified thermo-mechanical boundary value problem was devised. Four different martensitic evolution strategies using either a circular nucleus, a diagonal structure, an arbitrary switch, or a grain structure with or without individual grain orientations were defined for this purpose. It was found that a circular inclusion is not a feasible approach to depict the phase fractions accurately. For high fractions of martensite, the nucleus exceeds the boundary of the RVE domain and thus, the volume fractions do not match the computed percentages precisely. Moreover, a circular inclusion requires a very fine mesh density of the RVE, which leads to high computational efforts that are circumvented by the other possible RVE definitions. A diagonal structure does not differ from an arbitrary switch with regard to the macroscopic quantities, but needs a complex algorithm to define the RVE. Hence, both RVE types with a circular inclusion or a diagonal structure seem not reasonable and, instead, the focus is on the arbitrary switch and the grain structure. However, with respect to the latter, further microscopic studies and experimental measurements are essential. With these findings, last but not least, a two-scale investigation of the previously considered cylindrical specimen with eccentric hole was considered and analyzed with respect to the stress development on both scales. It is found that the grain size influences the stress evolution, i.e., finer grain sizes result in lower final residual stress values compared to coarser grain sizes. The resolution of microscopic residual stresses enabled the analysis of microscopic tensile stress peaks, which could promote crack growth in the microstructure but are not visible in the macroscopic stress results. It is open to analyze how adapted cooling leads to predefined stress distributions in the material and impacts the component's properties, initially as well as in the long term. Moreover, due to the knowledge of the importance of the third dimension, an extension of the boundary value problem on both scales is indispensable.

Thus, in this work, a material model was formulated to represent the austenite-to-martensite as well as the austenite-to-pearlite phase transformation. Using a simple but meaningful geometry, the accuracy of the material model could be proven. Single- and multi-scale finite element analyses showed good agreement with experimental investigations. Therefore, this material model can be used as a fundamental basis for further scientific investigations. On the one hand, the influence of these residual stresses on the component's properties should be quantitatively measured. On the other hand, there is the question of the stability of the residual stresses in the component over time. Both could be determined in an efficient and detailed way by means of an extension of the existing material model. In particular, multi-scale analyses provide information on the origin of the residual stresses, whether they are of thermal nature or related to occurring phase transformations, for instance. All this knowledge could be applied in manufacturing processes of components with complex geometries, which are exposed to challenging loading conditions. A numerical tool for predicting how residual stresses are effected by even small changes in the manufacturing process, and thus can lead to improved performance of the component in service, will save cost, time and material in industrial applications.

A Tensor calculus

In this thesis, the following notation for tensor calculus are used. In general, small letters refer to scalar quantities such as v. Vectors are represented by bold face normal letters, e.g. $\boldsymbol{u}$ or $\boldsymbol{x}$. Taking into account the Euclidean base $\boldsymbol{e}_1, \boldsymbol{e}_2, \boldsymbol{e}_3$, vectors, second order tensors or fourth order tensors can be written as

$$\begin{aligned} \text{vector} \quad & \boldsymbol{a} = a_i \boldsymbol{e}_i \\ \text{2nd order tensor} \quad & \boldsymbol{A} = A_{ij} \boldsymbol{e}_i \otimes \boldsymbol{e}_j \\ \text{4th order tensor} \quad & \boldsymbol{A} = A_{ijkl} \boldsymbol{e}_i \otimes \boldsymbol{e}_j \otimes \boldsymbol{e}_k \otimes \boldsymbol{e}_l \,. \end{aligned} \tag{A.1}$$

Utilized tensor operations and important tensors are summarized in Table A.1. Therein, δ_{ij} refers to the Kronecker-Delta, which is defined as

$$\delta_{ij} = \begin{cases} 1 & i = j \\ 0 & \text{else} \end{cases} \,. \tag{A.2}$$

Table A.1: Tensor operations.

single contraction (vectors)	$\boldsymbol{a} \cdot \boldsymbol{b}$	$= a_i \boldsymbol{e}_i \cdot b_j \boldsymbol{e}_j = A_i B_i$
single contraction (2nd and 2nd)	$\boldsymbol{A} \cdot \boldsymbol{B}$	$= A_{ij} \boldsymbol{e}_i \otimes \boldsymbol{e}_j \cdot B_{kl} \boldsymbol{e}_k \otimes \boldsymbol{e}_l = A_{ij} B_{jl} \boldsymbol{e}_i \otimes \boldsymbol{e}_l$
double contraction	$\boldsymbol{A} : \boldsymbol{B}$	$= A_{ij} \boldsymbol{e}_i \otimes \boldsymbol{e}_j : B_{kl} \boldsymbol{e}_k \otimes \boldsymbol{e}_l = A_{ij} B_{ij}$
double contraction (4th and 2nd)	$\mathbb{C} : \boldsymbol{A}$	$= \mathbb{C}_{ijkl} \boldsymbol{e}_i \otimes \boldsymbol{e}_j \otimes \boldsymbol{e}_k \otimes \boldsymbol{e}_l : A_{mn} \boldsymbol{e}_m \otimes \boldsymbol{e}_n$ $= \mathbb{C}_{ijkl} A_{kl} \boldsymbol{e}_i \otimes \boldsymbol{e}_j$
dyadic product	$\boldsymbol{A} \otimes \boldsymbol{B}$	$= A_{ij} \boldsymbol{e}_i \otimes \boldsymbol{e}_j \otimes B_{kl} \boldsymbol{e}_k \otimes \boldsymbol{e}_l$ $= A_{ij} B_{kl} \boldsymbol{e}_i \otimes \boldsymbol{e}_j \otimes \boldsymbol{e}_k \otimes \boldsymbol{e}_l$
2nd order unity tensor	$\boldsymbol{I}$	$= \delta_{ij}$
4th order unity tensor	$\mathbb{I}$	$= \frac{1}{2}(\delta_{ik}\delta_{jl} + \delta_{il}\delta_{jk})$
projection tensor	$\mathbb{P}$	$= \mathbb{I} - \frac{1}{3} \boldsymbol{I} \otimes \boldsymbol{I}$

Voigt notation

For the implementation of the material model, it is useful to take advantage of the symmetry of the strain tensor $\boldsymbol{\varepsilon}$ and the stress tensor $\boldsymbol{\sigma}$, respectively. Instead of writing the full tensor

$$\boldsymbol{\varepsilon} = \begin{bmatrix} \varepsilon_{11} & \varepsilon_{12} & \varepsilon_{13} \\ \varepsilon_{21} & \varepsilon_{22} & \varepsilon_{23} \\ \varepsilon_{31} & \varepsilon_{32} & \varepsilon_{33} \end{bmatrix} \quad \text{or} \quad \boldsymbol{\sigma} = \begin{bmatrix} \sigma_{11} & \sigma_{12} & \sigma_{13} \\ \sigma_{21} & \sigma_{22} & \sigma_{23} \\ \sigma_{31} & \sigma_{32} & \sigma_{33} \end{bmatrix} \,, \tag{A.3}$$

the following simplification in the Voigt notation is used

$$\boldsymbol{\varepsilon} = \begin{bmatrix} \varepsilon_{11} \\ \varepsilon_{22} \\ \varepsilon_{33} \\ 2\varepsilon_{12} \\ 2\varepsilon_{23} \\ 2\varepsilon_{13} \end{bmatrix} \quad \text{or} \quad \boldsymbol{\sigma} = \begin{bmatrix} \sigma_{11} \\ \sigma_{22} \\ \sigma_{33} \\ \sigma_{12} \\ \sigma_{23} \\ \sigma_{13} \end{bmatrix} \,. \tag{A.4}$$

The material tangent $\mathbb{C}$, which has dimensions 9×9,

$$\mathbb{C} = \begin{bmatrix}
\mathbb{C}_{1111} & \mathbb{C}_{1122} & \mathbb{C}_{1133} & \mathbb{C}_{1112} & \mathbb{C}_{1123} & \mathbb{C}_{1113} & \mathbb{C}_{1121} & \mathbb{C}_{1132} & \mathbb{C}_{1131} \\
\mathbb{C}_{2211} & \mathbb{C}_{2222} & \mathbb{C}_{2233} & \mathbb{C}_{2212} & \mathbb{C}_{2223} & \mathbb{C}_{2213} & \mathbb{C}_{2221} & \mathbb{C}_{2232} & \mathbb{C}_{2231} \\
\mathbb{C}_{3311} & \mathbb{C}_{3322} & \mathbb{C}_{3333} & \mathbb{C}_{3312} & \mathbb{C}_{3323} & \mathbb{C}_{3313} & \mathbb{C}_{3321} & \mathbb{C}_{3332} & \mathbb{C}_{3331} \\
\mathbb{C}_{1211} & \mathbb{C}_{1222} & \mathbb{C}_{1233} & \mathbb{C}_{1212} & \mathbb{C}_{1223} & \mathbb{C}_{1213} & \mathbb{C}_{1221} & \mathbb{C}_{1232} & \mathbb{C}_{1231} \\
\mathbb{C}_{2311} & \mathbb{C}_{2322} & \mathbb{C}_{2333} & \mathbb{C}_{2312} & \mathbb{C}_{2323} & \mathbb{C}_{2313} & \mathbb{C}_{2321} & \mathbb{C}_{2332} & \mathbb{C}_{2331} \\
\mathbb{C}_{1311} & \mathbb{C}_{1322} & \mathbb{C}_{1333} & \mathbb{C}_{1312} & \mathbb{C}_{3123} & \mathbb{C}_{3113} & \mathbb{C}_{3121} & \mathbb{C}_{3132} & \mathbb{C}_{3131} \\
\mathbb{C}_{2111} & \mathbb{C}_{2122} & \mathbb{C}_{2133} & \mathbb{C}_{2112} & \mathbb{C}_{2123} & \mathbb{C}_{2113} & \mathbb{C}_{2121} & \mathbb{C}_{2132} & \mathbb{C}_{2131} \\
\mathbb{C}_{3211} & \mathbb{C}_{3222} & \mathbb{C}_{3233} & \mathbb{C}_{3212} & \mathbb{C}_{3223} & \mathbb{C}_{3213} & \mathbb{C}_{3221} & \mathbb{C}_{3232} & \mathbb{C}_{3231} \\
\mathbb{C}_{3111} & \mathbb{C}_{3122} & \mathbb{C}_{3133} & \mathbb{C}_{3112} & \mathbb{C}_{3123} & \mathbb{C}_{3113} & \mathbb{C}_{3121} & \mathbb{C}_{3132} & \mathbb{C}_{3131}
\end{bmatrix} \tag{A.5}$$

can also be written in Voigt notation as 6×6 matrix, which is defined as

$$\mathbb{C} = \left[\begin{array}{c|c|c|c|c|c}
\mathbb{C}_{1111} & \mathbb{C}_{1122} & \mathbb{C}_{1133} & \begin{matrix}\frac{1}{2}(\mathbb{C}_{1112} \\ +\mathbb{C}_{1121})\end{matrix} & \begin{matrix}\frac{1}{2}(\mathbb{C}_{1123} \\ +\mathbb{C}_{1132})\end{matrix} & \begin{matrix}\frac{1}{2}(\mathbb{C}_{1113} \\ +\mathbb{C}_{1131})\end{matrix} \\ \hline
\mathbb{C}_{2211} & \mathbb{C}_{2222} & \mathbb{C}_{2233} & \begin{matrix}\frac{1}{2}(\mathbb{C}_{2212} \\ +\mathbb{C}_{2221})\end{matrix} & \begin{matrix}\frac{1}{2}(\mathbb{C}_{2223} \\ +\mathbb{C}_{2232})\end{matrix} & \begin{matrix}\frac{1}{2}(\mathbb{C}_{2213} \\ +\mathbb{C}_{2231})\end{matrix} \\ \hline
\mathbb{C}_{3311} & \mathbb{C}_{3322} & \mathbb{C}_{3333} & \begin{matrix}\frac{1}{2}(\mathbb{C}_{3312} \\ +\mathbb{C}_{3321})\end{matrix} & \begin{matrix}\frac{1}{2}(\mathbb{C}_{3323} \\ +\mathbb{C}_{3332})\end{matrix} & \begin{matrix}\frac{1}{2}(\mathbb{C}_{3313} \\ +\mathbb{C}_{3331})\end{matrix} \\ \hline
\begin{matrix}\frac{1}{2}(\mathbb{C}_{1211} \\ +\mathbb{C}_{2111})\end{matrix} & \begin{matrix}\frac{1}{2}(\mathbb{C}_{1222} \\ +\mathbb{C}_{2122})\end{matrix} & \begin{matrix}\frac{1}{2}(\mathbb{C}_{1233} \\ +\mathbb{C}_{2133}\end{matrix} & \begin{matrix}\frac{1}{4}(\mathbb{C}_{1212} \\ +\mathbb{C}_{2112} \\ +\mathbb{C}_{1221} \\ +\mathbb{C}_{2121})\end{matrix} & \begin{matrix}\frac{1}{4}(\mathbb{C}_{1223} \\ +\mathbb{C}_{2123} \\ +\mathbb{C}_{1232} \\ +\mathbb{C}_{2132})\end{matrix} & \begin{matrix}\frac{1}{4}(\mathbb{C}_{1213} \\ +\mathbb{C}_{2113} \\ +\mathbb{C}_{1231} \\ +\mathbb{C}_{2131})\end{matrix} \\ \hline
\begin{matrix}\frac{1}{2}(\mathbb{C}_{2311} \\ +\mathbb{C}_{3211})\end{matrix} & \begin{matrix}\frac{1}{2}(\mathbb{C}_{2322} \\ +\mathbb{C}_{3222})\end{matrix} & \begin{matrix}\frac{1}{2}(\mathbb{C}_{2333} \\ +\mathbb{C}_{3233}\end{matrix} & \begin{matrix}\frac{1}{4}(\mathbb{C}_{2312} \\ +\mathbb{C}_{3212} \\ +\mathbb{C}_{2321} \\ +\mathbb{C}_{3221})\end{matrix} & \begin{matrix}\frac{1}{4}(\mathbb{C}_{2323} \\ +\mathbb{C}_{3223} \\ +\mathbb{C}_{2332}) \\ +\mathbb{C}_{3232})\end{matrix} & \begin{matrix}\frac{1}{4}(\mathbb{C}_{2313} \\ +\mathbb{C}_{3213} \\ +\mathbb{C}_{2331} \\ +\mathbb{C}_{3231})\end{matrix} \\ \hline
\begin{matrix}\frac{1}{2}(\mathbb{C}_{1311} \\ +\mathbb{C}_{3111})\end{matrix} & \begin{matrix}\frac{1}{2}(\mathbb{C}_{1322} \\ +\mathbb{C}_{3122})\end{matrix} & \begin{matrix}\frac{1}{2}(\mathbb{C}_{1333} \\ +\mathbb{C}_{3133}\end{matrix} & \begin{matrix}\frac{1}{4}(\mathbb{C}_{1312} \\ +\mathbb{C}_{3112} \\ +\mathbb{C}_{1321} \\ +\mathbb{C}_{3121})\end{matrix} & \begin{matrix}\frac{1}{4}(\mathbb{C}_{1323} \\ +\mathbb{C}_{3123} \\ +\mathbb{C}_{1332} \\ +\mathbb{C}_{3132})\end{matrix} & \begin{matrix}\frac{1}{4}(\mathbb{C}_{1313} \\ +\mathbb{C}_{3113} \\ +\mathbb{C}_{1331} \\ +\mathbb{C}_{3131})\end{matrix}
\end{array}\right] . \tag{A.6}$$

B Discretization and linearization of a thermo-mechanical coupled boundary value problem

In addition to the presented discretization and linearization of a purely mechanical boundary value problem, this section deals with the realization of a thermo-mechanical material in FEM, taking into account small strain theory. Therefore, the balance of energy has to be considered with its weak form given in Equation (3.44). It can be reformulated and linearized to

$$\begin{aligned} G_\theta \;=& \int_B \rho\,\theta \frac{\partial^2\psi}{\partial\theta^2}\dot{\theta}\,\delta\theta\,\mathrm{d}v \;+\; \int_B \rho\,\theta \frac{\partial^2\psi}{\partial\theta\partial\boldsymbol{\varepsilon}} : \dot{\boldsymbol{\varepsilon}}\,\delta\theta\,\mathrm{d}v \\ &- \int_{\partial B} \boldsymbol{q}\cdot\boldsymbol{n}\,\delta\theta\,\mathrm{d}a \;+\; \int_B \boldsymbol{q}\cdot\mathrm{grad}\,\delta\theta\,\mathrm{d}v \;=\; 0\,, \end{aligned} \tag{B.1}$$

$$\begin{aligned} \text{and}\quad \Delta G_\theta \;=& \int_B \delta\theta^T \rho\,\frac{\partial^2\psi}{\partial\theta^2}\dot{\theta}\,\Delta\theta\,\mathrm{d}v \;+\; \int_B \delta\theta^T \rho\,\theta\frac{\partial^3\psi}{\partial\theta^3}\dot{\theta}\,\Delta\theta\,\mathrm{d}v + \int_B \delta\theta^T \rho\,\theta\frac{\partial^2\psi}{\partial\theta^2}\Delta\dot{\theta}\,\mathrm{d}v \\ &+ \int_B \delta\theta^T \rho\,\theta\frac{\partial^3\psi}{\partial\theta^2\partial\boldsymbol{\varepsilon}}\dot{\theta} : \Delta\boldsymbol{\varepsilon}\,\mathrm{d}v + \int_B \delta\theta^T \rho\,\frac{\partial^2\psi}{\partial\theta\partial\boldsymbol{\varepsilon}} : \dot{\boldsymbol{\varepsilon}}\Delta\theta\,\mathrm{d}v \;+\; \int_B \delta\theta^T \rho\,\theta\frac{\partial^3\psi}{\partial\theta^2\partial\boldsymbol{\varepsilon}} : \dot{\boldsymbol{\varepsilon}}\Delta\theta\,\mathrm{d}v \\ &+ \int_B \delta\theta^T \rho\,\theta\frac{\partial^2\psi}{\partial\theta\partial\boldsymbol{\varepsilon}} : \Delta\dot{\boldsymbol{\varepsilon}}\,\mathrm{d}v \;+\; \int_B \delta\theta^T \rho\,\theta\frac{\partial^3\psi}{\partial\theta\partial\boldsymbol{\varepsilon}^2} : \dot{\boldsymbol{\varepsilon}} : \Delta\boldsymbol{\varepsilon}\,\mathrm{d}v \;+\; \int_B (\mathrm{grad}\,\delta\theta)^T\cdot\Delta\boldsymbol{q}\,\mathrm{d}v\,. \end{aligned} \tag{B.2}$$

The linearization of the heat flux vector in the last term of Equation (B.2) can be computed with the non-negative heat conduction coefficient k as

$$\Delta\boldsymbol{q} \;=\; \frac{\partial\boldsymbol{q}}{\partial(\mathrm{grad}\,\theta)}\Delta(\mathrm{grad}\,\theta) \;=\; -k\Delta(\mathrm{grad}\,\theta) \;=\; -k\,\mathrm{grad}\,\Delta\theta\,. \tag{B.3}$$

If outer forces and acceleration terms are neglected, the extension of the weak form of the balance of linear momentum in Equation (3.47) is linearized with respect to the displacement $\boldsymbol{u}$ and the temperature θ as

$$\begin{aligned} G_u &= \int_{\mathcal{B}} \boldsymbol{\sigma} : \delta\boldsymbol{\varepsilon}\,\mathrm{d}v = 0\,, \\ \Rightarrow \Delta G_u &= \int_{\mathcal{B}} \delta\boldsymbol{\varepsilon}^{\mathrm{T}} : \rho\frac{\partial^2\psi}{\partial\boldsymbol{\varepsilon}^2} : \Delta\boldsymbol{\varepsilon}\,\mathrm{d}v + \int_{\mathcal{B}} \delta\boldsymbol{\varepsilon}^{\mathrm{T}} : \rho\frac{\partial^2\psi}{\partial\boldsymbol{\varepsilon}\partial\theta}\Delta\theta\,\mathrm{d}v\,, \end{aligned} \tag{B.4}$$

with $\delta\boldsymbol{\varepsilon} = \mathrm{grad}^{\mathrm{sym}}\,\delta\boldsymbol{u}$.

Time integration scheme

In order to derive expressions for the occurring time derivatives of the temperature and strains, $\dot{\theta}$ and $\dot{\boldsymbol{\varepsilon}}$, respectively, an implicit time integration scheme is utilized. As the acceleration is not taken into account, a backward Euler computation method is considered. Thereby, one obtains based on the value of the actual time step, indicated by $_{n+1}$, and the last time step, indicated by $_n$, as well as the time step size $\Delta t = t_{n+1} - t_n$

$$\dot{\bullet}_{n+1} \;=\; \frac{\bullet_{n+1} \;-\; \bullet_n}{\Delta t} \quad \text{with} \quad \bullet \in \{\theta, \boldsymbol{\varepsilon}\}\,, \tag{B.5}$$

which means that it holds

$$\Delta\dot{\theta} \;=\; \frac{1}{\Delta t}\Delta\theta \;\text{ and }\; \Delta\dot{\boldsymbol{\varepsilon}} \;=\; \frac{1}{\Delta t}\Delta\boldsymbol{\varepsilon}\,. \tag{B.6}$$

Inserting into Equation (B.2) yields for the linearization

$$\begin{aligned}\Delta G_\theta = &\int_B \delta\theta^T \rho\, \frac{\partial^2\psi}{\partial\theta^2}\dot{\theta}\,\Delta\theta\,\mathrm{d}v + \int_B \delta\theta^T \rho\,\theta\frac{\partial^3\psi}{\partial\theta^3}\dot{\theta}\,\Delta\theta\,\mathrm{d}v + \int_B \delta\theta^T \rho\,\theta\frac{\partial^2\psi}{\partial\theta^2}\frac{1}{\Delta t}\Delta\theta\,\mathrm{d}v \\ &+ \int_B \delta\theta^T \rho\,\theta\frac{\partial^3\psi}{\partial\theta^2\partial\boldsymbol{\varepsilon}}\dot{\theta} : \Delta\boldsymbol{\varepsilon}\,\mathrm{d}v + \int_B \delta\theta^T \rho\,\frac{\partial^2\psi}{\partial\theta\partial\boldsymbol{\varepsilon}} : \dot{\boldsymbol{\varepsilon}}\Delta\theta\,\mathrm{d}v + \int_B \delta\theta^T \rho\,\theta\frac{\partial^3\psi}{\partial\theta^2\partial\boldsymbol{\varepsilon}} : \dot{\boldsymbol{\varepsilon}}\Delta\theta\,\mathrm{d}v \\ &+ \int_B \delta\theta^T \rho\,\theta\frac{\partial^2\psi}{\partial\theta\partial\boldsymbol{\varepsilon}} : \frac{1}{\Delta t}\Delta\boldsymbol{\varepsilon}\,\mathrm{d}v + \int_B \delta\theta^T \rho\,\theta\frac{\partial^3\psi}{\partial\theta\partial\boldsymbol{\varepsilon}^2} : \dot{\boldsymbol{\varepsilon}} : \Delta\boldsymbol{\varepsilon}\,\mathrm{d}v - \int_B (\operatorname{grad}\delta\theta)^T \cdot k \operatorname{grad}\Delta\theta\,\mathrm{d}v\,. \end{aligned} \tag{B.7}$$

C Three-dimensional finite elements

The three-dimensional ansatz functions for linear (8 nodes) hexahedral elements, see Figure 3.3, are given by

$$\begin{aligned}
N_1(\xi,\eta,\zeta) &= \frac{1}{8}(1-\xi)(1-\eta)(1-\zeta)\,, & N_2(\xi,\eta,\zeta) &= \frac{1}{8}(1+\xi)(1-\eta)(1-\zeta)\,,\\
N_3(\xi,\eta,\zeta) &= \frac{1}{8}(1+\xi)(1+\eta)(1-\zeta)\,, & N_4(\xi,\eta,\zeta) &= \frac{1}{8}(1-\xi)(1+\eta)(1-\zeta)\,,\\
N_5(\xi,\eta,\zeta) &= \frac{1}{8}(1-\xi)(1-\eta)(1+\zeta)\,, & N_6(\xi,\eta,\zeta) &= \frac{1}{8}(1+\xi)(1-\eta)(1+\zeta)\,,\\
N_7(\xi,\eta,\zeta) &= \frac{1}{8}(1+\xi)(1+\eta)(1+\zeta)\,, & N_8(\xi,\eta,\zeta) &= \frac{1}{8}(1-\xi)(1+\eta)(1+\zeta)
\end{aligned}$$

and for quadratic (20 nodes) hexahedral elements by

$$\begin{aligned}
N_1(\xi,\eta,\zeta) &= \frac{1}{8}(1-\xi)(1-\eta)(1-\zeta)(-\xi-\eta-\zeta-2)\,, & N_{11}(\xi,\eta,\zeta) &= \frac{1}{8}(1-\xi^2)(1+\eta)(1-\zeta)^2\,,\\
N_2(\xi,\eta,\zeta) &= \frac{1}{8}(1+\xi)(1-\eta)(1-\zeta)(\ \ \xi-\eta-\zeta-2)\,, & N_{12}(\xi,\eta,\zeta) &= \frac{1}{8}(1-\xi)(1-\eta^2)(1-\zeta)^2\,,\\
N_3(\xi,\eta,\zeta) &= \frac{1}{8}(1+\xi)(1+\eta)(1-\zeta)(\ \ \xi+\eta-\zeta-2)\,, & N_{13}(\xi,\eta,\zeta) &= \frac{1}{8}(1-\xi^2)(1-\eta)(1+\zeta)^2\,,\\
N_4(\xi,\eta,\zeta) &= \frac{1}{8}(1-\xi)(1+\eta)(1-\zeta)(-\xi+\eta-\zeta-2)\,, & N_{14}(\xi,\eta,\zeta) &= \frac{1}{8}(1+\xi)(1-\eta^2)(1+\zeta)^2\,,\\
N_5(\xi,\eta,\zeta) &= \frac{1}{8}(1-\xi)(1-\eta)(1+\zeta)(-\xi-\eta+\zeta-2)\,, & N_{15}(\xi,\eta,\zeta) &= \frac{1}{8}(1-\xi^2)(1+\eta)(1+\zeta)^2\,,\\
N_6(\xi,\eta,\zeta) &= \frac{1}{8}(1+\xi)(1-\eta)(1+\zeta)(\ \ \xi-\eta+\zeta-2)\,, & N_{16}(\xi,\eta,\zeta) &= \frac{1}{8}(1-\xi)(1-\eta^2)(1+\zeta)^2\,,\\
N_7(\xi,\eta,\zeta) &= \frac{1}{8}(1+\xi)(1+\eta)(1+\zeta)(\ \ \xi+\eta+\zeta-2)\,, & N_{17}(\xi,\eta,\zeta) &= \frac{1}{8}(1-\xi)(1-\eta)(1-\zeta^2)^2\,,\\
N_8(\xi,\eta,\zeta) &= \frac{1}{8}(1-\xi)(1+\eta)(1+\zeta)(-\xi+\eta+\zeta-2)\,, & N_{18}(\xi,\eta,\zeta) &= \frac{1}{8}(1+\xi)(1-\eta)(1-\zeta^2)^2\,,\\
N_9(\xi,\eta,\zeta) &= \frac{1}{8}(1-\xi^2)(1-\eta)(1-\zeta)^2\,, & N_{19}(\xi,\eta,\zeta) &= \frac{1}{8}(1+\xi)(1+\eta)(1-\zeta^2)^2\,,\\
N_{10}(\xi,\eta,\zeta) &= \frac{1}{8}(1+\xi)(1-\eta^2)(1-\zeta)^2\,, & N_{20}(\xi,\eta,\zeta) &= \frac{1}{8}(1-\xi)(1+\eta)(1-\zeta^2)^2\,.
\end{aligned}$$

In Table C.1 the used integration points and their respective weights are given for linear and quadratic elements in three dimensions.

Table C.1: Gauss points with weighting factors for the three-dimensional case

dimension	n_{node}	n_p	i	coordinates of GP			weighting
				ξ_i	η_i	ζ_i	w_i
3D	8	8	1	$1/\sqrt{3}$	$1/\sqrt{3}$	$1/\sqrt{3}$	1
			2	$1/\sqrt{3}$	$1/\sqrt{3}$	$-1/\sqrt{3}$	1
			3	$1/\sqrt{3}$	$-1/\sqrt{3}$	$1/\sqrt{3}$	1
			4	$1/\sqrt{3}$	$-1/\sqrt{3}$	$-1/\sqrt{3}$	1
			5	$-1/\sqrt{3}$	$1/\sqrt{3}$	$1/\sqrt{3}$	1
			6	$-1/\sqrt{3}$	$1/\sqrt{3}$	$-1/\sqrt{3}$	1
			7	$-1/\sqrt{3}$	$-1/\sqrt{3}$	$1/\sqrt{3}$	1
			8	$-1/\sqrt{3}$	$-1/\sqrt{3}$	$-1/\sqrt{3}$	1
3D	20	14	1	$\sqrt{19/30}$	0	0	$320/361$
			2	$-\sqrt{19/30}$	0	0	$320/361$
			3	0	$\sqrt{19/30}$	0	$320/361$
			4	0	$-\sqrt{19/30}$	0	$320/361$
			5	0	0	$\sqrt{19/30}$	$320/361$
			6	0	0	$-\sqrt{19/30}$	$320/361$
			7	$\sqrt{19/30}$	$\sqrt{19/30}$	$\sqrt{19/30}$	$121/360$
			8	$-\sqrt{19/30}$	$\sqrt{19/30}$	$\sqrt{19/30}$	$121/360$
			9	$\sqrt{19/30}$	$-\sqrt{19/30}$	$\sqrt{19/30}$	$121/360$
			10	$-\sqrt{19/30}$	$-\sqrt{19/30}$	$\sqrt{19/30}$	$121/360$
			11	$\sqrt{19/30}$	$\sqrt{19/30}$	$-\sqrt{19/30}$	$121/360$
			12	$\sqrt{19/30}$	$-\sqrt{19/30}$	$-\sqrt{19/30}$	$121/360$
			13	$-\sqrt{19/30}$	$-\sqrt{19/30}$	$-\sqrt{19/30}$	$121/360$
			14	$-\sqrt{19/30}$	$\sqrt{19/30}$	$-\sqrt{19/30}$	$121/360$

D Derivation of Avrami exponent n and constant $K_{\mathbf{JMAK}}$ for JMAK equation

The derivation of the expressions of the Avrami exponent n and the constant K_{JMAK} for the JMAK equation presented in Section 4.1.1 reads as follows. One start with the relations $c(t_{01}) = 0.01\,c_{\mathrm{eq}}$ and $c(t_{99}) = 0.99\,c_{\mathrm{eq}}$ and derives with $t_0 = 1\,\mathrm{s}$ for standardization

$$
\begin{aligned}
& c(t_{01}) = 0.01c_{\mathrm{eq}} && c(t_{99}) = 0.99c_{\mathrm{eq}} \\
\Leftrightarrow\quad & c_{01} = \frac{c(t_{01})}{c_{\mathrm{eq}}} = 0.01 = \big(1 - \exp(-K_{\mathrm{JMAK}}(\frac{t_{01}}{t_0})^n)\big) && \\
& \qquad c_{99} = \frac{c(t_{99})}{c_{\mathrm{eq}}} = 0.99 = \big(1 - \exp(-K_{\mathrm{JMAK}}(\frac{t_{99}}{t_0})^n)\big) && \\
\Leftrightarrow\quad & \exp(-K_{\mathrm{JMAK}}(\frac{t_{01}}{t_0})^n) = 1 - c_{01} && \exp(-K_{\mathrm{JMAK}}(\frac{t_{99}}{t_0})^n) = 1 - c_{99} \\
\Leftrightarrow\quad & \exp(K_{\mathrm{JMAK}}(\frac{t_{01}}{t_0})^n) = \frac{1}{1 - c_{01}} && \exp(K_{\mathrm{JMAK}}(\frac{t_{99}}{t_0})^n) = \frac{1}{1 - c_{99}} \\
\Leftrightarrow\quad & K_{\mathrm{JMAK}} = \frac{\ln(\frac{1}{1-c_{01}})}{(\frac{t_{01}}{t_0})^n} && \frac{\ln(\frac{1}{1-c_{01}})}{(\frac{t_{01}}{t_0})^n}\,(\frac{t_{99}}{t_0})^n = \ln(\frac{1}{1 - c_{99}}) \\
\Leftrightarrow\quad & && \left(\frac{\frac{t_{99}}{t_0}}{\frac{t_{01}}{t_0}}\right)^n = \frac{\ln(\frac{1}{1-c_{99}})}{\ln(\frac{1}{1-c_{01}})} \\
\Leftrightarrow\quad & && n = \lg_{\frac{\frac{t_{99}}{t_0}}{\frac{t_{01}}{t_0}}} \frac{\ln(\frac{1}{1-c_{99}})}{\ln(\frac{1}{1-c_{01}})} \\
\Leftrightarrow\quad & \lg K_{\mathrm{JMAK}} = \lg\Big(\ln(\frac{1}{1 - c_{01}})\Big) - n\lg(\frac{t_{01}}{t_0}) && n = \frac{\lg\Big(\ln(\frac{1}{1-c_{99}})\Big) - \lg\Big(\ln(\frac{1}{1-c_{01}})\Big)}{\lg(\frac{t_{99}}{t_0}) - \lg(\frac{t_{01}}{t_0})} \\
\Rightarrow\quad & \ln K_{\mathrm{JMAK}} = \ln\Big(\ln(\frac{1}{c_{99}})\Big) - n\ln(t_{01}) && n = \frac{\ln\Big(\ln(\frac{1}{c_{01}})\Big) - \ln\Big(\ln(\frac{1}{c_{99}})\Big)}{\ln(t_{99}) - \ln(t_{01})}\,.
\end{aligned}
\tag{D.1}
$$

E HTCs for air and spray

Experimental investigation and single-scale numerical analysis are combined in order to determine the heat transfer coefficients for different cooling media. The data is required to investigate the cooling step of hot bulk forming processes in case surface elements are taken into account to describes the heat flux over the lateral surface. If the cylindrical specimen is cooled by air, a much lower HTC is set than for cooling in water, see Figure E.1. For the realization of cooling with a spray, the HTC applied in the spray exposed region is given in Figure E.2 depending on the temperature of the specimen. The boundary nodes which are not exposed to the spray are in contact with air and are thus provided with the according HTCs.

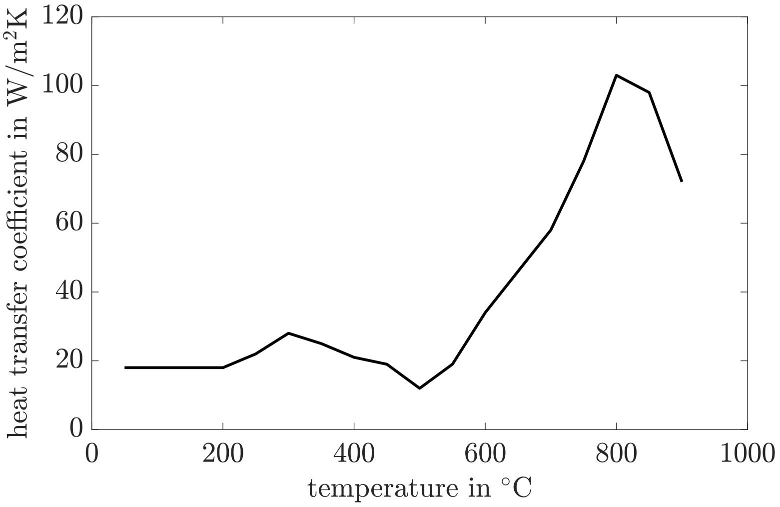

Figure E.1: Heat transfer coefficient for cooling by air in W/m^2K, cf. BEHRENS ET AL. [17].

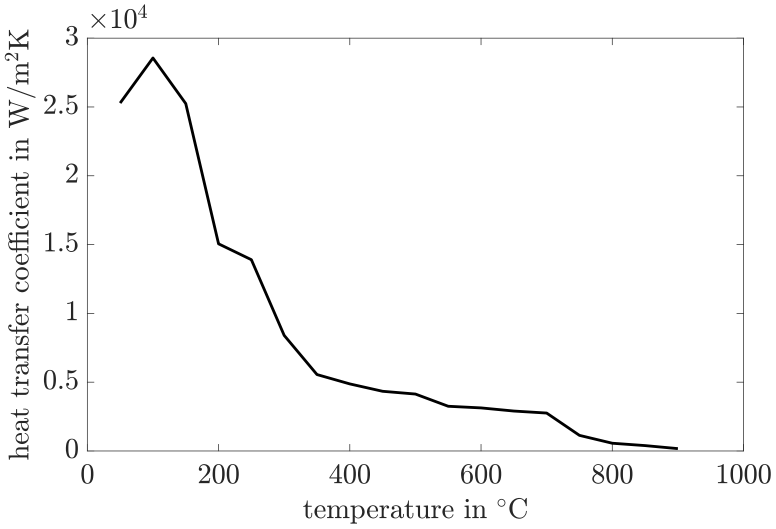

Figure E.2: Heat transfer coefficient for cooling with a spray in W/m^2K, cf. BEHRENS ET AL. [17].

F C-code for Voronoi tessellation

```
//*********** write number of voronoi cell **************//

#include <stdlib.h>
#include <float.h>
#include <stdio.h>
#include <math.h>

#define N 40
#define M 29
#define seed 1234

int main()
{
       srand(seed);
        double x[N], y[N];
        // x, y in [0,1)
        for(int i=0; i<N; i++)
        {
                x[i] = (double)rand()/RAND_MAX;
                y[i] = (double)rand()/RAND_MAX;
        }
        double dX=1.0/M;
        for(double X=0; X<1; X+=dX)
                for(double Y=0; Y<1; Y+=dX)
                {
                        int iMin=-1;
                        double dMin=DBL_MAX;
                        // find (x,y) with minimal periodic distance
                        for(int i=0; i<N; i++)
                        {
                                double dx = fabs(X-x[i]);
                                if(dx>0.5)
                                        dx = 1-dx;
                                double dy = fabs(Y-y[i]);
                                if(dy>0.5)
                                        dy = 1-dy;
                                double d=dx*dx+dy*dy;
                                if(d<dMin)
                                {
                                        dMin = d;
                                        iMin = i;
                                }
                        }
                        printf("%d ", iMin);
                }
        //flush
```

```
        printf("\n");
        return 0;
}
```

List of Figures

, “random 2, “random 3 and “random 4, i.e., different switching orders for one grain

List of Tables

References

[1] H. Altenbach. *Kontinuumsmechanik.* Springer Vieweg, 2018.

[2] A. Artemev, Y. Jin, and A. G. Khachaturyan. Three-dimensional phase field model and simulation of cubic → tetragonal martensitic transformation in polycrystals. *Philosophical Magazine A*, 82(6):1249–1270, 2002.

[3] M. Avrami. Kinetics of Phase Changes. I General Theory. *Journal of Chemical Physics*, 7(12):1103–1112, 1939.

[4] M. Avrami. Kinetics of Phase Changes. II Transformation-Time Relations for Random Distribution of Nuclei. *Journal of Chemical Physics*, 8(2):212–224, 1940.

[5] M. Avrami. Granulation, Phase Changes, and Microstructure. Kinetics of Phase Changes. III. *Journal of Chemical Physics*, 9(2):177–184, 1941.

[6] K. Babu and T. S. P. Kumar. Comparison of Austenite Decomposition Models During Finite Element Simulation of Water Quenching and Air Cooling of AISI 4140 Steel. *Metallurgical and Materials Transactions B*, 45B:1530–1544, 2014.

[7] E. C. Bain and N. Y. Dunkirk. The nature of martensite. *Transactions of the American Institute of Mining and Metallurgical Engineers*, 70:25–47, 1924.

[8] E. C. Bain and W. E. Griffiths. An introduction to the iron-chromium-nickel alloys. *Transactions of the American Institute of Mining and Metallurgical Engineers*, 75: 166–211, 1927.

[9] B. Barrogqueiro, J. D. de Oliveira, J. P. da Cruz, and A. Andrade-Campos. Multiscale analysis of heat treatments in steels: Theory and practice. *Finite Elements in Analysis and Design*, 114:39–56, 2016.

[10] B. Barroqueiro, J. P. da Cruz, J. D. de Oliveira, and A. Andrada-Campos. A reduced multiscale model for heat treatments in multiphase steels. *Mechanics of Materials*, 102:7–14, 2016.

[11] T. Bartel and K. Hackl. Multiscale modeling of martensitic phase transformations: On the numerical determination of heterogeneous mesostructures within shape-memory alloys induced by precipitates. *Technische Mechanik*, 30(4):324–342, 2010.

[12] A. Basak and V. I. Levitas. Nanoscale multiphase phase field approach for stress- and temperature-induced martensitic phase transformations with interfacial stresses at finite strains. *Journal of the Mechanics and Physics of Solids*, 113:162–196, 2018.

[13] K.-J. Bathe. *Finite-Element-Methoden.* Springer-Verlag, Berlin, 2nd edition, 2002.

[14] B.-A. Behrens, A. Chugreev, and C. Kock. Macroscopic FE-Simulation of Residual Stresses in Thermo-mechanically Processed Steels considering Phase Transformation Effects. In E. Oñate, D. Owen, D. Peric, M. Chiumenti, and E. de Souza Neto, editors, *COMPLAS XV: proceedings of the XV International Conference on Computational Plasticity: fundamentals and applications*, pages 211–222. CIMNE, 2019.

[15] B.-A. Behrens, J. Schröder, D. Brands, L. Scheunemann, R. Niekamp, A. Chugreev, M. Sarhil, S. Uebing, and C. Kock. Experimental and numerical investigations on the development of residual stresses in thermo-mechanically processed Cr-alloyed steel 1.3505. *metals*, 2019.

[16] B.-A. Behrens, K. Brunotte, H. Wester, and C. Kock. Experimental investigations on the interactions between the process parameters of hot forming and the resulting residual stresses in the component. *Procedia Manufacturing*, 50:706–712, 2020.

[17] B.-A. Behrens, K. Brunotte, H. Wester, and C. Kock. Targeted adjustment of residual stresses in hot-formed components by means of process design based on finite element simulation. *Archive of Applied Mechanics*, 91:3579–3602, 2021.

[18] B.-A. Behrens, J. Schröder, D. Brands, K. Brunotte, H. Wester, L. Scheunemann, S. Uebing, and C. Kock. Numerische Prozessauslegung zur gezielten Eigenspannungseinstellung in warmmassivumgeformten Bauteilen unter Berücksichtigung von Makro- und Mikroskala. *Forschung im Ingenieurwesen (Engineering Research)*, 2021. doi: 10.1007/s10010-021-00482-x.

[19] B.-A. Behrens, J. Schröder, H. Wester, D. Brands, S. Uebing, and C. Kock. Experimental and numerical investigations on the development and stability of residual stresses arising from hot forming processes. In *Forming the Future*, pages 2289–2301. Springer, Cham, 2021.

[20] R. Berthelsen and A. Menzel. Computational homogenisation of thermo-viscoplastic composites: Large strain formulation and weak micro-periodicity. *Computer methods in applied mechanics and engineering*, 348:575–603, 2019.

[21] H. K. D. H. Bhadeshia and J. W. Christian. Bainite in Steels. *Metallurgical Transactions A*, 21A:767–797, 1990.

[22] K. Bhattacharya. *Microstructure of martensite, why it forms and how it gives rise to the shape-memory effect.* Oxford University Press, 2003.

[23] B. Budiansky. On the elastic moduli of some heterogeneous materials. *Journal of the Mechanics and Physics of Solids*, 13:223–227, 1965.

[24] D. Camilleri, N. McPherson, and T. G. F. Gray. The applicability of using low transformation temperature welding wire to minimize unwanted residual stresses and distortions. *International Journal of Pressure Vessels and Piping*, 110:2–8, 2013.

[25] C. Celada-Casero, J. Sietsma, and M. J. Santofimia. The role of austenite grain size in the martensitic transformation in low carbon steels. *Materials and Design*, 167: 107625 (10 pages), 2019.

[26] G. Chatzigeorgioua, N. Charalambakisb, Y. Chemiskya, and F. Meraghnia. Periodic homogenization for fully coupled thermomechanical modeling of dissipative generalized standard materials. *International Journal of Plasticity*, 2016.

[27] J. Chen, Z. Zuo, S. Zhou, X. Wang, Y. Chen, and G. Ling. Study on the Compressive Stress Retention in Quenched Cam of 100Cr6 Steel Based on Coupled Thermomechanical and Metallurgical Modeling. *materials*, 14:5912 (18 pages), 2021.

[28] J. W. Christian. *The Theory of Transformations in Metals and Alloys*. Pergamon, 2002.

[29] M. Cloots, A. Spierings, and K. Wegener. *Schweißen und Wärmebehandlung*, chapter Thermomechanisches Multilayer-Modell zur Simulation von Eigenspannungen in SLM-Proben, pages 59–69. Förderverein der numerischen Analyse der Wärmebehandlungs- und Schweißprozesse, 2013.

[30] D. S. Connolly, C. P. Kohar, R. K. Mishra, and K. Inal. A new coupled thermomechanical framework for modeling formability in transformation induced plasticity steels. *International Journal of Plasticity*, 103:39–66, 2018.

[31] M. Coret, S. Calloch, and A. Combescure. Experimental study of the phase transformation plasticity of 16MND5 low carbon steel under multiaxial loading. *International Journal of Plasticity*, 18:1707–1727, 2002.

[32] S. Denis, A. Simon, and G. Beck. Analysis of the thermomechanical behaviour of steel during martensitic quenching and calculation of internal stresses. pages 211–238. E. Macherauch and V. Hauk (Eds.), 1983.

[33] W. J. Drugan and J. R. Willis. A micromechanics-based nonlocal constitutive equation and estimates of representative volume element size for elastic composites. *Journal of the Mechanics and Physics of Solids*, 44:497–524, 1996.

[34] M. Eden and A. Muntean. Homogenization of a fully coupled thermoelasticity problem for a highly heterogeneous medium with a priori known phase transformations. *Mathematical Methods in the Applied Sciences*, 40:3955–3972, 2016.

[35] H. I. Ene. On linear thermoelasticity of composite materials. *International Journal of Engineering Science*, 21(5):443–448, 1983.

[36] A. C. Eringen. *Mechanics of continua*. John Wiley & Sons, 1967.

[37] A. K. Esfahani, M. Babaei, and S. Sarrami-Foroushani. A numerical model coupling phase transformation to predict microstructure evolution and residual stress during quenching of 1045 steel. *Mathematics and Computers in Simulation*, 179:1–22, 2021.

[38] S. E. Esfahani, I. Ghamarian, V. I. Levitas, and P. C. Collins. Microscale phase field modeling of the martensitic transformation during cyclic loading of NiTi single crystal. *International Journal of Solids and Structures*, 146:80–96, 2018.

[39] J. D. Eshelby. The determination of the elastic field of an ellipsoidal inclusion, and related problems. *Proceedings of the Royal Society London A*, 241:376–396, 1957.

[40] J. D. Eshelby. The elastic field outside an ellipsoidal inclusion. *Proceedings of the Royal Society London A*, 252:561–569, 1959.

[41] E. B. Farahani, B. S. Aragh, and W. J. Mansur. Three-dimensional finite element modelling of welding residual stresses of medium carbon steel pipes with consideration of solid-state austenite-martensite transformation and post-weld heat treatment. *Journal of Materials Design and Applications*, 233(11):2352–2364, 2019.

[42] C. A. Felippa. A historical outline of matrix structural analysis: a play in three acts. *Computers and Structures*, 79:1313–1324, 2001.

[43] R. Fernández, S. Ferreira-Barragáns, J. Ibáñez, and G. González-Doncel. A multiscale analysis of the residual stresses developed in a single-phase alloy cylinder after quenching. *Materials and Design*, 137:117–127, 2018.

[44] F. Feyel. Multiscale FE^2 elastoviscoplastic analysis of composite structures. *Computational Materials Science*, 16:344–354, 1999.

[45] F. Feyel and J.-L. Chaboche. FE^2 multiscale approach for modelling the elastoviscoplastic behavior of long fibre SiC/Ti composite materials. *Computer Methods in Applied Mechanics and Engineering*, 183:309–330, 2000.

[46] F. Fischer. A micromechanical model for transformation plasticity in steels. *Acta metallurgica materials*, 38:1535–1546, 1990.

[47] F. Fischer, M. Berveiller, K. Tanaka, and E. Oberaigner. Continuum mechanical aspects of phase transformations in solids. *Archive of Applied Mechanics*, 64:54–85, 1994.

[48] F. Fischer, Q.-P. Sun, and K. Tanaka. Transformation induced plasticity (TRIP). *Applied Mechanics Reviews*, 49:317–364, 1996.

[49] F. D. Fischer. Transformation induced plasticity in triaxially loaded steel specimens subjected to a martensitic transformation. *European journal of mechanics*, 11:233–244, 1992.

[50] F. D. Fischer. Modeling and Simulation of Transformation Induced Plasticity in Elasto-plastic Materials. In M. Berveiller and F. Fischer, editors, *Mechanics of Solids with Phase Changes*, volume 368 of *CISM Courses and Lectures*, pages 189–237. Springer, 1997.

[51] F. D. Fischer, G. Reisner, E. Werner, K. Tanaka, G. Cailletraud, and T. Antretter. A new view on transformation induced plasticity (TRIP). *International Journal of Plasticity*, 16:723–748, 2000.

[52] J. Fish and A. Wagiman. Multiscale finite element method for a locally nonperiodic heterogeneous medium. *Computational Mechanics*, 12:164–180, 1993.

[53] R. Fleischhauer, M. Božić, and M. Kaliske. A novel approach to computational homogenization and its application to fully coupled two-scale thermomechanics. *Computational Mechanics*, 58:769–796, 2016.

[54] R. Fleischhauer, T. Thomas, J. Kato, K. Terada, and M. Kaliske. Finite thermoelastic decoupled two-scale analysis. *International Journal for Numerical Methods in Engineering*, 121:355–392, 2020.

[55] R. Fuller. Geodesic Structures, August 1965.

[56] E. Gautier, A. Simon, and X. M. Zhang. Transformation plasticity and resulting microstructures for strain-induced martensitic transformation in Fe-Ni-C alloys. In E. Sciences, editor, *European Symposium on Martensitic Transformations*, pages 451–458, 1989.

[57] M. G. D. Geers, V. Kouznetsova, and W. A. M. Brekelmans. Multi-scale first order and second order computational homogenization of microstructures towards ontinua. *International Journal for Numerical Methods in Engineering*, 1:371–386, 2003.

[58] M. G. D. Geers, V. G. Kouznetsova, and W. A. M. Brekelmans. Multi-scale computational homogenization: Trends and challenges. 234(7):2175–2182, 2010. Fourth International Conference on Advanced Computational Methods in Engineering (ACOMEN 2008).

[59] P. Germain, Q. S. Nguyen, and P. Suquet. Continuum Thermodynamics. *Transaction of the American Society of Mechanical Engineers*, 50:1010–1020, 1983.

[60] S. Ghosh, K. Lee, and S. Moorthy. Multiple scale analysis of heterogeneous elastic structures using homogenization theory and voronoi cell finite element method. *International Journal of Solids and Structures*, 32:27–62, 1995.

[61] C. Gierden, J. Kochmann, J. Waimann, B. Svendsen, and S. Reese. A Review of FE-FFT-Based Two-Scale Methods for Computational Modeling of Microstructure Evolution and Macroscopic Material Behavior. *Archives of Computational Methods in Engineering*, pages 1–24, 2022.

[62] G. W. Greenwood and R. H. Johnson. The Deformation of Metals Under Small Stresses During Phase Transformations. *Proceedings of the Royal Society of London. Series A, Mathematical and Physical Sciences*, 283:403–422, 1965.

[63] J. Grum, M. Zupančič, and S. Božič. Measurement and Analysis of Surface Residual Stresses Occurring under Different Quenching Conditions. *Materials Science Forum*, 404-407:629–634, 2002.

[64] J. M. Guedes and N. Kikuchi. Preprocessing and postprocessing for materials based on the homogenization method with adaptive finite element methods. *Computer Methods in Applied Mechanics and Engineering*, 83:143–198, 1990.

[65] K. Gustafson and T. Abe. The third boundary condition - was it Robin's? *Mathematical Intelligencer*, 20(1):63–71, 1998.

[66] D. D. Hall and I. Mudawar. Experimental and numerical study of quenching complex-shaped metallic alloys with multiple, overlapping sprays. *International journal of heat and mass transfer*, 38(7):1201–1216, 1995.

[67] H. Hallberg, P. Håkansson, and M. Ristinmaa. A constitutive model for the formation of martensite in austenitic steels under large strain plasticity. *International Journal of Plasticity*, 23(7):1213–1239, 2007. ISSN 0749-6419.

[68] H. Hallberg, P. Håkansson, and M. Ristinmaa. Thermo-mechanically coupled model for diffusionless phase transformation in austenitic steels. *International Journal of Solids and Structures*, 47:1580–1591, 2010.

[69] G. Han, Z. Guan, Z. Li, M. Zhang, T. Bian, and S. Du. Multi-Scale Modeling and Damage Analysis of Composite with Thermal Residual Stress. *Applied Composite Materials*, 22:289–305, 2015.

[70] Z. Hashin. Analysis of composite materials - a survey. *Journal of Applied Mechanics*, 50:481–505, 1983.

[71] Z. Hashin. The differential scheme and its application to cracked materials. *Journal of the Mechanics and Physics of Solids*, 36(6):719–734, 1988. ISSN 0022-5096.

[72] Z. Hashin and S. Shtrikman. A variational approach to the theory of the elastic behaviour of polycrystals. *Journal of the Mechanics and Physics of Solids*, 10(4): 343–352, Oct. 1962. ISSN 0022-5096.

[73] Z. Hashin and S. Shtrikman. On some variational principles in anisotropic and nonhomogeneous elasticity. *Journal of the Mechanics and Physics of Solids*, 10: 335–342, 1962.

[74] Z. Hashin and S. Shtrikman. A variational approach to the theory of the elastic behaviour of multiphase materials. *Journal of the Mechanics and Physics of Solids*, 11:127–140, 1963.

[75] C. Heinze, A. Pittner, M. Rethmeier, and S. S. Babu. Dependency of martensite start temperature on prior austenite grain size and its influence on welding-induced residual stresses. *Computational Materials Science*, 69:251–260, 2013.

[76] S. Hellebrand, D. Brands, L. Scheunemann, and J. Schröder. A multiscale approach to investigate residual stresses due to targeted cooling of hot bulk formed parts. In A. Zingoni, editor, *Current Perspectives and New Directions in Mechanics, Modelling and Design of Structural Systems: Proceedings of the 8th International Conference on Structural Engineering, Mechanics and Computation (SEMC 2022), Cape Town, South Africa.* 2022.

[77] C. Herrmann, E. Schoof, D. Schneider, F. Schwab, A. Reiter, M. Selzer, and B. Nestler. Multiphase-field model of small strain elasto-plasticity according to the mechanical jump conditions. *Computational Mechanics*, page (14 pages), 2018.

[78] R. Hill. Elastic properties of reinforced solids – some theoretical principles. *Journal of the Mechanics and Physics of Solids*, 11:357–372, 1963.

[79] R. Hill. Theory of mechanical properties of fibre-strengthened materials 3. self-consistent model. *Journal of the Mechanics and Physics of Solids*, 13:189–198, 1965.

[80] H. P. Hougardy. Transformation of Steels During Cooling. In B. Liščić, H. Tensi, and W. Luty, editors, *Theory and Technology of Quenching - A Handbook*, pages 1–18. Springer Science+Business Media, LLC, 1992.

[81] C. Hütter, M. Lin, D. Schicci, M. Hunkel, U. Prahl, and R. Spatschek. A multiscale perspective on the kinetics of solid state transformations with application to bainite formation. *AIMS Materials Science*, 2(4):319–345, 2015.

[82] J. Ilmola, A. Pohjonen, O. Seppälä, O. Leinonen, J. Larkiola, J. Jokisaari, E. Putaansuu, and P. Lehtikangas. Coupled multiscale and multiphysical analysis of hot steel strip mill and microstructure formation during water cooling. *Procedia Manufacturing*, 15:65–71, 2018.

[83] JMatPro. Practical software for materials properties, https://www.sentesoftware.co.uk/jmatpro. Aug. 2018.

[84] W. Johnson and R. F. Mehl. Reaction Kinetics in Processes of Nucleation and Growth. In *American Institute of Mining and Metallurgical Engineers*, 1939.

[85] M. Jung and U. Langer. *Methode der finiten Elemente für Ingenieure, Eine Einführung in die numerischen Grundlagen und Computersimulation.* Springer Vieweg, 2013.

[86] F. A. Kandil, J. D. Lord, A. T. Fry, and P. V. Grant. A Review of Residual Stress Measurement Methods - A Guide to Technique Solution. Technical report, NPL Materials Centre, Teddington, Middlesex, UK, 2001.

[87] S.-H. Kang and Y.-T. Im. Three-dimensional thermo-elastic-plastic finite element modeling of quenching process of plain-carbon steel in couple with phase transformation. *International Journal of Mechanical Sciences*, 49:423–439, 2006.

[88] M. Kästner and W. Volk, editors. *Archive of Applied Mechanics*, volume 91, chapter Special Issue: Forming Induced Residual Stresses - Experiment, Modelling, Simulation, pages 3463–3723. 2021.

[89] H. Kim, J. Lee, F. Barlat, D. Kim, and M.-G. Lee. Experiment and modeling to investigate the effect of stress state, strain and temperature on martensitic phase transformation in TRIP-assisted steel. *Acta Materialia*, 97:435–444, 2015.

[90] F. Klaproth and F. Vollertsen. Residual stress formation relating to peak temperature- and austenite grain size-based phase transformation of S355 steel. *Physics Procdia*, 56:1343–1352, 2014.

[91] K. H. Kloos. Eigenspannungen, Definition und Entstehungsursachen. *Zeitschrift für Werkstofftechnik*, 10:293–302, 1979.

[92] K. Knothe and H. Wessels. *Finite Elemente, eine Einführung für Ingenieure.* Springer, 2017.

[93] D. P. Koistinen and R. E. Marburger. A General Equation Prescribing Extent of Austenite-Martensite Transformation in Pure Fe-C Alloy and Plain Carbon Steels. *Acta Metall*, 7(1):59–60, 1959.

[94] A. N. Kolmogorov. A statistical theory of metal crystallization. *Acad. Nauk USSR, Ser. Math.*, 3:355, 1937.

[95] R. F. Kubler, M. Berveillier, and P. Buessler. Semi phenomenological modelling of the behavior of TRIP steels. *International Journal of Plasticity*, 27(3):299–327, 2011.

[96] I. Kurzhöfer. *Mehrskalen-Modellierung polykristalliner Ferroelektrika basierend auf diskreten Orientierungsverteilungsfunktionen.* PhD thesis, Institut für Mechanik, Universität Duisburg-Essen, 2007.

[97] I. Kurzhöfer, J. Schröder, and H. Romanowski. Simulation of polycrystalline ferroelectrics based on discrete orientation distribution functions. *Proceedings in Applied Mathematics and Mechanics*, 5:307–308, 2005.

[98] M. Labusch, J. Schröder, and M.-A. Keip. An FE^2-Scheme for Magneto-Electro-Mechanically Coupled Boundary Value Problems. In J. Schröder and D. Lupascu, editors, *Ferroic Functional Materials - Experiment, Modeling and Simulation*, volume 581 of *CISM Courses and Lectures*, pages 227–262. Springer, 2018.

[99] J. B. Leblond. Mathematical Modelling of Transformation Plasticity in Steels II: Coupling with Strain Hardening Phenomena. *International Journal of Plasticity*, 5: 873–591, 1989.

[100] J. B. Leblond, G. Mottet, and J. C. Devaux. A theoretical and numerical approach to the plastic behaviour of steels during phase transformations – I derivation of general relations. *Journal of the Mechanics and Physics of Solids*, 34(4):411–432, 1986.

[101] J. B. Leblond, G. Mottet, and J. C. Devaux. A theoretical and numerical approach to the plastic behaviour of steels during phase transformations – II study of the classical plasticity for ideal-plastic phases. *Journal of the Mechanics and Physics of Solids*, 34(4):395–409, 1986.

[102] V. I. Levitas. Thermomechanical theory of martensitic phase transformation in inelastic materials. *International Journal of Solids Structures*, 45:923–947, 1998.

[103] V. I. Levitas. Phase transformations, fracture, and other structural changes in inelastic materials. *International Journal of Plasticity*, 140:102914 (51 pages), 2021.

[104] V. I. Levitas and D. L. Preston. Three-dimensional Landau theory for multivariant stress-induced martensitic phase transformations. I. Austenite → martensite. *Physical Review B*, 66:134206 (9 pages), 2002.

[105] V. I. Levitas, A. V. Idesman, G. B. Olson, and E. Stein. Numerical modelling of martensitic growth in an elastoplastic material. *Philosophical Magazine A*, 82(3): 429–462, 2002.

[106] J. Lubliner. *Plasticity Theory.* Macmillan Publishing Company, New York, 1990.

[107] E. Macherauch and O. Vöhringer. Residual Stresses After Quenching. In B. Liščić, H. Tensi, and W. Luty, editors, *Theory and Technology of Quenching*, pages 117–181. Springer, Berlin, Heidelberg, 1992.

[108] E. Macherauch, H. Wohlfahrt, and U. Wolfstied. *Härterei-Technische Mitteilungen - Zeitschrift für Werkstoffe, Wärmebehandlung, Fertigung*, 28(3):201–211, 1973.

[109] C. L. Magee and H. W. Paxton. *Transformation Kinetics, Microplasticity and Martensite in Fe-31 Ni.* PhD thesis, Carnegie Institute of Teechnology Pittsburgh, 1966.

[110] R. Mahnken, A. Schneidt, and T. Antretter. Macro modelling and homogenization for transformation induced plasticity of a low-alloy steel. *International Journal of Plasticity*, 25(2):183–204, 2009.

[111] R. Mahnken, A. Schneidt, S. Tschumak, and H. J. Maier. On the simulation of austenite to bainite phase transformation. *Computational Materials Science*, 50: 1823–1829, 2011.

[112] R. Mahnken, M. Wolff, A. Schneidt, and M. Böhm. Multi-phase transformations at large strains - Thermodynamic framework and simulation. *International Journal of Plasticity*, 39:1–26, 2012.

[113] R. Mahnken, A. Schneidt, T. Antretter, U. Ehlenbröker, and M. Wolff. Multi-scale modeling of bainitic phase transformation in multi-variant polycrystalline low alloy steels. *International Journal of Solids and Structures*, 54:156–171, 2015.

[114] M. Mamivand, M. A. Zaeem, and H. E. Kadiri. A review on phase field modeling of martensitic phase transformation. *Computational Materials Science*, 77:304–311, 2013.

[115] Z. Marciniak and K. Kuczyński. Limit strains in the processes of stretch-forming sheat metal. *International Journal of Mechanical Sciences*, 9(9):609–620, 1967.

[116] I. Medina-Juárez, J. A. de Oliveria, R. J. Moat, and F. García-Pastor. On the Accuracy of Finite Element Models Predicting Residual Stresses in Quenched Stainless Steel. *Metals*, 9(12):1308(19 pages), 2019.

[117] P. Michaleris, K. Dantzig, and D. Tortorelli. Minimization of welding residual stress and distortion in large structures. *Welding Journal - New York*, 78:361–366, 1999.

[118] J. C. Michel, H. Moulinec, and P. Suquet. Effective properties of composite materials with periodic microstructure: a computational approach. *Computer Methods in Applied Mechanics and Engineering*, 172:109–143, 1999.

[119] C. Miehe. *Kanonische Modelle multiplikativer Elasto-Plastizität. Thermodynamische Formulierung und Numerische Implementation.* Universität Hannover, Institut für Baumechanik und Numerische Mechanik, Bericht-Nr. F93/1, 1993. Habilitationsschrift.

[120] C. Miehe and A. Koch. Computational micro-to-macro transitions of discretized microstructures undergoing small strains. *Archive of Applied Mechanics*, 72(4):300–317, 2002.

[121] C. Miehe, J. Schotte, and J. Schröder. Computational micro-macro transitions and overall moduli in the analysis of polycrystals at large strains. *Computational Materials Science*, 16(1-4):372–382, 1999. ISSN 0927-0256.

[122] C. Miehe, J. Schröder, and J. Schotte. Computational homogenization analysis in finite plasticity. Simulation of texture development in polycrystalline materials. *Computer Methods in Applied Mechanics and Engineering*, 171(3-4):387–418, 1999.

[123] M. Militzer, J. J. Hoyt, N. Provatas, J. Rottler, C. W. Sinclair, and H. S. Zurob. Multiscale Modeling of Phase Transformations in Steels. *The Minerals, Metals & Materials Society*, 66(5):740–746, 2014.

[124] W. Mitter. *Umwandlungsplastizität und ihre Berücksichtigung bei der Berechnung von Eigenspannungen.* Gebrüder Borntraeger Berlin Stuttgart, 1987.

[125] E. Monteiro, J. Yvonnet, and Q. C. He. Computational homogenization for nonlinear conduction in heterogeneous materials using model reduction. *Computational Materials Science*, 42:704–712, 2008.

[126] T. Mori and K. Tanaka. Average stress in matrix and average elastic energy of materials with misfitting inclusions. *Acta Mechanica*, 21:571–574, 1973.

[127] H. Moulinec and P. Suquet. A numerical method for computing the overall response of nonlinear composites with complex microstructure. *Computer Methods in Applied Mechanics and Engineering*, 157:69–94, 1998.

[128] A. K. Nallathambi, Y. Kaymak, E. Specht, and A. Bertram. Distortion and Residual Stresses during Metal Quenching Process. In *Micro-Macro-interaction*, pages 145–157. Springer, 2008.

[129] Neper. Polycrystal Generation and Meshing, https://neper.info/. 2022.

[130] Z. Nishiyama. *Martensitic transformation.* Elsevier, 1978.

[131] A. N. Norris. A differential scheme for the effective moduli of composites. *Mechanics of Materials*, 4(1):1–16, 1985. ISSN 0167-6636.

[132] R. W. Ogden. *Non-linear elastic deformations.* Dover Publications, 1984.

[133] P. Olle. *Numerische und experimentelle Untersuchungen zum Presshärten.* PhD thesis, Fakultät für Maschinenbau, Gottfried Wilhelm Leibniz Universität Hannover, 2010.

[134] G. B. Olson and M. Azrin. Transformation Behavior of TRIP Steels. *Army Materials and Mechanics Research Center Watertown*, 1977.

[135] M. Ortiz and J. B. Martin. Symmetry-preserving return mapping algorithms and incrementally extremal paths: a unification of concepts. *International Journal for Numerical Methods in Engineering*, 28:1839–1853, 1989.

[136] M. Ortiz and E. P. Popov. Accuaracy and stability of integration algorithms for elastoplastic constitutive relations. *International Journal for Numerial Methods in Engineering*, 21:1561–1576, 1985.

[137] M. Ostoja-Starzewski. The use, misuse, and abuse of stochastic random media. In *Proceedings of European Conference on Computational Mechanics*, 2001.

[138] I. Özdemir, W. A. M. Brekelmans, and M. G. D. Geers. Computational homogenization for heat conduction in heterogeneous solids. *International Journal for Numerical Methods in Engineering*, 73:185–204, 2008a.

[139] I. Özdemir, W. A. M. Brekelmans, and M. G. D. Geers. FE^2 computational homogenization for the thermo-mechanical analysis of heterogeneous solids. *Computer Methods in Applied Mechanics and Engineering*, 198:6, 2008b.

[140] B. Paliwal, R. D. Moser, C. D. Barrett, W. R. Whittington, H. Rhee, Y. Paudel, S. Mujahid, and H. E. Kadiri. Martensitic microstructure evolution in austenitic steel: A thermomechanical polycrystalline phase field study. *Journal of materials research*, 36:1376–1399, 2020.

[141] M. Pernach, K. Bzowski, L. Rauch, and M. Pietrzyk. Analysis of predictive capabilities of multiscale phase transformation models based on the numerical solution of heat transfer and diffusion equations. *International Journal for Multiscale Computational Engineering*, 15(5):413–430, 2017.

[142] S. Petit-Grostabussiat, L. Taleb, and J.-F. Jullien. Experimental results on classical plasticity of steels subjected to structural transformations. *International Journal of Plasticity*, 20:1371–1386, 2004.

[143] M. Pietrzyk, J. Kusiak, R. Kuziak, L. Madej, D. Szeliga, and R. Golab. Conventional and Multiscale Modeling of Microstructure Evolution During Laminar Cooling of DP Steel Strips. *Metallurgical and Materials Transactions A*, 45A:5835–5851, 2014.

[144] S. Prüger, A. Ghandi, and D. Balzani. Influence of microstructure morphology on multi-scale modeling of low-alloyed TRIP-steel. *Engineering Computations*, 35(2): 499–528, 2018.

[145] A. Reuss. Berechnung der Fließgrenze von Mischkristallen auf Grund der Plastizitätsbedingung für Einkristalle. *Zeitschrift für angewandte Mathematik und Mechanik*, 9(1):49–58, 1929. ISSN 1521-4001.

[146] C. Rohrbach, editor. *Handbuch für experimentelle Spannungsanalyse.* Springer-Verlag, 1989.

[147] A. L. Roitburd. Martensitic Transformation as a Typical Phase Transformation in Solids. *Solid State Physics*, 33:317–390, 1978.

[148] N. S. Rossini, M. Dassisti, K. Y. Benyounis, and A. G. Olabi. Methods of measuring residual stresses in components. *Materials and Design*, 35:572–588, 2012.

[149] F. Roters, P. Eisenlohr, L. Hantcherli, D. D. Tjahjanto, T. R. Bieler, and D. Raabe. Overview of constitutive laws, kinematics, homogenization and multiscale methods in crystal plasticity finite-element modeling: Theory, experiments, applications. *Acta Materialia*, 58:1152–1211, 2009.

[150] E. Sanchez-Palencia. Homogenization in mechanics. A survey of solved and open problems. *Rend. Sem. Mat. Univers. Politecn. Torino*, 44:1–45, 1986.

[151] O. Schenk and K. Gärtner. Solving unsymmetric sparse systems of linear equations with PARDISO. *Journal of Future Generation Computer Systems*, 20:475–487, 2004.

[152] D. S. Schicchi, A. Caggiano, M. Hunkel, and E. A. B. Koenders. Thermodynamically consistent multiscale formulation of a thermo-mechanical problem with phase transformations. *Continuum Mechanics and Thermodynamics*, 31:273–299, 2019.

[153] R. Schmitt. *A Phase Field Model for Martensitic Transformations and Crystal Plasticity*. PhD thesis, TU Kaiserslautern, 2015.

[154] R. Schmitt, C. Kuhn, R. Müller, and K. Bhattacharya. Crystal Plasticity and Martensitic Transformations - A Phase Field Approach. *Technische Mechanik*, 34: 23–28, 2014.

[155] D. Schneider, S. Schmid, M. Selzer, T. Böhlke, and B. Nestler. Small strain elasto-plastic multiphase-field model. *Computational Mechanics*, 55:27–35, 2015.

[156] D. Schneider, F. Schwab, E. Schoof, A. Reiter, C. Herrmann, M. Selzer, T. Böhlke, and B. Nestler. On the stress calculation within phase-field approaches: a model for finite deformations. *Computational Mechanics*, 60:203–217, 2017.

[157] D. Schneider, E. Schoof, O. Tschukin, A. Reiter, C. Herrmann, F. Schwaab, M. Selzer, and B. Nestler. Small strain multiphase-field model accounting for configurational forces and mechanical jump conditions. *Computational Mechanics*, 61: 277–295, 2018.

[158] E. Schoof. *Chemomechanische Modellierung der Wärmebehandlung von Stählen mit der Phasenfeldmethode*. PhD thesis, Karlsruher Institut für Technologie, 2021.

[159] E. Schoof, D. Schneider, N. Streichhan, T. Mittnacht, M. Selzer, and B. Nestler. Multiphase-field modeling of martensitic phase transformation in a dual-phase microstructure. *International Journal of Solids and Structures*, 134(1):181–194, 2017.

[160] E. Schoof, C. Herrmann, N. Streichhan, M. Selzer, D. Schneider, and B. Nestler. On the multiphase-field modeling of martensitic phase transformation in dual-phase steel using J2-viscoplasticity. *Modelling and Simulation in Materials Science and Engineering*, 27:025010 (24 pages), 2019.

[161] J. Schröder. *Homogenisierungsmethoden der nichtlinearen Kontinuumsmechanik unter Beachtung von Stabilitätsproblemen*. Bericht aus der Forschungsreihe des Instituts für Mechanik (Bauwesen), Lehrstuhl I, Universität Stuttgart, 2000. Habilitation.

[162] J. Schröder. A numerical two-scale homogenization scheme: the FE^2–method. In J. Schröder and K. Hackl, editors, *Plasticity and Beyond - Microstructures, Crystal-Plasticity and Phase Transitions*, volume 550 of *CISM Courses and Lectures*, pages 1–64. Springer, 2014.

[163] J. Schröder, M. Labusch, and M.-A. Keip. Algorithmic two-scale transition for magneto-electro-mechanically coupled problems - FE^2-scheme: Localization and homogenization. *Computer Methods in Applied Mechanics and Engineering*, 302:253–280, 2016.

[164] A. Sengupta, P. Papadopoulos, and R. L. Taylor. Multiscale finite element modeling for superelastic in Nitinol polycrystals. *Computational Mechanics*, 43:573–584, 2009.

[165] A. Sengupta, P. Papadopoulos, and R. L. Taylor. A multiscale finite element method for modeling fully coupled thermomechanical problems in solids. *International Journal for Numerical Methods in Engineering*, 91:1386–1405, 2012.

[166] J. Simo and T. Hughes. *Computational Inelasticity.* Springer-Verlag, 1998.

[167] J. Simo and C. Miehe. Associative coupled thermoplasticity at finite strains: Formulation, numerical analysis and implementation. *Computer Methods in Applied Mechanics and Engineering*, 98(1):41–104, 1992.

[168] J. C. Simo. A framework for finite strain elastoplasticity based on maximum plastic dissipation and the multiplicative decomposition: Part I. continuum formulation. *Computer Methods in Applied Mechanics and Engineering*, 66:199–219, 1988.

[169] C. Simsir and C. H. Gür. 3D FEM simulation of steel quenching and investigation of the effect of asymmetric geometry on residual stress distribution. *Journal of Materials Processing Technology*, 207:211–221, 2008.

[170] R. Smit, W. Brekelmans, and H. Meijer. Prediction of the mechanical behavior of nonlinear heterogeneous systems by multi-level finite element modeling. *Computer Methods in Applied Mechanics and Engineering*, 155:181–192, 1998.

[171] R. J. M. Smit. *Toughness of heterogeneous polymeric systems.* PhD thesis, Eindhoven University of Technology, 1998.

[172] I. Steinbach and F. Pezzolla. A generalized field method for multiphase transformations using interface fields. *Physica D: Nonlinear Phenomena*, 134(4):385–393, 1999. ISSN 0167-2789.

[173] I. Steinbach, F. Pezzolla, B. Nestler, M. Seeßelberg, R. Prieler, G. J. Schmitz, and J. L. L. Rezende. A phase field concept for multiphase systems. *Physica D: Nonlinear Phenomena*, 94(3):135–147, 1996. ISSN 0167-2789.

[174] M. Stroeven, H. Askes, and L. J. Sluys. A numerical approach to determine representative volumes for granular materials. In *Fifth World Congress on Computational Mechanics (WCCM V).* Vienna University of Technology, 2002.

[175] P. M. Suquet. *Elements of homogenization for inelastic solid mechanics*, pages 193–278. Springer, 1987.

[176] M. Takahashi and H. K. D. H. Bhadeshia. Model for transition from upper to lower bainite. *Materials Science and Technology*, 6:592–603, 1990.

[177] R. L. Taylor. *FEAP – A Finite Element Analysis Program Version 8.2 User Manual.* Department of Civil and Environmental Engineering, University of California at Berkeley, Berkeley, California 94720-1710, March 2008.

[178] I. Temizer. On the asymptotic expansion treatment of two-scale finite thermoelasticity. *International Journal of Engineering Science*, 53:74–84, 2012.

[179] I. Temizer and P. Wriggers. Homogenization in finite thermoelasticity. *Journal of the Mechanics and Physics of Solids*, 59:344–372, 2011.

[180] I. Temizer and T. I. Zohdi. A numerical method for homogenization in non-linear elasticity. *Computational Mechanics*, 40:281–298, 2007.

[181] K. Terada and N. Kikuchi. A class of general algorithms for multi-scale analyses of heterogeneous media. *Computer Methods in Applied Mechanics and Engineering*, 190(40-41):5427–5464, 2001.

[182] K. Terada, M. Hori, T. Kyoya, and N. Kikuchi. Simulation of the multi-scale convergence in computational homogenization approach. *International Journal of Solids and Structures*, 37:2285–2311, 2000.

[183] K. Terada, M. Kurumatani, T. Ushida, and N. Kikuchi. A method of two-scale thermo-mechanical analysis for porous solids with micro-scale heat transfer. *Computational Mechanics*, 46:269–285, 2010.

[184] J. Tiaden, B. Nestler, H. J. Diepers, and I. Steinbach. The multiphase-field model with an integrated concept for modelling solute diffusion. *Physica D: Nonlinear Phenomena*, 115(1):73–86, 1998. ISSN 0167-2789.

[185] Y. Tian, Z. Tan, H. Li, B. Gao, J. Zhu, Y. Liu, and M. Zhang. A new finite element model for Mn-Si-Cr bainitic/martensitic product quenching process: Simulation and experimental validation. *Journal of Materials Processing Technology*, 294:117137, 2021.

[186] C. Truesdell and W. Noll. The nonlinear field theories of mechanics. In S. Flügge, editor, *Encyclopedia of Physics*, volume III/3. Springer, 1965.

[187] S. Turteltaub and A. S. J. Suiker. A multiscale thermomechanical model for cubic to tetragonal martensitic phase transformations. *International Journal of Solids and Structures*, 43:4509–4545, 2006.

[188] S. Uebing, D. Brands, L. Scheunemann, and J. Schröder. A numerical study of the effect of phase evolution on residual stresses during cooling. *Proceedings of Applied Mathematics and Mechanics*, 20(1):e202000236, 2020.

[189] S. Uebing, D. Brands, L. Scheunemann, C. Kock, H. Wester, B.-A. Behrens, and J. Schröder. Residual Stresses in Hot Bulk Formed Parts - A Phenomenological Approach for the Austenite-to-Martensite Phase Transformation. *13th ICTP*, pages 2345–2355, 2021.

[190] S. Uebing, D. Brands, L. Scheunemann, and J. Schröder. On the evolution of residual stresses due to cooling considering martensitic phase transformation. *Proceedings in Applied Mathematics and Mechanics*, 21(1):e202100031, 2021.

[191] S. Uebing, D. Brands, L. Scheunemann, and J. Schröder. Residual stresses in hot bulk formed parts - Two-scale approach for austenite-to-martensite phase transformation. *Archive of Applied Mechanics*, 91:545–562, 2021. doi: 10.10007/s00419-020-01836-7.

[192] S. Uebing, D. Brands, L. Scheunemann, and J. Schröder. Residual stresses in hot bulk formed parts - Microscopic stress analysis for austenite-to-martensite phase transformation. *Archive of Applied Mechanics*, 91:3603–3625, 2021.

[193] W. Voigt. *Lehrbuch der Kristallphysik.* B. G. Teubner, 1910.

[194] W. Volk, editor. *Production Engineering, Research and Development*, volume 13, chapter Special Issue: Residual Stresses in Production Technology, pages 119–246. 2019.

[195] W. Volk, editor. *Forschung im Ingenieurwesen (Engineering Research)*, volume 85, chapter SPP 2013, pages 703–837. 2021.

[196] Y. Wang and A. G. Khachaturyan. Three-dimensional field model and computer modeling of martensitic transformations. *Acta materialia*, 45(2):759–773, 1997.

[197] Y. Wang and A. G. Khachaturyan. Multi-scale phase field approach to martensitic transformations. *Materials Science and Engineering A*, 438–440:55–63, 2006.

[198] M. S. Wechsler. On the theory of the formation of martensite. *Trans Aime*, 197: 1503–1515, 1953.

[199] D. Wicht, M. Schneider, and T. Böhlke. Computing the effective response of heterogeneous materials with thermomechanically coupled constituents by an implicit fast Fourier transform-based approach. *International Journal of Numerical Methods in Engineering*, 122:1307–1332, 2020.

[200] J. R. Willis. Variational and related methods for the overall properties of composites. *Advances in Applied Mechanics*, 21, 1983.

[201] P. J. Withers and H. K. D. H. Bhadeshia. Residual stress Part 1 - Measurement techniques. *Materials Science and Technology*, 17:355–365, 2001.

[202] P. J. Withers and H. K. D. H. Bhadeshia. Residual stress Part 2 - Nature and origins. *Materials Science and Technology*, 17:355–365, 2001.

[203] M. Wolff, S. Boettcher, and M. Böhm. Phase transformations in steel in the multiphase case - general modelling and parameter identification. Technical Report 07-02, Zentrum für Technomathematik, Universität Bremen, 2007.

[204] M. Wolff, F. Frerichs, and N. Lysenko. Bewerten von Modellen der Martensitbildung bei nichtmonotoner Abkühlung für den Stahl 100Cr6. Technical Report 07-01, Zentrum für Technomathematik, Universität Bremen, 2007.

[205] M. Wolff, M. Böhm, and D. Helm. Material behavior of steel - Modeling of complex phenomena and thermodynamic consistency. *International Journal of Plasticity*, 24:746–774, 2008.

[206] P. Wriggers. *Nichtlineare Finite-Element-Methoden.* Springer-Verlag, Berlin, 2001.

[207] H. K. Yeddu. Phase-field modeling of austenite grain size effect on martensitic transformation in stainless steels. *Computational Materials Science*, 154:75–83, 2018.

[208] H. K. Yeddu, A. Malik, J. Ågren, G. Amberg, and A. Borgenstam. Three-dimensional phase-field modeling of martensitic microstructure evolution in steels. *Acta materialia*, 60:1538–1547, 2012.

[209] J. Zeman. *Analysis of Composite Materials with Random Microstructure*. PhD thesis, University of Prague, 2003.

[210] O. Zienkiewicz and R. Taylor. *The finite element method - for solid and structural mechanics*. Elsevier, 6 edition, 2005.

Der Lebenslauf ist in der Online-Version aus Gründen des Datenschutzes nicht enthalten.

In dieser Schriftenreihe bisher erschienene Berichte:

Nr. 1 (2004) *Ein Modell zur Beschreibung finiter anisotroper elasto-plastischer Deformationen unter Berücksichtigung diskreter Rissausbreitung*, J. Löblein, Dissertation, 2004.

Nr. 2 (2006) *Polyconvex Anisotropic Energies and Modeling of Damage applied to Arterial Walls*, D. Balzani, Dissertation, 2006.

Nr. 3 (2006) *Kontinuumsmechanische Modellierung ferroelektrischer Materialien im Rahmen der Invariatentheorie*, H. Romanowski, Dissertation, 2006.

Nr. 4 (2007) *Mehrskalen-Modellierung polykristalliner Ferroelektrika basierend auf diskreten Orientierungsverteilungsfunktionen*, I. Kurzhöfer, Dissertation, 2007.

Nr. 5 (2007) *Proceedings of the First Seminar on the Mechanics of Multifunctional Materials*, J. Schröder, D.C. Lupascu, D. Balzani (Ed.), Tagungsband, 2007.

Nr. 6 (2008) *Zur Modellierung und Simulation diskreter Rissausbreitungsvorgänge*, O. Hilgert, Dissertation, 2008.

Nr. 7 (2009) *Least-Squares Mixed Finite Elements for Solid Mechanics*, A. Schwarz, Dissertation, 2009.

Nr. 8 (2010) *Design of Polyconvex Energy Functions for All Anisotropy Classes*, V. Ebbing, Dissertation, 2010.

Nr. 9 (2012) *Modeling of Electro-Mechanically Coupled Materials on Multiple Scales*, M.-A. Keip, Dissertation, 2012.

Nr. 10 (2012) *Geometrical Modeling and Numerical Simulation of Heterogeneous Materials*, D. Brands, Dissertation, 2012.

Nr. 11 (2012) *Modeling and simulation of arterial walls with focus on damage and residual stresses*, S. Brinkhues, Dissertation, 2012.

Nr. 12 (2014) *Proceedings of the Second Seminar on the Mechanics of Multifunctional Materials*, J. Schröder, D.C. Lupascu, M.-A. Keip, D. Brands (Ed.), Tagungsband, 2014.

Nr. 13 (2016) *Mixed least squares finite element methods based on inverse stress-strain relations in hyperelasticity*, B. Müller, Dissertation, 2016.

Nr. 14 (2016) *Electromechanical Modeling and Simulation of Thin Cardiac Tissue Constructs*, R. Frotscher, Dissertation, 2016.

Nr. 15 (2017) *Least-squares mixed finite elements for geometrically nonlinear solid mechanics*, K. Steeger, Dissertation, 2017.

Nr. 16 (2017)	*Scale-Bridging of Elasto-Plastic Microstructures using Statistically Similar Representative Volume Elements*, L. Scheunemann, Dissertation, 2017.
Nr. 17 (2018)	*Modeling of Self-healing Polymers and Polymeric Composite Systems*, S. Specht, Dissertation, 2017.
Nr. 18 (2018)	*Proceedings of the Third Seminar on the Mechanics of Multifunctional Materials*, J. Schröder, D.C. Lupascu, H. Wende, D. Brands (Ed.), Tagungsband, 2018.
Nr. 19 (2018)	*Least-squares finite element methods with applications in fluid and solid mechanics*, C. Nisters, Dissertation, 2018.
Nr. 20 (2018)	*A two-scale homogenization scheme for the prediction of magneto-electric product properties*, M. Labusch, Dissertation, 2018.
Nr. 21 (2019)	*Modeling the passive mechanical response of soft tissues: constitutive modeling approaches, efficient parameter selection and subsequent adjustments due to residual stresses*, M. von Hoegen, Dissertation, 2019.
Nr. 22 (2019)	*Constitutive modeling of female pelvic floor dysfunctions and reconstructive surgeries using prosthetic mesh implants*, A. Bhattarai, Dissertation, 2019.
Nr. 23 (2019)	*A contribution to stress-displacement based mixed galerkin finite elements for hyperelasticity*, N. Viebahn, Dissertation, 2019.
Nr. 24 (2020)	*Gefrier- und Auftauprozesse in gesättigten porösen Materialien - ein Modellierungskonzept im Rahmen der Theorie poröser Medien*, W.M. Bloßfeld, Dissertation, 2020.
Nr. 25 (2021)	*Electromechanical modelling and simulation of hiPSC-derived cardiac cell cultures*, A. Jung, Dissertation, 2021.
Nr. 26 (2021)	*Mixed and Hybrid Least-Squares FEM in Nonlinear Solid Mechanics*, M. Igelbüscher, Dissertation, 2021.
Nr. 27 (2023)	*The Material Point Method for dynamic Metal Processing*, S. Maassen, Dissertation, 2023.
Nr. 28 (2023)	*Modeling of Fluid-Structure Interactions with the Least-Squares FEM*, S. Averweg, Dissertation, 2023.